Bioinspired synthesis and self-assembly of hybrid organic–inorganic nanomaterials

by

Honghu Zhang

A dissertation submitted to the graduate faculty

in partial fulfillment of the requirements for the degree of

DOCTOR OF PHILOSOPHY

Major: Materials Science and Engineering

Program of Study Committee:
Mufit Akinc, Co-Major Professor
Surya K. Mallapragada, Co-Major Professor
Kaitlin Bratlie
David C. Jiles
Xiaoli Tan

Iowa State University

Ames, Iowa

2016

TABLE OF CONTENTS

Page

ACKNOWLEDGMENTS

First of all, I would like to express my sincere gratitude to my major professors Dr. Mufit Akinc and Dr. Surya Mallapragada for their guidance and support throughout the course of my Ph.D. study and related research. I am grateful for their patience, enthusiasm, encouragement, immense knowledge and great insight. Their supervisions have led to marked improvements in my knowledge, experience and capabilities, and have a profound impact on my career and life in the future. I sincerely thank my committee members Dr. Kaitlin Bratlie, Dr. David C. Jiles and Dr. Xiaoli Tan for their continuous support and insightful comments.

I also would like to offer my appreciation to all my collaborators in the bioinspired materials project. I thank Dr. David Vaknin for his efforts to train me to think critically and work dedicatedly by sharing a wealth of first-hand experience in science, Dr. Alex Travesset for his thoughtful discussion and valuable inspiration, Dr. Wenjie Wang for his patient helps and constructive suggestions as both a mentor and a friend. I thank all other collaborators including Dr. Marit Nilsen-Hamilton, Dr. Klaus Schmidt-Rohr, Dr. Andrew Hillier, Dr. Thomas Koschny, Dr. Tanya Prozorov, Dr. Shuren Feng, Dr. Pierre E. Palo, Dr. Lee Bendickson and Nathan Horst for their kind collaborations. I also acknowledge APS beam scientists Dr. Xiaobing Zuo, Dr. Hua Zhou and Dr. Ivan Kuzmenko for their technical support in X-ray scattering which is crucial to this dissertation.

My thanks go to current and previous group members from Dr. Akinc's group: Dr. Pratik Ray, Dr. Simge Cinar, Dr. Gaoyuan Ouyang, Boyce Chang, Tyler Bell, Dr. Tuba Karahan, Qinwen Ge, Landi Zhong, Dr. Mohammad Imteyaz Ahmad, Dr. Sergiy Markutsya,

Weijie Wang, Kevin Severs and Luke Klosterman, and from Dr. Mallapragada's group: Dr. Xunpei Liu, Dr. Feng Jia, Srikanth Nayak, Dr. Metin Uz, Benjamin Schlichtmann, Sujata Senapati, Dr. William Colonna, Dr. Anup Sharma, Dr. Justin Adams and Dr. Vikash Malik. In particular, I really appreciate Dr. Xunpei Liu's continuous help through the past years.

I would like to thank my friends who have shown support over the past years in Ames. I am grateful for the enjoyable and unforgettable experience at Iowa State University.

Lastly I am grateful to my parents, my wife, my sister and my aunt for their unconditional care, love and support. Special thanks go to my beloved wife, Peiyu Guan. She is the Captain on the wonderful journey of life.

ABSTRACT

Nature is replete with complex organic–inorganic hierarchical materials of diverse yet specific functions. These materials are intricately designed under physiological conditions through biomineralization and biological self-assembly processes. Tremendous efforts have been devoted to investigating mechanisms of such biomineralization and biological self-assembly processes as well as gaining inspiration to develop biomimetic methods for synthesis and self-assembly of functional nanomaterials. In this work, we focus on the bioinspired synthesis and self-assembly of functional inorganic nanomaterials templated by specialized macromolecules including proteins, DNA and polymers. The *in vitro* biomineralization process of the magnetite biomineralizing protein Mms6 has been investigated using small-angle X-ray scattering. Templated by Mms6, complex magnetic nanomaterials can be synthesized on surfaces and in the bulk. DNA and synthetic polymers have been exploited to construct macroscopic two- and three-dimensional (2D and 3D) superlattices of gold nanocrystals. Employing X-ray scattering and spectroscopy techniques, the self-assembled structures and the self-assembly mechanisms have been studied, and theoretical models have been developed. Our results show that specialized macromolecules including proteins, DNA and polymers act as effective templates for synthesis and self-assembly of nanomaterials. These bottom-up approaches provide promising routes to fabricate hybrid organic–inorganic nanomaterials with rationally designed hierarchical structures, targeting specific functions.

CHAPTER 1. GENERAL INTRODUCTION

1.1 Dissertation Organization

This dissertation covers two major topics related to bioinspired nanomaterials – synthesis and self-assembly. It is organized into eight chapters, including one chapter on a literature review (Chapter 1), three chapters on bioinspired synthesis of magnetic nanomaterials (Chapter 2–4), three chapters on bioinspired self-assembly of plasmonic nanomaterials (Chapter 5–7) and one chapter on conclusions and future work (Chapter 8).

Chapter 1 is a general introduction including a literature review related to bioinspired synthesis and self-assembly of nanomaterials templated by specialized macromolecules including proteins, DNA and polymers. Magnetotactic bacteria and the biomineralization protein Mms6 are introduced.

Chapters 2–4 focus on the bioinspired synthesis of magnetic nanomaterials in the bulk and on surfaces, and investigating the role of the biomineralization protein Mms6 in the *in vitro* synthesis mechanism. Chapter 2 is modified from a paper published in *Langmuir*. In this paper, small-angle X-ray scattering (SAXS) was employed to study morphological transformations of Mms6 in the absence and presence of iron ions to probe the mechanism of Mms6 biomineralization *in vitro*. As the first author, my contribution to this work includes new experimental design, sample preparation, SAXS measurements, SAXS data processing and partial manuscript writing. SAXS data analysis and major manuscript writing were done by the co-author Wenjie Wang. Chapter 3 is revised from a paper published in *Journal of Magnetism and Magnetic Materials*. In this work, we investigated aqueous-phase synthesis of magnetite nanoparticles with tunable sizes and magnetic properties using Gd doping, with and without

Mms6. My contribution as the first author includes experimental design, sample preparation, sample characterization (XRD, XPS and TEM), all the data analysis and manuscript writing. Chapter 4 is modified from a paper published in *Industrial & Engineering Chemistry Research*. This work focused on fabrication of magnetite nanoparticles on surfaces mediated by the immobilized Mms6 through hydrophobic interactions with solid substrates. This work was initiated by the first author Xunpei Liu, the former graduate student working on this project. As the joint first author, my contribution includes partial sample preparation, sample characterization (SEM, EDS and XRD), data analysis (XPS) and partial manuscript writing.

Chapters 5–7 deal with the use of DNA as well as synthetic polymer templates in the presence of salts to self-assemble nanoparticle assemblies in two and three dimensions, and using X-ray scattering methods to understand the assembly processes. Chapter 5 is revised from a paper published in *Advanced Materials Interfaces*. In this paper, we reported that DNA-functionalized gold nanoparticles formed two-dimensional (2D) superlattices at the air–water interfaces induced by divalent salts. My contribution as the first author to this work includes the experimental design, sample preparation, X-ray scattering and spectroscopy measurements, data analysis (SAXS, GISAXS and fluorescence) and writing manuscript. The theoretical analysis was provided by the co-author Alex Travesset. Chapter 6 is modified from a paper published in *Nanoscale*. In this study, we found that polyethylene-glycol-capped gold nanoparticles (PEG-AuNPs) self-assembled into macroscopic and tunable superlattices at the air–water interfaces by adjusting concentrations of a salt (K_2CO_3) and nanoparticles. As the first author, my contribution to this work includes experimental design, sample preparation, samples characterization (GISAXS, reflectivity, SAXS, DLS and TGA), data analysis (GISAXS, SAXS and phase diagram) and manuscript writing. The theoretical modeling was done by the co-author Alex

Travesset. Chapter 7 is revised from a paper to be submitted to a journal. This paper focuses on 3D self-assembly of PEG-AuNPs via colloidal destabilization in the presence of high concentrations of K_2CO_3. My contribution as the first-author includes sample preparation and characterization (SAXS, DLS and UV–Vis), all the data analysis and writing manuscript. The theoretical work was performed by the co-author Alex Travesset.

Chapter 8 summarizes the major findings in this dissertation. Perspective towards the future direction is provided.

1.2 Literature Review

1.2.1 Biomineralization

As a gift from evolution, living organisms of all sorts, from unicellular bacteria to complex multicellular plants and animals, have the capability to exploit metal ions selectively obtained from the local environments to construct inorganic–organic hierarchical materials for diverse functions.[1-5] This process, named biomineralization, exhibits high level of control over the composition, structure, size, morphology and aggregation of biominerals.[3, 4, 6, 7] Almost every organism has evolved its own strategies for synthesizing biogenic minerals that are unique to that species and tailor-made for their functions.[1-4] Thus, nature has succeeded in giving rise to an impressive variety of hybrid materials of amazing complexity, arranged from nanoscale to the macroscale, and fascinating properties, such as structural support, protection, locomotion, navigation and storage.[1-7] Both the life and the environment have been fundamentally changed by the advent of biomineralization, from formation of bones, teeth and shells to the global cycling of elements including fossilization.[3-5]

It is known that about 26 essential elements are required by living organisms. Around half of them are incorporated in biominerals.[3] Among these, calcium has a distinguished place as

it is widespread and the principal constituent of skeletal structures such as bones and shells.[3] Bones are composed of calcium phosphate, while shells are built from calcium carbonate. Bone is composed of mineralized collagen fibrils, in which hydroxyapatite ($Ca_{10}(PO_4)_6(OH)_2$) crystals are embedded, with complex structures, described in terms of up to 7 hierarchical levels of organization that is optimized to the functional need.[8-12] Calcium carbonate minerals have six different structures, and of these polymorphs, calcite ($CaCO_3$, trigonal) and aragonite ($CaCO_3$, orthorhombic) are the most thermodynamically stable forms under ambient conditions,[3, 13] and are typically present in mollusk shells, sea urchin spines, sponges and corals.[2, 3] Interestingly, inorganically synthetic calcite is very brittle as it cleaves easily along the "cleavage rhombohedron" plane, while aragonite usually has a strong tendency to form spherulitic cluster of crystals with high porosity.[14] However, organisms overcome these limitations either by having proteins occluded inside the calcite crystal and introducing anisotropic fracture behavior, or by organizing of aragonite into large superstructures where plate-shaped aragonite crystals are arranged into parallel layers that are separated by a sheet of organic matrix.[2, 3, 14-16] Even though most biominerals are ionic salts, many unicellular organisms produce remarkable structures from amorphous silica.[3, 5] The famous representatives of biosilicifying organisms are the diatoms and radiolarians, since they use the silica to build their cell walls and microskeletons, which are nano- and micropatterned lace-like structures with remarkable level of control.[3, 5, 17] Another class of biominerals is iron oxides, such as magnetite (Fe_3O_4) nanocrystals, which are aligned in well-ordered chains in magnetotactic bacteria for navigation through the geomagnetic field.[1-3, 18] These magnetite nanocrystals have specific sizes, well-defined morphologies, high magnetic moment and stable oxidation state of the iron ions, which are under strict biological control

found in the numerous forms of bacteria such as cocci, spirilli, vibrios, rod bacteria, and multicellular bacteria.[2, 3, 15, 18, 19]

The above examples illustrate a big picture of sophistication of inorganic–organic hierarchical materials produced through biomineralization processes. Apparently, these processes are biologically controlled. Proteins and other macromolecules, interacting with mineral crystals in biological systems, play an important role in these controlled processes.[20-22] Although relatively little is precisely known in different specific mechanisms, there are some general principles that seem to be common to many organisms.[3] For instance, some biomineralization processes are chemically controlled, where physicochemical factors such as solubility, supersaturation, nucleation, and crystal growth are regulated by controlling the ionic composition of the medium as well as through special macromolecules by promoting or inhibiting the nucleation, growth and phase transformation.[2, 14, 20, 23, 24] Such processes have been a source of inspiration for many chemists, physicists, and materials scientists to develop diverse routes to synthesize of novel inorganic–organic materials with promising applications.[2, 25-27] However, fabrication of these organic–inorganic composite materials with controllable structures and the morphologies is still a challenge and it requires a profound fundamental knowledge of the mechanisms involved in the biogenic processes, which need further investigation.[2, 3, 5]

1.2.2 Bioinspired synthesis of organic–inorganic materials

Specialized organic macromolecules, such as proteins, deoxyribonucleic acid (DNA) and polysaccharides, are an indispensable part of biomineralization by directly or indirectly controlling the formation of hierarchically inorganic-organic structures.[20-22, 27] Such structures are generally optimized for their specific functions and are superior to many synthetic materials.[9,

[25] Thus, biomineralization has been considered as a valuable lesson that we can learn from nature.[2, 25, 26] Functional molecules and self-assemblies have been used as templates to mimic biomineralization processes and synthesize functional materials with tunable properties.

1.2.2.1 Bioinspired synthesis mediated by proteins and peptides

Functional molecules have been selected to induce the nucleation of specific inorganic materials and control the crystal structure and size of inorganic particles by adsorbing to specific crystal faces.[2, 27, 28] One example of such functional molecules is peptides that contain two different domains, each being specific for a different compound.[2, 29] Each domain of the peptide will control the nucleation of a different mineral phase, thereby resulting in the synthesis of hybrid particles that are composed of two different materials. For instance, core–shell CdSe–ZnS semiconductor nanocrystals were synthesized using a peptide containing a CdSe-specific domain (Cys-Thr-Tyr-Ser-Arg-Lys-His-Lys-Cys, with the two Cys residues forming a disulfide bridge) and a ZnS-binding domain (Lys-Arg-Arg-Ser-Ser-Glu-Ala-His-Asn-Ser-lle-Val) (Figure 1.1).[29] The size of the core is under precise control by peptide-induced nucleation, and the thickness of the shell can be further modulated through controllable growth process.[29] Since the peptide sequ-

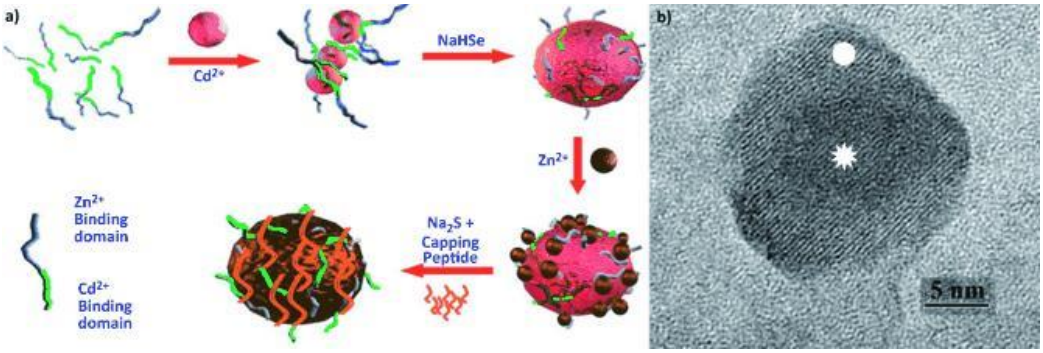

Figure 1.1 (a) A schematic representation of CdSe–ZnS core–shell nanocrystal synthesis using the bi-functional peptide. (b) A HRTEM image showing a ZnS shell grown on top of the CdSe core for the CdSe/ZnS core–shell nanocrystal.[29] (Adapted from ref 29. Copyright © 2010 The Royal Society of Chemistry.)

ences are tunable according to the desired inorganic compound, a highly controlled formation of crystals can be obtained.

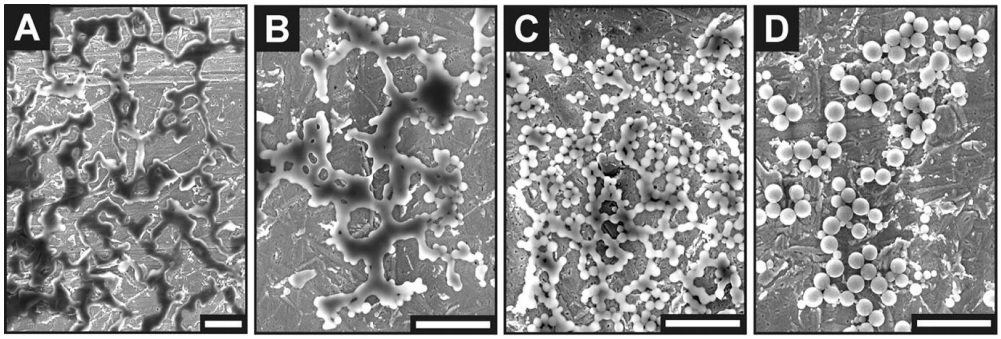

Figure 1.2 Time-resolved analysis of silica morphogenesis in vitro mediated by natSil-1A. Scanning electron images of silica structures formed (A) 3.5 min, (B) 4.5 min, (C) 5 min, and (D) 8 min after the addition of natSil-1A to a buffered monosilicic acid solution (50 mM sodium acetate, pH = 5.5), bar = 2 μm.[30] (Adapted from ref 30. Copyright © 2002 American Association for the Advancement of Science.)

Proteins and peptides are also exploited to regulate the morphology of inorganic crystals, resulting in formation of synthetic minerals with specific size and shapes.[1, 2, 31] Particularly, this kind of templating is evident in the case of silica-based materials, since silica is amorphous and in the absence of any control, it precipitates as formless gels or spherical colloidal particles.[2] When proteins or peptides derived from proteins involved in silica biomineralization are present, silica particles with morphologies such as nanospheres, hexagonal plates, organized fibrillar structures, and three-dimensional structures with periodic voids are obtained.[30-33] For example, silaffins, a family of proteins isolated from the cell wall of diatoms *C. fusiformis*, have been implicated in the biogenesis of diatom biosilica.[31] One active peptide from silaffin, natSil-1A, has shown remarkable ability to induce silica precipitation in the shape of nanospheres *in vitro* (Figure 1.2).[30]

1.2.2.2 Bioinspired synthesis mediated by block copolymers

Templating of block copolymers that self-assemble into vesicles has the advantage of molecular-level control with ability to extend to the macroscale hierarchical ordering.[34] To mimic natural bone, block copolymers have been used to act as templates for the nucleation and

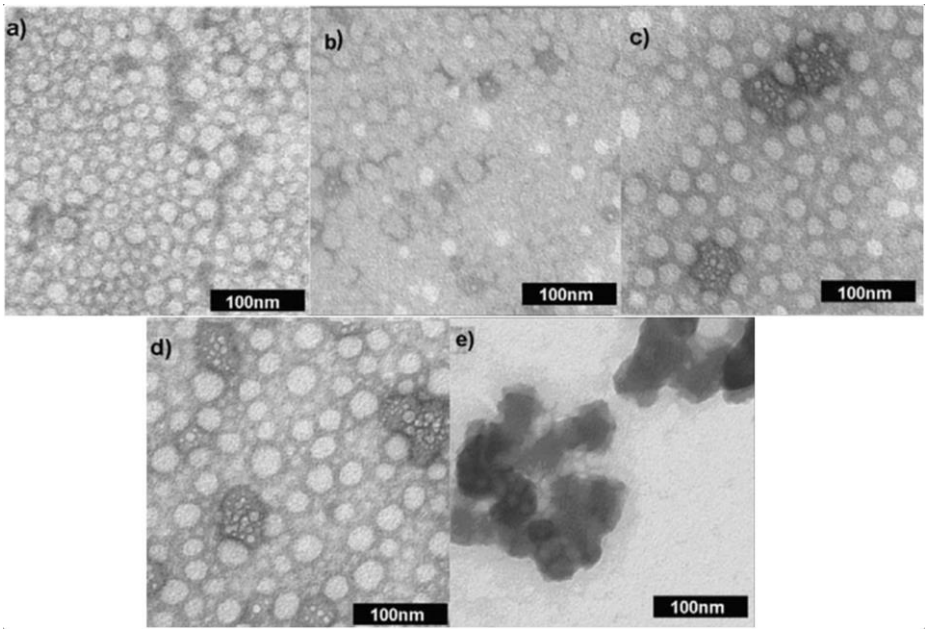

Figure 1.3 Transmission electron micrographs of (a) 0.5 wt.% poly(2-diethylaminoethyl methacrylate, PDEAEM) modified Pluronic® F127 pentablock copolymer micelles in deionized water, (b) 0.5 wt.% pentablock copolymer micelles in pH 3.0 calcium phosphate—aged 30 min, (c) 0.5 wt.% pentablock copolymer micelles in pH 3.0 calcium phosphate—aged 1 hour, and (d, e) different regions of 0.5 wt.% pentablock copolymer micelles in pH 3.0 calcium phosphate—aged 24 hours.[35] (Adapted from ref 35. Copyright © 2007 The Royal Society of Chemistry.)

growth of the calcium phosphate crystals.[35-39] For instance, a thermoreversible amphiphilic block copolymer, Pluronic® F127 (poly(ethylene oxide)-*b*-poly(propylene oxide)-*b*-poly(ethylene oxide) (PEO_{100}-PPO_{65}-PEO_{100}) triblock copolymer) and its derivatives (pentablock copolymers, ionic block copolymers, block copolymer-peptide conjugates) have been shown to facilitate formation of calcium phosphate nanocomposites using bottom-up approaches developed by our group (Figure 1.3).[35-39] Pluronic® exhibits temperature-dependent micellization.[40-43] It self-

assembles into micelles at low temperature and concentrations in aqueous solutions and these micelles entangle to form viscous gels at higher temperatures or concentrations, typically above 25 °C.[40-44] The temperature-dependent phase transformation of the copolymers allows mixing of the solutions of copolymer and inorganic constituents followed by precipitation of calcium phosphates on nanoscale micelles and then self-assemble further into macroscale gels and solids by manipulating the temperature and/or pH of the solution.[35-39] The self-assembled gel exhibits FCC or BCC structure, and it can preserve its structure in the presence of phosphate nanocrystals, but with the nanocrystal in between the micelles.[35-39] With addition of citrate, it has been demonstrated that citrate stabilizes hydroxyapatite (HAp) over other calcium phosphate species without disturbing the supramolecular structures of the polymer gel.[37] The crystal size of HAp within the polymer matrix decreases with increasing the citrate concentration, which enables fine control over the size.[37] In addition, mesoporous zirconia has been synthesized in completely aqueous media in the presence of these block copolymers.[45, 46] Overall, block copolymers with self-assemble properties have been considered as effective tools to facilitate mineralization on nanoscale and create further macroscopically hierarchical structures.

1.2.2.3 Bioinspired synthesis mediated by DNA

Various macromolecules have served as substrates to control self-organization of nanoparticles by deposition. One example is DNA strands. The negatively charged phosphate groups in the DNA backbone can control the adsorption and binding of positively charged metal ions, while the DNA strands themselves can be synthesized with tailor-made structures and patterns because of their ability to hybridize with other DNA strands.[47-50] Furthermore, the ends of the DNA strands can be modified with other functional groups. For example, DNA has been used as a sophisticated template for the targeted attachment of a conductive metal wire to

construct functional nanoscale electronic devices.[51] In this study, DNA molecules were employed to make bridges between two gold electrodes and used as a template for the vectorial growth of a 12 μm long, 100 nm wide conductive silver wire.[51] DNA strands provide desired templates for precise metallization of gold, silver, platinum, palladium, copper, cobalt, etc.[52-62] This bottom-up approach exhibits promising applications in microelectronics technology and industry.

1.2.3 Magnetotactic bacteria and the biomineralization protein Mms6

1.2.3.1 Magnetotactic bacteria

Magnetotactic bacteria, which can produce magnetic nanoparticles with precise control, have been employed as an ideal model for the studies of biomineralization mechanisms and synthesis of bioinspired materials.[63-65] Magnetotactic bacteria is a diverse family of aquatic prokaryotes that have ability to orient themselves along the local geomagnetic field.[66] After the discovery of the first magnetotactic bacterial strain reported in 1975, a series of magnetotactic bacterial strains have been reported in fresh water such as pools, lakes and rivers, transitions between brackish water and sea water, and even in marine water.[1, 67-69] The cellular morphologies of magnetotactic bacteria vary from cocci, spirilli, vibrios, rod bacteria, and multicellular.[19, 70, 71] They all have unique intracellular compartments, named magnetosomes, which are vesicles each with a magnetite nanocrystal (usually 35–120 nm in diameter) inside and a lipid bilayer membrane with similar composition as the cytoplasmic membrane.[71-73] These vesicles are organized into chains by cytoskeletal filaments and fixed inside the cells.[73] The current explanation of the magnetotactic trait is that magnetotactic bacteria use magnetosomes aligned in chains inside themselves to act as compass needles to direct their migration downwards along the tilted geomagnetic line to find the optimal microaerobic or anaerobic

environment for their growth.[71, 73] The magnetite nanoparticles are the physical basis of the magnetotactic trait and the chain alignment of the magnetosome vesicles is the biological basis for this trait.[73, 74] Recent results also demonstrated that magnetotactic bacteria move more quickly and efficiently towards the preferred microaerobic or anaerobic in an applied magnetic field.[75]

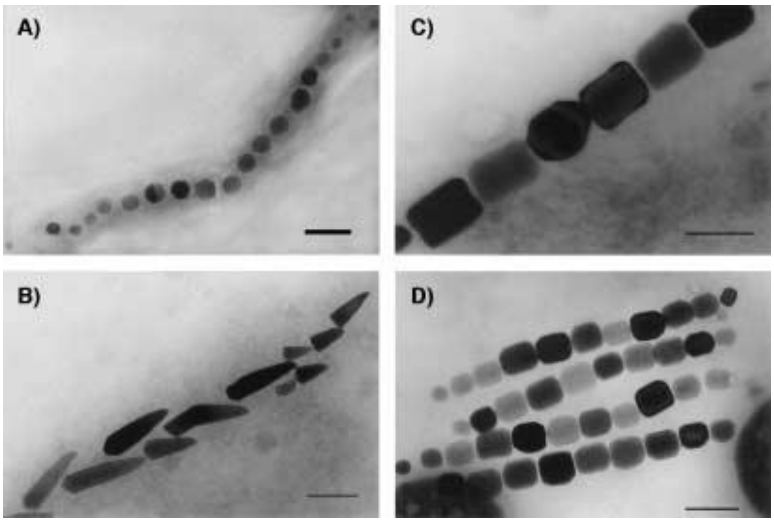

Figure 1.4 Crystal morphologies and intracellular organization of magnetosomes from magnetotactic bacteria: A) cubooctahedral; B) bulletshaped; C, D) pseudohexagonal.[1] The magnetosomes are arranged in one (C) or more (D) chains, bars = 100 nm. (Adapted from ref 1. Copyright © 2003 Wiley-VCH.)

Magnetite crystals with well-defined sizes and morphologies are found in the numerous forms of bacteria and both sizes and morphologies seem to be specific to the respective species of bacteria.[1] These crystal morphologies generally can be classified into cubooctahedral, pseudohexagonal, and bullet-shaped (Figure 1.4).[1, 76] The unexpected and unusual features of these biogenic magnetite crystals is not only a narrow size distribution, but above all, a diameter range of 35–120 nm, which thus allocates them the highest magnetic moment.[1, 76] This size range corresponds to magnetite crystals with a single magnetic domain.[77] Since magnetite crystals from inorganic synthetic routes under mild conditions offer neither a similar narrow size distribution

with uniform magnetic properties nor such a variety of crystal morphologies, magnetotactic bacteria have been considered as effective tools to study biomineralization of magnetic crystals and sources of inspiration to create functional materials.[1, 78-83]

1.2.3.2 Magnetite

Magnetite, Fe_3O_4, one class of magnetic iron oxides, is widespread in almost all of the different compartments of the global system.[84] It is a black, ferrimagnetic mineral containing both Fe(II) and Fe(III) and it is mainly responsible for the magnetic properties of rocks.[84] Magnetite has the highest saturation magnetization among the iron oxides.[84, 85] However, as magnetite has an isotropic magnetic structure, magnetite has a low coercivity and behaves as a magnetically soft material.[84, 85]

Finite-size effect gives rise to various special features of magnetite.[79] Bulk magnetite is ferrimagnetic with a multiple domain structure, but when the size of magnetite nanoparticles is below a threshold size d_0 (80 – 100 nm), these particles can no longer support static domain walls, and thus they exhibit stable single-domain ferrimagntetism with an intrinsic remanent dipole.[77, 86-88] When the size decreases further to a critical point d_s (20 – 30 nm), the magnetite nanoparticles become superparamagnetic at room temperature, as their magnetic moments are equilibrated due to thermally induced spin flipping.[77, 86-88] Magnetite exhibits such intriguing magnetic properties that it has wide applications in magnetic data storage, magnetic resonance imaging (MRI) contrast enhancement, hyperthermia cancer treatment and targeted drug delivery.[79, 81, 82, 88] Applications in data recording and spintronics require magnetic nanoparticles with single domains, while medical use of ferrofluids usually needs superparamagnetic nanoparticles.[81, 82, 87, 89, 90] Bioinspired synthesis of magnetite nanoparticles with controlled properties to meet specific requirements will greatly expand the spectrum of applications.

Magnetite has an inverse cubic spinel structure (Space group: *Fd-3m*), in which 32 O^{2-} ions form a face-centered cubic (FCC) packed along the [111] direction, and each unit cell contains eight formula units ($Fe_{24}O_{32}$) (Figure 1.5).[84] The lattice parameter of the pure bulk magnetite is 0.8396 nm. There are 64 tetrahedral sites and 32 octahedral sites in each unit cell. Eight tetrahedral sites are occupied by Fe^{3+} ions, while 16 octahedral sites are shared with equal

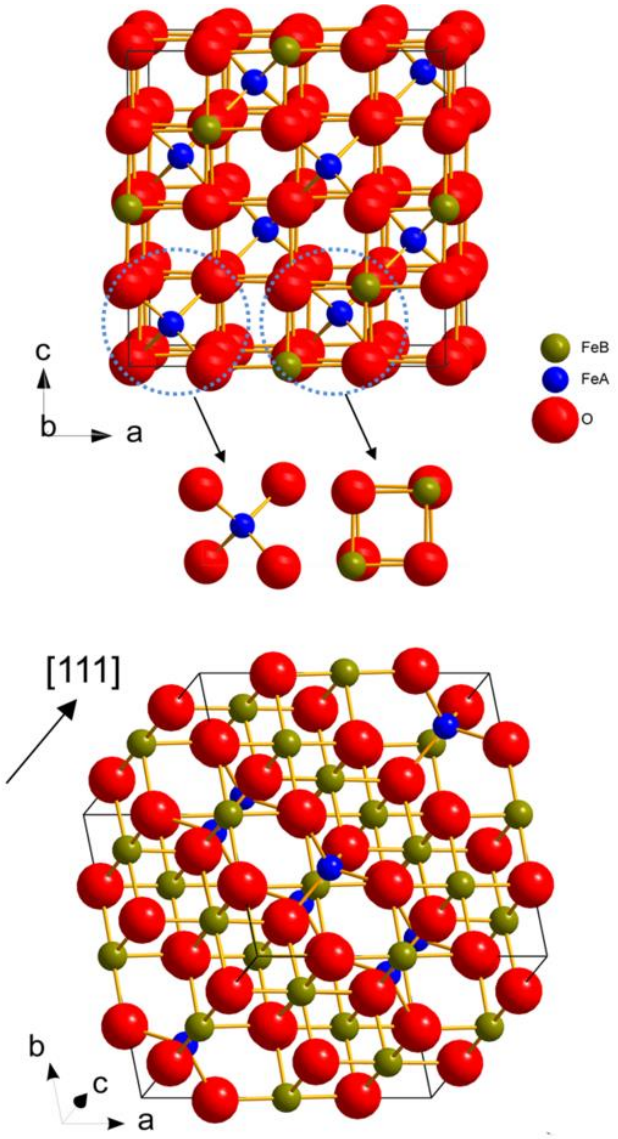

Figure 1.5 Crystal structure of magnetite. O represents oxygen ions, and FeA and FeB represent iron ions in the tetrahedral sites and the octahedral sites of the oxygen face-centered cubic structure, respectively. The relative size difference between FeA, FeB and O is given as a guide to the eye. All the structures are plotted by Diamond software (version 3.1) from Crystal Impact.

number of Fe^{2+} ions and Fe^{3+} ions. The structure consists of octahedral and mixed tetrahedral/octahedral layers stacked along the [111] direction (Figure 1.5).[84] In octahedral sites, the magnetic moments of Fe^{3+} ions are aligned with those of Fe^{2+} ions, but they are antiparallel to the magnetic moments of Fe^{3+} ions in tetrahedral sites. Therefore, the magnetic properties of magnetite are determined by the moment of the Fe^{2+} ions in octahedral sites.[91]

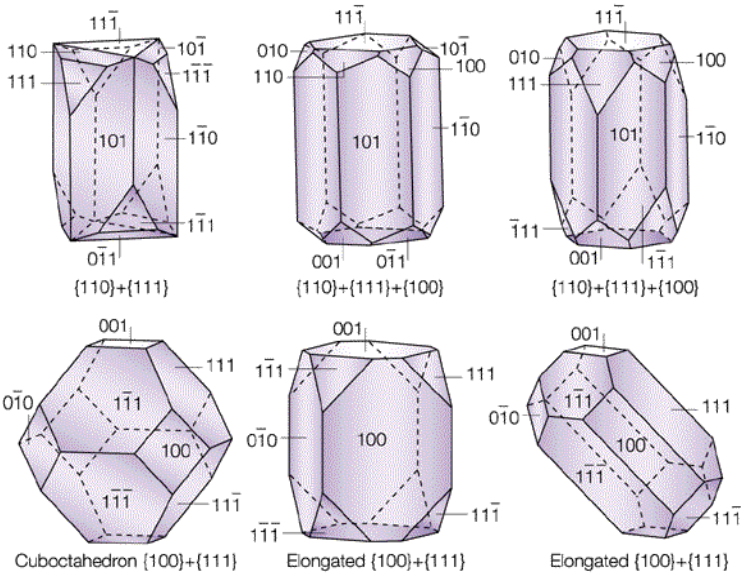

Figure 1.6 Idealized crystal morphology of magnetite.[66, 76] (Modified from ref 76. Copyright © 1998 Mineralogical Society of America. Adapted from ref 66. Copyright © 2004 Nature Publishing Group.)

Magnetite nanoparticles are ideally surrounded by {111} planes and exhibit octahedral morphology[66, 83], since the high-index planes usually have higher surface energy (γ),[92] and the sequence of $\gamma(111) < \gamma(100) < \gamma(110) < \gamma(220)$ for the face-centered-cubic phase can be generated from the distance between those planes and the central Wulff's point.[93] However, the crystal shape is defined by the ratio (R) of growth rate in the <100> direction to that in the <111> direction.[83] Ideally, faster growth along the <111> direction can lead to cubic octahedral particles, while faster growth along the <110> and <100> directions can generate particles with dodecahedral and cubic forms, respectively.[66] Usually magnetite crystals in magnetosomes are

cuboctahedra composed of {111} and {100} (Figure 1.6), but shapes of some crystals with combinations of {111}, {110} and {100} (Figure 1.6) are also found in some magnetotactic strains.[1, 66] Control on the growth rate of different facets of the nuclei is applied to get various morphologies of magnetite,[83] which also opens opportunities to investigate the mechanisms of biomineralization in magnetotactic bacteria.

1.2.3.2 Mms6 Protein

Mms6, one of several proteins tightly bound to the magnetosome magnetite crystal in magnetotactic bacteria *Magnetospirillum magneticum* AMB-1, has been implicated in the biomineralization of magnetite.[88, 94-96] The most intriguing feature of Mms6 in the first report is that Mms6 has ability to promote the formation of magnetite nanoparticles with similar morphology to bacterial magnetites *in vitro*.[94] Our group has recently used recombinant Mms6 to mediate the formation of uniform superparamagnetic magnetite nanocrystals at room temperature and mild conditions *in vitro*.[97, 98] Magnetite nanoparticles synthesized via the classical co-precipitation method by elevating the pH of stoichiometric mixture of ferrous and ferric salts in aqueous medium at room temperature, are mostly less than 20 nm and non-uniform in size.[81] In contrast, in the presence of Mms6 and Pluronic® gel, magnetite slowly grows to 30 nm diameter superparamagnetic nanoparticles of uniform size and cubo-octahedral shapes.[97, 98] Mms6 also has been found to promote *in vitro* synthesis of other advanced functionalized materials that are not known to be present in any living organisms, such as cobalt ferrite, cobalt doped magnetite and magnetic nanoparticle arrays via co-precipitation of Fe^{2+} and Fe^{3+} salts or partial oxidation of Fe^{2+} salts.[99-103] Such magnetic materials synthesized with Mms6 have promising potential applications in targeted drug delivery, magnetic resonance imaging (MRI) contrast agents, and high density data storage.[88]

Progress has been made recently in understanding the structure and properties of Mms6.[98, 104] It is an amphiphilic protein with hydrophobic N-terminal and hydrophilic C-terminal, is believed to exist as a membrane protein *in vivo*, and self-assembles *in vitro* to form a micellar complex larger than 300 kDa.[98, 104] The C-terminal domains bind iron ions and complexes with very high affinity.[98, 105] The interactions between Mms6 and iron are believed to be the initial steps of biomineralization, and also to be important in determining the shape of the magnetite nanoparticles.[95, 98] Meanwhile, Mms6 may control the morphology and size of magnetite in magnetotactic bacteria by regulating the surface of crystal during crystal growth by *in vivo* study.[95] The Mms6-iron interactions at various pH values have been previously observed on aqueous surfaces, where Mms6 was deposited on the surface of an iron solute subphase to form a monolayer, taking advantage of its amphiphilic behavior.[105] Moreover, using *in situ* liquid cell scanning transmission electron microscopy, recombinant Mms6 micelles were found to mediate nucleation of iron oxide on their surfaces.[106]

Significant research efforts have been led to elucidate the mechanism of Mms6 biomineralization *in vivo*, synthesizing a variety of magnetic nanomaterials *in vitro* and thereby expanding the biomineralization mechanisms beyond natural materials. However, the detailed mechanism of biomineralization by Mms6 is still unclear and the potential properties of Mms6 are also under investigation.

1.2.4 Biological self-assembly

Like biomineralization, self-assembly is a ubiquitous process in nature by which the individual components spontaneously organize themselves into a complexed structure with specific order through their mutual noncovalent interactions.[107] The precise organization is crucial to the function of biological self-assembled structures.[107, 108] The components can be

molecules or segments of a macromolecule that interact with one another.[107-109] The noncovalent interactions in biological self-assembly include electrostatic interactions, hydrophobic effects, aromatic stacking (π-π stacking), hydrogen bonding and van der Waals forces.[107-109] Generally, the strength of these interactions is individually weaker than that of covalent bonds, but the cumulative effect with sufficient number of these interactions is high enough to generate stable assemblies with particular structures and shapes.[108]

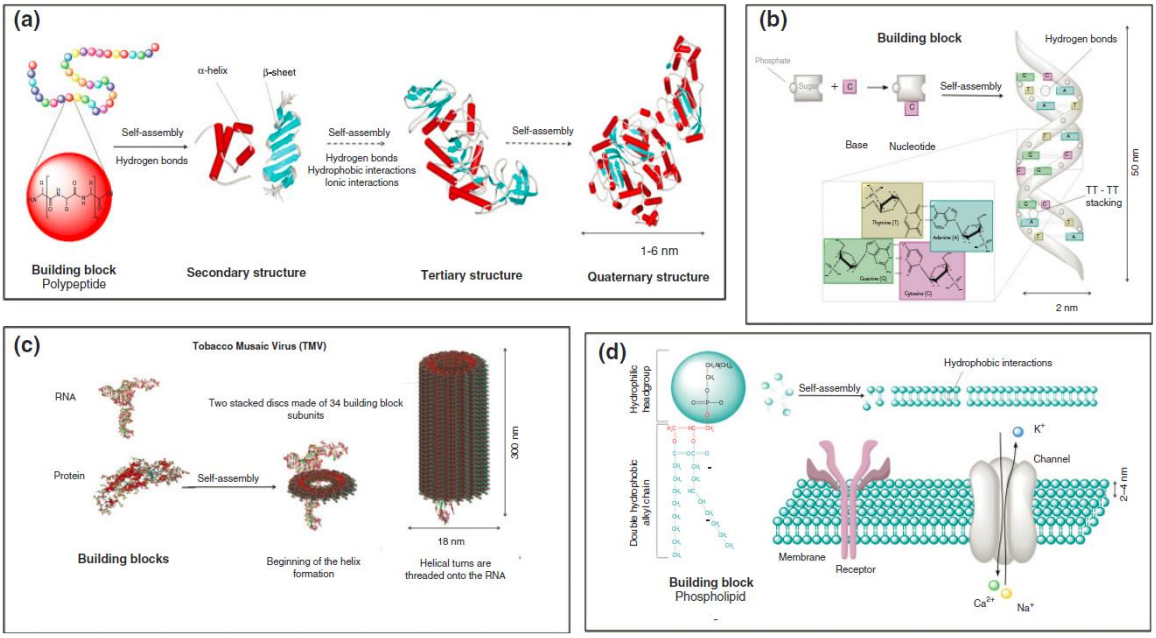

Figure 1.7 Examples of biological self-assembled structures showing the building blocks and the relevant interactions involved in the self-assembly process. (a) Protein folding; (b) dsDNA; (c) tobacco mosaic virus (TMV); and (d) cell membrane. (Adapted from ref 108. Copyright © 2013 Wiley-VCH.)

A variety of sophisticated self-assembled structures have been developed in nature. Figure 1.7 illustrates some examples of biological self-assembled structures, from proteins and nucleic acids to viruses and cell membranes.[108] The primary biomolecular building blocks arrange into final functional self-assembled structures through a process with relevant interactions at molecular level.[107, 108] For instance, a protein synthetically can be considered as a linear strand of 20 possible amino acids (polypeptide). As shown in Figure 1.7a, a polypeptide self-assembles

into a secondary structure constituted by α-helices and β-sheets through hydrogen bonding, further packs α-helices and β-sheets to form protein subunits (local structural motifs) leading to a tertiary structure, and eventually arranges into a mature protein with a specific function via interactions between subunits previously formed.[107, 108] The self-assembly process in a protein is named as protein folding, involving formation of relatively simple local structures (intermediates) and structure-specific association of these intermediates.[107, 108] Another example of biological self-assembly is double-stranded DNA (dsDNA) (Figure 1.7b). Two complimentary single-stranded DNA (ssDNA) wrap into a double helix, which is stabilized by hydrogen bonds between the paired nucleobases from two ssDNA chains and π-π stacking between nucleobases inside each ssDNA chain.[108] These kinds of dsDNA structures with high stability, precise reproducibility and operational simplicity have been widely used in current biological and biomimetic nanotechnology such as molecular recognition and self-assembly techniques.[107] In addition, a cell membrane (cytoplasmic membrane) is also a self-assembled structure, in which the building blocks (i.e., amphiphilic phospholipid molecules composed of a hydrophilic head group and a hydrophobic tail.) self-organize into a bilayer resulting from the hydrophobic effect.[108] Large lipid variability in polarities with different head groups and tail lengths leads to various dynamic or compartmentalized self-assembled structures in aqueous environment.[108]

The biological self-assembly plays an important role in life as the assembled structures determine the relevant functions. Interestingly, the principles of biological self-assembly can be applied to synthetic building blocks that are not naturally available, like block copolymers. Moreover, the relevant noncovalent interactions are at the molecular level, but the building blocks are not limited to molecules or macromolecule. The sizes of building blocks range from the molecular to mesoscopic, macroscopic levels and even higher (such as colloidal crystals),

and self-assembly can widely occur under appropriate conditions.[109, 110] Therefore, self-assembly has been considered as one of general strategies to spontaneously construct rationally designed structures via bottom-up approaches.

1.2.5 Self-assembly of colloidal nanocrystals

Colloidal nanocrystals are solution-grown inorganic nanocrystal cores stabilized by a layer of surface-bound ligands.[111, 112] In the past two decades, tremendous efforts have been devoted to controllable synthesis of colloidal nanocrystals with uniform size and morphologies.[113-117] Such colloidal nanocrystals have different types of functionalities such magnetic, plasmonic, catalytic and luminescent properties.[92, 112-116, 118, 119] Meanwhile, advances in post-synthetic surface-functionalization of colloidal nanocrystals enable self-assembly of individual nanocrystals into macroscopic superlattices with various structures in different dimensions.[114, 120-123] These superlattices possess intriguing collective properties that are different from those of individual ones, thus exhibiting great potential in technological applications.[124, 125] Although numerous strategies have been developed for nanocrystal self-assembly, the self-assembly process is determined by the nanocrystal size and shape and the interparticle interactions, similar to the biological self-assembly.[107, 111] The surface-bound ligands have been primarily used to control the interparticle interactions. Structural and functional diversity of molecules has been employed to functionalize nanocrystals, such as DNA,[122, 123] proteins,[126] polymers[127] and hydrocarbons.[128] In addition to functional ligands, the properties of assembly environment, such the temperature, solvent and physical confinement, have a decisive effect on the interparticle interactions and further structures and properties of the resulting assemblies.[111, 121, 129, 130] In parallel with experimental designs, theoretical modelling has also been explored.[131-136] Practically, the experimental and theoretical studies point out that the self-assembly of

nanocrystals allows for high flexibility in compositions and structures and has been viewed as a promising tool to fabricate next-generation materials such as metamaterials.[124, 125, 137-139]

1.2.5.1 Self-assembly of nanocrystals functionalized with DNA

The self-assembly properties of DNA are employed to control the organization of nanoparticles into larger structures with longer length scales due to its programmable recognition properties, i.e., hybridization. An example under intensive investigation is DNA-mediated nanoparticle superlattices.[122, 125, 129, 140-147] Nanoparticles coated with single stranded DNA can self-assemble into one-, two- and three-dimensional structures.[122, 125, 129, 140-153] Such superlattices can be made from nanoparticles with different types of functionalities, such as plasmonic (gold),

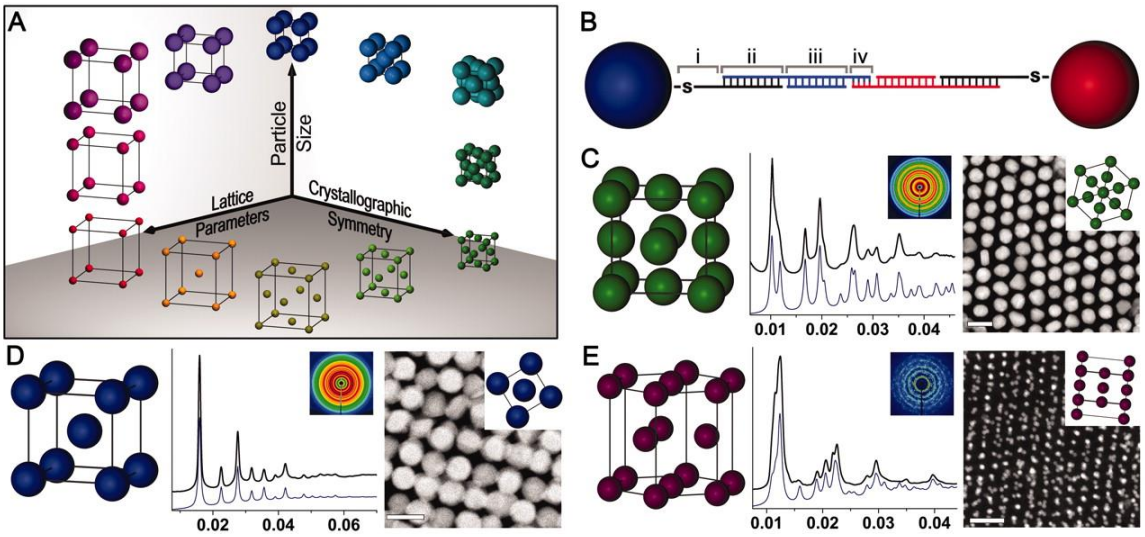

Figure 1.8 A) Nanoparticle superlattice engineering with DNA allows for independent control of three important design parameters (particle size, lattice parameters, and crystallographic symmetry) by separating the identity of the particle from the variables that control its assembly. (B) The DNA strands that assemble these nanoparticle superlattices consist of (i) an alkyl-thiol moiety and 10-base nonbinding region, (ii) a recognition sequence that binds to a DNA linker, (iii) a spacer sequence of programmable length to control interparticle distances, and (iv) a "sticky end" sequence that drives nanoparticle assembly via DNA hybridization interactions. (C to E) The superlattices reported herein are isostructural with (C) FCC, (D) BCC, (E) HCP. (Adapted from ref 142. Copyright © 2011 American Association for the Advancement of Science.)

magnetic (iron oxide), catalytic (palladium) and luminescent (CdSe@ZnS) properties.[125] Homogeneous systems with same types of nanoparticles and binary systems with two different types of nanoparticles have exhibited different phase behaviors.[125] Moreover, particle shapes (sphere, rod, octahedral, triangular prism) have shown a strong influence on the crystallization parameters of DNA-functionalized nanoparticles, resulting in affecting superlattice dimensionality, crystallographic symmetry and phase behavior.[141] Meanwhile, DNA-functionalized anisotropic polyhedral nanoparticles have been reported to coordinate isotropic spherical nanoparticles via shape-induced directional binding.[154] In addition, through precise control of nanoparticle size, interparticle distance and periodicity, several kinds of crystal structures have been realized using DNA-functionalized gold nanoparticles, including simple cubic (SC), FCC, BCC, HCP and other structures with the lattice parameters ranging from 25 to 150 nm.[142] Besides single-stranded DNA, DNA origami frames have also been used to construct nanoparticle superlattices, in which nanoparticles are spatially coordinated in a prescribed manner.[155] Thus, even diamond type of nanoparticle superlattices can be obtained using rationally design DNA origami frames.[156] State-of-the-art developments of DNA-programmable nanoparticle self-assembly enable future construction of new crystallographic arrangements that have emergent properties for use in the fields of plasmonics, photonics, catalysis, and potentially many others.[142, 143]

1.2.5.2 Self-assembly of nanocrystals templated by proteins

Crystallizing proteins have been extensively studied in structural biology and directed assembly of proteins into diffraction-quality crystals has also been reported recently.[157-160] Meanwhile, owing to the inherent functionalities, it has been found that proteins can act as molecular linkers and templates to mediate self-assembly nanocrystals.[126, 161-166] The antibodies

were attached to the surfaces of gold nanoparticles and macroscopic nanoparticle networks with higher-order structures were generated through the high specificity of antibody–antigen recognition.[165] Engineered crystalline protein templates (chaperonin) with hollow double-ring structures have been used as a guide to direct self-assembly of nanoparticles into ordered arrays.[164] Protein-based nanocages (such as ferritin and viral capsids) encapsulating various nan oparticle cores have been developed to organize nanoparticles into superlattices both at the interfaces[167] and in solutions.[168] The negatively charged cages with the core of iron oxide nanoparticles interact with positively charged gold nanoparticles, leading to tunable binary nanoparticle superlattices.[126] Similarly, the complementarily charged protein containers independent of nanoparticle cores have been developed as general templates to use electrostatic

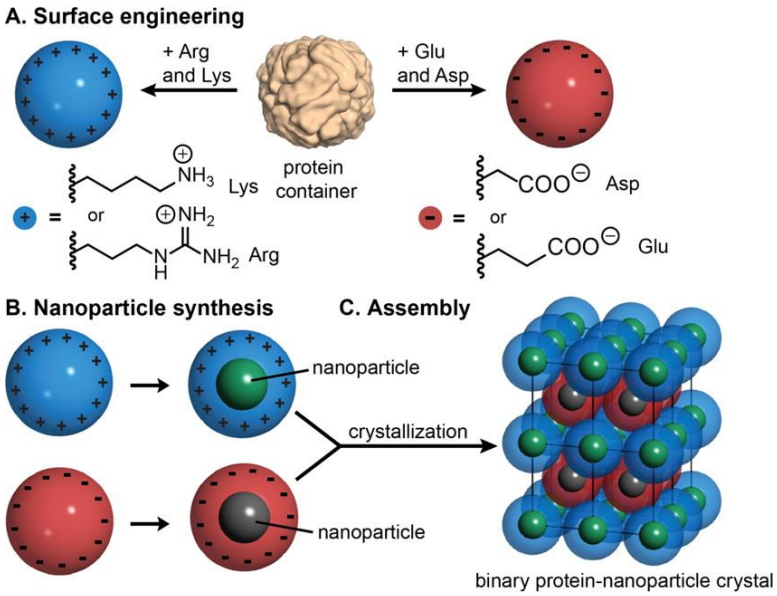

Figure 1.9 A general scheme for the assembly of binary nanoparticle superlattices based on charged protein containers. (A) The surface of a native protein container is engineered to produce containers with a positively charged (left) and negatively charged surface (right). (B) Nanoparticle synthesis is carried out separately in each protein container type. (C) Self-assembly of the protein container nanoparticle composites yields highly ordered three-dimensional superlattices. (Adapted from ref 166. Copyright © 2016 American Chemical Society.)

interactions to assemble nanoparticles into macroscopic superlattices with a high degree of ordering[166] (Figure 1.9).

1.2.5.3 Self-assembly of nanocrystals grafted with polymers

The pristine surface-bound ligands on nanoparticles can be changed to polymers via ligand exchange with end-functionalized polymers or through surface-initiated polymerization,[169] and the synthetic polymer-grafted nanoparticles readily self-assemble into superlattices.[170] The ordering of these nanoparticles was found to be determined by the brush architecture (the particle size, the molecular weight of tether polymer and the grafting density).[171] Using conventional aliphatic ligands with tuning the molecular brush architecture, 10 different binary nanocrystal superlattices with 2D and 3D order were fabricated using an evaporation-based method. This method led to controlled co-crystallization of a binary mixture of nanoparticles on top of an immiscible liquid subphase at room temperature.[127] The Langmuir–Blodgett technique has been used to assemble nanocrystals into macroscopic 2D superlattices, such as polyhedral silver nanocrystal arrays with high tunability of the optical response.[130] By grafting thermoresponsive polymers such as poly(*N*-isopropylacrylamide), the behavior of nanoparticle superlattices can be manipulated by external temperature.[172-174] The polymer functionalization allows for self-assembly of nanoparticle in polymer matrices to form nanocomposites,[175] and the dispersibility of polymer-grafted nanoparticles is associated with the wetting the polymer brushes by the matrices.[176] The length of grafted polymer, grafting density as well as interaction strength between nanoparticle surfaces have an effect on the phase behaviors (dispersion or controllable aggregation) of polymer-grafted nanoparticles in host matrices.[177-179]

Similar to lipids, amphiphilic block copolymers have been tethered to nanoparticles to form self-assemble structures. For instance, amphiphilic nanoparticles were obtained by grafting with block copolymers poly(2-(2-methoxyethoxy)ethyl methacrylate)-*b*-polystyrene (PMEO2MA-*b*-PS) or poly(ethyloxide)-*b*-polystyrene (PEO-*b*-PS), and using film rehydration method these block polymer-grafted nanoparticles assemble into well-defined vesicles or tubules (Figure 1.10).[180] The morphologies depend on the size of nanoparticles and the molecular weight of block copolymers as well as the properties of the solvent.[180, 181] Alternatively, vesicular self-assembly of such block copolymer-grafted nanoparticles can occur in microfluidic devices.[182] The strong plasmonic coupling of gold nanoparticles in the assembled vesicles and their biodegradability facilitate their multi-functional biomedical applications in photoacoustic imaging and photothermal therapy.[181, 183, 184]

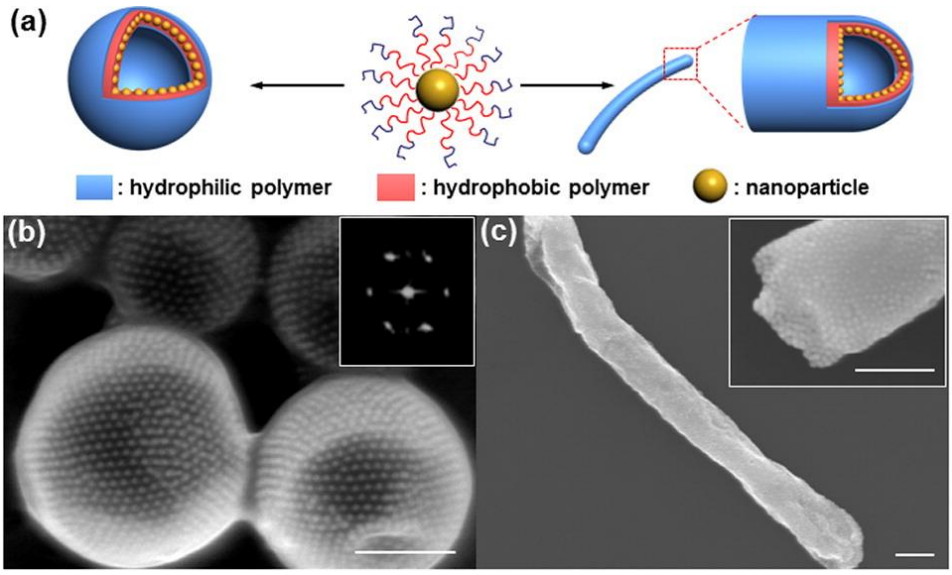

Figure 1.10 (a) Amphiphilic block copolymers-assisted self-assembly of nanoparticles into vesicles or tubules. Representative SEM images of vesicles (b) and tubules (c) obtained from self-assembly of Au-P1 and Au-P2, respectively. Scale bars: 200 nm in (b–c). Inset in (b) is the FFT pattern of SEM images. (Adapted from ref 180. Copyright © 2012 American Chemical Society.)

1.2.5.4 Self-assembly of nanocrystals capped by hydrocarbons

In addition to macromolecules mentioned above, relatively short hydrocarbon chains have been utilized to coat nanoparticles for self-assembly. 2D superlattices can be fabricated on solid substrates through evaporation of an organic solvent, which is a kinetically driven non-equilibrium process.[185-188] The self-assembly can occur with multiple types of nanoparticles at air-liquid interfaces with slight evaporation and further transfer to a solid support.[189] The evaporation-based method has been extended to 3D self-assembly of nanoparticles. Various organic solvents have been found to effectively induce nanoparticle superlattices with long-range ordering.[128, 190-196] Overall 16 unique binary nanoparticle superlattice structures have been reported, ranging from simple NaCl type structures to dodecagonal quasicrystals.[128, 191-196] Non-solvent diffusion has been found to promote destabilization-based self-assembly of hydrocarbon-capped nanoparticles.[120, 121, 197] Flat platelets and multiply twinned polyhedral superlattices have been observed in such assemblies.[197] Among a diversity of binary nanoparticle superlattice structures, most cases exhibit lower sphere packing density than the combination of phase-separated closed-packed assemblies consisting of single-type nanoparticles.[111] The anisotropic brush contacts between nearest neighbors gives rise to corona deformation and the soft chains are allowed to fill the space with higher efficiency than a hard sphere, thus leading to possible higher density than that within the hard sphere approximation.[111, 194] Energetic interactions (including entropic contributions) have an effect on the superlattice formation, and various types of structures were found to depend on the temperature.[195] Even though there are a few theoretical analyses recently reported, the full explanation of the observed structural diversity is still a challenge.[132, 198, 199]

1.2.5.5 Summary

In the past decade, major advances have been made in experimental investigations on nanocrystal self-assembly mediated by organic molecules as discussed above. Considering fundamental aspects of interactions of nanoparticles with themselves and with the surrounding environment, mechanisms of superlattice formation, as well as the stability, yield, and scale of production, though, it is still challenging to develop a novel method to fabricate nanoparticle superlattices that is robust yet inexpensive, and able to render these superlattices technologically viable. Concomitant with 3D superlattices with diverse structures, 2D self-assembly of nanoparticles on solid substrates or liquid surfaces exhibits less complexity due to the reduced dimensions, thereby providing an alternative and suitable platform to investigate self-assembly and crystallization of nanoparticles, understand the general mechanisms, and direct controllable self-assembly processes in other dimensions. Therefore, our efforts have been devoted to unraveling the underlying mechanisms of 2D superlattice assemblies of DNA-functionalized nanoparticles at the air–water interfaces using surface sensitive synchrotron X-ray scattering and spectroscopy techniques. Our findings have been readily applied to the 2D self-assembly of polymer- and polyelectrolyte-functionalized nanoparticles. In addition, guided by our theoretical model on formation of 2D superlattices, 3D nanoparticle self-assembly has also been explored.

References

1. Bäuerlein, E. Biomineralization of Unicellular Organisms: An Unusual Membrane Biochemistry for the Production of Inorganic Nano- and Microstructures. *Angew. Chem. Int. Ed.* 2003, 42, 614-641.
2. Nudelman, F.; Sommerdijk, N. A. J. M. Biomineralization as an Inspiration for Materials Chemistry. *Angew. Chem. Int. Ed.* 2012, 51, 6582-6596.
3. Mann, S. *Biomineralization: Principles and Concepts in Bioinorganic Materials Chemistry*. Oxford University Press: 2001.
4. Veis, A. Crystals and Life: An Introduction. In *Biomineralization*, John Wiley & Sons, Ltd: 2010; pp 1-35.

5. Lowenstam, H. A.; Weiner, S. *On Biomineralization*. Oxford University Press, USA: 1989.
6. Fratzl, P.; Weinkamer, R. Nature's hierarchical materials. *Prog. Mater. Sci.* 2007, 52, 1263-1334.
7. Liu, X.; Mallapragada, S. K. Bioinspired Synthesis of Organic/Inorganic Nanocomposite Materials Mediated by Biomolecules. In *On Biomimetics*, 2011.
8. Hulmes, D. J.; Wess, T. J.; Prockop, D. J.; Fratzl, P. Radial packing, order, and disorder in collagen fibrils. *Biophys. J.* 1995, 68, 1661-1670.
9. Weiner, S.; Wagner, H. D. THE MATERIAL BONE: Structure-Mechanical Function Relations. *Annu. Rev. Mater. Sci.* 1998, 28, 271-298.
10. Dunlop, J. W. C.; Fratzl, P. Biological Composites. *Annu. Rev. Mater. Res.* 2010, 40, 1-24.
11. Fratzl, P.; Gupta, H. S.; Paschalis, E. P.; Roschger, P. Structure and mechanical quality of the collagen-mineral nano-composite in bone. *J. Mater. Chem.* 2004, 14, 2115-2123.
12. Fratzl, P. Bone fracture: When the cracks begin to show. *Nat. Mater.* 2008, 7, 610-612.
13. Jamieson, J. C. Phase Equilibrium in the System Calcite-Aragonite. *J . Chem. Phys.* 1953, 21, 1385-1390.
14. Weiner, S.; Addadi, L. Design strategies in mineralized biological materials. *J. Mater. Chem.* 1997, 7, 689-702.
15. Smith, B. L.; Schaffer, T. E.; Viani, M.; Thompson, J. B.; Frederick, N. A.; Kindt, J.; Belcher, A.; Stucky, G. D.; Morse, D. E.; Hansma, P. K. Molecular mechanistic origin of the toughness of natural adhesives, fibres and composites. *Nature* 1999, 399, 761-763.
16. Cusack, M.; Freer, A. Biomineralization: Elemental and Organic Influence in Carbonate Systems. *Chem. Rev.* 2008, 108, 4433-4454.
17. Hildebrand, M. Diatoms, Biomineralization Processes, and Genomics. *Chem. Rev.* 2008, 108, 4855-4874.
18. Faivre, D.; Schüler, D. Magnetotactic Bacteria and Magnetosomes. *Chem. Rev.* 2008, 108, 4875-4898.
19. DeLong, E. F.; Frankel, R. B.; Bazylinski, D. A. Multiple Evolutionary Origins of Magnetotaxis in Bacteria. *Science* 1993, 259, 803-806.
20. Falini, G.; Albeck, S.; Weiner, S.; Addadi, L. Control of Aragonite or Calcite Polymorphism by Mollusk Shell Macromolecules. *Science* 1996, 271, 67-69.
21. Belcher, A. M.; Wu, X. H.; Christensen, R. J.; Hansma, P. K.; Stucky, G. D.; Morse, D. E. Control of crystal phase switching and orientation by soluble mollusc-shell proteins. *Nature* 1996, 381, 56-58.
22. Gordon, L. M.; Joester, D. Nanoscale chemical tomography of buried organic-inorganic interfaces in the chiton tooth. *Nature* 2011, 469, 194-197.
23. Addadi, L.; Weiner, S. Interactions between acidic proteins and crystals: stereochemical requirements in biomineralization. *Proc. Natl. Acad. Sci. USA* 1985, 82, 4110-4114.
24. Addadi, L.; Moradian, J.; Shay, E.; Maroudas, N. G.; Weiner, S. A chemical model for the cooperation of sulfates and carboxylates in calcite crystal nucleation: Relevance to biomineralization. *Proc. Natl. Acad. Sci. USA* 1987, 84, 2732-2736.
25. Sommerdijk, N. A. J. M.; Cölfen, H. Lessons from Nature—Biomimetic Approaches to Minerals with Complex Structures. *MRS Bull.* 2010, 35, 116-121.
26. Aizenberg, J. New Nanofabrication Strategies: Inspired by Biomineralization. *MRS Bull.* 2010, 35, 323-330.

27. Sarikaya, M.; Tamerler, C.; Jen, A. K. Y.; Schulten, K.; Baneyx, F. Molecular biomimetics: nanotechnology through biology. *Nat. Mater.* 2003, 2, 577-585.
28. Aizenberg, J.; Weaver, J. C.; Thanawala, M. S.; Sundar, V. C.; Morse, D. E.; Fratzl, P. Skeleton of Euplectella sp.: Structural Hierarchy from the Nanoscale to the Macroscale. *Science* 2005, 309, 275-278.
29. Singh, S.; Bozhilov, K.; Mulchandani, A.; Myung, N.; Chen, W. Biologically programmed synthesis of core-shell CdSe/ZnS nanocrystals. *Chem. Commun.* 2010, 46, 1473-1475.
30. Kröger, N.; Lorenz, S.; Brunner, E.; Sumper, M. Self-Assembly of Highly Phosphorylated Silaffins and Their Function in Biosilica Morphogenesis. *Science* 2002, 298, 584-586.
31. Kröger, N.; Deutzmann, R.; Sumper, M. Polycationic Peptides from Diatom Biosilica That Direct Silica Nanosphere Formation. *Science* 1999, 286, 1129-1132.
32. Patwardhan, S. V.; Mukherjee, N.; Steinitz-Kannan, M.; Clarson, S. J. Bioinspired synthesis of new silica structures. *Chem. Commun.* 2003, 1122-1123.
33. Naik, R. R.; Whitlock, P. W.; Rodriguez, F.; Brott, L. L.; Glawe, D. D.; Clarson, S. J.; Stone, M. O. Controlled formation of biosilica structures in vitro. *Chem. Commun.* 2003, 238-239.
34. Bates, F. S.; Fredrickson, G. H. Block copolymers—designer soft materials. *Phys. Today* 2008, 52, 32-38.
35. Enlow, D.; Rawal, A.; Kanapathipillai, M.; Schmidt-Rohr, K.; Mallapragada, S.; Lo, C. T.; Thiyagarajan, P.; Akinc, M. Synthesis and characterization of self-assembled block copolymer templated calcium phosphate nanocomposite gels. *J. Mater. Chem.* 2007, 17, 1570-1578.
36. Kanapathipillai, M.; Yusufoglu, Y.; Rawal, A.; Hu, Y. Y.; Lo, C. T.; Thiyagarajan, P.; Kalay, Y. E.; Akinc, M.; Mallapragada, S.; Schmidt-Rohr, K. Synthesis and Characterization of Ionic Block Copolymer Templated Calcium Phosphate Nanocomposites. *Chem. Mater.* 2008, 20, 5922-5932.
37. Hu, Y. Y.; Liu, X. P.; Ma, X.; Rawal, A.; Prozorov, T.; Akinc, M.; Mallapragada, S. K.; Schmidt-Rohr, K. Biomimetic Self-Assembling Copolymer−Hydroxyapatite Nanocomposites with the Nanocrystal Size Controlled by Citrate. *Chem. Mater.* 2011, 23, 2481-2490.
38. Yusufoglu, Y.; Hu, Y.; Kanapathipillai, M.; Kramer, M.; Kalay, Y. E.; Thiyagarajan, P.; Akinc, M.; Schmidt-Rohr, K.; Mallapragada, S. Bioinspired synthesis of self-assembled calcium phosphate nanocomposites using block copolymer-peptide conjugates. *J. Mater. Res.* 2008, 23, 3196-3212.
39. Hu, Y.-Y.; Yusufoglu, Y.; Kanapathipillai, M.; Yang, C.-Y.; Wu, Y.; Thiyagarajan, P.; Deming, T.; Akinc, M.; Schmidt-Rohr, K.; Mallapragada, S. Self-assembled calcium phosphate nanocomposites using block copolypeptide templates. *Soft Matter* 2009, 5, 4311-4320.
40. Wanka, G.; Hoffmann, H.; Ulbricht, W. The aggregation behavior of poly-(oxyethylene)-poly-(oxypropylene)-poly-(oxyethylene)-block-copolymers in aqueous solution. *Colloid Polym. Sci.* 1990, 268, 101-117.
41. Alexandridis, P.; Holzwarth, J. F.; Hatton, T. A. Micellization of Poly(ethylene oxide)-Poly(propylene oxide)-Poly(ethylene oxide) Triblock Copolymers in Aqueous Solutions: Thermodynamics of Copolymer Association. *Macromolecules* 1994, 27, 2414-2425.

42. Goldmints, I.; von Gottberg, F. K.; Smith, K. A.; Hatton, T. A. Small-Angle Neutron Scattering Study of PEO−PPO−PEO Micelle Structure in the Unimer-to-Micelle Transition Region. *Langmuir* 1997, 13, 3659-3664.
43. Wu, G.; Chu, B.; Schneider, D. K. SANS Study of the Micellar Structure of PEO/PPO/PEO Aqueous Solution. *J. Phys. Chem.* 1995, 99, 5094-5101.
44. Determan, M. D.; Cox, J. P.; Seifert, S.; Thiyagarajan, P.; Mallapragada, S. K. Synthesis and characterization of temperature and pH-responsive pentablock copolymers. *Polymer* 2005, 46, 6933-6946.
45. Liu, X.; Ge, Q.; Rawal, A.; Parada, G.; Schmidt-Rohr, K.; Akinc, M.; Mallapragada, S. K. Templated and Bioinspired Aqueous Phase Synthesis and Characterization of Mesoporous Zirconia. *Sci. Adv. Mater.* 2013, 5, 354-365.
46. Ge, Q.; Liu, X.; Parada, G.; Mallapragada, S. K.; Akinc, M. Synthesis of Mesoporous Zirconia Templated by Block Copolymer-Lysozyme Conjugate in Aqueous Media. *Sci. Adv. Mater.* 2014, 6, 2106-2114.
47. Rothemund, P. W. K. Folding DNA to create nanoscale shapes and patterns. *Nature* 2006, 440, 297-302.
48. Han, D.; Pal, S.; Liu, Y.; Yan, H. Folding and cutting DNA into reconfigurable topological nanostructures. *Nat. Nanotechnol.* 2010, 5, 712-717.
49. Seeman, N. C. DNA in a material world. *Nature* 2003, 421, 427-431.
50. Sone, E. D.; Zubarev, E. R.; Stupp, S. I. Semiconductor Nanohelices Templated by Supramolecular Ribbons. *Angew. Chem. Int. Ed.* 2002, 41, 1705-1709.
51. Braun, E.; Eichen, Y.; Sivan, U.; Ben-Yoseph, G. DNA-templated assembly and electrode attachment of a conducting silver wire. *Nature* 1998, 391, 775-778.
52. Fang, C.; Fan, Y.; Kong, J. M.; Zhang, G. J.; Linn, L.; Rafeah, S. DNA-templated preparation of palladium nanoparticles and their application. *Sens. Actuator B Chem.* 2007, 126, 684-690.
53. Deng, Z.; Mao, C. DNA-Templated Fabrication of 1D Parallel and 2D Crossed Metallic Nanowire Arrays. *Nano Lett.* 2003, 3, 1545-1548.
54. Monson, C. F.; Woolley, A. T. DNA-Templated Construction of Copper Nanowires. *Nano Lett.* 2003, 3, 359-363.
55. Keren, K.; Berman, R. S.; Braun, E. Patterned DNA Metallization by Sequence-Specific Localization of a Reducing Agent. *Nano Lett.* 2004, 4, 323-326.
56. Richter, J.; Mertig, M.; Pompe, W.; Mönch, I.; Schackert, H. K. Construction of highly conductive nanowires on a DNA template. *Appl. Phys. Lett.* 2001, 78, 536-538.
57. Mertig, M.; Colombi Ciacchi, L.; Seidel, R.; Pompe, W.; De Vita, A. DNA as a Selective Metallization Template. *Nano Lett.* 2002, 2, 841-844.
58. Gu, Q.; Cheng, C.; Haynie, D. T. Cobalt metallization of DNA: toward magnetic nanowires. *Nanotechnology* 2005, 16, 1358.
59. Richter, J.; Seidel, R.; Kirsch, R.; Mertig, M.; Pompe, W.; Plaschke, J.; Schackert, H. K. Nanoscale Palladium Metallization of DNA. *Adv. Mater.* 2000, 12, 507-510.
60. Richter, J. Metallization of DNA. *Phys. E* 2003, 16, 157-173.
61. Burley, G. A.; Gierlich, J.; Mofid, M. R.; Nir, H.; Tal, S.; Eichen, Y.; Carell, T. Directed DNA Metallization. *J. Am. Chem. Soc.* 2006, 128, 1398-1399.
62. Liu, J.; Geng, Y.; Pound, E.; Gyawali, S.; Ashton, J. R.; Hickey, J.; Woolley, A. T.; Harb, J. N. Metallization of Branched DNA Origami for Nanoelectronic Circuit Fabrication. *ACS Nano* 2011, 5, 2240-2247.

63. Siponen, M. I.; Legrand, P.; Widdrat, M.; Jones, S. R.; Zhang, W.-J.; Chang, M. C. Y.; Faivre, D.; Arnoux, P.; Pignol, D. Structural insight into magnetochrome-mediated magnetite biomineralization. *Nature* 2013, 502, 681-684.
64. Fdez-Gubieda, M. L.; Muela, A.; Alonso, J.; García-Prieto, A.; Olivi, L.; Fernández-Pacheco, R.; Barandiarán, J. M. Magnetite Biomineralization in Magnetospirillum gryphiswaldense: Time-Resolved Magnetic and Structural Studies. *ACS Nano* 2013, 7, 3297-3305.
65. Kolinko, I.; Lohsze, A.; Borg, S.; Raschdorf, O.; Jogler, C.; Tu, Q.; Posfai, M.; Tompa, E.; Plitzko, J. M.; Brachmann, A.; Wanner, G.; Muller, R.; Zhang, Y.; Schuler, D. Biosynthesis of magnetic nanostructures in a foreign organism by transfer of bacterial magnetosome gene clusters. *Nat. Nanotechnol.* 2014, 9, 193-197.
66. Bazylinski, D. A.; Frankel, R. B. Magnetosome formation in prokaryotes. *Nat. Rev. Microbiol.* 2004, 2, 217-230.
67. Blakemore, R. Magnetotactic bacteria. *Science* 1975, 190, 377-379.
68. Bazylinski, D. A.; Frankel, R. B.; Heywood, B. R.; Mann, S.; King, J. W.; Donaghay, P. L.; Hanson, A. K. Controlled Biomineralization of Magnetite (Fe3O4) and Greigite (Fe3S4) in a Magnetotactic Bacterium. *Appl. Environ. Microbiol.* 1995, 61, 3232-9.
69. Blakemore, R.; Maratea, D.; Wolfe, R. Isolation and pure culture of a freshwater magnetic spirillum in chemically defined medium. *J. Bacteriol.* 1979, 140, 720-729.
70. Blakemore, R. P. Magnetotactic bacteria. *Annu. Rev. Microbiol.* 1982, 36, 217-238.
71. Bazylinski, D. A.; Frankel, R. B. Magnetosome formation in prokaryotes. *Nature Reviews Microbiology* 2004, 2, 217-230.
72. Balkwill, D.; Maratea, D.; Blakemore, R. Ultrastructure of a magnetotactic spirillum. *J. Bacteriol.* 1980, 141, 1399-1408.
73. Komeili, A. Molecular mechanisms of magnetosome formation. *Annu. Rev. Biochem.* 2007, 76, 351-366.
74. Frankel, R. B.; Bazylinski, D. A. How magnetotactic bacteria make magnetosomes queue up. *Trends Microbiol.* 2006, 14, 329-331.
75. Smith, M.; Sheehan, P.; Perry, L.; O'Connor, K.; Csonka, L.; Applegate, B.; Whitman, L. Quantifying the magnetic advantage in magnetotaxis. *Biophys. J.* 2006, 91, 1098-1107.
76. Devouard, B.; Posfai, M.; Hua, X.; Bazylinski, D. A.; Frankel, R. B.; Buseck, P. R. Magnetite from magnetotactic bacteria: Size distributions and twinning. *Am. Mineral.* 1998, 83, 1387-1398.
77. Butler, R. F.; Banerjee, S. K. Theoretical single-domain grain size range in magnetite and titanomagnetite. *J. Geophys. Res.* 1975, 80, 4049-4058.
78. Park, J.; An, K.; Hwang, Y.; Park, J.-G.; Noh, H.-J.; Kim, J.-Y.; Park, J.-H.; Hwang, N.-M.; Hyeon, T. Ultra-large-scale syntheses of monodisperse nanocrystals. *Nat. Mater.* 2004, 3, 891-895.
79. Lu, A.-H.; Salabas, E. L.; Schüth, F. Magnetic Nanoparticles: Synthesis, Protection, Functionalization, and Application. *Angew. Chem., Int. Ed.* 2007, 46, 1222-1244.
80. Kim, D.; Lee, N.; Park, M.; Kim, B. H.; An, K.; Hyeon, T. Synthesis of Uniform Ferrimagnetic Magnetite Nanocubes. *J. Am. Chem. Soc.* 2009, 131, 454-455.
81. Laurent, S.; Forge, D.; Port, M.; Roch, A.; Robic, C.; Vander Elst, L.; Muller, R. N. Magnetic Iron Oxide Nanoparticles: Synthesis, Stabilization, Vectorization, Physicochemical Characterizations, and Biological Applications. *Chem. Rev.* 2008, 108, 2064-2110.

82. Gupta, A. K.; Gupta, M. Synthesis and surface engineering of iron oxide nanoparticles for biomedical applications. *Biomaterials* 2005, 26, 3995-4021.
83. Yang, C.; Wu, J.; Hou, Y. Fe3O4 nanostructures: synthesis, growth mechanism, properties and applications. *Chem. Commun.* 2011, 47, 5130-5141.
84. Cornell, R. M.; Schwertmann, U. *The iron oxides: structure, properties, reactions, occurrences and uses*. John Wiley & Sons: 2003.
85. Peters, C.; Dekkers, M. J. Selected room temperature magnetic parameters as a function of mineralogy, concentration and grain size. *Phys. Chem. Earth* 2003, 28, 659-667.
86. Dunlop, D. J. Superparamagnetic and single-domain threshold sizes in magnetite. *J. Geophys. Res.* 1973, 78, 1780-1793.
87. Krishnan, K. M.; Pakhomov, A. B.; Bao, Y.; Blomqvist, P.; Chun, Y.; Gonzales, M.; Griffin, K.; Ji, X.; Roberts, B. K. Nanomagnetism and spin electronics: materials, microstructure and novel properties. *J. Mater. Sci.* 2006, 41, 793-815.
88. Prozorov, T.; Bazylinski, D. A.; Mallapragada, S. K.; Prozorov, R. Novel magnetic nanomaterials inspired by magnetotactic bacteria: Topical review. *Mater. Sci. Eng. R* 2013, 74, 133-172.
89. Pankhurst, Q. A.; Connolly, J.; Jones, S. K.; Dobson, J. Applications of magnetic nanoparticles in biomedicine. *J. Phys. D: Appl. Phys.* 2003, 36, R167.
90. Xu, C.; Sun, S. Superparamagnetic nanoparticles as targeted probes for diagnostic and therapeutic applications. *Dalton Trans.* 2009, 5583-5591.
91. Jiles, D. C. *Introduction to Magnetism and Magnetic Materials, Second Edition*. Taylor & Francis: 1998.
92. Sun, S.; Zeng, H. Size-Controlled Synthesis of Magnetite Nanoparticles. *J. Am. Chem. Soc.* 2002, 124, 8204-8205.
93. Wang, Z. L. Transmission Electron Microscopy of Shape-Controlled Nanocrystals and Their Assemblies. *J. Phys. Chem. B* 2000, 104, 1153-1175.
94. Arakaki, A.; Webb, J.; Matsunaga, T. A novel protein tightly bound to bacterial magnetic particles in Magnetospirillum magneticum strain AMB-1. *J. Biol. Chem.* 2003, 278, 8745-8750.
95. Tanaka, M.; Mazuyama, E.; Arakaki, A.; Matsunaga, T. MMS6 protein regulates crystal morphology during nano-sized magnetite biomineralization in vivo. *J. Biol. Chem.* 2011, 286, 6386-6392.
96. Wang, L.; Nilsen-Hamilton, M. Biomineralization proteins: from vertebrates to bacteria. *Front. Biol.* 2013, 8, 234-246.
97. Prozorov, T.; Mallapragada, S. K.; Narasimhan, B.; Wang, L.; Palo, P.; Nilsen-Hamilton, M.; Williams, T. J.; Bazylinski, D. A.; Prozorov, R.; Canfield, P. C. Protein-Mediated Synthesis of Uniform Superparamagnetic Magnetite Nanocrystals. *Adv. Funct. Mater.* 2007, 17, 951-957.
98. Wang, L.; Prozorov, T.; Palo, P. E.; Liu, X.; Vaknin, D.; Prozorov, R.; Mallapragada, S.; Nilsen-Hamilton, M. Self-Assembly and Biphasic Iron-Binding Characteristics of Mms6, A Bacterial Protein That Promotes the Formation of Superparamagnetic Magnetite Nanoparticles of Uniform Size and Shape. *Biomacromolecules* 2012, 13, 98-105.
99. Prozorov, T.; Palo, P.; Wang, L.; Nilsen-Hamilton, M.; Jones, D.; Orr, D.; Mallapragada, S. K.; Narasimhan, B.; Canfield, P. C.; Prozorov, R. Cobalt Ferrite Nanocrystals: Out-Performing Magnetotactic Bacteria. *ACS Nano* 2007, 1, 228-233.

100. Amemiya, Y.; Arakaki, A.; Staniland, S. S.; Tanaka, T.; Matsunaga, T. Controlled formation of magnetite crystal by partial oxidation of ferrous hydroxide in the presence of recombinant magnetotactic bacterial protein Mms6. *Biomaterials* 2007, 28, 5381-5389.
101. Arakaki, A.; Masuda, F.; Amemiya, Y.; Tanaka, T.; Matsunaga, T. Control of the morphology and size of magnetite particles with peptides mimicking the Mms6 protein from magnetotactic bacteria. *J. Colloid Interface Sci.* 2010, 343, 65-70.
102. Galloway, J. M.; Arakaki, A.; Masuda, F.; Tanaka, T.; Matsunaga, T.; Staniland, S. S. Magnetic bacterial protein Mms6 controls morphology, crystallinity and magnetism of cobalt-doped magnetite nanoparticles in vitro. *J. Mater. Chem.* 2011, 21, 15244-15254.
103. Galloway, J. M.; Bramble, J. P.; Rawlings, A. E.; Burnell, G.; Evans, S. D.; Staniland, S. S. Biotemplated Magnetic Nanoparticle Arrays. *Small* 2012, 8, 204-208.
104. Feng, S.; Wang, L.; Palo, P.; Liu, X.; Mallapragada, S.; Nilsen-Hamilton, M. Integrated self-assembly of the mms6 magnetosome protein to form an iron-responsive structure. *Int. J. Mol. Sci.* 2013, 14, 14594-14606.
105. Wang, W.; Bu, W.; Wang, L.; Palo, P. E.; Mallapragada, S.; Nilsen-Hamilton, M.; Vaknin, D. Interfacial Properties and Iron Binding to Bacterial Proteins That Promote the Growth of Magnetite Nanocrystals: X-ray Reflectivity and Surface Spectroscopy Studies. *Langmuir* 2012, 28, 4274-4282.
106. Kashyap, S.; Woehl, T. J.; Liu, X.; Mallapragada, S. K.; Prozorov, T. Nucleation of Iron Oxide Nanoparticles Mediated by Mms6 Protein in Situ. *ACS Nano* 2014, 8, 9097-9106.
107. Whitesides, G.; Mathias, J.; Seto, C. Molecular self-assembly and nanochemistry: a chemical strategy for the synthesis of nanostructures. *Science* 1991, 254, 1312-1319.
108. Mendes, A. C.; Baran, E. T.; Reis, R. L.; Azevedo, H. S. Self-assembly in nature: using the principles of nature to create complex nanobiomaterials. *Wiley Interdiscip. Rev. Nanomed. Nanobiotechnol.* 2013, 5, 582-612.
109. Whitesides, G. M.; Boncheva, M. Beyond molecules: Self-assembly of mesoscopic and macroscopic components. *Proc. Natl. Acad. Sci. USA* 2002, 99, 4769-4774.
110. Whitesides, G. M.; Grzybowski, B. Self-Assembly at All Scales. *Science* 2002, 295, 2418-2421.
111. Boles, M. A.; Engel, M.; Talapin, D. V. Self-Assembly of Colloidal Nanocrystals: From Intricate Structures to Functional Materials. *Chem. Rev.* 2016, 116, 11220-11289.
112. Yin, Y.; Alivisatos, A. P. Colloidal nanocrystal synthesis and the organic-inorganic interface. *Nature* 2005, 437, 664-670.
113. Wang, X.; Zhuang, J.; Peng, Q.; Li, Y. A general strategy for nanocrystal synthesis. *Nature* 2005, 437, 121-124.
114. Sun, S.; Murray, C. B.; Weller, D.; Folks, L.; Moser, A. Monodisperse FePt Nanoparticles and Ferromagnetic FePt Nanocrystal Superlattices. *Science* 2000, 287, 1989-1992.
115. Frey, N. A.; Peng, S.; Cheng, K.; Sun, S. Magnetic nanoparticles: synthesis, functionalization, and applications in bioimaging and magnetic energy storage. *Chem. Soc. Rev.* 2009, 38, 2532-2542.
116. Murray, C. B.; Kagan, C. R.; Bawendi, M. G. Synthesis and Characterization of Monodisperse Nanocrystals and Close-Packed Nanocrystal Assemblies. *Annu. Rev. Mater. Sci.* 2000, 30, 545-610.

117. Tao, A. R.; Habas, S.; Yang, P. Shape Control of Colloidal Metal Nanocrystals. *Small* 2008, 4, 310-325.
118. Sun, Y.; Xia, Y. Shape-Controlled Synthesis of Gold and Silver Nanoparticles. *Science* 2002, 298, 2176-2179.
119. Murray, C. B.; Norris, D. J.; Bawendi, M. G. Synthesis and characterization of nearly monodisperse CdE (E = sulfur, selenium, tellurium) semiconductor nanocrystallites. *J. Am. Chem. Soc.* 1993, 115, 8706-8715.
120. Murray, C. B.; Kagan, C. R.; Bawendi, M. G. Self-Organization of CdSe Nanocrystallites into Three-Dimensional Quantum Dot Superlattices. *Science* 1995, 270, 1335-1338.
121. Talapin, D. V.; Shevchenko, E. V.; Kornowski, A.; Gaponik, N.; Haase, M.; Rogach, A. L.; Weller, H. A New Approach to Crystallization of CdSe Nanoparticles into Ordered Three-Dimensional Superlattices. *Adv. Mater.* 2001, 13, 1868-1871.
122. Mirkin, C. A.; Letsinger, R. L.; Mucic, R. C.; Storhoff, J. J. A DNA-based method for rationally assembling nanoparticles into macroscopic materials. *Nature* 1996, 382, 607-609.
123. Alivisatos, A. P.; Johnsson, K. P.; Peng, X.; Wilson, T. E.; Loweth, C. J.; Bruchez, M. P.; Schultz, P. G. Organization of 'nanocrystal molecules' using DNA. *Nature* 1996, 382, 609-611.
124. Nie, Z.; Petukhova, A.; Kumacheva, E. Properties and emerging applications of self-assembled structures made from inorganic nanoparticles. *Nat. Nanotechnol.* 2010, 5, 15-25.
125. Zhang, Y.; Lu, F.; Yager, K. G.; van der Lelie, D.; Gang, O. A general strategy for the DNA-mediated self-assembly of functional nanoparticles into heterogeneous systems. *Nat. Nanotechnol.* 2013, 8, 865-872.
126. Kostiainen, M. A.; Hiekkataipale, P.; Laiho, A.; Lemieux, V.; Seitsonen, J.; Ruokolainen, J.; Ceci, P. Electrostatic assembly of binary nanoparticle superlattices using protein cages. *Nat. Nanotechnol.* 2013, 8, 52-56.
127. Ye, X.; Zhu, C.; Ercius, P.; Raja, S. N.; He, B.; Jones, M. R.; Hauwiller, M. R.; Liu, Y.; Xu, T.; Alivisatos, A. P. Structural diversity in binary superlattices self-assembled from polymer-grafted nanocrystals. *Nat. Commun.* 2015, 6.
128. Shevchenko, E. V.; Talapin, D. V.; Kotov, N. A.; O'Brien, S.; Murray, C. B. Structural diversity in binary nanoparticle superlattices. *Nature* 2006, 439, 55-59.
129. Nykypanchuk, D.; Maye, M. M.; van der Lelie, D.; Gang, O. DNA-guided crystallization of colloidal nanoparticles. *Nature* 2008, 451, 549-552.
130. Tao, A.; Sinsermsuksakul, P.; Yang, P. Tunable plasmonic lattices of silver nanocrystals. *Nat. Nanotechnol.* 2007, 2, 435-440.
131. Dreyfus, R.; Leunissen, M. E.; Sha, R.; Tkachenko, A. V.; Seeman, N. C.; Pine, D. J.; Chaikin, P. M. Simple Quantitative Model for the Reversible Association of DNA Coated Colloids. *Phys. Rev. Lett.* 2009, 102, 048301.
132. Travesset, A. Binary nanoparticle superlattices of soft-particle systems. *Proc. Natl. Acad. Sci. USA* 2015, 112, 9563-9567.
133. Knorowski, C.; Burleigh, S.; Travesset, A. Dynamics and Statics of DNA-Programmable Nanoparticle Self-Assembly and Crystallization. *Phys. Rev. Lett.* 2011, 106, 215501.
134. Knorowski, C.; Travesset, A. Materials design by DNA programmed self-assembly. *Curr. Opin. Solid State Mater. Sci.* 2011, 15, 262-270.

135. Knorowski, C.; Travesset, A. Self-Assembly and Crystallization of Hairy (f-Star) and DNA-Grafted Nanocubes. *J. Am. Chem. Soc.* 2014, 136, 653-659.
136. Travesset, A. Topological structure prediction in binary nanoparticle superlattices. *Soft Matter* 2016.
137. Fontana, J.; Naciri, J.; Rendell, R.; Ratna, B. R. Macroscopic Self-Assembly and Optical Characterization of Nanoparticle–Ligand Metamaterials. *Adv. Opt. Mater.* 2013, 1, 100-106.
138. Young, K. L.; Ross, M. B.; Blaber, M. G.; Rycenga, M.; Jones, M. R.; Zhang, C.; Senesi, A. J.; Lee, B.; Schatz, G. C.; Mirkin, C. A. Using DNA to Design Plasmonic Metamaterials with Tunable Optical Properties. *Adv. Mater.* 2014, 26, 653-659.
139. Talapin, D. V.; Lee, J.-S.; Kovalenko, M. V.; Shevchenko, E. V. Prospects of Colloidal Nanocrystals for Electronic and Optoelectronic Applications. *Chem. Rev.* 2010, 110, 389-458.
140. Maye, M. M.; Nykypanchuk, D.; van der Lelie, D.; Gang, O. DNA-Regulated Micro- and Nanoparticle Assembly. *Small* 2007, 3, 1678-1682.
141. Jones, M. R.; Macfarlane, R. J.; Lee, B.; Zhang, J.; Young, K. L.; Senesi, A. J.; Mirkin, C. A. DNA-nanoparticle superlattices formed from anisotropic building blocks. *Nat. Mater.* 2010, 9, 913-917.
142. Macfarlane, R. J.; Lee, B.; Jones, M. R.; Harris, N.; Schatz, G. C.; Mirkin, C. A. Nanoparticle Superlattice Engineering with DNA. *Science* 2011, 334, 204-208.
143. Macfarlane, R. J.; Jones, M. R.; Senesi, A. J.; Young, K. L.; Lee, B.; Wu, J.; Mirkin, C. A. Establishing the Design Rules for DNA-Mediated Programmable Colloidal Crystallization. *Angew. Chem. Int. Ed.* 2010, 49, 4589-4592.
144. Maye, M. M.; Nykypanchuk, D.; van der Lelie, D.; Gang, O. A Simple Method for Kinetic Control of DNA-Induced Nanoparticle Assembly. *J. Am. Chem. Soc.* 2006, 128, 14020-14021.
145. Xiong, H.; van der Lelie, D.; Gang, O. DNA Linker-Mediated Crystallization of Nanocolloids. *J. Am. Chem. Soc.* 2008, 130, 2442-2443.
146. Park, S. Y.; Lytton-Jean, A. K. R.; Lee, B.; Weigand, S.; Schatz, G. C.; Mirkin, C. A. DNA-programmable nanoparticle crystallization. *Nature* 2008, 451, 553-556.
147. Cademartiri, L.; Bishop, K. J. M. Programmable self-assembly. *Nat. Mater.* 2015, 14, 2-9.
148. Tan, S. J.; Kahn, J. S.; Derrien, T. L.; Campolongo, M. J.; Zhao, M.; Smilgies, D.-M.; Luo, D. Crystallization of DNA-Capped Gold Nanoparticles in High-Concentration, Divalent Salt Environments. *Angew. Chem. Int. Ed.* 2014, 53, 1316-1319.
149. Campolongo, M. J.; Tan, S. J.; Smilgies, D.-M.; Zhao, M.; Chen, Y.; Xhangolli, I.; Cheng, W.; Luo, D. Crystalline Gibbs Monolayers of DNA-Capped Nanoparticles at the Air–Liquid Interface. *ACS Nano* 2011, 5, 7978-7985.
150. Srivastava, S.; Nykypanchuk, D.; Fukuto, M.; Halverson, J. D.; Tkachenko, A. V.; Yager, K. G.; Gang, O. Two-Dimensional DNA-Programmable Assembly of Nanoparticles at Liquid Interfaces. *J. Am. Chem. Soc.* 2014, 136, 8323-8332.
151. Srivastava, S.; Nykypanchuk, D.; Fukuto, M.; Gang, O. Tunable Nanoparticle Arrays at Charged Interfaces. *ACS Nano* 2014, 8, 9857-9866.
152. Vial, S.; Nykypanchuk, D.; Yager, K. G.; Tkachenko, A. V.; Gang, O. Linear Mesostructures in DNA–Nanorod Self-Assembly. *ACS Nano* 2013, 7, 5437-5445.

153. Cheng, W.; Campolongo, M. J.; Cha, J. J.; Tan, S. J.; Umbach, C. C.; Muller, D. A.; Luo, D. Free-standing nanoparticle superlattice sheets controlled by DNA. *Nat. Mater.* 2009, 8, 519-525.
154. Lu, F.; Yager, K. G.; Zhang, Y.; Xin, H.; Gang, O. Superlattices assembled through shape-induced directional binding. *Nat. Commun.* 2015, 6.
155. Tian, Y.; Wang, T.; Liu, W.; Xin, H. L.; Li, H.; Ke, Y.; Shih, W. M.; Gang, O. Prescribed nanoparticle cluster architectures and low-dimensional arrays built using octahedral DNA origami frames. *Nat. Nanotechnol.* 2015, 10, 637-644.
156. Liu, W.; Tagawa, M.; Xin, H. L.; Wang, T.; Emamy, H.; Li, H.; Yager, K. G.; Starr, F. W.; Tkachenko, A. V.; Gang, O. Diamond family of nanoparticle superlattices. *Science* 2016, 351, 582-586.
157. Sontz, P. A.; Bailey, J. B.; Ahn, S.; Tezcan, F. A. A Metal Organic Framework with Spherical Protein Nodes: Rational Chemical Design of 3D Protein Crystals. *J. Am. Chem. Soc.* 2015, 137, 11598-11601.
158. Brodin, J. D.; Ambroggio, X. I.; Tang, C.; Parent, K. N.; Baker, T. S.; Tezcan, F. A. Metal-directed, chemically tunable assembly of one-, two- and three-dimensional crystalline protein arrays. *Nat. Chem.* 2012, 4, 375-382.
159. Lanci, C. J.; MacDermaid, C. M.; Kang, S.-g.; Acharya, R.; North, B.; Yang, X.; Qiu, X. J.; DeGrado, W. F.; Saven, J. G. Computational design of a protein crystal. *Proc. Natl. Acad. Sci. USA* 2012, 109, 7304-7309.
160. Sinclair, J. C.; Davies, K. M.; Venien-Bryan, C.; Noble, M. E. M. Generation of protein lattices by fusing proteins with matching rotational symmetry. *Nat. Nanotechnol.* 2011, 6, 558-562.
161. Wei, H.; Wang, Z.; Zhang, J.; House, S.; Gao, Y.-G.; Yang, L.; Robinson, H.; Tan, L. H.; Xing, H.; Hou, C.; Robertson, I. M.; Zuo, J.-M.; Lu, Y. Time-dependent, protein-directed growth of gold nanoparticles within a single crystal of lysozyme. *Nat. Nanotechnol.* 2011, 6, 93-97.
162. Sun, J.; DuFort, C.; Daniel, M.-C.; Murali, A.; Chen, C.; Gopinath, K.; Stein, B.; De, M.; Rotello, V. M.; Holzenburg, A.; Kao, C. C.; Dragnea, B. Core-controlled polymorphism in virus-like particles. *Proc. Natl. Acad. Sci. USA* 2007, 104, 1354-1359.
163. Hu, M.; Qian, L.; Briñas, R. P.; Lymar, E. S.; Hainfeld, J. F. Assembly of Nanoparticle–Protein Binding Complexes: From Monomers to Ordered Arrays. *Angew. Chem. Int. Ed.* 2007, 46, 5111-5114.
164. McMillan, R. A.; Paavola, C. D.; Howard, J.; Chan, S. L.; Zaluzec, N. J.; Trent, J. D. Ordered nanoparticle arrays formed on engineered chaperonin protein templates. *Nat. Mater.* 2002, 1, 247-252.
165. Shenton, W.; Davis, S. A.; Mann, S. Directed Self-Assembly of Nanoparticles into Macroscopic Materials Using Antibody–Antigen Recognition. *Adv. Mater.* 1999, 11, 449-452.
166. Künzle, M.; Eckert, T.; Beck, T. Binary Protein Crystals for the Assembly of Inorganic Nanoparticle Superlattices. *J. Am. Chem. Soc.* 2016, 138, 12731-12734.
167. Alloyeau, D.; Stéphanidis, B.; Zhao, X.; Larquet, E.; Boisset, N.; Ricolleau, C. Biotemplated Synthesis of Metallic Nanoclusters Organized in Tunable Two-Dimensional Superlattices. *J. Phys. Chem. C* 2011, 115, 20926-20930.
168. Kostiainen, M. A.; Ceci, P.; Fornara, M.; Hiekkataipale, P.; Kasyutich, O.; Nolte, R. J. M.; Cornelissen, J. J. L. M.; Desautels, R. D.; van Lierop, J. Hierarchical Self-Assembly

and Optical Disassembly for Controlled Switching of Magnetoferritin Nanoparticle Magnetism. *ACS Nano* 2011, 5, 6394-6402.

169. Hui, C. M.; Pietrasik, J.; Schmitt, M.; Mahoney, C.; Choi, J.; Bockstaller, M. R.; Matyjaszewski, K. Surface-Initiated Polymerization as an Enabling Tool for Multifunctional (Nano-)Engineered Hybrid Materials. *Chem. Mater.* 2014, 26, 745-762.
170. Ofir, Y.; Samanta, B.; Rotello, V. M. Polymer and biopolymer mediated self-assembly of gold nanoparticles. *Chem. Soc. Rev.* 2008, 37, 1814-1825.
171. Choi, J.; Hui, C. M.; Schmitt, M.; Pietrasik, J.; Margel, S.; Matyjazsewski, K.; Bockstaller, M. R. Effect of Polymer-Graft Modification on the Order Formation in Particle Assembly Structures. *Langmuir* 2013, 29, 6452-6459.
172. Gupta, S.; Agrawal, M.; Uhlmann, P.; Simon, F.; Stamm, M. Poly(N-isopropyl acrylamide)−Gold Nanoassemblies on Macroscopic Surfaces: Fabrication, Characterization, and Application. *Chem. Mater.* 2010, 22, 504-509.
173. Karg, M.; Hellweg, T.; Mulvaney, P. Self-Assembly of Tunable Nanocrystal Superlattices Using Poly-(NIPAM) Spacers. *Adv. Funct. Mater.* 2011, 21, 4668-4676.
174. Li, B.; Smilgies, D.-M.; Price, A. D.; Huber, D. L.; Clem, P. G.; Fan, H. Poly(N-isopropylacrylamide) Surfactant-Functionalized Responsive Silver Nanoparticles and Superlattices. *ACS Nano* 2014, 8, 4799-4804.
175. Kumar, S. K.; Jouault, N.; Benicewicz, B.; Neely, T. Nanocomposites with Polymer Grafted Nanoparticles. *Macromolecules* 2013, 46, 3199-3214.
176. Corbierre, M. K.; Cameron, N. S.; Sutton, M.; Laaziri, K.; Lennox, R. B. Gold Nanoparticle/Polymer Nanocomposites: Dispersion of Nanoparticles as a Function of Capping Agent Molecular Weight and Grafting Density. *Langmuir* 2005, 21, 6063-6072.
177. Gao, B.; Arya, G.; Tao, A. R. Self-orienting nanocubes for the assembly of plasmonic nanojunctions. *Nat. Nanotechnol.* 2012, 7, 433-437.
178. Gurunatha, K. L.; Marvi, S.; Arya, G.; Tao, A. R. Computationally Guided Assembly of Oriented Nanocubes by Modulating Grafted Polymer–Surface Interactions. *Nano Lett.* 2015, 15, 7377-7382.
179. Akcora, P.; Liu, H.; Kumar, S. K.; Moll, J.; Li, Y.; Benicewicz, B. C.; Schadler, L. S.; Acehan, D.; Panagiotopoulos, A. Z.; Pryamitsyn, V.; Ganesan, V.; Ilavsky, J.; Thiyagarajan, P.; Colby, R. H.; Douglas, J. F. Anisotropic self-assembly of spherical polymer-grafted nanoparticles. *Nat. Mater.* 2009, 8, 354-359.
180. He, J.; Liu, Y.; Babu, T.; Wei, Z.; Nie, Z. Self-Assembly of Inorganic Nanoparticle Vesicles and Tubules Driven by Tethered Linear Block Copolymers. *J. Am. Chem. Soc.* 2012, 134, 11342-11345.
181. He, J.; Huang, X.; Li, Y.-C.; Liu, Y.; Babu, T.; Aronova, M. A.; Wang, S.; Lu, Z.; Chen, X.; Nie, Z. Self-Assembly of Amphiphilic Plasmonic Micelle-Like Nanoparticles in Selective Solvents. *J. Am. Chem. Soc.* 2013, 135, 7974-7984.
182. He, J.; Wang, L.; Wei, Z.; Yang, Y.; Wang, C.; Han, X.; Nie, Z. Vesicular Self-Assembly of Colloidal Amphiphiles in Microfluidics. *ACS Appl. Mater. Interfaces* 2013, 5, 9746-9751.
183. Huang, P.; Lin, J.; Li, W.; Rong, P.; Wang, Z.; Wang, S.; Wang, X.; Sun, X.; Aronova, M.; Niu, G.; Leapman, R. D.; Nie, Z.; Chen, X. Biodegradable Gold Nanovesicles with an Ultrastrong Plasmonic Coupling Effect for Photoacoustic Imaging and Photothermal Therapy. *Angew. Chem.* 2013, 125, 14208-14214.

184. Liu, Y.; He, J.; Yang, K.; Yi, C.; Liu, Y.; Nie, L.; Khashab, N. M.; Chen, X.; Nie, Z. Folding Up of Gold Nanoparticle Strings into Plasmonic Vesicles for Enhanced Photoacoustic Imaging. *Angew. Chem.* 2015, 127, 16035-16038.
185. Mueggenburg, K. E.; Lin, X.-M.; Goldsmith, R. H.; Jaeger, H. M. Elastic membranes of close-packed nanoparticle arrays. *Nat. Mater.* 2007, 6, 656-660.
186. Bigioni, T. P.; Lin, X.-M.; Nguyen, T. T.; Corwin, E. I.; Witten, T. A.; Jaeger, H. M. Kinetically driven self assembly of highly ordered nanoparticle monolayers. *Nat. Mater.* 2006, 5, 265-270.
187. Jiang, Z.; Lin, X.-M.; Sprung, M.; Narayanan, S.; Wang, J. Capturing the Crystalline Phase of Two-Dimensional Nanocrystal Superlattices in Action. *Nano Lett.* 2010, 10, 799-803.
188. Narayanan, S.; Wang, J.; Lin, X.-M. Dynamical Self-Assembly of Nanocrystal Superlattices during Colloidal Droplet Evaporation by \textit{in situ} Small Angle X-Ray Scattering. *Phys. Rev. Lett.* 2004, 93, 135503.
189. Dong, A.; Chen, J.; Vora, P. M.; Kikkawa, J. M.; Murray, C. B. Binary nanocrystal superlattice membranes self-assembled at the liquid-air interface. *Nature* 2010, 466, 474-477.
190. Talapin, D. V.; Murray, C. B. PbSe Nanocrystal Solids for n- and p-Channel Thin Film Field-Effect Transistors. *Science* 2005, 310, 86-89.
191. Shevchenko, E. V.; Talapin, D. V.; O'Brien, S.; Murray, C. B. Polymorphism in AB13 Nanoparticle Superlattices: An Example of Semiconductor−Metal Metamaterials. *J. Am. Chem. Soc.* 2005, 127, 8741-8747.
192. Shevchenko, E. V.; Talapin, D. V.; Murray, C. B.; O'Brien, S. Structural Characterization of Self-Assembled Multifunctional Binary Nanoparticle Superlattices. *J. Am. Chem. Soc.* 2006, 128, 3620-3637.
193. Boneschanscher, M. P.; Evers, W. H.; Qi, W.; Meeldijk, J. D.; Dijkstra, M.; Vanmaekelbergh, D. Electron Tomography Resolves a Novel Crystal Structure in a Binary Nanocrystal Superlattice. *Nano Lett.* 2013, 13, 1312-1316.
194. Boles, M. A.; Talapin, D. V. Many-Body Effects in Nanocrystal Superlattices: Departure from Sphere Packing Explains Stability of Binary Phases. *J. Am. Chem. Soc.* 2015, 137, 4494-4502.
195. Bodnarchuk, M. I.; Kovalenko, M. V.; Heiss, W.; Talapin, D. V. Energetic and Entropic Contributions to Self-Assembly of Binary Nanocrystal Superlattices: Temperature as the Structure-Directing Factor. *J. Am. Chem. Soc.* 2010, 132, 11967-11977.
196. Talapin, D. V.; Shevchenko, E. V.; Bodnarchuk, M. I.; Ye, X.; Chen, J.; Murray, C. B. Quasicrystalline order in self-assembled binary nanoparticle superlattices. *Nature* 2009, 461, 964-967.
197. Rupich, S. M.; Shevchenko, E. V.; Bodnarchuk, M. I.; Lee, B.; Talapin, D. V. Size-Dependent Multiple Twinning in Nanocrystal Superlattices. *J. Am. Chem. Soc.* 2010, 132, 289-296.
198. Travesset, A. Phase diagram of power law and Lennard-Jones systems: Crystal phases. *J . Chem. Phys.* 2014, 141, 164501.
199. Horst, N.; Travesset, A. Prediction of binary nanoparticle superlattices from soft potentials. *J . Chem. Phys.* 2016, 144, 014502.

CHAPTER 2. MORPHOLOGICAL TRANSFORMATIONS IN THE MAGNETITE BIOMINERALIZING PROTEIN MMS6 IN IRON SOLUTIONS: A SMALL-ANGLE X-RAY SCATTERING STUDY

Modified from a paper published in *Langmuir*[†]

Honghu Zhang, Xunpei Liu, Shuren Feng, Wenjie Wang[*], Klaus Schmidt-Rohr, Mufit Akinc, Marit Nilsen-Hamilton, David Vaknin, and Surya Mallapragada[*]

2.1 Abstract

Magnetotactic bacteria that produce magnetic nanocrystals of uniform size and well-defined morphologies have inspired the use of biomineralization protein Mms6 to promote formation of uniform magnetic nanocrystals *in vitro*. Small angle X-ray scattering (SAXS) studies in physiological solutions reveal that Mms6 forms compact globular three-dimensional (3D) micelles (approximately 10 nm in diameter) that are, to a large extent, independent of concentration. In the presence of iron ions in the solutions, the general micellar morphology is preserved, however, with associations among micelles that are induced by iron ions. Compared with Mms6, the m2Mms6 mutant (with the sequence of hydroxyl/carboxyl containing residues in the C-terminal domain shuffled) exhibits subtle morphological changes in the presence of iron ions in solutions. The analysis of the SAXS data is consistent with a hierarchical core–corona micellar structure similar to that found in amphiphilic polymers. The addition of ferric and ferrous iron ions to the protein solution induces morphological changes in the micellar structure

[*] Corresponding Authors: wwang@ameslab.gov (W. Wang), suryakm@iastate.edu (S. Mallapragada).

by transforming the 3D micelles into objects of reduced dimensionality of 2, with fractal-like characteristics (including Gaussian-chain-like) or, alternatively, platelet-like structures.

2.2 Introduction

It is well-known that many living organisms, whether unicellular or multicellular, are capable of developing complex inorganic–organic hierarchical materials for various functions such as skeletal support, protection, locomotion, and navigation.[1, 2] These materials are intricately designed under physiological conditions through biomineralization with a high level of control on their particle sizes, morphologies, structures, compositions, aggregation, and crystallographic orientation, and hence exhibit remarkably controlled mechanical, optical, and magnetic properties.[1-3] Tremendous efforts have been devoted to investigating mechanisms of such biomineralization as well as gaining inspiration from nature to develop biomimetic synthetic routes for advanced functionalized materials.[4-7] Proteins and other biological macromolecules, interacting with mineral crystals in biological systems, play an important role in the controlled process of mineralization, which have attracted considerable research interest in recent decades.[8-10] For instance, magnetotactic bacteria, a diverse family of aquatic prokaryotes, have the particular ability to align with the geomagnetic field due to the presence of the magnetosome, an organelle made of a lipid vesicle, in which biomineralized magnetite (Fe_3O_4) or greigite (Fe_3S_4) crystals of uniform sizes and well-defined shapes are embedded.[11] Therefore, they have been employed as effective tools to study biomineralization of magnetic crystals.[12-14]

Mms6, one of several proteins tightly bound to the magnetosome magnetite crystal in magnetotactic bacteria *Magnetospirillum magneticum* AMB-1, has been implicated in the biomineralization of magnetite.[15-19] It has been shown to promote the formation of uniform superparamagnetic magnetite nanocrystals at room temperature and mild conditions *in vitro*.[15, 20,

[21] In addition, Mms6 promotes *in vitro* synthesis of other advanced functionalized materials, such as cobalt ferrite, cobalt doped magnetite, and magnetic nanoparticle arrays.[22-26] Such magnetic materials synthesized with Mms6 have many promising potential applications in targeted drug delivery, magnetic resonance imaging (MRI) contrast agents, and high density data storage.[18] Therefore, significant research efforts have led to understanding the mechanism of Mms6 biomineralization *in vivo*,[16] synthesizing a variety of magnetic nanomaterials *in vitro*, and thereby expanding the biomineralization processes beyond natural materials.[22, 25, 26] Progress has been made recently in understanding the structure and properties of Mms6.[21, 27] Mms6 is an amphiphilic protein with hydrophobic N-terminal and hydrophilic C-terminal, is believed to exist as a membrane protein *in vivo*, and self-assembles *in vitro* to form a multimeric micellar complex larger than 300 kDa.[19, 21, 27, 28] The C-terminal domains bind ferric iron ions and complexes with very high affinity.[21, 28] Shuffling the amino acid sequence in a protein affects its function and thus is a good test to understand the mechanism of biomineralization. A C-terminal mutant, m2Mms6, has been designed that shows much lower iron binding than the wild-type Mms6.[21] Here, we further examine the global morphology of the protein and its C-terminal modified mutant to understand its role in biomineralization. The role of Mms6 in magnetite synthesis *in vitro* is still under investigation.[18-20] With the highly hydrophobic N-terminal domain and larger complex formed by Mms6, it is challenging to determine in detail how Mms6 interacts with iron precursors at atomic resolution by either X-ray crystallography or nuclear magnetic resonance (NMR) spectroscopy. Great caution has to be taken when interpreting data collected with “dry” methods such as AFM and TEM for biomacromolecules like Mms6 due to sample damage or distortion.[27] Here we report on synchrotron radiation small-angle X-ray scattering (SAXS) of Mms6 to determine its morphological characteristics in various solution conditions, as SAXS can

provide an overall three-dimensional structural/morphological information for biological macromolecular complexes in solutions.[29, 30]

Magnetite nanoparticles synthesized via the classical coprecipitation method by elevating the pH of a stoichiometric mixture of ferrous and ferric salts in aqueous medium at room temperature are mostly less than 20 nm and nonuniform in size.[31] In contrast, in the presence of Mms6, magnetite slowly grows to ∼30-nm-diameter superparamagnetic nanoparticles of uniform size and cuboctahedral shapes.[20, 21] The interactions between Mms6 and iron are believed to be the initial steps of biomineralization, and also to be important in determining the shape of the magnetite nanoparticles.[16, 21] The Mms6–iron interactions at various pH values have been previously investigated on aqueous surfaces, where Mms6 was deposited on the surface of an iron solute subphase to form a monolayer, taking advantage of its amphiphilic behavior.[28] In this SAXS study, we investigate the interactions of Mms6 with iron salts in Tris/KCl solutions under very similar conditions to room temperature *in vitro* synthesis of magnetite.[20, 21] The role of pH in the morphology of the protein is also reported as a control in that the presence of iron in solutions affects the pH. The work presented here deals with the interaction of the biomineralization protein with the iron ions, which is the first step in the formation of magnetic nanoparticles using this bioinspired approach. However, the uniform nanoparticles are formed only after these Mms6/iron solutions are exposed to sodium hydroxide (see ref 20 for more details) to elevate the pH significantly and cause coprecipitation, and after a long incubation period of days, which is a step that we have not included in these SAXS studies, since we are studying the role of iron on Mms6. Therefore, in this study it is not intended to form magnetic nanoparticles. It is worth noting that the concentrations of proteins subjected to SAXS measurements are increased to the level of ∼1 mg/mL in order to achieve acceptable data

quality, while most reported Mms6 concentrations used for magnetic nanocrystal synthesis are less than 0.07 mg/mL to use the minimal amount of protein needed to facilitate nanocrystal formation.[15, 20, 21, 25]

2.3 Experimental

2.3.1 Reagents and materials

Iron (III) chloride hexahydrate ($FeCl_3 \cdot 6H_2O$, 98%) and iron (II) chloride tetrahydrate ($FeCl_2 \cdot 4H_2O$, 99.99%) were apurchased from Sigma-Aldrich, and potassium chloride (KCl, 99%), and tris base (99.8%) were purchased from Fisher Scientific. All chemicals were used as received without further treatment. $FeCl_3$ and $FeCl_2$ stock solutions were degassed and purged with nitrogen prior to use.

The mature form of Mms6 protein used in this study was expressed with a poly(histidine) tag (His-tag) on its N-terminal end.[20, 21] His-tagged m2Mms6 was generated by shuffling the hydroxyl/carboxyl containing amino acid residues in the C-terminal domain of His-tagged Mms6, such that m2Mms6 shares the same hydropathy profile as Mms6.[21, 27] For simplicity, the His-tagged Mms6 and m2Mms6 are simply referred to as Mms6 and m2Mms6 (both consisting of 99 amino acid residues, molecular weight (MW) ≈ 10 kDa, average molecular volume $v_{mol} \approx 1.3 \times 10^4$ Å^3).[32] Mms6 and m2Mms6 were purified in inclusion bodies, refolded as previously reported,[20, 21, 27] and dissolved in the buffer BC100 (20 mM Tris, 100 mM KCl, pH 7.5). Proteins in BC100 were flash-frozen with liquid nitrogen and kept frozen prior to use.

2.3.2 Sample preparation for X-ray measurements

Two independent batches of Mms6 and m2Mms6 proteins were used for the SAXS study. Pure Mms6 and m2Mms6 solutions at pH 7.5 with concentrations of 0.067–10 mg/mL were

prepared by dilution from stock solutions with BC100 buffer solution, and it was found that concentrations ≳0.67 mg/mL ensure repeatability of X-ray measurements. 1.0 mg/mL Mms6 and m2Mms6 at pH 3 were also prepared by adding small amount of HCl to the original samples (pH 7.5), in which we observed that one batch of Mms6 looked cloudy upon lowering the pH, while the other batches of Mms6 and m2Mms6 were clear, suggesting a metastable state of some Mms6 proteins susceptible to abrupt drop in pH. Nevertheless, independent experiments including DNA sequencing (of gene coding for Mms6 proteins), SDS-PAGE of purified and refolded proteins, and FPLC gel filtration chromatograpy show the integrity of the protein, albeit at a different aggregation state.

All the mixtures of proteins and iron contained 83 mM $FeCl_3$, 42 mM $FeCl_2$, 6.7 mM Tris, and 33 mM KCl with pH 2.1–2.3. In a typical preparation of the sample with 0.33 mg/mL Mms6, a glass vial was put in a glovebox and charged with 100 μL of degassed water, 50 μL of 500 mM $FeCl_3$, 50 μL of 250 mM $FeCl_2$, and 100 μL of 1.0 mg/mL Mms6 in BC100 buffer as reported.[21] Iron-containing solutions were sealed and maintained under nitrogen at 4 °C for storage. The samples were brought up to room temperature for 2–4 h prior to the scattering measurements. Several sample conditions were tested including (a) samples stored at 4 °C for 2 months, (b) samples stored at 4 °C for 3 days, and (c) freshly prepared samples, which were made with the same stock solutions of proteins at room temperature without use of a glovebox 2–4 h before measurements. All protein/iron solutions prepared at different times (2 months, 3 days, or 2–4 h prior to scattering) were clear, except for the samples with high protein concentrations (⩾2.0 mg/mL) that visibly showed minute precipitates. The measurements of several mixtures of buffer and iron solutions without proteins were used as background.

2.3.3 SAXS setup

SAXS data presented in this study were collected using the synchrotron radiation at the beamline 12ID-B (X-ray energy E = 14.0 keV) at the Advanced Photon Source (APS), Argonne National Laboratory, and were repeatable for each sample conditions. A preselected set of sample conditions were also repeated at 12BM-B (APS) (X-ray energy E = 12.0 keV) to further ensure the repeatability and reproducibility of the collected data. At the 12ID-B, a two-dimensional (2D) detector Pilatus2m was used and the scattering vector magnitude Q, ($Q = 4\pi \sin(\theta)/\lambda$, 2θ being the scattering angle and λ being the X-ray wavelength), was calibrated with silver behenate scattering. The sample solutions were loaded into a flow cell (capillary tube, 1 mm in diameter) that was vertically mounted and normal to the incident X-ray beam. Furthermore, a commonly used, calibrating-protein standard, namely, lysozymes (prepared in NaOAc buffer, 40 mM NaOAc, 150 mM NaCl; pH 3.8), were used to validate the calibration of the SAXS apparatus. During the X-ray exposure period, the solutions flows at a constant rate controlled by a Hamilton Microlab 600 diluter. For each sample condition, multiple frames (30 frames) of scattering were collected to ensure data reproducibility and were later averaged to improve counting statistics. Exposure time (2 s) per frame was carefully chosen to minimize radiation damage while still providing acceptable signal/noise ratio. The 2D data were converted to one-dimensional (1D) plots of intensity versus Q. Most data were collected within Q range 0.005–0.5 $Å^{-1}$. A number of selected samples were even measured to an extended Q range up to 1 $Å^{-1}$. The recorded scattering intensity is further corrected for background subtraction and normalization (to incident beam intensity and exposure time).[30, 33, 34] In this study, the aqueous solutions of Tris/KCl with or without iron are considered as a uniform medium and protein and protein–iron compounds are embedded scattering particles of interest in the medium. All SAXS

intensities for the protein and protein/iron particles shown below are obtained by subtraction of a corresponding signal from the bare solutions without the protein and referred to as $I(Q)$ hereafter.

2.4 Results and Discussion

2.4.1 Mms6 and m2Mms6 assemblies in the absence of iron

SAXS intensities of Mms6 proteins at three concentrations, i.e., 0.67, 1, and 2 mg/mL, are shown in Figure 2.1a. Within the measured Q-range, the SAXS intensities scale proportionally with the Mms6 concentrations. Figure 2.1b shows that the SAXS intensities for different Mms6 concentrations overlap after normalization to the concentrations except for the

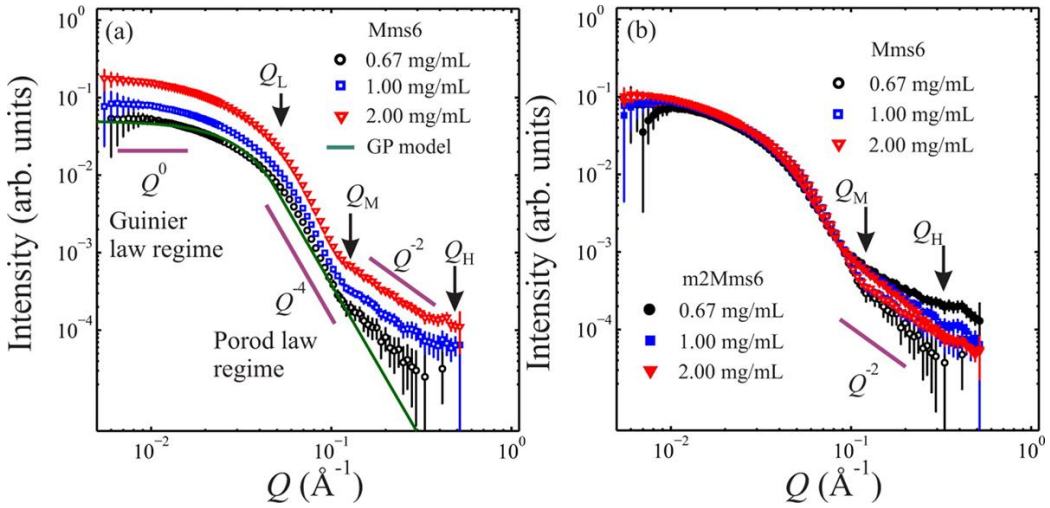

Figure 2.1 (a) SAXS intensities for Mms6 at 0.67, 1, and 2 mg/mL. (b) The SAXS intensities for Mms6 (empty symbols) and m2Mms6 (filled symbols) normalized to the concentrations. The symbols Q_L, Q_M, and Q_H indicate the boundaries of Q-ranges for different power-law behavior of scattering intensities. Three segments of slope 0, −2, and −4 are given as a guide to the eye.

large Q range. This indicates that the particles formed by proteins (characterized with the aggregation number n_{agg}) suspended in the solutions are not correlated and can be viewed as free particles as expected in the dilute solution limit where the scattering intensity is proportional to the number concentration, that is

$$I(Q) \propto N \times n_{agg} \times (\Delta\rho \times v_{mol})^2 \times P(Q) \quad (2.1)$$

where N is the total number of protein molecules in the irradiated solution volume. $P(Q)$ is the form factor of a single, isolated particle, which depends only on particle size and shape, and $P(0) = 1$. $\Delta\rho$ is the excess scattering length density (SLD) of a particle with respect to that of the medium, i.e., solution. A semiquantitative examination of the SAXS intensities shows three prominent Q-regimes, in each of which the scattering is characteristic of a power-law, i.e., $I(Q) \propto Q^{-\alpha}$, where $\alpha = 0, 4, 2$, for $Q < Q_L$, $Q_L < Q < Q_M$, and $Q_M < Q < Q_H$, as indicated in Figure 2.1a. The power-law features for $Q < Q_M$ can be analyzed empirically by the Guinier-Porod (GP) model.[35, 36] The GP model, an approximation of $P(Q)$, combines the Guinier-law feature of scattering intensity at low-Q regime which determines the global shape and size of the particle at relatively large length scale, and the Porod-law feature at the relatively high-Q regime which provides the more local structural information at smaller length scales.[30, 33, 34] The GP model provides an average radius of gyration R_g and the inherent polydispersity of the scattering particles that causes the smearing and disappearance of the oscillations at the Porod-law regime on scattering from monodisperse solid spheres with sharp surfaces.[35, 36] At low-Q, the GP model is given by $P(Q) \propto Q^{-s}\exp(-Q^2R_g^2/3)$, while at higher-$Q$, the $P(Q) \propto Q^{-d}$. As a first step in the analysis, we fit the SAXS intensity with a curve using the GP model with $R_g = 50$ Å, $s = 0$, and $d = 4$, corresponding to a solid, spherical scattering particle ($s = 0$) (Figure 2.1) with sharp surface ($d = 4$), with some deviations at both low-Q and high-Q. The $s = 0$ at Guinier-law regime unequivocally suggests the protein particles are approximately spherical (generally, $s = 1$ and $s = 2$ behaviors correspond to rod- or disk-like particles). A better fit of the SAXS intensities in the low-Q, Guinier-law regime ($Q < Q_L$) results in a larger R_g value, but it underestimates the intensity at the high-Q (Porod-law regime, i.e., $Q_L < Q < Q_M$), and vice versa. This is a direct

consequence of the reciprocity between the size of the scattering objects and the spread of scattering intensity in reciprocal Q-space. A rule of thumb states that the SAXS intensity is concentrated on $Q < 2\pi/L$ for a scattering object of average size L.[30] The fact that a single apparent R_g of GP model fails to fit the SAXS data in the entire selected Q-regime suggests a broader polydispersity than the one neglected in the GP-model. The Q^{-2}-dependence at $Q_M < Q < Q_H$ is reminiscent of the Debye function for scattering of a Gaussian polymer chain which gives rise to Q^{-2} dependence in the high-Q regime.[33, 34] In view of these observations, we use the core–corona model developed by Pedersen originally for block copolymer micelles,[37] that in general can explain, at least qualitatively, all three regions of the SAXS mentioned above.

The core–corona model[37] assumes a micelle constructed of hydrophobic segments that are densely packed into a spherical core of radius R_{core} and N_{chain} slightly hydrophilic chains that are evenly distributed and attached to the surface of the spherical core and extend into the aqueous medium as an ideal polymer chain (referred to as a Gaussian chain) in θ-solvent with a characteristic radius of gyration R_{chain}, as depicted in Figure 2.2a. The scattering intensity from such a micelle, modeled as a function of Q, and paramtrized with R_{core}, R_{chain}, and so forth, is referred to as $I_1(Q; R_{core}, ...)$ and given by

$$I_1(Q;R_{core},...) \propto \begin{aligned} &\beta_{core}^2 P_{core}(Q;R_{core}) \\ &+\frac{1}{N_{chain}}\beta_{corona}^2 P_{chain}(Q;R_{chain}) \\ &+\left(\frac{N_{chain}-1}{N_{chain}}\right)\beta_{corona}^2 S_{chain/chain}(Q;R_{core},R_{chain}) \\ &+2\beta_{corona}\beta_{core}S_{core/chain}(Q;R_{core},R_{chain}) \end{aligned} \tag{2.2}$$

where β_{core} and β_{corona} are the total number of excess scattering length in the core and corona, respectively. The core resembles a solid sphere and the corona chains resemble Gaussian polym-

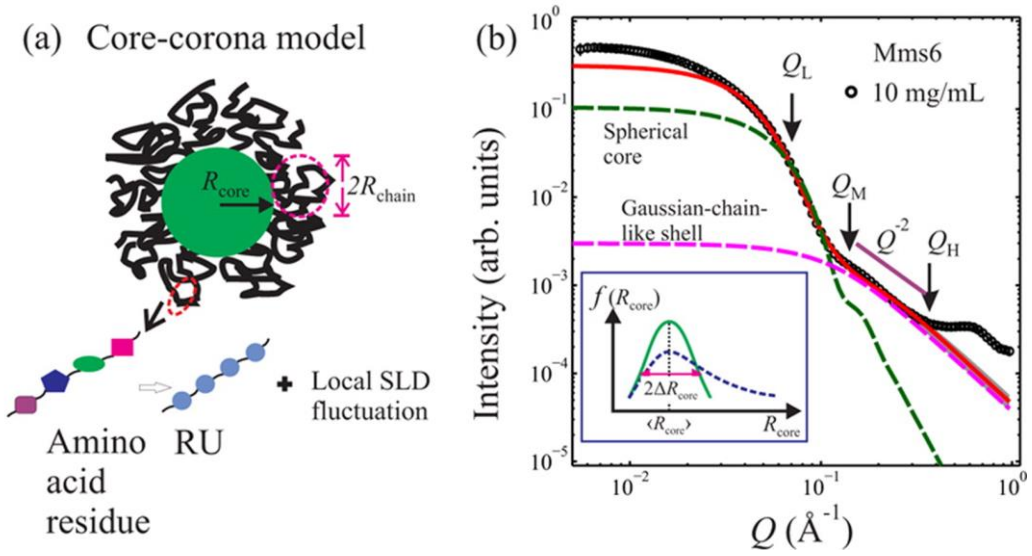

Figure 2.2 (a) Illustration of core–corona model. The spherical core is composed of densely packed, hydrophobic segments. The corona shell is approximated as Gaussian polymer chains attached on the core. Any deviations from the ideal Gaussian-polymer-chain model are viewed as only influencing locally structure on much smaller length scale. (b) SAXS intensity from a 10 mg/mL Mms6 solution. The solid (red) line is one of the best-model fitting curves in terms of Equation 2.2. The narrow, gray area contains the model-fitting curves based on a range of structural parameters as follows: N_{chain} = 31 ± 14, $\langle R_{core} \rangle$ = 39 ± 4 Å, ΔR_{core} = 8 Å, R_{chain} = 11 ± 2 Å, and $\beta_{corona}/\beta_{core}$ = 0.9 ± 0.4. The SAXS intensity is mainly from scattering from the spherical core (green dashed line) at $Q_L < Q < Q_M$ and from the Gaussian chains in the corona (magenta dashed line) at $Q_M < Q < Q_H$. The segment of slope −2 serves as a guide to the eye. To account for particle polydispersity, a statistical distribution of R_{core} is assumed. The inset presents conceptual sketches of statistical distribution of R_{core}, $f(R_{core})$. The solid line in the inset is a sketch of a symmetrical, Gaussian-like distribution of R_{core} (centered at $\langle R \rangle$). The dashed line in the inset is a sketch of an asymmetric distribution in R_{core} that is skewed to large R_{core}. The additional portion in larger R_{core} with respect to the Gaussian distribution results in SAXS intensities concentrated more in small Q-regime while carrying negligible weights at high Q-regime.

er chains. Accordingly, the first two terms in Equation 2.2, $P_{core}(Q, R_{core})$ and $P_{chain}(Q, R_{chain})$, correspond to the form factor of a solid sphere of radius R_{core} and a Gaussian chain of radius of gyration R_{chain}, respectively. The last two terms that contain $S_{chain/chain}(Q; ...)$ and $S_{core/chain}(Q; ...)$ represent contributions from chain–chain correlations in the corona and from chain–core correlation, respectively. Details of the functions can be found in ref 37. At $Q = 0$, $I_1(0) \propto (\beta_{core}$ +

$\beta_{corona})^2$, in which (β_{core} + β_{corona}) is the total excess scattering length of the micelle. As there are two types of scattering entities (core and corona chain) and there is no deterministic way of knowing the polydispersity of size in each, we only assume the core radius obeys a Gaussian distribution (see an illustration in Figure 2.2b), i.e., $f(R_{core}) = 1/((2\pi)^{1/2}\Delta R_{core}) \exp[-(R_{core} - \langle R_{core}\rangle)^2/2\Delta R_{core}^2]$, where $\langle R_{core}\rangle$ and ΔR_{core} represent the mean and spread of the core radius, respectively. So, the total scattering intensity from such a distribution of micelles, $I(Q)$, is proportional to $\int f(R_{core}) I_1(Q; R_{core}, ...)\, dR_{core}$.

By applying the core–corona model to protein particles, we assume that to a reasonable approximation structural variations among amino acids residues forming the corona can be neglected. Figure 2.2a depicts the protein as a sequence of amino acid residues, simplified to an idealized polymer chain of repeating units (RU) that are averaged over all amino acid residues. The deviation of SLD of the actual amino acid from that of the RU is restricted on a length scale of a few angstroms (dimension of an amino acid) and is expected to only influence the X-ray intensity at the wide angle regime. The N-terminal domain with multiple hydrophobic amino acid residues forms a core, and the C-terminal domain and His-tag, characterized with hydrophilic amino acid residues, form the corona, that give rise to the Q^{-2}-dependence of intensity at high-Q. Figure 2.2b shows that the solid line is the best fit using optimal parameters (N_{chain} = 31 ± 14, $\langle R_{core}\rangle$ = 39 ± 4 Å, ΔR_{core} = 8 Å, R_{chain} = 11 ± 2 Å, and $\beta_{corona}/\beta_{core}$ = 0.9 ± 0.4) based on Equation 2.2, whereas the two dashed lines represent the contributions from the first term and second term in Equation 2.2 to illustrate the principal contributions to the SAXS intensity at the two consecutive power-law regimes. At $Q_L < Q < Q_M$, the scattering is dominated by the core yielding the Q^{-4}-dependence, while at $Q_M < Q < Q_H$, the scattering is dominated by dangling residues that resemble Gaussian polymer chains with Q^{-2}-dependence. Given the radius

of the core, the percentage of the protein chain contained in the core, and the average molecular volume of a single Mms6 (1.3×10^4 Å^3, calculated in terms of Mms6 amino acid sequence),[32] the aggregation number of the micelle (n_{agg}) is estimated to be 40 ± 10 at most based on the space-filling model, i.e., the core is constituted by densely packed protein segments. The apparent failure in fitting the SAXS data at $Q < Q_L$ suggests that the assumption of a symmetrical, Gaussian distribution in R_{core} underestimates the actual distribution that may contain substantially more particles with larger R_{core}. The deviation of the SAXS intensity at $Q > Q_H$, which appears for all samples, scales with concentrations originating from the details of the micelle structure at much smaller length scales. The peak at $Q \approx 0.65$ Å^{-1} corresponding to a repeat distance of ~10 Å is reproducible and likely related to a repeat unit in the protein of which the origin awaits further investigation.

Overlaying the SAXS patterns of Mms6 and m2Mms6 shows that the large-scale morphology of the two is similar, as demonstrated in Figure 2.1b. However, the high-Q regime shows that the differences between the two that, although subtle, may be important to their affinity to iron, as has been observed in other studies.[21] After concentration normalization, the SAXS intensities at $Q < Q_M$ collapse into a single curve indicating that m2Mms6 and Mms6 have virtually similar micellar core. However, the $Q^{-\alpha}$-dependence over $Q_M < Q < Q_H$ (dictated by corona chains) for m2Mms6 is evidently different from that of wild-type Mms6, indicating that the corona chains of m2Mms6 deviate from an ideal Gaussian chain ($\alpha = 2$). Noting that a positive (negative) deviation from $\alpha = 2$ is indicative of unfavorable (favorable) chain–solvent interaction,[38] the observation of a positive deviation from $\alpha = 2$ for m2Mms6 at high concentration (2 mg/mL) suggests a more compact chain conformation, and the negative deviation for m2Mms6 at low concentration (0.67 mg/mL) suggests a more extended chain

conformation. These subtle but important observations demonstrate that, while Mms6 and m2Mms6 form similar micellar cores, they arrange their amino acid residues in the C-terminal domains differently in the corona, namely, the functional region that primarily interacts with relevant ions to initiate crystal nucleation.

2.4.2 Protein–iron complexes (particles) produced by the combination of protein and iron

The presence of iron in the protein solutions results in significant changes of the SAXS patterns compared to those of protein without iron in solution. Figure 2.3 shows SAXS from proteins in saturated iron solutions after the subtraction of the iron solution contribution thus representing the scattering from protein–iron complexes only. Figure 2.3a shows SAXS intensities of two independent preparations of Mms6 (labeled "prep-1", empty symbols using a

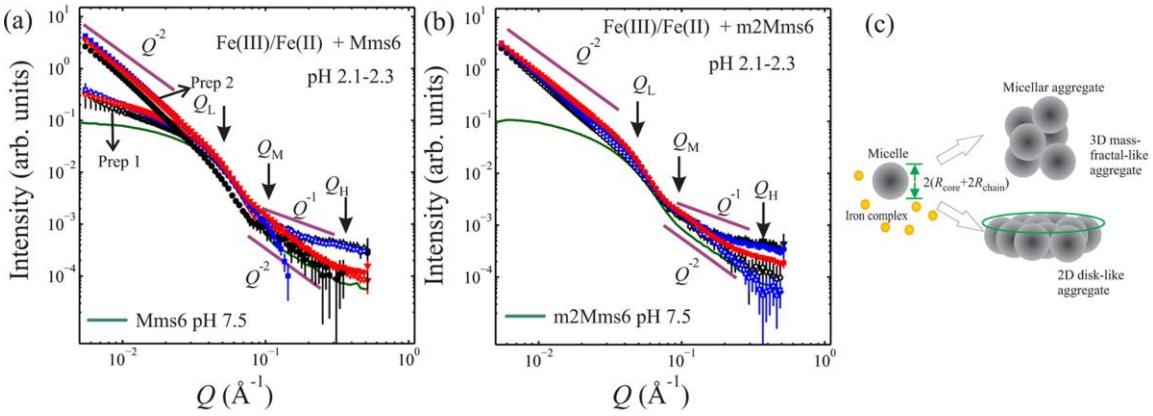

Figure 2.3 (a) Concentration-normalized SAXS data (iron background subtracted) for Mms6 solutions of 0.67 (◯), 1 (□), and 2 mg/mL (∇) in the presence of $FeCl_3$ and $FeCl_2$. The empty and filled symbols represent two preparations of Mms6, denoted prep 1 and 2, respectively. (b) Concentration-normalized SAXS data for m2Mms6 at 0.67 (◯), 1 (□), and 2 mg/mL (∇) in the presence of $FeCl_3$ and $FeCl_2$. The empty symbols and filled symbols represent solutions prepared 2 months and 3 days prior to SAXS measurements. The overlap of intensities suggests that the sample conditions in the presence of iron are stable. Solid lines represent scattering data collected at high pH (7.5) for comparison. The symbols Q_L, Q_M, and Q_H indicate the boundaries of Q-ranges for different power-law behavior of scattering intensities. (c) Illustration of aggregates made up of micelles as building blocks for $S(Q) \propto Q^{-2}$. Segments of slope −1 and −2 serve as a guide to the eye.

single independent batch of Mms6, and "prep-2", filled symbols using a pooled preparation of four independent batches of Mms6). Within each preparation, the SAXS intensities overlay reasonably well upon normalization to concentration, indicating negligible correlations among protein–iron complexed particles. Whereas the SAXS of prep-1 shows some deviation from that of the pure protein (solid line) prep-2 shows a stronger deviation at the low-Q regime ($Q < Q_L$) with a power-law $Q^{-\alpha}$-dependence ($\alpha \approx 2$). We note that, in an independent study of a third preparation of Mms6/iron, the SAXS displayed the same $Q^{-\alpha}$-dependence ($\alpha \approx 2$) at the low-Q regime (data not shown) as in prep-2. The difference may be due to the presence of different levels of residual detergent molecules in the proteins.[39] A similar power-law feature at the low-Q regime is also observed for m2Mms6, as shown in Figure 2.3b. For the $Q_L < Q < Q_H$ region, the curves seem to almost coincide with those of the pure protein preparations, suggesting the original protein micelles remain almost intact in the presence of iron. At $Q_M < Q < Q_H$, the Q^{-2} dependence (except for the anomaly for prep-1) is characteristic of scattering from the polymer-coil-like structure.

The emergence of $Q^{-\alpha}$-dependence ($\alpha \approx 2$) intensities over the low-Q regime ($Q < Q_L$) can be interpreted as arising from the spatial correlation of the micelles. Two levels of structural hierarchy and complexities are presented as follows in a simplistic manner. In the absence of iron, as discussed in the preceding section, the total number N of proteins are dispersed in the irradiated volume to form N/n_{agg} micelles (first level of hierarchy), each of which scatters X-ray independently, as expressed in Equation 2.1. In response to changes by the addition of iron ions, these free-roaming micelles interact with one another to form an assembly of a higher hierarchy. Assuming they remain intact after association, the intensity from these protein/iron particles, $I(Q)$, can be modeled as follows

$$I(Q) \propto N \times n_{agg} \times (\Delta\rho \times v_{mol})^2 \times S(Q) \times P(Q) \quad (2.3)$$

where $S(Q)$ is referred to as structure factor accounting for the correlation among micelles. The power-law in $I(Q)$ at $Q < Q_L$, i.e., $I(Q) \propto Q^{-\alpha}$ ($\alpha \approx 2$) is ascribed to $S(Q)$ for an assembly of building blocks (micelles, in this case) packed in an open, mass-fractal-like manner.[40] Mathematically, $S(Q)$ of a mass fractal dominates the intensity up to $Q \simeq a^{-1}$ below which $P(Q)$ is approximately unity, and a is a characteristic length of its building blocks.[40] For $Q \gtrsim a^{-1}$, $S(Q) \sim 1$ and Equation 2.3 is reduced to Equation 2.1.[40] This explains a new power-law for low-Q range ($Q < Q_L$) in Figure 2.3a,b. Alternatively, the $\alpha \approx 2$ at the low-Q regime is also consistent with lateral micelle association forming planar larger, disk-like objects. The total intensity for such a disk-like structure, in terms of the GP-model, is $Q^{-s} \exp(-Q^2R_g^2/3)$, where $s = 2$ for a disk-like object at low and medium Q range.[35, 36] These two picures of the protein micellar assemblies are depicted as disk-like objects and mass-fractal-like aggregates in Figure 2.3c.

The fact that the scattering intensities at high-Q regime ($Q_M < Q < Q_H$) still exhibit a distinctive $Q^{-\alpha}$-dependence, albeit subtle deviations from $\alpha = 2$ and slightly higher than those for proteins in the absence of iron, indicates the existence of similar polymer-coil-like structure on a similar length scale of the corona chains on protein micelles. The corona giving rise to slightly higher intensities in the presence of iron may suggest SLD enhancement due to the iron enrichment, which necessitate validation by other techniques.

Introducing iron into a pH neutral aqueous solution results in significant pH reduction due to iron hydrolysis; therefore, we conducted control experiments under similar pH values in the absence of iron in solutions to evaluate the effect of pH alone on protein associations. Figure 2.4 shows a comparison of SAXS from Mms6 at various pH values (without iron in the solutions). The intensity profiles are clearly different than those shown in Figure 2.3 both in abs-

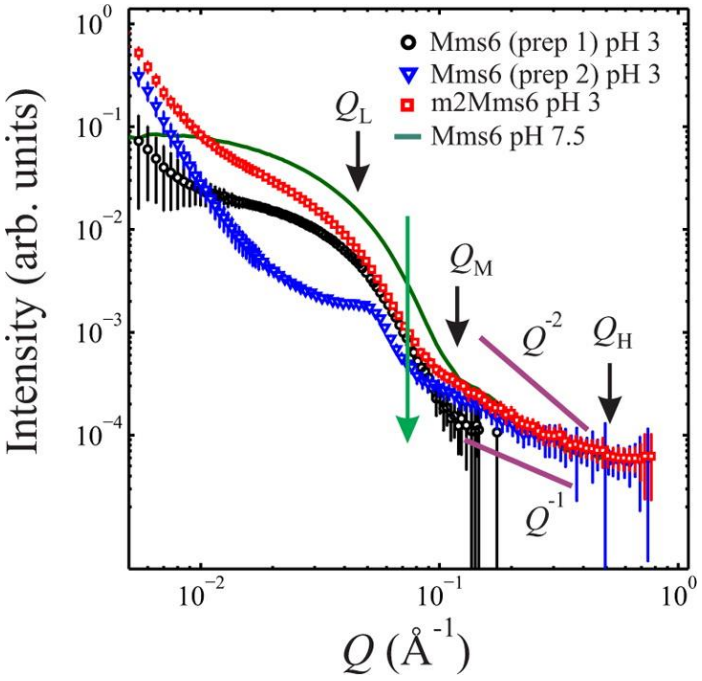

Figure 2.4 SAXS scattering from Mms6 and m2Mms6 at low pH (3) (only intensities that are substantially above background are shown). Solid lines represent scattering data collected at high pH (7.5) for comparison. The symbols Q_L, Q_M, and Q_H indicate the boundaries of Q-ranges for different power-law behavior of scattering intensities. The arrow (green) at $Q_L < Q < Q_M$ indicates the reduction in intensities supposedly from micelle cores upon lowering pH. Segments of slope −1 and −2 serve as a guide to the eye.

olute intensity and in shape. Qualitative examination of the data at $Q_L < Q < Q_M$ suggests that lowering the pH has a dramatic effect on the protein structure. Although independent micelles may still be present in the solution, the lower intensity compared to that at pH 7.5 is evidence of a much lower core density of these micelles and deterioration of the core structure compared to micelles at pH 7.5. The observation of a weak peak in one of Mms6 preps at $Q \approx 0.05$ Å^{-1} may correspond to an average particle size of ~120 Å in correlated aggregates, which is on the same length scale as that obtained from the core–corona model. Considering that the isoelectric point (IP) of Mms6 is ~5.2, as calculated from its primary amino acid sequence, lowering the pH from 7.5 to 3.0 forces the protein to pass the IP abruptly. This may transform the micellar state to a metastable state that may lead to precipitation at low pH. At low-Q regime ($Q < Q_L$), the upturn

in intensities is attributed to correlations between micelles, giving rise to a structure factor $S(Q)$, as in Equation 2.3. At the high-Q regime that is supposedly dictated by the corona, the Q^{-2}-dependence of intensities is replaced by a Q^{-1}-dependence upon lowering the pH to 3, indicating a significant change in conformation of corona chains. The Q^{-1}-dependence is commonly regarded as originating from rod-like scattering objects.

2.5 Conclusions

Using synchrotron radiation SAXS, we determined the micellar morphology of the protein Mms6 that is implicated in promoting the growth of nanocrystal magnetite in magnetotactic bacteria. The morphology of Mms6 is compared with that of its mutant, m2Mms6, that does not bind iron, in Tris/KCl solutions with or without Fe(II) and Fe(III) in solutions. Our main results are summarized as follows: (1) The Mms6 and m2Mms6 proteins both aggregate as micelles that resemble core–corona structures of block polymer micelles. The core is likely formed by hydrophobic segments of the proteins and is modeled as a sphere of average radius ~40 Å. The corona shell consists of hydrophilic residues that give rise to typical Gaussian-polymer-chain-like structure extending the radius of the core by ~20 Å. We find subtle but relevant differences between the corona of Mms6 and its mutant m2Mms6, the charged regions of the protein responsible for the initial binding of ions and nucleation. (2) The presence of Fe(II)/Fe(III) ions in solutions to a large extent preserves the micellar structure in the absence of iron and induces weak association among micelles. This iron-induced association produces larger particles in the form of a disk-like particles or a mass-fractal-like structure. (3) While the morphology of the cores is similar, we qualitatively infer some differences in the corona conformation of the protein particles in the presence and absence of iron isolations. Relatively higher protein concentrations lead to aggregation, first into micelles at neutral pH, and into larger

micellar aggregates in the presence of iron. (4) Control experiments at pH values that are comparable to those obtained by the addition of iron ions in solutions reduce core densities. By contrast, Fe ions in solutions at low pH values preserve the integrity of the micellar structure of the protein.

2.6 Acknowledgements

We thank Xiaobin Zuo at beamline 12ID-B and Benjamin Reinhart at beamline 12BM-B of APS for technical support in SAXS. We thank Pierre E. Palo (Ames Laboratory) for kindly preparing the proteins. Research supported by the U.S. Department of Energy, Office of Basic Energy Sciences, Division of Materials Sciences and Engineering. Ames Laboratory is operated for the U.S. Department of Energy by Iowa State University under Contract No. DE-AC02-07CH11358. Use of the Advanced Photon Source, an Office of Science User Facility operated for the U.S. Department of Energy (DOE) Office of Science by Argonne National Laboratory, was supported by the U.S. DOE under Contract No. DE-AC02-06CH11357.

References

1. Mann, S. *Biomineralization: Principles and Concepts in Bioinorganic Materials Chemistry*. Oxford University Press: 2001.
2. Veis, A. Crystals and Life: An Introduction. In *Biomineralization*, John Wiley & Sons, Ltd: 2010; pp 1-35.
3. Fratzl, P.; Weinkamer, R. Nature's hierarchical materials. *Prog. Mater. Sci.* 2007, 52, 1263-1334.
4. Sarikaya, M.; Tamerler, C.; Jen, A. K. Y.; Schulten, K.; Baneyx, F. Molecular biomimetics: nanotechnology through biology. *Nat. Mater.* 2003, 2, 577-585.
5. Cölfen, H.; Mann, S. Higher-Order Organization by Mesoscale Self-Assembly and Transformation of Hybrid Nanostructures. *Angew. Chem. Int. Ed.* 2003, 42, 2350-2365.
6. Aizenberg, J.; Weaver, J. C.; Thanawala, M. S.; Sundar, V. C.; Morse, D. E.; Fratzl, P. Skeleton of Euplectella sp.: Structural Hierarchy from the Nanoscale to the Macroscale. *Science* 2005, 309, 275-278.
7. Liu, X.; Mallapragada, S. K. Bioinspired Synthesis of Organic/Inorganic Nanocomposite Materials Mediated by Biomolecules. In *On Biomimetics*, 2011.

8. Falini, G.; Albeck, S.; Weiner, S.; Addadi, L. Control of Aragonite or Calcite Polymorphism by Mollusk Shell Macromolecules. *Science* 1996, 271, 67-69.
9. Belcher, A. M.; Wu, X. H.; Christensen, R. J.; Hansma, P. K.; Stucky, G. D.; Morse, D. E. Control of crystal phase switching and orientation by soluble mollusc-shell proteins. *Nature* 1996, 381, 56-58.
10. Gordon, L. M.; Joester, D. Nanoscale chemical tomography of buried organic-inorganic interfaces in the chiton tooth. *Nature* 2011, 469, 194-197.
11. Bazylinski, D. A.; Frankel, R. B. Magnetosome formation in prokaryotes. *Nat. Rev. Microbiol.* 2004, 2, 217-230.
12. Siponen, M. I.; Legrand, P.; Widdrat, M.; Jones, S. R.; Zhang, W.-J.; Chang, M. C. Y.; Faivre, D.; Arnoux, P.; Pignol, D. Structural insight into magnetochrome-mediated magnetite biomineralization. *Nature* 2013, 502, 681-684.
13. Fdez-Gubieda, M. L.; Muela, A.; Alonso, J.; García-Prieto, A.; Olivi, L.; Fernández-Pacheco, R.; Barandiarán, J. M. Magnetite Biomineralization in Magnetospirillum gryphiswaldense: Time-Resolved Magnetic and Structural Studies. *ACS Nano* 2013, 7, 3297-3305.
14. Kolinko, I.; Lohsze, A.; Borg, S.; Raschdorf, O.; Jogler, C.; Tu, Q.; Posfai, M.; Tompa, E.; Plitzko, J. M.; Brachmann, A.; Wanner, G.; Muller, R.; Zhang, Y.; Schuler, D. Biosynthesis of magnetic nanostructures in a foreign organism by transfer of bacterial magnetosome gene clusters. *Nat. Nanotechnol.* 2014, 9, 193-197.
15. Arakaki, A.; Webb, J.; Matsunaga, T. A novel protein tightly bound to bacterial magnetic particles in Magnetospirillum magneticum strain AMB-1. *J. Biol. Chem.* 2003, 278, 8745-8750.
16. Tanaka, M.; Mazuyama, E.; Arakaki, A.; Matsunaga, T. MMS6 protein regulates crystal morphology during nano-sized magnetite biomineralization in vivo. *J. Biol. Chem.* 2011, 286, 6386-6392.
17. Wang, L.; Nilsen-Hamilton, M. Biomineralization proteins: from vertebrates to bacteria. *Front. Biol.* 2013, 8, 234-246.
18. Prozorov, T.; Bazylinski, D. A.; Mallapragada, S. K.; Prozorov, R. Novel magnetic nanomaterials inspired by magnetotactic bacteria: Topical review. *Mater. Sci. Eng. R* 2013, 74, 133-172.
19. Kashyap, S.; Woehl, T. J.; Liu, X.; Mallapragada, S. K.; Prozorov, T. Nucleation of Iron Oxide Nanoparticles Mediated by Mms6 Protein in Situ. *ACS Nano* 2014, 8, 9097-9106.
20. Prozorov, T.; Mallapragada, S. K.; Narasimhan, B.; Wang, L.; Palo, P.; Nilsen-Hamilton, M.; Williams, T. J.; Bazylinski, D. A.; Prozorov, R.; Canfield, P. C. Protein-Mediated Synthesis of Uniform Superparamagnetic Magnetite Nanocrystals. *Adv. Funct. Mater.* 2007, 17, 951-957.
21. Wang, L.; Prozorov, T.; Palo, P. E.; Liu, X.; Vaknin, D.; Prozorov, R.; Mallapragada, S.; Nilsen-Hamilton, M. Self-Assembly and Biphasic Iron-Binding Characteristics of Mms6, A Bacterial Protein That Promotes the Formation of Superparamagnetic Magnetite Nanoparticles of Uniform Size and Shape. *Biomacromolecules* 2012, 13, 98-105.
22. Prozorov, T.; Palo, P.; Wang, L.; Nilsen-Hamilton, M.; Jones, D.; Orr, D.; Mallapragada, S. K.; Narasimhan, B.; Canfield, P. C.; Prozorov, R. Cobalt Ferrite Nanocrystals: Out-Performing Magnetotactic Bacteria. *ACS Nano* 2007, 1, 228-233.
23. Amemiya, Y.; Arakaki, A.; Staniland, S. S.; Tanaka, T.; Matsunaga, T. Controlled formation of magnetite crystal by partial oxidation of ferrous hydroxide in the presence

of recombinant magnetotactic bacterial protein Mms6. *Biomaterials* 2007, 28, 5381-5389.

24. Arakaki, A.; Masuda, F.; Amemiya, Y.; Tanaka, T.; Matsunaga, T. Control of the morphology and size of magnetite particles with peptides mimicking the Mms6 protein from magnetotactic bacteria. *J. Colloid Interface Sci.* 2010, 343, 65-70.
25. Galloway, J. M.; Arakaki, A.; Masuda, F.; Tanaka, T.; Matsunaga, T.; Staniland, S. S. Magnetic bacterial protein Mms6 controls morphology, crystallinity and magnetism of cobalt-doped magnetite nanoparticles in vitro. *J. Mater. Chem.* 2011, 21, 15244-15254.
26. Galloway, J. M.; Bramble, J. P.; Rawlings, A. E.; Burnell, G.; Evans, S. D.; Staniland, S. S. Biotemplated Magnetic Nanoparticle Arrays. *Small* 2012, 8, 204-208.
27. Feng, S.; Wang, L.; Palo, P.; Liu, X.; Mallapragada, S.; Nilsen-Hamilton, M. Integrated self-assembly of the mms6 magnetosome protein to form an iron-responsive structure. *Int. J. Mol. Sci.* 2013, 14, 14594-14606.
28. Wang, W.; Bu, W.; Wang, L.; Palo, P. E.; Mallapragada, S.; Nilsen-Hamilton, M.; Vaknin, D. Interfacial Properties and Iron Binding to Bacterial Proteins That Promote the Growth of Magnetite Nanocrystals: X-ray Reflectivity and Surface Spectroscopy Studies. *Langmuir* 2012, 28, 4274-4282.
29. Rambo, R. P.; Tainer, J. A. Super-resolution in solution X-ray scattering and its applications to structural systems biology. *Annu. Rev. Biophys* 2013, 42, 415-441.
30. Svergun, D. I.; Koch, M. H.; Timmins, P. A.; May, R. P. *Small angle X-ray and neutron scattering from solutions of biological macromolecules*. Oxford University Press: 2013; Vol. 19.
31. Laurent, S.; Forge, D.; Port, M.; Roch, A.; Robic, C.; Vander Elst, L.; Muller, R. N. Magnetic Iron Oxide Nanoparticles: Synthesis, Stabilization, Vectorization, Physicochemical Characterizations, and Biological Applications. *Chem. Rev.* 2008, 108, 2064-2110.
32. Online peptide property calculator http://www.basic.northwestern.edu/biotools/proteincalc.html.
33. Als-Nielsen, J.; McMorrow, D. *Elements of modern X-ray physics*. John Wiley & Sons: 2011.
34. Narayanan, T. Synchrotron Small-Angle X-Ray Scattering. In *Soft Matter Characterization*, Borsali, R.; Pecora, R., Eds. Springer Netherlands: 2008; pp 899-952.
35. Hammouda, B. Analysis of the Beaucage model. *J. Appl. Crystallogr.* 2010, 43, 1474-1478.
36. Hammouda, B. A new Guinier-Porod model. *J. Appl. Crystallogr.* 2010, 43, 716-719.
37. Pedersen, J. S. Structure factors effects in small-angle scattering from block copolymer micelles and star polymers. *J . Chem. Phys.* 2001, 114, 2839-2846.
38. Rubinstein, M.; Colby, R. *Polymers Physics*. Oxford: 2003.
39. Note: In this study, Tergitol-type NP-40 detergent, as a solubilizing agent for membrane proteins, was used during the protein purification stage. In prep-1, special attention was given to lowering the potential residual levels of NP-40 to the lowest possible. Both prep-1 and prep-2 present same SAXS intensity profiles in the absence of iron.
40. Teixeira, J. Small-angle scattering by fractal systems. *J. Appl. Crystallogr.* 1988, 21, 781-785.

CHAPTER 3. SYNTHESIS AND CHARACTERIZATION OF GD-DOPED MAGNETITE NANOPARTICLES

Modified from a paper published in *Journal of Magnetism and Magnetic Materials*‡

Honghu Zhang, Vikash Malik, Surya Mallapragada, and Mufit Akinc*

3.1 Abstract

Synthesis of magnetite nanoparticles has attracted increasing interest due to their importance in biomedical and technological applications. Tunable magnetic properties of magnetite nanoparticles to meet specific requirements will greatly expand the spectrum of applications. Tremendous efforts have been devoted to studying and controlling the size, shape and magnetic properties of magnetite nanoparticles. Here we investigate gadolinium (Gd) doping to influence the growth process as well as magnetic properties of magnetite nanocrystals via a simple co-precipitation method under mild conditions in aqueous media. Gd doping was found to affect the growth process leading to synthesis of controllable particle sizes under the conditions tested (0-10 at.% Gd^{3+}). Typically, undoped and 5 at.% Gd-doped magnetite nanoparticles were found to have crystal sizes of about 18 and 44 nm, respectively, supported by X-ray diffraction and transmission electron microscopy. Our results showed that Gd-doped nanoparticles retained the magnetite crystal structure, with Gd^{3+} randomly incorporated in the crystal lattice, probably in the octahedral sites. The composition of 5 at.% Gd-doped magnetite was $Fe_{(3-x)}Gd_xO_4$ (x=0.085±0.002), as determined by inductively coupled plasma mass spectrometry. 5 at.% Gd-

* Corresponding Author: makinc@iastate.edu.

doped nanoparticles exhibited ferrimagnetic properties with small coercivity (~65 Oe) and slightly decreased magnetization at 260 K in contrast to the undoped, superparamagnetic magnetite nanoparticles. Templation by the bacterial biomineralization protein Mms6 did not appear to affect the growth of the Gd-doped magnetite particles synthesized by this method.

3.2 Introduction

In the past few decades, magnetic nanoparticles have attracted increasing research interest, not only for their fundamental science but also for their biological and technological applications[1, 2]. Especially, magnetite (Fe_3O_4)—a magnetic iron oxide widespread in almost all of the different compartments of the global system [3]—nanoparticles have been investigated for many applications, such as magnetic data storage, magnetic resonance imaging (MRI) contrast enhancement, hyperthermia, and targeted drug delivery [4, 5].

The magnetic behavior of magnetite nanoparticles greatly depends on their size, shape, purity and crystal structure, which determines their applications. For instance, the size of magnetic particles typically used in biomedicine needs to be in the nanoscale range, so that their dimensions are smaller than or comparable to those of a cell, virus, protein or gene[6]. However, the smallest sized nanoparticles are not necessarily the best because they are often associated with very small magnetic moments and very weak magnetic anisotropy, which dramatically increase difficulties in manipulating the particles for applications with an external magnetic field at ambient temperature [5]. Bulk magnetite is ferrimagnetic with a multiple-domain structure, but when the size of magnetite nanoparticles is below a threshold size d_0 (80 – 100 nm), these particles can no longer support static domain walls, and thus they exhibit ferrimagnetism with a stable single domain[5, 7-9]. When the size decreases further to a critical point d_s (20 – 30 nm), the magnetite nanoparticles become superparamagnetic at room temperature, as their magnetic

moments are thermally equilibrated [5, 7-9]. Applications in data recording and spintronics require magnetic nanoparticles with single domains, while medical use of ferrofluids usually needs superparamagnetic nanoparticles[1, 4, 6, 9, 10]. Therefore, size-controlled synthesis of magnetite nanoparticles for a desired purpose will have a huge impact on the technological and biological industries.

Numerous synthetic routes for magnetite nanoparticles have been developed, such as thermal decomposition of organometallic precursors in high-boiling organic solvents[1, 2, 4, 11, 12]. Although some of these methods produce size-controlled magnetite nanoparticles[13-16], they generally require extreme reaction conditions, such as high temperatures and toxic reagents. The classical co-precipitation method industrially used is by elevating the pH of a stoichiometric mixture of Fe(II) and Fe(III) ions in aqueous solution at room temperature, which is inexpensive, high-yield and safe [1, 2]. But this method typically produces small (< 20 nm) superparamagnetic nanoparticles with little control over the size[1, 2]. Studies with focus on the size control of magnetite nanoparticles via simple co-precipitation method under ambient conditions are still lacking[17, 18].

Chemical purity is another important factor affecting the properties of magnetite. Magnetite has an inverse cubic spinel structure (Space group: *Fd-3m*), in which 32 O^{2-} ions form a face-centered cubic (FCC) unit cell containing eight formula units ($Fe_{24}O_{32}$) with the stoichiometric cations (Fe(III) / Fe(II) = 2)[3, 19]. Magnetite is frequently non-stoichiometric, in which case some other cations (such as Al, Mn, Ni, Cu, Co, etc.) are substituted for Fe due to the flexibility of the oxygen framework[3, 19]. Impurity doping introduces preferred magnetic orientation and alters the magnetic properties[20, 21]. Meanwhile, impurity doping plays a crucial role in nucleation and growth of nanocrystals and is successfully used to modify the size of

nanocrystals[22, 23]. However, relatively little attention has been paid to the size control of magnetite nanoparticles by chemical doping[20, 21], especially in high-yield and industrially robust co-precipitation methods under mild conditions.

Doping is one of the effective routes to modulating magnetism in magnetite nanoparticles[20, 21, 24-27]. Doping magnetite with lanthanide ions has been reported[24-27], as lanthanides potentially offer unique optical and magnetic properties due to their partially occupied 4f electronic state[28]. Particularly, the gadolinium (Gd) ion is interesting, since it has a large magnetic moment resulting in an excellent magnetic resonance imaging effect and is used as a common MRI contrast agent[29-31]. Several chemical synthetic routes for magnetite nanoparticles have been employed to obtain Gd-doped magnetite nanoparticles, including thermal decomposition of organometallic precursors[24], hydrothermal method[25, 26] and a precipitation method with elevated temperatures[27]. Some of these methods produce high-quality magnetite nanoparticles, but they usually require high-temperature treatment, toxic reactants, or complicated operations. In addition, very little work has been focused on the role of Gd doping in the crystal growth process.

In this work, we introduce Gd ions to the conventional simple co-precipitation method to synthesize Gd-doped magnetite nanoparticles under ambient conditions in aqueous media, and investigate the effect of Gd doping on crystal size, structure and magnetic properties of magnetite nanoparticles. We also examine the ability of a biomineralization protein Mms6 from magnetotactic bacteria[32] to synthesize Gd-doped magnetite nanoparticles, as Mms6 was recently found to bind iron ions with high affinity[33-36] and promote growth of uniform magnetite nanocrystals using the co-precipitation process[37].

3.3 Experimental

3.3.1 Chemicals and materials

Iron (III) chloride hexahydrate ($FeCl_3 \cdot 6H_2O$, ≥ 98%), gadolinium chloride hexahydrate ($GdCl_3 \cdot 6H_2O$, 99.999%), and iron (II) chloride tetrahydrate ($FeCl_2 \cdot 4H_2O$, 99.99%) were all purchased from Sigma-Aldrich, and sodium hydroxide (NaOH, ≥ 98%), potassium chloride (KCl, ≥ 99%), and Tris base (≥ 99.8%) were purchased from Fisher Scientific. All chemicals were used as received without further treatment. The mature form of Mms6 protein used in this study was expressed with a poly-histidine tag (His-tag) on its N-terminal end as reported earlier[33, 35, 37]. It consists of 99 amino acid residues with a molecular mass of ~10 kDa.

3.3.2 Synthesis of Gd-doped magnetite nanoparticles

Gd-doped magnetite nanoparticles were synthesized in aqueous solutions via a co-precipitation method. All solutions were degassed and purged with nitrogen prior to use. In a typical magnetite synthesis procedure, a precursor was prepared in a 1.7 mL plastic vial. The vial was placed in an ice bath and charged with 100 µL protein solution containing 20 µg Mms6, 20 mM Tris, and 100 mM KCl (pH ~7.5), 100 µL of 0.5 M $FeCl_3$, and 100 µL of 0.25 M $FeCl_2$. For 5 at.% Gd-doped magnetite synthesis 5 µL of $FeCl_3$ was replaced by 5 µL of 0.5 M $GdCl_3$. The precursor was purged with nitrogen, sealed with Parafilm® and incubated at room temperature for one hour. Meanwhile, 2.5 mL of 0.1 M NaOH solution was added to a 5 mL pear-bottom flask. The flask was then degassed and filled with nitrogen. After incubation, the precursor was added dropwise into the NaOH solution in the flask under constant nitrogen flow. Upon contact with the NaOH solution, the precursor drop formed a black precipitate. The precipitate was aged at room temperature in the sealed flask under nitrogen purge for 5 days. The precipitate was

collected at the bottom of the flask with a magnet, and the supernatant was removed. The precipitate was washed with degassed water (3 × 5 mL) three times prior to characterization.

3.3.3 Characterization

3.3.3.1 Powder X-ray Diffraction (XRD)

XRD analysis of the powders (on pre-cleaned microscope slides) was performed using a PANalytical X'Pert Pro diffraction system equipped X'pert Data collector. The diffractometer was operated at 45 kV and 40 mA. A cobalt Kα radiation source with a wavelength of 0.17903 nm was employed. The scan rate was 0.02°/s with a step size of 0.017° over the 2θ range of 20-80° at a θ-2θ step-scan mode. Data analysis was carried out using PANalytical X'Pert HighScore Plus software.

3.3.3.2 Inductively Coupled Plasma Mass Spectrometry (ICP-MS)

ICP-MS analysis was carried out using a Bruker Aurora Elite inductively coupled plasma mass spectrometer. Magnetite samples were dissolved in 70% nitric acid and then diluted with 3% nitric acid. Plasma conditions were optimized with a standard solution for maximum signals, CeO^+/Ce^+ ratios less than 2%, and Ba^{++}/Ba^+ ratios less than or equal to 3%.

3.3.3.3 X-ray Photoelectron Spectroscopy (XPS)

XPS analysis was conducted using a PHI 5500 multi-technique system with the non-monochromated Al Kα ($h\nu$ = 1486.6 eV) radiation source. The vacuum dried powder samples were mounted on a two-sided tape. Binding energy was calibrated with the adventitious C1*s* (E_b = 284.8 eV).

3.3.3.4 Transmission Electron Microscopy (TEM)

Magnetite nanoparticles were imaged with an FEI Tecnai G^2 F20 Scanning Transmission Electron Microscope operating at 200 kV. Diluted nanoparticle suspensions were placed on holey carbon-coated copper grids and dried in air at room temperature. Multiple areas of each sample were randomly chosen and examined.

3.3.3.5 Magnetization Measurements

Magnetic properties of the nanoparticles samples were measured using a 5T Quantum Design Magnetic Properties Measurement System (MPMS). A suspension of nanoparticles was tightly sealed in a gelatin capsule and all measurements were taken at or below 260 K at which solution is frozen in order to prevent particle movement during measurements. Magnetic hysteresis loops were measured at 5 K and 260 K.

3.4 Results and Discussion

3.4.1 Crystal structure and chemical composition

Structural analysis of the samples was carried out by XRD to assess the effect of Gd doping and the Mms6 protein on the structure of magnetite particles. In a typical study, 5 at.% Gd^{3+} ions as fraction of trivalent ions ($[Gd^{3+}] / ([Fe^{3+}] + [Gd^{3+}]) \times 100\%$) were used to replace Fe3+ ions in magnetite. X-ray diffraction patterns showed that all the displayed peak line positions and relative intensities of undoped and 5 at.% Gd-doped nanocrystals, with or without Mms6 biomineralization protein, were consistent with inverse cubic spinel structure of magnetite (JCPDS# 19-0629) (Figure 3.1).

In general, based on the XRD patterns alone, it is not easy to distinguish magnetite from maghemite (γ-Fe_2O_3), since magnetite can be transformed into maghemite by oxidation[1] and ma-

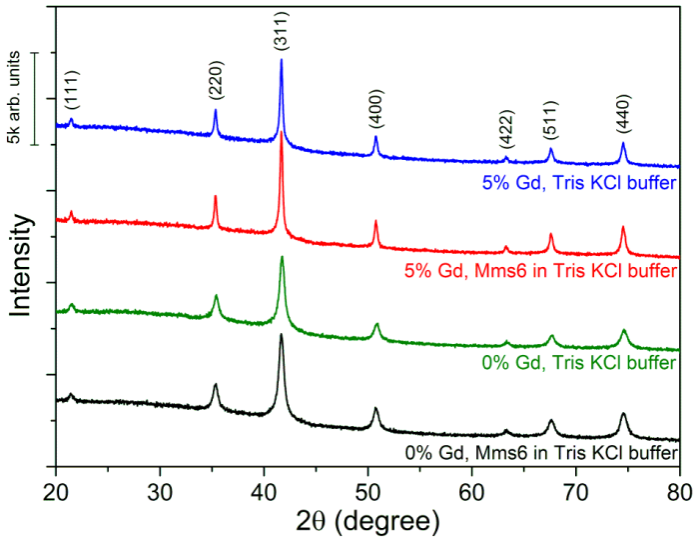

Figure 3.1 X-ray powder diffraction patterns of magnetite nanoparticles prepared with and without 5 at.% Gd doping in the presence and absence of Mms6 protein. The patterns clearly show that the as-prepared materials exhibit magnetite structure with no discernible impurity phases.

ghemite possesses the same spinel structure and almost identical lattice parameters (Space group: $P4_132$, a = 0.8352 nm) as magnetite. Although it is known that maghemite phase has several characteristic peaks such as (210) and (211) peaks, the intensity of these peaks are only 5% of highest intensity in the full standard spectrum[38] (JCPDS# 39-1346). A copper anode is normally employed for routine XRD analysis, but it is difficult to identify the maghemite phases with the Cu X-ray, because the Fe fluorescence activated by the Cu X-ray causes a strong fluorescence signal that can smear the characteristic peaks of maghemite. In the present study, a cobalt anode was used to minimize the Fe fluorescence emission as the electron binding energy of Fe K1*s* is 7.1 keV, which is smaller than the energy of Cu Kα X-ray (8.03-8.05 keV) but greater than the energy of Co Kα X-ray (6.92-6.93 keV). The XRD data with Co X-ray were of high quality, and even (111) peaks with weak intensity at low 2θ angle could be clearly observed (Figure 3.1). In the standard maghemite pattern, the (111) peak is located at 2θ = 21.38°, the (210) peak is at 2θ = 27.68°, and the (211) peak is at 2θ = 30.41°. In Figure 3.1, the characteristic peaks of

maghemite, (210) and (211) peaks were not observed, while peak (111) shows up. Moreover, there were no clear doublets at (511) and (440) peaks at high 2θ angles. Therefore, it was concluded that all these samples exhibit magnetite phases.

Upon close examination of the XRD patterns of the samples doped with Gd, no diffraction peaks from gadolinium hydroxide ($2\theta_{(100)}$ = 18.62°, $2\theta_{(110)}$ = 32.68°, $2\theta_{(101)}$ = 34.11°; JCPDS# 38-1042), gadolinium oxide ($2\theta_{(222)}$ = 33.30°, $2\theta_{(400)}$ = 38.64°, $2\theta_{(440)}$ = 55.79°; JCPDS# 12-797), gadolinium orthoferrite ($GdFeO_3$; $2\theta_{(111)}$ = 30.00°, $2\theta_{(112)}$ = 38.33°, $2\theta_{(200)}$ = 39.07°; JCPDS# 47-67) or gadolinium-iron garnet ($Gd_3Fe_5O_{12}$; $2\theta_{(400)}$ = 33.43°, $2\theta_{(420)}$ = 37.40°, $2\theta_{(422)}$ = 41.16°; JCPDS# 48-77) were observed. XRD patterns confirmed that the 5 at.% Gd-doped samples have a pure, single phase magnetite. Furthermore, peaks in all the different magnetite samples have nearly identical 2θ positions. The *d* spacing of the (311) peaks with highest intensity were calculated to be ~2.516 Å for all samples. No measurable peak shift could be observed in 5 at.% Gd-doped samples relative to pure magnetite. This indicates that the Gd-doped samples maintained the inverse cubic spinel structure of magnetite, and Gd did not alter either the crystal structure or the lattice parameter of as-synthesized parent magnetite.

Table 3.1 The elemental analysis of as-synthesized 5 at.% Gd-doped magnetite nanoparticles by ICP-MS. Gd molar doping percentage as fraction of trivalent ions is expressed as [Gd3+] / ([Fe3+] + [Gd3+]) × 100%. It was assumed that [Fe2+] / ([Fe3+] + [Gd3+]) = 0.5 in the Gd-doped magnetite samples.

Gd-doped magnetite nanoparticles	~5% Gd with Mms6	~5% Gd without Mms6
Measured Gd, % of Fe3+	4.19 ± 0.43	4.35 ± 0.08
Gd : Fe atomic ratio	0.0287 ± 0.0030	0.0298 ± 0.0005
x in Fe(3-*x*)Gd*x*O4	0.084 ± 0.009	0.087 ± 0.002

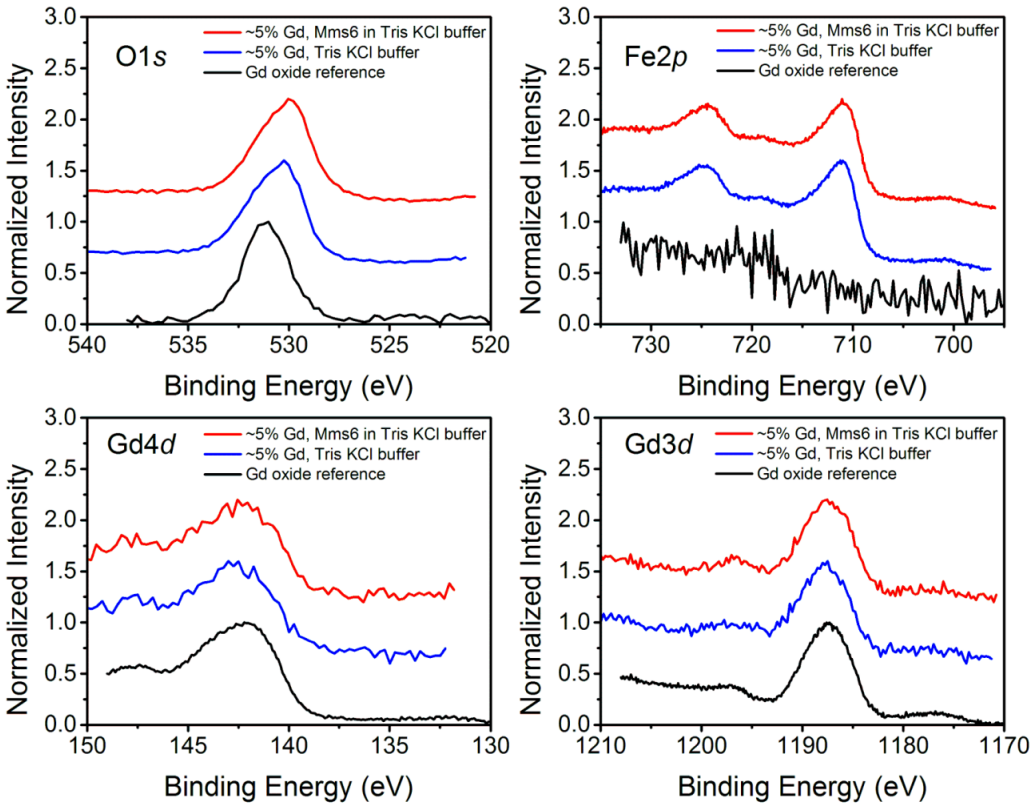

Figure 3.2 XPS spectra of O1*s*, Fe2*p*, Gd4*d* and Gd3*d* for 5 at.% Gd-doped magnetite nanoparticles prepared in the absence of Mms6 (blue) and in the presence of Mms6 (red), and the Gd oxide on the Gd metal as a reference (black). The binding energy was calibrated with C1*s* (E_b = 284.8 eV).

ICP-MS and XPS were performed to determine the elemental composition of the as-synthesized magnetite nanoparticles and verify the presence and form of Gd in the samples (Table 3.1 and Figure 3.2). Elemental analysis by ICP-MS confirmed the presence of Gd in the 5 at.% Gd-doped magnetite nanoparticles. The percentages of Gd as a fraction of trivalent ions calculated from ICP-MS data were found to be 4.19 ± 0.43% and 4.35 ± 0.08% for samples with and without Mms6 respectively, which are slightly lower than the initial Gd content (~5%) in the precursors (Table 3.1). For elemental analysis of Gd by XPS, an oxidized gadolinium metal was used as a reference, since the XPS spectra of lanthanide ions are not well studied and different binding energies have been observed, according to the XPS spectra reported[24]. In Figure 3.2, Gd3*d* peaks of 5 at.% Gd-doped samples exhibited a similar shape and position to that of Gd

oxide reference, which also verified the presence of Gd in the samples. The XPS results show that with and without Mms6, the 5 at.% Gd-doped magnetite nanoparticles have the same binding energy of Gd3*d* (1187.6 eV), which suggests no discernable effect of Mms6 on the binding energy. The binding energy of Gd3*d* in doped magnetite is close to that in the Gd oxide reference (1187.3 eV), indicating that the Gd ions are in +3 state in the doped samples.

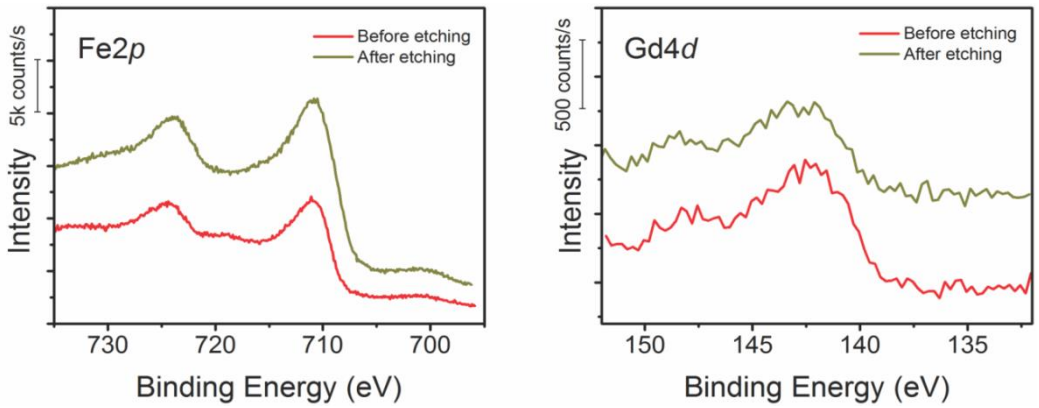

Figure 3.3 XPS spectra of Fe2*p* and Gd4*d* for Gd-doped magnetite nanoparticles prepared in the presence of Mms6 before etching (red) and after etching (olive green) with calibration via C1*s* (E_b = 284.8 eV).

One concern in cation substitution is the distribution of the substituents within the crystals. As reported, Co, Ni and Zn are randomly distributed within the magnetite structure, while Cu, Mn and Cd appear to be concentrated near the surface of the crystals[3]. In this study, ion etching removed around a 4 nm thick layer from the surface. Figure 3.3 shows the original XPS peaks of Fe2*p* and Gd4*d* for 5 at.% Gd-doped magnetite nanoparticles before and after ion etching. The intensity of signals showed little change, including the Gd4*d* peak. This indicated that Gd ions were within the bulk of the magnetite crystals and not just on the surface. Therefore, XRD, ICP-MS and XPS analyses together confirmed that Gd ions are present in the magnetite crystals at the levels that Gd are doped with initially, and it appears that Gd is distributed in the lattice homogeneously. Based on ICP-MS results (Table 3.1), the composition of 5 at.% Gd-

doped magnetite nanoparticles (with or without Mms6) are $Fe_{(3-x)}Gd_xO_4$ (where $x = 0.085 \pm 0.002$).

Gd^{3+} has the crystal ionic radius of 1.078 Å for coordination number (CN) of VI, which is much larger than that of the Fe^{3+} ion (in high-spin state, 0.63 Å for CN = IV and 0.785 Å for CN = VI) and that of the Fe^{2+} ion (in high-spin state, 0.92 Å for CN = VI)[12, 39]. Here, the substituted trivalent cation percentage is 5 at.%, which was much higher than the level of lanthanide elements incorporated in magnetite in natural rocks [40]. Thus, 5 at.% Gd doping may introduce lattice distortion and change of the lattice parameter. XRD patterns showed no measurable peak shift in 5 at.% Gd-doped magnetite nanoparticles compared with undoped ones. We note that the oxygen framework in magnetite is fairly open and flexible and it can expand or contract without much strain to accommodate ions of larger size than interstitial sites[3]. For instance, all the Fe^{2+} ions are incorporated in octahedral sites of magnetite, but the ionic radii of Fe^{2+} ions (0.92 Å) are greater than the radii of octahedral sites (0.7357-0.8285 Å) in magnetite. Moreover, assuming that 10 at.% Fe^{3+} are substituted by Gd^{3+} and all the Gd^{3+} ions are randomly incorporated in the octahedral sites, the average ionic radii of trivalent ions at octahedral sites are $0.8r_{Fe3+} + 0.2r_{Gd3+} = 0.8436$ Å, which is still smaller than the radius of Fe^{2+} ion (0.92Å) at octahedral sites. Thus, a lattice increase corresponding to 10 at.% Gd substitution for Fe^{3+} may not lead to a detectable lattice expansion and corresponding peak position shift. More importantly, low crystallinity due to nanoscale size, a common occurrence in the co-precipitation method[1] as evident from XRD and TEM results (see below), also makes it difficult to observe any change in diffraction peak positions. We argue that crystallinity is the dominant effect on measurements of lattice distortion in nanoparticles. Even though 5 at.% Gd-doped magnetite has a large crystal size (see below) leading to sharp diffraction peaks with high intensity, Gd doping may not increase the

crystallinity significantly to show the lattice distortion. Thermal annealing has been reported as a more effective way to improve the crystallinity[41]. Thus, heat treatment was applied in order to show the peak position shift if lattice distortion exists. In addition, the initial Gd percentage was increased to 10% from the original 5%, and the final doping amount was 8.8 ± 0.8%, as measured by ICP-MS. The as-synthesized 10 at.% Gd-doped magnetite nanoparticles were heat-

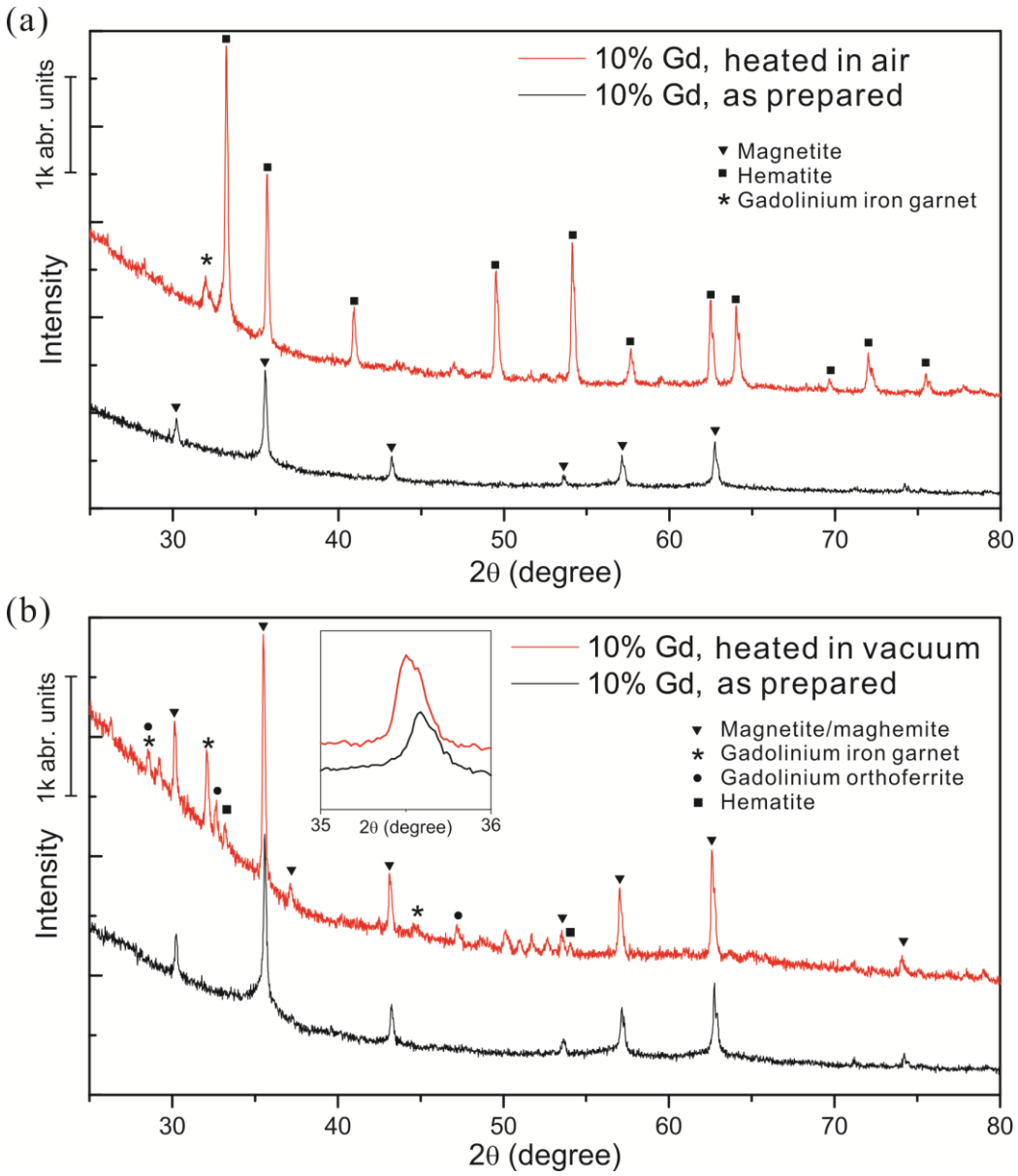

Figure 3.4 X-ray powder diffraction patterns of as-prepared 10 at.% Gd-doped magnetite samples before and after heat treatment (a) in air and (b) in vacuum (Inset: peak 311). A copper Kα radiation source with a wavelength of 0.154187 nm was employed.

ed to 900°C for 4 hours in air and in vacuum (Figure 3.4). After heating in air, the magnetite phase was oxidized to hematite, mixed with a very small amount of gadolinium iron garnet (Figure 3.4a). XRD patterns of 10 at.% Gd-doped magnetite heated in vacuum (in a sealed glass tube) showed magnetite and/or maghemite, which were difficult to discriminate under the experimental conditions used (Figure 3.4b). The position of highest-intensity peak (311) shifted about 0.1 degree to a lower Bragg angle, corresponding to an increase of 0.006 Å in d spacing and 0.02 Å in lattice parameter, which is close to the reported results of Gd-doped Ni–Zn ferrite [42] and Ca-doped magnetite [43] since Ca^{2+} has a similar ionic radius (1.14 Å for CN = VI) [39]. In addition, there were several minor Gd containing phases including gadolinium iron garnet and gadolinium orthoferrite, suggesting that the Gd-doped magnetite might be a metastable phase which decomposes to Gd-ferrite, Gd-iron garnet and magnetite at high temperatures[44].

3.4.2 Crystal growth through Gd doping

In Figure 3.1, it is clear that the 5 at.% Gd-doped magnetite nanoparticles exhibit sharper peaks than the ones without Gd, suggesting that the Gd-doped samples have larger crystal sizes. The well-known Scherrer equation (Equation 3.1) was applied to determine the crystal size of magnetite particles [45] without considering the effect of lattice strains.

$$D = K\lambda/(\beta\cos\theta) \tag{3.1}$$

The instrumental broadening was determined using the NIST standard reference materials (SRM) 640c silicon powder and corrected for peak broadening due to crystal size. Five diffraction peaks with relatively high intensity (i.e., (220), (311), (400), (511) and (440) peaks) were used to estimate the average crystal size and standard deviation (Table 3.2). As evident from Table 3.2, the crystal size of magnetite nanoparticles doubled for samples doped with 5%

Gd, which clearly showed that Gd doping has an effect on the growth of magnetite crystals using an aqueous co-precipitation method.

Table 3.2 The size of updoped and 5 at.% Gd-doped magnetite nanoparticles characterized by XRD and TEM.

Magnetite synthesized in different conditions	0% Gd	0% Gd	~5% Gd	~5% Gd
	with Mms6	without Mms6	with Mms6	without Mms6
Crystal size estimated by XRD (nm)	17 ± 2	16 ± 2	44 ± 7	42 ± 4
Particle size measured in TEM (nm)	20 ± 6	18 ± 6	46 ±13	44 ± 12

The as-synthesized magnetite nanoparticles with and without Gd doping were observed under TEM (Figure 3.5a-d). The particle size was measured and the histograms of size distribution for nanoparticles synthesized at different conditions are shown in Figure S3.1. Without Gd^{3+}, the magnetite particles exhibited cuboidal shape and the particle size was 18-20 nm (Figure 3.5a-b, S3.1, Table 3.2), which is similar to the values reported previously[32, 33]. But the effect of Mms6 on the growth of magnetite nanoparticles was suppressed. In the presence of Gd^{3+}, the particle size of magnetite particles increased to around 44-46 nm and the size distribution became broader (Figure 3.5c-d, S3.1, Table 3.2). Magnetite nanoparticles as large as 100-130 nm could be seen, along with particles of similar shape and size as those without Gd doping (Figure S3.1-S3.2). TEM micrographs and histograms confirm that crystal size increased with Gd doping, which was consistent with XRD results presented above, even though due to the low crystallinity of nanoparticles the mean particle size measured using TEM is slightly larger than the crystal size estimated by XRD and the size distribution from TEM results is broader than that calculated using XRD results. The effect of Gd doping or the effect of doping with other lanthanide ions on the crystal size of magnetite synthesized via precipitation method has

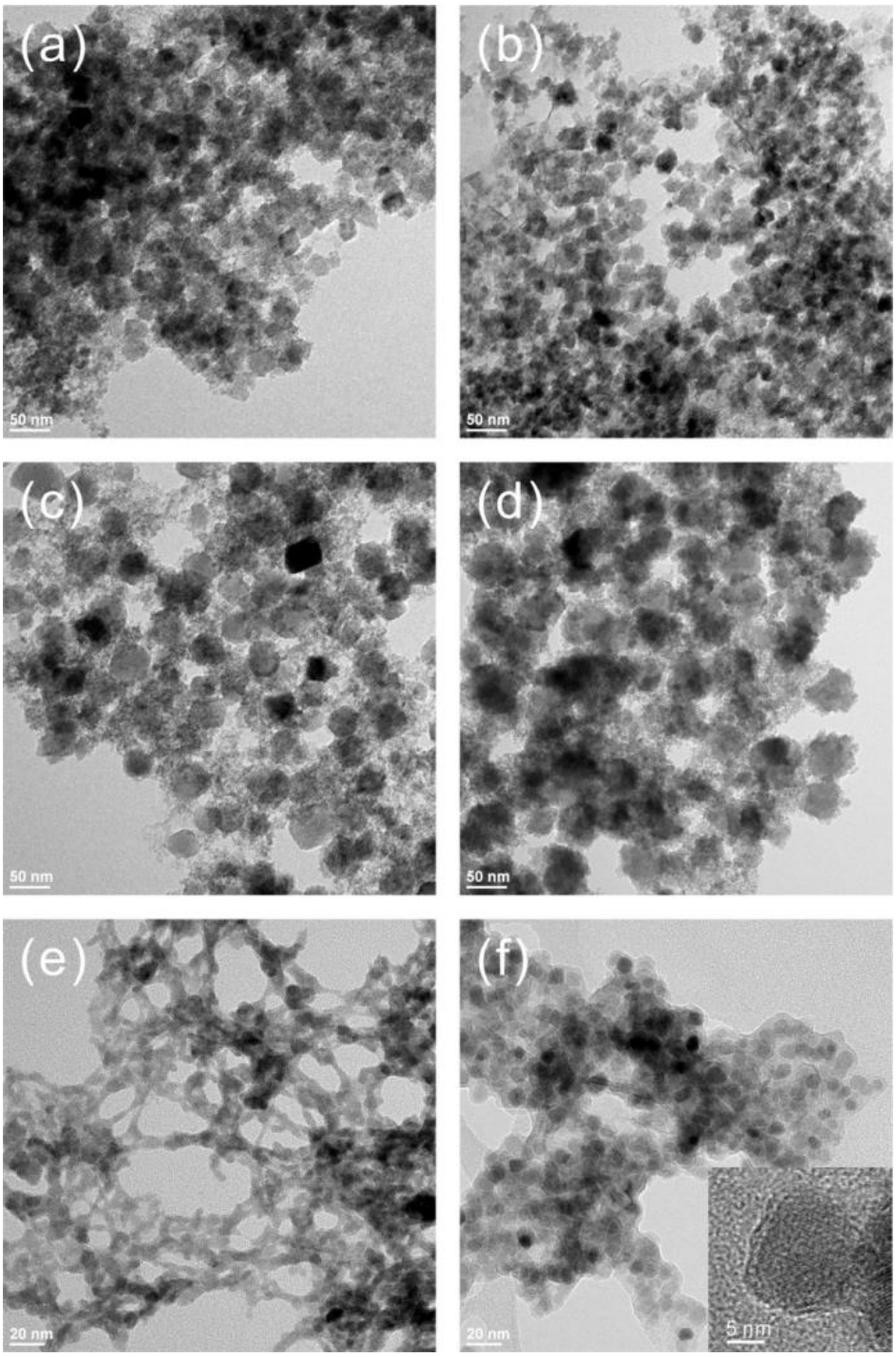

Figure 3.5 TEM images of nanoparticles synthesized via co-precipitation method: (a) updoped magnetite in the absence of Mms6, (b) updoped magnetite in the presence of Mms6, (c) 5 at.% Gd-doped magnetite in the absence of Mms6, and (d) 5 at.% Gd-doped magnetite in the presence of Mms6, (e) Gd hydroxide synthesized by precipitation of $GdCl_3$ in NaOH, and (f) magnetite nanoparticles covered with gelatinous Gd hydroxide layer (Inset: HRTEM image) prepared by adding mixture of $FeCl_2$ and $FeCl_3$ to the NaOH solution followed by precipitation of $GdCl_3$.

not been reported before, but Co doping was observed to have a similar effect [21]. The large Gd-doped magnetite nanoparticles did not show well-defined shapes under the TEM (Figure S3.2) because there were some fine particles aggregated on the surface of Gd-doped magnetite nanoparticles due to interparticle interactions (e.g., dipole-dipole, van der Waals electrical double layer)[5, 37].

Using the same method, $GdCl_3$ without iron was added to the base solution to get the pure Gd hydroxide precipitates as a control sample. Figure 3.5e shows the morphology of as-prepared Gd hydroxide. It was amorphous and had no defined morphology, which was quite different from the magnetite nanocrystals. Moreover, a physical mixture of magnetite nanoparticles and Gd hydroxide was prepared via this method by adding mixture of $FeCl_2$ and $FeCl_3$ to the base solution followed by precipitation of Gd. In Figure 3.5f, very fine magnetite nanocrystals were covered by a thin layer of the amorphous Gd hydroxide. Obviously, crystal growth brought about by Gd doping was related to the initial nucleation stage and/or growth process. Consequently, addition of Gd ions to the solution of $FeCl_2$+$FeCl_3$ prior to precipitation resulted in Gd incorporated to the lattice of the magnetite nanoparticles.

To verify the effect of Gd doping on crystal size, different levels of Gd^{3+} (0, 2, 4, 6, 8 and 10 at.%) were substituted for Fe^{3+}. ICP-MS was used to measure the amount of Gd in the magnetite nanoparticles and plotted against the average crystal size as shown in Figure 3.6. Clearly, the size of the magnetite nanocrystals increased with Gd content, while the size distribution became broader.

Classical crystal formation from solution is described by two stages[1, 12, 46]: a rapid burst of nucleation followed by a slow growth of the nuclei by diffusion of the solutes[46]. However, magnetite nanoparticles synthesized from aqueous solution form via complicated pathways invo-

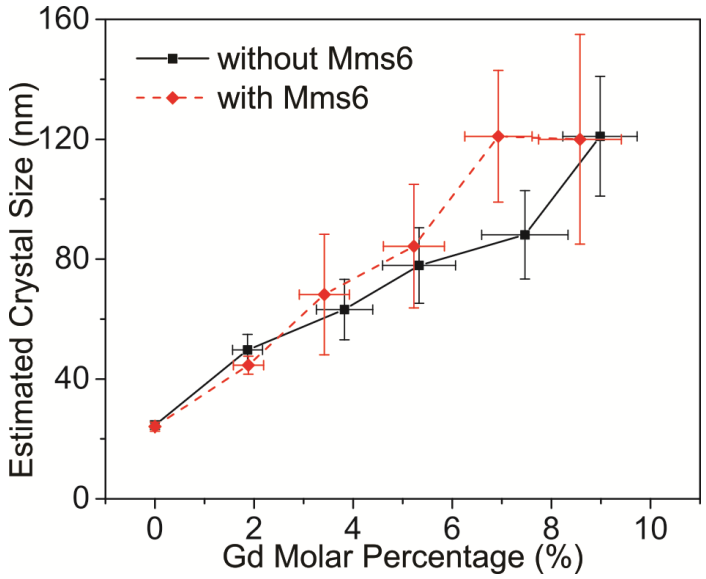

Figure 3.6 Crystal size of magnetite nanoparticles synthesized with different amounts of Gd. Gd molar percentages as fraction of trivalent ions were measured by ICP-MS, while the crystal size was calculated using Scherrer equation from XRD data.

lving phase transformation of several different iron oxyhydroxide species[47]. During nucleation and growth of magnetite nanocrystals from solution, a non-classical crystal nucleation pathway has been reported recently, which does not involve the formation of an intermediate amorphous phase[48, 49]. Nucleation of magnetite proceeds by rapid agglomeration of primary particles, 1~2 nm in size, consisting of a disordered iron (hydr)oxide phase that may arise from interaction of Fe^{2+} with a $Fe(OH)_3$ hydrogel that is formed locally in the first stage[48, 50]. The nuclei grow by the accretion and fusion of primary particles attaching to their surfaces, which follows classical theory[48, 51]. In our synthesis procedure, the precursor of mixed Fe^{3+}, Gd^{3+} and Fe^{2+} ions was prepared at a low pH (~1.9), and then the pH was rapidly increased to ~12 with NaOH. At pH ~1.9, polynuclear ferric oxide hydrogel, which for simplicity is designated as $Fe(OH)_3$, forms due to the low solubility product of $Fe(OH)_3$ ($K_{sp} = 10^{-38.8}$) and the relatively high initial concentration of Fe(III)[3, 52]. We should point out that ion product for ferric and hydroxide ions

exceeds the solubility product, K_{sp}, which is a necessary but not a sufficient condition for the formation of a solid phase, as the solubility product is determined from solubility of bulk crystalline solid, from dissolution of $Fe(OH)_3$ and in low ionic strength solution. Precipitation of solid phase on the other hand, involves supersaturation, and activity coefficients are lower than unity. Nevertheless, various polynuclear species including $Fe(OH)_3$ (aq) are expected to form. Based on the solubility product value, ~98% of Fe(III) was consumed to convert to polynuclear species forming a hydrogel, while all of Gd(III) and Fe(II) ions existed in solution as hydrated complexes as the solubility products of $Gd(OH)_3$ and $Fe(OH)_2$ are $10^{-25.7}$ and $10^{-15.1}$ respectively[52]. When precursors were added dropwise to the NaOH solution pH ≈ 12, $Gd(OH)_3$ hydrogel (Figure 3.5e) and $Fe(OH)_2$ solid formed immediately[52]. At this high pH, interaction of $Fe(OH)_3$ hydrogel with free Fe^{2+} ions resulted in the formation of primary particles, which led to the resorption of $Fe(OH)_2$ and $Gd(OH)_3$ hydrogels. If, on the other hand, the $Gd(OH)_3$ hydrogel was not resorbed, primary magnetite particles would be surrounded by $Gd(OH)_3$ hydrogel (as was observed in the sequential precipitation process) covering the magnetite nanoparticles (Figure 3.5f). Although the details of interactions between $Fe(OH)_3$ and Gd^{3+} were not clearly resolved in the present work, it is clear that the presence of Gd^{3+} ions leads to enhancement of crystal growth presumably by aggregation and fusion of primary particles.

Experimental data on the role (or lack thereof) of Mms6 on the crystal size of the Gd-doped crystals is limited to make any conclusive assessments. However, it is safe to assume that within the limits of the experimental conditions employed in this study, Mms6 has no discernable effect on the crystal size. It is possible that the high pH employed in the precipitation might have caused deterioration of Mms6 or altering its normal configuration rendering it ineffective. In addition, different synthesis conditions employed in the previous work, in which a

polymeric gel was used to slow down the diffusion rates of reagents, may have led to differences in crystal growth in the presence of Mms6.[37]

3.4.3 Magnetic properties

Magnetic hysteresis for updoped and 5 at.% Gd-doped magnetite was measured at 5 K and 260 K as shown in Figure 3.7 (with Mms6) and Figure S3.3 (without Mms6). No significant differences were observed between the 5 at.% Gd-doped magnetite synthesized with and without Mms6. The saturation magnetization of magnetite nanoparticles decreased with Gd doping by

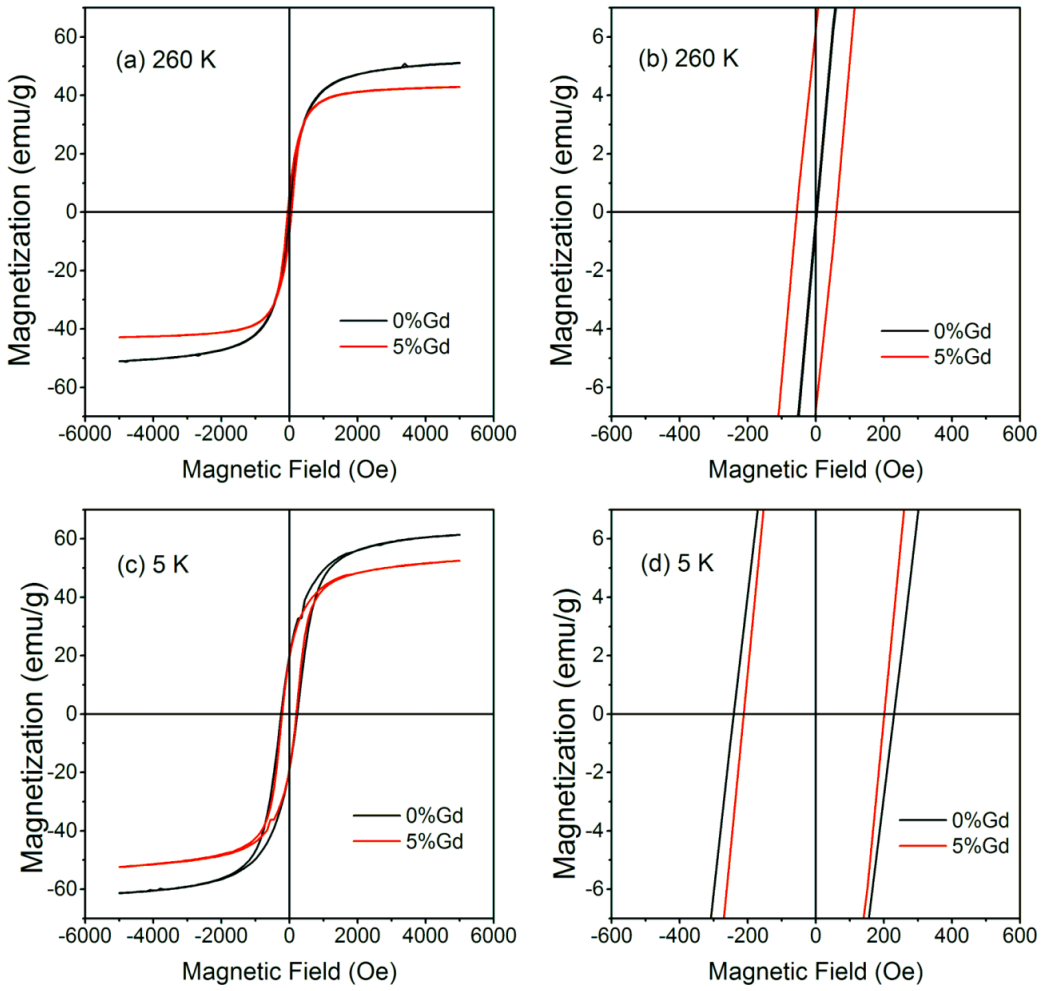

Figure 3.7 Magnetization (M) vs. magnetic field (H) curves for magnetite nanoparticles synthesized in the presence of Mms6, without Gd doping (black) and with 5 at.% Gd doping (red): (a) at 260K, and (b) corresponding low field curves at 260K; (c) at 5K, and (d) corresponding low field curves at 5K.

~15 % at 5 K and by ~16 % at 260 K at H = 5000 Oe for the samples with Mms6. At 260 K, the undoped sample does not exhibit any hysteresis as shown in low magnetic fields curves, whereas an irreversible *M(H)* curve is observed for the doped samples (Figure 3.7b, S3.3b), which was close to properties of magnetite doped with other lanthanide ions reported previously[24]. However, only a slight difference in the coercivity and remnant magnetization at 5 K were observed with Gd doping. Compared with the 5 at.% Gd-doped magnetite sample, magnetite mixed with 5% $Gd(OH)_3$ (Figure 3.5f) exhibited higher saturation magnetization and zero coercivity (Figure S3.4), similar to that observed with undoped magnetite. The small but distinct differences between doped and physically mixed samples indicate the change of magnetic behaviors from superparamagnetism to ferrimagnetism, which resulted from the effect of Gd doping and simultaneous increase in size.

As mentioned before, the particle size of magnetite affects its magnetic properties. In theory, the coercivity, H_c, of undoped magnetite nanoparticles is zero when the size is below the superparamagnetic threshold size ($d < d_s$), and increases slowly from zero as a function of particle size d ($H_c \propto (1 - (d_s/d)^{1.5})$) in the single-domain region ($d_s < d < d_0$)[53]. Meanwhile, Gd doping may also increase H_c as it can introduce magnetic anisotropy[24]. Size-dependence of saturation magnetization, M_s, has also been reported[15, 54] and M_s increases gradually through superparamagnetic region and single-domain region, but Gd substitution decreases M_s in the spinel structure[42, 55-57]. Here, we observed the increased H_c (from 0 to ~65 Oe) and decreased magnetization at H = 5000 Oe, where the measured magnetization was almost totally saturated. Clearly, Gd doping and simultaneous increase in size contributed together to result in the increase of H_c, while the effect of Gd doping on M_s is the dominant one compared to the size effect. The decrease of M_s might be attributed to the site preference of Gd ions, probably

octahedral sites in magnetite[19, 58]; variations in the compositions concomitant with Fe-Gd interactions which are different from Fe-Fe interactions; as well as change of the surface effect resulting from the unpaired surface spins on the magnetic nanoparticles[42, 57], and require further study.

3.5 Conclusions

Using an aqueous co-precipitation method under mild conditions, Gd doping has been demonstrated to influence the crystal growth and magnetic properties of magnetite nanoparticles. 5 at.% Gd-doped magnetite nanoparticles of pure phase have been successfully synthesized and experimental evidence from XRD, ICP-MS and XPS points to the random incorporation of Gd ions in the magnetite lattice. The chemical composition of 5 at.% Gd-doped magnetite was $Fe_{(3-x)}Gd_xO_4$ ($x = 0.085 \pm 0.002$) determined by ICP-MS. Gd doping plays an important role in the crystal growth process, and was shown to make magnetite nanoparticles grow larger. Typically the crystal size of 5 at.% Gd-doped magnetite nanoparticles increased about two-fold, which was confirmed by XRD and TEM. However, the effect of the bacterial biomineralization protein Mms6 on the growth of magnetite particles was not prominent in this synthesis method. Gd doping with simultaneous crystal growth leads to clear differences in magnetic properties. The 5 at.% Gd-doped magnetite nanoparticles showed ferrimagnetic properties with small coercivity at 260 K in contrast to the undoped, superparamagnetic magnetite nanoparticles.

3.6 Acknowledgements

Thanks to Prof. Marit Nilsen-Hamilton's group from Iowa State University for providing the Mms6 protein and for useful discussions. We also thank Ms. Jonna Berry (Prof. Robert S Houk's group) from Ames Laboratory for conducting ICP-MS measurements. Research was supported by the U.S. Department of Energy, Office of Basic Energy Sciences. The Ames

Laboratory is operated for the U.S. Department of Energy by Iowa State University under Contract No. DE-AC02-07CH11358.

3.7 Supplementary information (SI)

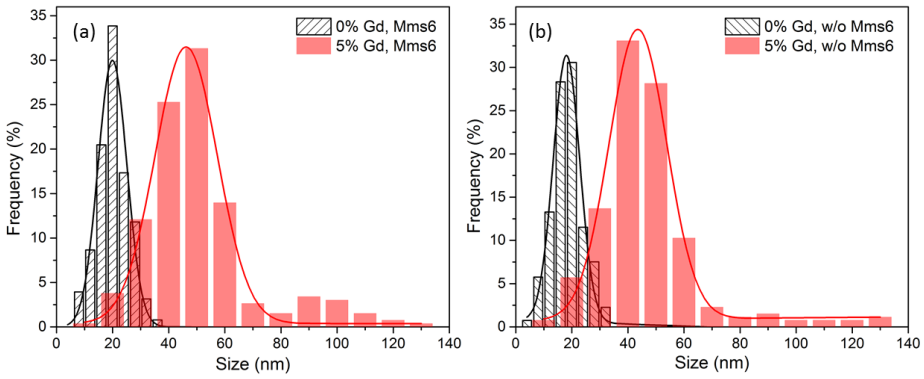

Figure S3.1 Histograms of particle size measured in TEM for undoped and 5% Gd-doped magnetite nanoparticles synthesized in the presence of Mms6 (a) and in the absence of Mms6 (b). Each histogram is outlined with a Gaussian distribution function.

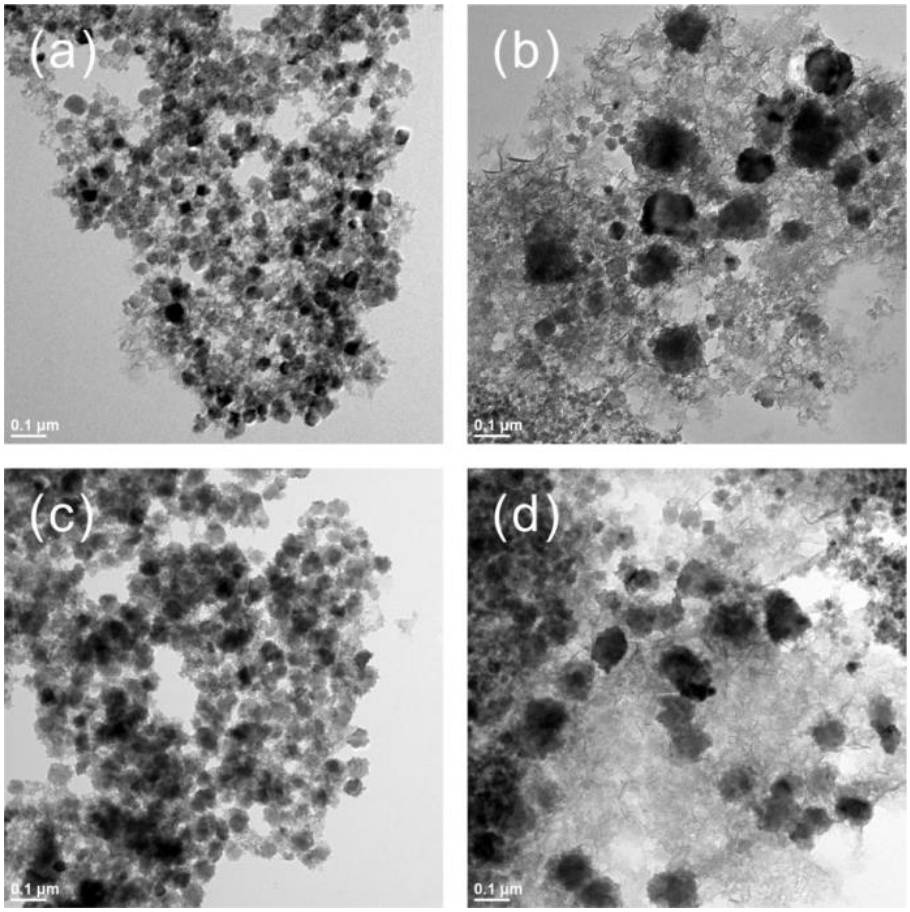

Figure S3.2 Typical TEM images for 5 at.% Gd-doped magnetite nanoparticles synthesized via co-precipitation method in the absence of Mms6 (a, b) and in the presence of Mms6 (c, d).

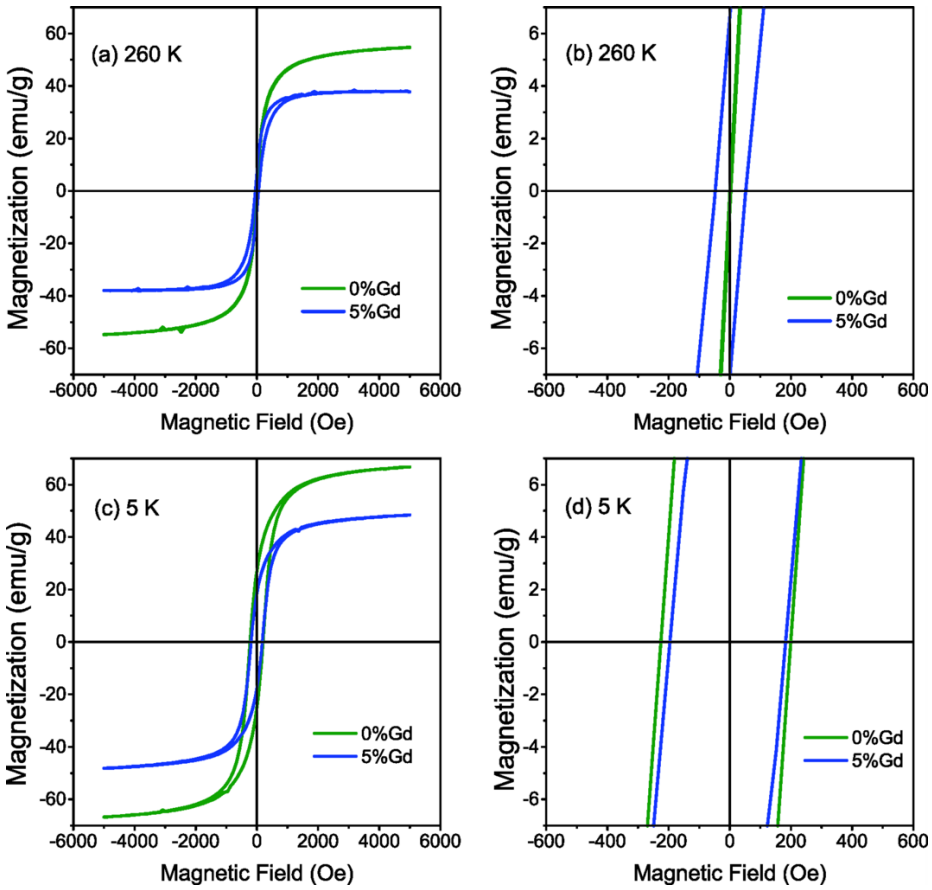

Figure S3.3 Magnetization (M) vs. magnetic field (H) curves for magnetite nanoparticles synthesized in the absence of Mms6, without Gd doping (green) and with 5% Gd doping (blue): (a) at 260 K, and (b) corresponding low field curves at 260 K; (c) at 5 K, and (d) corresponding low field curves at 5 K.

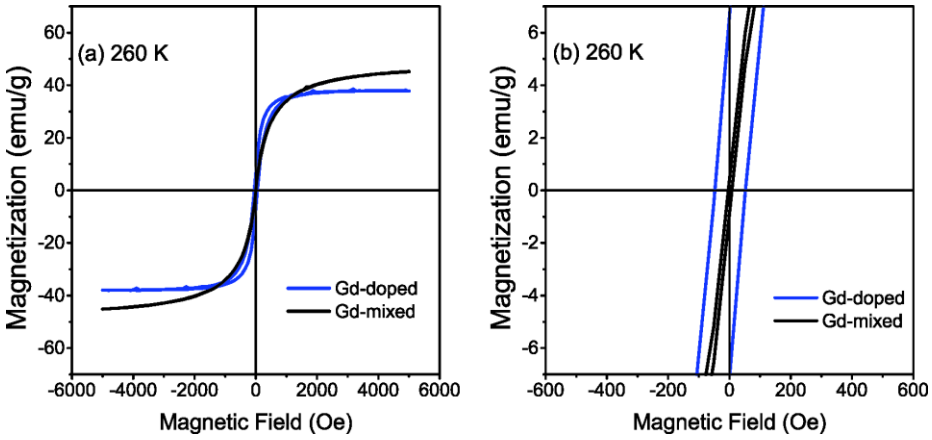

Figure S3.4 Magnetization (M) vs. magnetic field (H) curves at 260 K for magnetite nanoparticles synthesized in the absence of Mms6, (a) doped with 5% Gd (blue) and mixed with 5% $Gd(OH)_3$ (**black**) and (b) corresponding low field curves.

References

1. Laurent, S.; Forge, D.; Port, M.; Roch, A.; Robic, C.; Vander Elst, L.; Muller, R. N. Magnetic Iron Oxide Nanoparticles: Synthesis, Stabilization, Vectorization, Physicochemical Characterizations, and Biological Applications. *Chem. Rev.* 2008, 108, 2064-2110.
2. Lu, A.-H.; Salabas, E. L.; Schüth, F. Magnetic Nanoparticles: Synthesis, Protection, Functionalization, and Application. *Angew. Chem. Int. Ed.* 2007, 46, 1222-1244.
3. Cornell, R. M.; Schwertmann, U. *The iron oxides: structure, properties, reactions, occurrences and uses*. John Wiley & Sons: 2003.
4. Gupta, A. K.; Gupta, M. Synthesis and surface engineering of iron oxide nanoparticles for biomedical applications. *Biomaterials* 2005, 26, 3995-4021.
5. Prozorov, T.; Bazylinski, D. A.; Mallapragada, S. K.; Prozorov, R. Novel magnetic nanomaterials inspired by magnetotactic bacteria: Topical review. *Mater. Sci. Eng. R* 2013, 74, 133-172.
6. Pankhurst, Q. A.; Connolly, J.; Jones, S. K.; Dobson, J. Applications of magnetic nanoparticles in biomedicine. *J. Phys. D: Appl. Phys.* 2003, 36, R167.
7. Dunlop, D. J. Superparamagnetic and single-domain threshold sizes in magnetite. *J. Geophys. Res.* 1973, 78, 1780-1793.
8. Butler, R. F.; Banerjee, S. K. Theoretical single-domain grain size range in magnetite and titanomagnetite. *J. Geophys. Res.* 1975, 80, 4049-4058.
9. Krishnan, K. M.; Pakhomov, A. B.; Bao, Y.; Blomqvist, P.; Chun, Y.; Gonzales, M.; Griffin, K.; Ji, X.; Roberts, B. K. Nanomagnetism and spin electronics: materials, microstructure and novel properties. *J. Mater. Sci.* 2006, 41, 793-815.
10. Xu, C.; Sun, S. Superparamagnetic nanoparticles as targeted probes for diagnostic and therapeutic applications. *Dalton Trans.* 2009, 5583-5591.
11. Majewski, P.; Thierry, B. Functionalized magnetite nanoparticles—synthesis, properties, and bio-applications. *Crit. Rev. Solid State Mater. Sci.* 2007, 32, 203-215.
12. Schwertmann, U.; Cornell, R. M. *Iron Oxides in the Laboratory: Preparation and Characterization*. Wiley: 2000.
13. Sun, S.; Zeng, H. Size-Controlled Synthesis of Magnetite Nanoparticles. *J. Am. Chem. Soc.* 2002, 124, 8204-8205.
14. Jana, N. R.; Chen, Y.; Peng, X. Size- and Shape-Controlled Magnetic (Cr, Mn, Fe, Co, Ni) Oxide Nanocrystals via a Simple and General Approach. *Chem. Mater.* 2004, 16, 3931-3935.
15. Santoyo Salazar, J.; Perez, L.; de Abril, O.; Truong Phuoc, L.; Ihiawakrim, D.; Vazquez, M.; Greneche, J.-M.; Begin-Colin, S.; Pourroy, G. Magnetic Iron Oxide Nanoparticles in 10−40 nm Range: Composition in Terms of Magnetite/Maghemite Ratio and Effect on the Magnetic Properties. *Chem. Mater.* 2011, 23, 1379-1386.
16. Kim, D.; Lee, N.; Park, M.; Kim, B. H.; An, K.; Hyeon, T. Synthesis of Uniform Ferrimagnetic Magnetite Nanocubes. *J. Am. Chem. Soc.* 2009, 131, 454-455.
17. Nyir; Kósa, I.; Csákberé Nyinagy, D.; Pósfai, M. Size and shape control of precipitated magnetite nanoparticles. *Eur. J. Mineral.* 2009, 21, 293-302.
18. Baumgartner, J.; Bertinetti, L.; Widdrat, M.; Hirt, A. M.; Faivre, D. Formation of Magnetite Nanoparticles at Low Temperature: From Superparamagnetic to Stable Single Domain Particles. *PLoS ONE* 2013, 8, e57070.

19. O'Handley, R. C. *Modern Magnetic Materials: Principles and Applications*. Wiley: 1999.
20. Staniland, S.; Williams, W.; Telling, N.; Van Der, L.; Harrison, A.; Ward, B. Controlled cobalt doping of magnetosomes in vivo. *Nat. Nanotechnol.* 2008, 3, 158-162.
21. Galloway, J. M.; Arakaki, A.; Masuda, F.; Tanaka, T.; Matsunaga, T.; Staniland, S. S. Magnetic bacterial protein Mms6 controls morphology, crystallinity and magnetism of cobalt-doped magnetite nanoparticles in vitro. *J. Mater. Chem.* 2011, 21, 15244-15254.
22. Wang, F.; Han, Y.; Lim, C. S.; Lu, Y.; Wang, J.; Xu, J.; Chen, H.; Zhang, C.; Hong, M.; Liu, X. Simultaneous phase and size control of upconversion nanocrystals through lanthanide doping. *Nature* 2010, 463, 1061-1065.
23. Chen, D.; Wang, Y. Impurity doping: a novel strategy for controllable synthesis of functional lanthanide nanomaterials. *Nanoscale* 2013, 5, 4621-4637.
24. De Silva, C. R.; Smith, S.; Shim, I.; Pyun, J.; Gutu, T.; Jiao, J.; Zheng, Z. Lanthanide(III)-Doped Magnetite Nanoparticles. *J. Am. Chem. Soc.* 2009, 131, 6336-6337.
25. Liang, X.; Wang, X.; Zhuang, J.; Chen, Y.; Wang, D.; Li, Y. Synthesis of Nearly Monodisperse Iron Oxide and Oxyhydroxide Nanocrystals. *Adv. Funct. Mater.* 2006, 16, 1805-1813.
26. Wang, G.; Peng, Q.; Li, Y. Lanthanide-Doped Nanocrystals: Synthesis, Optical-Magnetic Properties, and Applications. *Acc. Chem. Res.* 2011, 44, 322-332.
27. Drake, P.; Cho, H.-J.; Shih, P.-S.; Kao, C.-H.; Lee, K.-F.; Kuo, C.-H.; Lin, X.-Z.; Lin, Y.-J. Gd-doped iron-oxide nanoparticles for tumour therapy via magnetic field hyperthermia. *J. Mater. Chem.* 2007, 17, 4914-4918.
28. Liu, G.; Chen, X. Chapter 233 Spectroscopic properties of lanthanides in nanomaterials. In *Handbook on the Physics and Chemistry of Rare Earths*, Karl A. Gschneidner, J.-C. B.; Vitalij, K. P., Eds. Elsevier: 2007; Vol. Volume 37, pp 99-169.
29. Sakai, N.; Zhu, L.; Kurokawa, A.; Takeuchi, H.; Yano, S.; Yanoh, T.; Wada, N.; Taira, S.; Hosokai, Y.; Usui, A. In *Synthesis of Gd2O3 nanoparticles for MRI contrast agents*, J Phys Conf Ser., IOP Publishing: 2012; p 012008.
30. Zhou, Z.; Huang, D.; Bao, J.; Chen, Q.; Liu, G.; Chen, Z.; Chen, X.; Gao, J. A Synergistically Enhanced T1–T2 Dual-Modal Contrast Agent. *Adv. Mater.* 2012, 24, 6223-6228.
31. Bae, K. H.; Kim, Y. B.; Lee, Y.; Hwang, J.; Park, H.; Park, T. G. Bioinspired Synthesis and Characterization of Gadolinium-Labeled Magnetite Nanoparticles for Dual Contrast T1- and T2-Weighted Magnetic Resonance Imaging. *Bioconjugate Chem.* 2010, 21, 505-512.
32. Arakaki, A.; Webb, J.; Matsunaga, T. A novel protein tightly bound to bacterial magnetic particles in Magnetospirillum magneticum strain AMB-1. *J. Biol. Chem.* 2003, 278, 8745-8750.
33. Wang, L.; Prozorov, T.; Palo, P. E.; Liu, X.; Vaknin, D.; Prozorov, R.; Mallapragada, S.; Nilsen-Hamilton, M. Self-Assembly and Biphasic Iron-Binding Characteristics of Mms6, A Bacterial Protein That Promotes the Formation of Superparamagnetic Magnetite Nanoparticles of Uniform Size and Shape. *Biomacromolecules* 2012, 13, 98-105.
34. Wang, W.; Bu, W.; Wang, L.; Palo, P. E.; Mallapragada, S.; Nilsen-Hamilton, M.; Vaknin, D. Interfacial Properties and Iron Binding to Bacterial Proteins That Promote the Growth of Magnetite Nanocrystals: X-ray Reflectivity and Surface Spectroscopy Studies. *Langmuir* 2012, 28, 4274-4282.

35. Feng, S.; Wang, L.; Palo, P.; Liu, X.; Mallapragada, S.; Nilsen-Hamilton, M. Integrated self-assembly of the mms6 magnetosome protein to form an iron-responsive structure. *Int. J. Mol. Sci.* 2013, 14, 14594-14606.
36. Zhang, H.; Liu, X.; Feng, S.; Wang, W.; Schmidt-Rohr, K.; Akinc, M.; Nilsen-Hamilton, M.; Vaknin, D.; Mallapragada, S. Morphological Transformations in the Magnetite Biomineralizing Protein Mms6 in Iron Solutions: A Small-Angle X-ray Scattering Study. *Langmuir* 2015, 31, 2818-2825.
37. Prozorov, T.; Mallapragada, S. K.; Narasimhan, B.; Wang, L.; Palo, P.; Nilsen-Hamilton, M.; Williams, T. J.; Bazylinski, D. A.; Prozorov, R.; Canfield, P. C. Protein-Mediated Synthesis of Uniform Superparamagnetic Magnetite Nanocrystals. *Adv. Funct. Mater.* 2007, 17, 951-957.
38. Kim, W.; Suh, C.-Y.; Cho, S.-W.; Roh, K.-M.; Kwon, H.; Song, K.; Shon, I.-J. A new method for the identification and quantification of magnetite–maghemite mixture using conventional X-ray diffraction technique. *Talanta* 2012, 94, 348-352.
39. Shannon, R. Revised effective ionic radii and systematic studies of interatomic distances in halides and chalcogenides. *Acta Crystallogr. Sect. A* 1976, 32, 751-767.
40. Schock, H. H. Distribution of rare-earth and other trace elements in magnetites. *Chem. Geol.* 1979, 26, 119-133.
41. Chen, K. J.; Fang, T. H.; Hung, F. Y.; Ji, L. W.; Chang, S. J.; Young, S. J.; Hsiao, Y. J. The crystallization and physical properties of Al-doped ZnO nanoparticles. *Appl. Surf. Sci.* 2008, 254, 5791-5795.
42. Mahesh Kumar, A.; Chaitanya Varma, M.; Choudary, G. S. V. R. K.; Prameela, P.; Rao, K. H. Influence of gadolinium on magnetization and DC resistivity of Ni–Zn nanoferrites. *J. Magn. Magn. Mater* 2012, 324, 68-71.
43. de Sitter, J.; Govaert, A.; de Grave, E.; Chambaere, D.; Robbrecht, G. A mössbauer study of Ca2+-containing magnetites. *Phys. Status Solidi A* 1977, 43, 619-624.
44. Buscaglia, V.; Buscaglia, M. T.; Giordano, L.; Martinelli, A.; Viviani, M.; Bottino, C. Growth of ternary oxides in the Gd2O3–Fe2O3 system. A diffusion couple study. *Solid State Ion.* 2002, 146, 257-271.
45. Langford, J. I.; Wilson, A. J. C. Scherrer after sixty years: A survey and some new results in the determination of crystallite size. *J. Appl. Crystallogr.* 1978, 11, 102-113.
46. Mullin, J. W. *Crystallization*. Elsevier Science: 2001.
47. Ahn, T.; Kim, J. H.; Yang, H.-M.; Lee, J. W.; Kim, J.-D. Formation Pathways of Magnetite Nanoparticles by Coprecipitation Method. *J. Phys. Chem. C* 2012, 116, 6069-6076.
48. Baumgartner, J.; Dey, A.; Bomans, P. H. H.; Le Coadou, C.; Fratzl, P.; Sommerdijk, N. A. J. M.; Faivre, D. Nucleation and growth of magnetite from solution. *Nat. Mater.* 2013, 12, 310-314.
49. De Yoreo, J. Crystal nucleation: More than one pathway. *Nat. Mater.* 2013, 12, 284-285.
50. Jolivet, J. P.; Belleville, P.; Tronc, E.; Livage, J. Influence of Fe(II) on the formation of the spinel iron oxide in alkaline medium. *Clays Clay Miner.* 1992, 40, 531-539.
51. Fratzl, P.; Lebowitz, J. L.; Penrose, O.; Amar, J. Scaling functions, self-similarity, and the morphology of phase-separating systems. *Phys. Rev. B* 1991, 44, 4794-4811.
52. Martell, A. E.; Smith, R. M. *Critical stability constants. 4. Inorganic complexes*. Plenum Press: 1976.

53. Dunlop, D. J.; Özdemir, Ö. *Rock Magnetism: Fundamentals and Frontiers*. Cambridge University Press: 1997.
54. Li, Z.; Sun, Q.; Gao, M. Preparation of Water-Soluble Magnetite Nanocrystals from Hydrated Ferric Salts in 2-Pyrrolidone: Mechanism Leading to Fe3O4. *Angew. Chem. Int. Ed.* 2005, 44, 123-126.
55. Peng, J.; Hojamberdiev, M.; Xu, Y.; Cao, B.; Wang, J.; Wu, H. Hydrothermal synthesis and magnetic properties of gadolinium-doped CoFe2O4 nanoparticles. *J. Magn. Magn. Mater* 2011, 323, 133-137.
56. Panda, R. N.; Shih, J. C.; Chin, T. S. Magnetic properties of nano-crystalline Gd- or Pr-substituted CoFe2O4 synthesized by the citrate precursor technique. *J. Magn. Magn. Mater* 2003, 257, 79-86.
57. Issa, B.; Obaidat, I.; Albiss, B.; Haik, Y. Magnetic Nanoparticles: Surface Effects and Properties Related to Biomedicine Applications. *Int. J. Mol. Sci.* 2013, 14, 21266-21305.
58. Navrotsky, A.; Kleppa, O. J. The thermodynamics of cation distributions in simple spinels. *J. Inorg. Nucl. Chem.* 1967, 29, 2701-2714.

CHAPTER 4. EFFECT OF SURFACE HYDROPHOBICITY ON THE FUNCTION OF THE IMMOBILIZED BIOMINERALIZATION PROTEIN MMS6

Modified from a paper published in *Industrial & Engineering Chemistry Research*[§]

Xunpei Liu,[+] Honghu Zhang,[+] Srikanth Nayak, German Parada, James Anderegg, Shuren Feng, Marit Nilsen-Hamilton, Mufit Akinc, and Surya Mallapragada[*]

4.1 Abstract

Magnetotactic bacteria produce magnetic nanocrystals with uniform shapes and sizes in nature, which has inspired *in vitro* synthesis of uniformly sized magnetite nanocrystals under mild conditions. Mms6, a biomineralization protein from magnetotactic bacteria with a hydrophobic N-terminal domain and a hydrophilic C-terminal domain, can promote formation of magnetite nanocrystals *in vitro* with well-defined shape and size in gels under mild conditions. Here we investigate the role of surface hydrophobicity on the ability of Mms6 to template magnetite nanoparticle formation on surfaces. Our results confirmed that Mms6 can form a protein network structure on monolayer of hydrophobic octadecanethiol (ODT)-coated gold surfaces, and facilitate magnetite nanocrystal formation with uniform sizes close to those seen in nature, in contrast to its behavior on more hydrophilic surfaces. We propose that this hydrophobicity effect might be due to the amphiphilic nature of the Mms6 protein, and its tendency to incorporate the hydrophobic N-terminal domain into the hydrophobic lipid bilayer

---

[+] X. Liu and H. Zhang are joint first authors.

[*] Corresponding Author: suryakm@iastate.edu.

environment of the magnetosome membrane, exposing the hydrophilic C-terminal domain that promotes biomineralization. Supporting this hypothesis, the larger and well-formed magnetite nanoparticles were found to be preferentially located on ODT surfaces covered with Mms6 as compared to control samples, as characterized by SEM, XRD, XPS and AFM studies. A C-terminal mutant of this protein did not form the same network structure as wild-type Mms6, suggesting that the network structure is important for the magnetite nanocrystal formation. This study provides valuable insights into the role of surface hydrophilicity on the action of the biomineralization protein Mms6 to synthesize magnetic nanocrystals, and provides a facile route to controlling bioinspired nanocrystal synthesis *in vitro*.

4.2 Introduction

Magnetic nanoparticles exhibit many interesting properties that can be exploited in a variety of applications such as catalysis, biomedicine, quantum computing, and data storage.[1-4] Magnetic nanoparticles can be synthesized using sol-gel methods, high-pressure hydrothermal methods, liquid phase co-precipitation, gas phase thermal decomposition etc.[1-6] However, these methods usually require high temperature treatments[6, 7] or cannot generate nanoparticles with uniform size and shape, which can potentially limit their applications.[8] In nature, magnetotactic bacteria produce magnetic nanocrystals under mild conditions and have high chemical purity, narrow size ranges, and species-specific crystal morphologies.[9-11] These nanocrystals, usually magnetite (Fe_3O_4) or greigite (Fe_3S_4), are surrounded by a lipid bilayer membrane about 3-4 nm thick to form the unique intracellular structures called magnetosomes.[9, 10] Using these aligned nanocrystals, the magnetotactic bacteria can orient themselves and navigate along geomagnetic field lines.[12, 13] Although magnetotactic bacteria were discovered almost four decades ago, little is known about the mechanisms by which bacteria synthesize these magnetic crystals.[9, 11, 14]

Recently, with the discovery and isolation of new bacterial strains and the development of new techniques, there has been progress in understanding magnetosome formation.[9, 15, 16] Inspired by nature, the chemical synthesis of hybrid materials with unusual morphologies at several length scales has received considerable interest from the research community.[17, 18] Bioinspired *in vitro* synthetic routes offer room-temperature pathways for the production of a variety of hybrid magnetic nanostructures with exceptional control over nanoparticle nucleation and growth, and are expected to ultimately enable the fabrication of structurally perfect and functional hierarchical systems with sizes, shapes, and properties not easily realizable via conventional synthetic techniques under mild conditions.[19] Synthesis of magnetic nanomaterials using magnetotacic bacteria *in vivo* or related proteins *in vitro* has progressed quickly.[19, 20] However, the role of surface hydrophobicity on the action of biomineralization proteins has not been well-studied, and could have significant implications in bioinspired nanocrystal synthesis.

Mms6 is a biomineralization protein found associated with the magnetite nanocrystals inside the magnetosomes of *Magnetospirillum magneticum* AMB-1, which promotes the formation of superparamagnetic magnetite nanocrystals under room temperature and mild conditions *in vitro*.[21-25] Mms6 is an amphiphilic protein with a hydrophobic N-terminal domain and a hydrophilic C-terminal domain. The protein self-assembles into micelles in solution and the C-terminus can bind iron with very high affinity.[25] The interaction between Mms6 and iron is believed to be the initial step of biomineralization,[25-27] and several mutants were synthesized to investigate the biomineralization mechanism. For instance, in a mutant m2Mms6, the hydrophilic C-terminal domain of the protein was altered such that the amino acid residues containing hydroxyl or carboxyl groups are shuffled with respect to one another, still maintaining the same hydropathy plot as Mms6.[25, 28] Compared with Mms6, m2Mms6 does not bind iron.[22, 25]

Recently, magnetite nanoparticles were synthesized with Mms6 on planar substrates by bottom-up approaches, in which Mms6 immobilized on surfaces provided interaction sites with irons and initiated magnetite formation.[29-31] The non-specific binding of Mms6 to the octadecyltrimethoxy-silane monolayer on a silicon substrate results in formation of multiple layers of iron oxide nanoparticles.[29] Mms6 has also been chemically immobilized onto surfaces by soft-lithography to promote magnetite nanoparticles' growth on surfaces, which could be potentially used for high density data storage.[30] This chemical immobilization was achieved by using N-hydroxysuccinimide (NHS)/ethyl(dimethylaminopropyl) (EDC) chemistry to attach the amine groups in the protein to the carboxyl group on the surface. However, there are 13 amine groups in an Mms6 molecule, and non-specific linkage reactions could alter the structure or function of Mms6.[30, 31]

As Mms6 is an amphiphilic membrane protein, and is believed to be embedded in the phosphate lipid bilayer membrane in bacteria, in this study, we physically incorporated Mms6 onto surfaces with different hydrophobicities without covalent linkages. This allowed us to investigate the role of surface hydrophilicity on Mms6 structure and function. Three different kinds of surfaces were used: hydrophobic 1-octadecanethiol (ODT), gold, and a relatively hydrophilic poly(ethylene glycol) surface. Mms6 was coated on these surfaces to study its ability to promote magnetite nanocrystal growth.

4.3 Materials and Methods

4.3.1 Materials

Mms6 and its mutant m2Mms6 were prepared and purified as reported before.[25, 28, 32] m2Mms6 includes the same sequence as Mms6 in the N-terminal (hydrophobic) domain and an altered sequence in the C-terminal (hydrophilic) domain. The hydroxyl/carboxyl containing

amino acid residues in the C-terminal domain are shuffled with respect to wild-type Mms6. Compared with Mms6, m2Mms6 does not bind iron.[22, 25] The m2Mms6 and Mms6 used in this study were expressed with an N-terminal poly-histidine tag (His-tag). For simplicity, the His-tagged Mms6 or m2Mms6 are referred to here as Mms6 or m2Mms6. Mms6 consists of 133 amino acid residues, is ~ 10 kDa with a calculated molecular volume of ~1.3×10^4 $Å^3$. The Mms6 solution used in this study was 0.2 mg/mL in 20 mM Tris buffer with 100 mM KCl (pH 7.5).

1-Octadecanethiol (ODT) and lysozyme were purchased from Sigma Aldrich. Poly(ethylene glycol) methyl ether thiol (henceforth referred to as PEG) (average M_n =2000) was purchased from NOF America corporation. Iron (III) chloride hexahydrate ($FeCl_3 \cdot 6H_2O$, ≥ 98%), iron (II) chloride tetrahydrate ($FeCl_2 \cdot 4H_2O$, 99.99%) and Pluronic® F-127 were purchased from Sigma-Aldrich, and potassium chloride (KCl, ≥ 99%) and tris base (≥ 99.8%) were purchased from Fisher Scientific. All chemicals were used without further purification. ODT or PEG were dissolved in ethanol to make a 2 mM solution. Both solutions were freshly made and sonicated for 5 min to dissolve the solute. $FeCl_3$ and $FeCl_2$ stock solutions were degassed and purged with inert gas (nitrogen or argon) prior to use.

4.3.2 Surface preparation

All the surface samples were prepared on 1 × 1 cm squares glass microscope slides, and the flat gold surfaces were obtained by a template-stripping method.[33] Briefly, template-stripped gold was prepared by resistively evaporating about 250 nm of gold onto a 4-in. silicon wafer with an Edwards 306A resistive evaporator. Glass microscope slides were cut into 1 × 1 cm squares and sonicated in diluted 5% Contrad 70 liquid detergent, deionized water, and ethanol (twice), each for 30 min, and dried under a nitrogen stream. The clean glass substrates were

glued to the gold-coated wafer with two-part epotek 377 (Epoxy Technology) and heated at 150 °C for 1.75 h. The glass substrates were then gently detached from the silicon wafer. The sandwiched gold film remained on the topside of the glass substrate to yield a smooth gold surface. The process is shown schematically in Figure 4.1A.

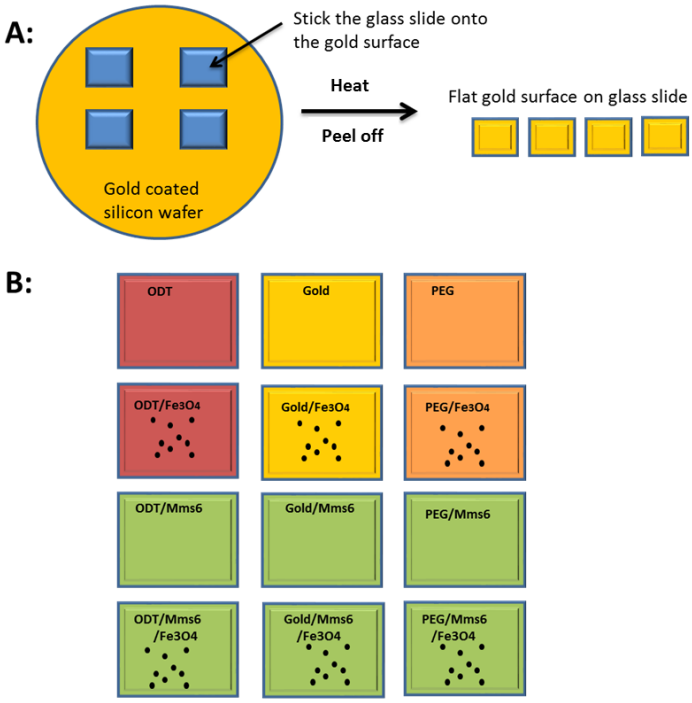

Figure 4.1 Schematic representation of sample preparation steps. A, gold surface fabrication; B, experiment design and characterization.

The smooth gold surface was dipped into 2 mM ODT or PEG solution in a small glass dish, and was incubated overnight at room temperature to create a self-assembled monolayer of ODT or PEG. The surface was then dried by nitrogen flow. The ODT or PEG coated gold surface is referred to as ODT surface or PEG surface henceforth, as shown schematically in the first row of Figure 4.1B.

Thirty µL of 0.2 mg/mL Mms6 in Tris buffer was added to the gold or ODT or PEG surface and incubated overnight in a humidity chamber at 4 °C. The surface was then washed in Tris buffer and water with 0.5% Tween® 20, and dried under nitrogen stream for tests. The

drying step here was skipped for the Mms6-coated surface used for the magnetite formation. The surfaces are referred to as ODT/Mms6, gold/Mms6, and PEG/Mms6, as shown in Figure 4.1B on the third row.

4.3.3 Magnetite growth on the surfaces

Magnetite nanoparticles were grown on the surfaces by a co-precipitation method. The method was developed based on our previous bulk solution synthesis of magnetite nanoparticles.[22, 25] All solutions used in the following procedures were prepared using degassed water. Briefly, a stock solution with polymer and iron ions was prepared at 4 °C using the following ratio: 100 µL of 25 wt% Pluronic F127 solution, 50 µL of 0.25 M $FeCl_2$ solution, 50 µL of 0.5 M $FeCl_3$ solution, and 100 µL of Tris buffer. In a glove box charged with inert gas (nitrogen or argon), glass substrates treated with ODT/PEG and Mms6 were added to wells in a 24-well plate. Two hundred µL of the stock solution containing polymer and iron ions was brought up to room temperature and slowly added to each well by micropipette, and incubated for 2 hours at room temperature without controlling the humidity. Then 750 µL of 0.1M NaOH solution was slowly added to each well, and all the samples were incubated under an oxygen free environment for 5 days. The surface samples were then washed three times using degassed water, and sealed under nitrogen gas until subsequent characterization tests. The black precipitate in the suspension was collected and washed for powder X-ray diffraction (XRD) characterization. The surface samples with magnetite nanoparticles are shown schematically in Figure 4.1B in Row 2 and Row 4.

4.3.4 Measurements

Atomic force microscopy **(**AFM) topographic images were acquired using a Nanoscope III Digital Instruments AFM (Veeco) in tapping mode. XRD analysis of the powders was

performed using a PANalytical X'Pert Pro diffraction system equipped X'pert Data collector in which a cobalt Kα radiation source with a wavelength of 0.17903 nm was employed. Formation of magnetite nanoparticles on surfaces was examined with scanning electron microscopy (SEM, FEI Quanta 250). Magnetic force microscopy (MFM) images were obtained using MESP (Bruker) at the Center for Nanoscale Materials at the Argonne National Lab. X-ray photoelectron spectroscopy (XPS) surface analysis was performed with a PHI 5500 spectrometer using Al-Kα1 radiation with a 45° electron collection angle, corresponding to the maximal penetration depth of about 10 nm. For contact angle measurements, 2μL of nanopure water was dropped on the surface of interest, and the drops were photographed with Canon EOS Rebel T3i EF 100mm f/2.8L Macro IS USM. Half-angle method was used to obtain the contact angles.

4.4 Results and Discussion

The gold surface obtained by the template stripped method was very flat, as shown in Figure 4.2b. The roughness of the gold surface was about 2-3 nm, determined by the line cross-sectional view of the AFM images. Such a flat surface provided the ability to image the nanoparticles on the surface. Self-assembled monolayers of ODT or surfaces covered with PEG were formed on the flat gold surfaces after overnight incubation. The ODT surface is hydrophobic,[34] and the PEG surface is hydrophilic,[35] as observed during Mms6 incubation, which is verified by the contact angle measurements, shown in Figure 4.3. There were no obvious differences seen in the images between the ODT and gold surfaces (Figure 4.2a-b), since the alkyl chains from *n*-alkanethiols prefer a parallel alignment on the gold surface and formation of a close-packed monolayer with the ellipsometric thickness of about 2 nm for ODT.[34] However, PEG did not uniformly cover the gold surface (Figure 4.2c). In a self-assembled monolayer, the PEG chain is not "extended", but rather folds on itself sometimes.[35, 36] Unlike the

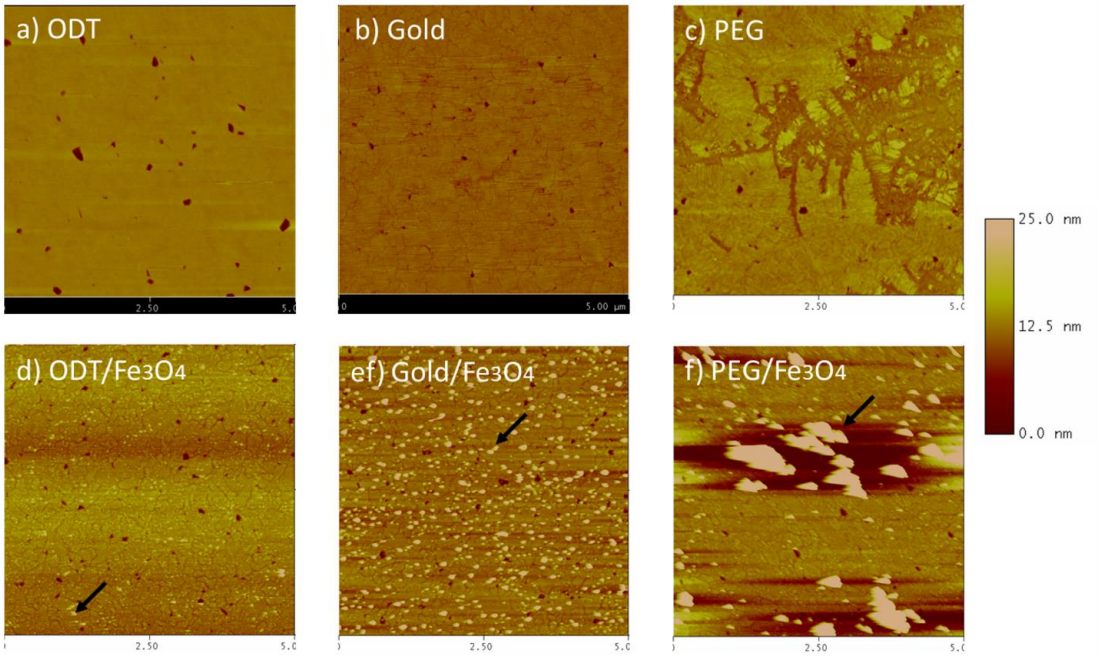

Figure 4.2 AFM scans of surfaces without Mms6 before magnetite nanoparticles synthesized on a) ODT, b) gold and c) PEG surfaces; and after synthesis of magnetite nanoparticles: d) magnetite grown on ODT surface, e) magnetite grown on gold surface, and f) magnetite grown on PEG surface. Arrows are used to highlight particles on surfaces. Scan area 5 μm × 5 μm.

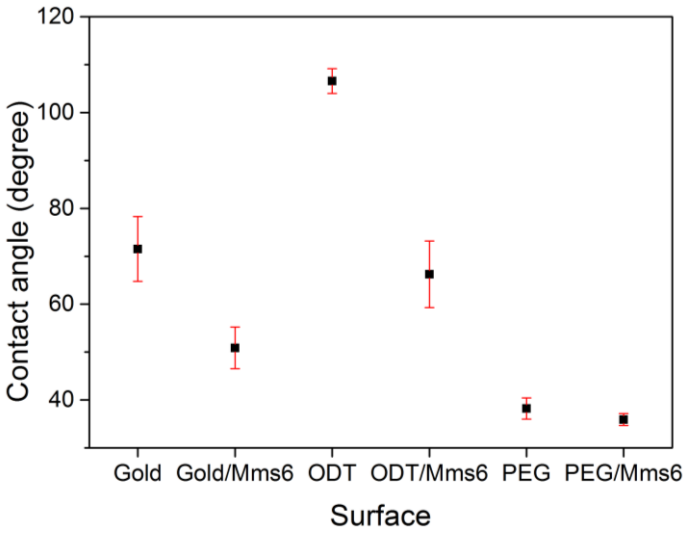

Figure 4.3 Contact angles for gold, ODT and PEG surfaces with and without Mms6 coating.

"brush" conformation of ODT on gold, PEG chains sometimes arrange in "island" or "mushroom" conformations.[37, 38] In addition, the PEG used in this study had a much larger

molecular weight (M_n = 2000) than ODT (M_w = 286.56), indicating that PEG had longer, disorganized chains, which might further prevent the formation of a uniform and dense monolayer.[35, 36]

Magnetite nanoparticles were synthesized by the co-precipitation method on ODT, PEG and bare gold surfaces. Assuming that magnetite nanoparticles do not interact strongly with ODT, PEG and gold surfaces, in the absence of Mms6 there should be no magnetite nanoparticles left on the surface after the washing process. However, the images show that there were a few residual magnetite nanoparticles and aggregates left on the surface even after washing process (Figure 4.2d-f), implying that it was difficult to completely wash off the magnetite particles even from the perfectly smooth surfaces with just the water flow. The lighter spots (see arrows) in the AFM images in Figure 4.2d-f correspond to areas with greater height, corresponding to the presence of the magnetite nanoparticles. It is also possible that during washing process at neutral pH, the negatively charged gold surface might attract slightly positively charged magnetite particles, since the isoelectric points (IEP) of gold and magnetite nanoparticles are around 2.5 and 8, respectively as reported.[39, 40]

Mms6 was coated on ODT, PEG and bare gold surfaces (Figure 4.4a-c, S4.1a-c). On the gold surface, Mms6 formed spherical nanomicellar structures. This is consistent with previous observations that Mms6 self-assembles to form micelles in solution,[25, 28] which explains the micellar structure formation on the gold surface probably due to adsorption. Mms6 showed very different morphology on the ODT surface than on the gold surface. As can be seen from Figure 4.4a and Figure S4.1a, Mms6 formed larger self-assembled units that resemble a connected protein network. However, there were no obvious significant differences between Mms6 on the PEG surface and for PEG alone, as seen in Figure 4.2c, Figure 4.4c and Figure S4.1c. This may

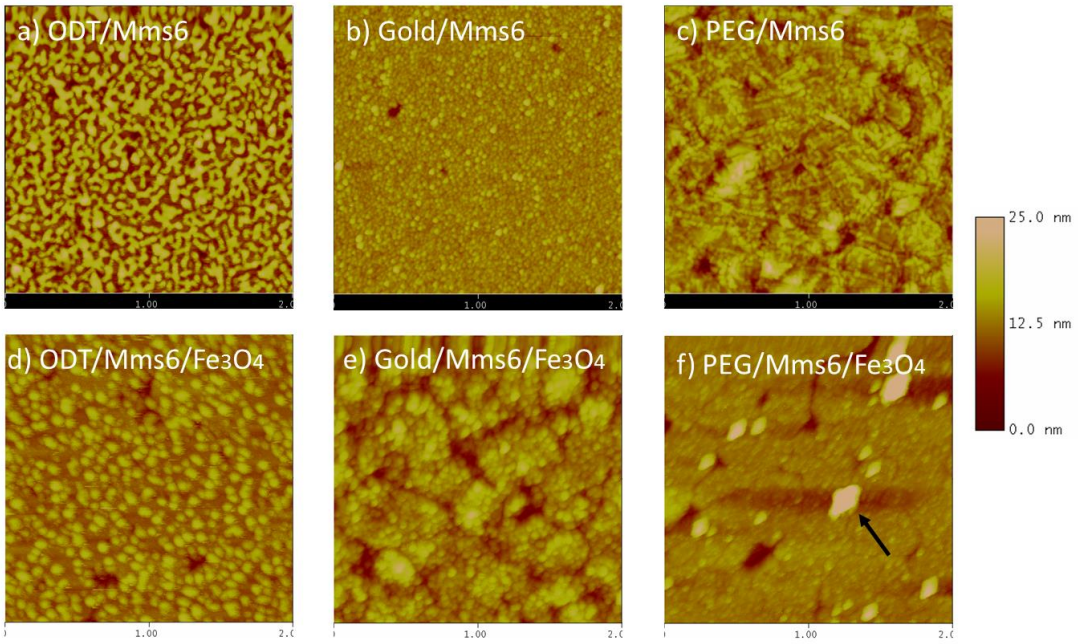

Figure 4.4 AFM scan of surfaces with Mms6 prior to magnetite nanoparticle synthesis: a) Mms6 coated ODT, b) Mms6 coated gold and c) Mms6 coated PEG surfaces; and after synthesis of magnetite nanoparticles: d) magnetite grown on Mms6-ODT surface, e) magnetite grown on Mms6-gold surface, and f) magnetite grown on Mms6-PEG surface. Scan area 2 μm × 2 μm.

be caused by the well-known protein resistant property of the PEG.[41] Contact angle measurements done on these surfaces after Mms6 incubation (Figure 4.3) also indicate protein coated on the gold and ODT surfaces as opposed to the PEG surface. After Mms6 coating, the contact angles of the gold and ODT surfaces decreased by 10-30° and 30-50°, respectively, while no change of contact angle was observed on the PEG surface.

Figure 4.4d-f and Figure S4.1d-f show the magnetite nanoparticles grown on the Mms6 coated surfaces. Comparing with Figure 4.2d-f, there were significantly more magnetite nanoparticles seen on ODT and gold surfaces with Mms6 than without, while magnetite nanoparticles grown on PEG surface with and without Mms6 looked similar. This suggests that Mms6 remained on the ODT and gold surfaces and not the PEG and, in that form, could promote the formation of magnetite nanoparticles on surfaces, similar to what is seen in bulk solution[22, 25].

The collected black precipitates from the solution during synthesis of magnetite on Mms6 coated ODT surface were also confirmed as magnetite by XRD (Figure S4.2). In the presence of Mms6, magnetite nanoparticles were uniformly distributed on the ODT surface without formation of the aggregates as were seen on the gold surface. The particles on the ODT surfaces were larger than those on gold, with a size of about 20 nm, which is close to the size of the magnetite nanocrystals generated by magnetotactic bacteria.[19] On the Mms6-coated gold surface, aggregates of uniform sized magnetite nanoparticles were also formed, with smaller sizes than those on the ODT surfaces.

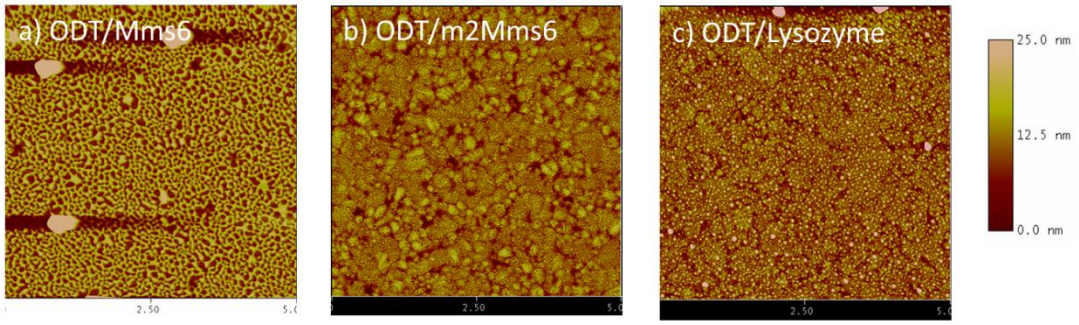

Figure 4.5 AFM scan of ODT surface with a) Mms6, b) m2Mms6 or c) lysozyme. Scan area 5 μm × 5 μm. Only Mms6 can form a "protein network" on the ODT surface, while mutant m2Mms6 or lysozyme cannot, which indicates the "network" may be important for the formation of magnetite with uniform size.

Figure 4.5 shows the influence of two other proteins m2Mms6 and lysozyme used as a control coated on the ODT surface. In previous study, both m2Mms6[25] and lysozyme[22] have been shown to be much less effective as Mms6 in facilitating magnetite nanocrystal formation in the bulk. Here, neither m2Mms6 nor lysozyme could facilitate the formation of the protein network structure seen with Mms6, which indicated that the type of protein as well as the amino acid sequence is important for the interaction of the protein with the ODT surface. In our previous work[28], we have demonstrated that the ability of Mms6 to self-assemble into a multimeric micelle depends on both N-terminal hydrophobic domain and the C-terminal iron

binding domain. Although the C-terminal domain overall is highly charged, it also contains several hydrophobic residues that may be involved in the interaction with N-terminal hydrophobic domain (Leucine128, Leucine132 in C-terminal domain). Admittedly, the intact N-terminal domain itself still enables the protein to self-assemble into a multimeric complex and interact with the hydrophobic surface (Figure 4.5b), but the structure of the complex formed without the "native C-terminal" is likely to be different from the wild-type Mms6 complex. Only the wild type Mms6 could form a protein network on the ODT surface, suggesting that the Mms6 molecular conformation and especially the arrangement of OH and COOH groups play a critical role in promoting the formation of the protein network. This, in turn, potentially impacts the proteins' ability to facilitate magnetite nanocrystal formation. This is also consistent with our previous observations of Mms6 self-assembly that is coordinated by both N-terminal and C-terminal domain.[28]

The chemical states of different surfaces were investigated by XPS. In Figure 4.6, it shows that there are well-defined spectra for O1s and N1s in case of Mms6-ODT surface, as opposed to the ODT surface treated with pure Tris buffer without Mms6. The O1s spectrum corresponds to oxygen atoms from C-O (531.8 eV) and C=O (533.2 eV) groups, and N1s spectrum ascribes to nitrogen atoms in C-N (400.3 eV) group. Meanwhile, compared to C1s spectrum of ODT surface with only one carbon component (C-C/C-H, 284.8 eV), there are two additional moieties in C1s spectrum of Mms6-ODT surface, which are assigned to carbon atoms from C-O/C-N (285.6 eV) and C=O/N-C=O (288.5 eV) groups. In addition, both ODT and Mms6-ODT surfaces contain low-intensity S2p peaks. These results confirm the presence of Mms6 protein on the coated ODT surface, since C-O, C-N, C=O, N-C=O shown in XPS spectra are all from the Mms6 protein. Figure 4.7 shows surface characterization of magnetite grown on

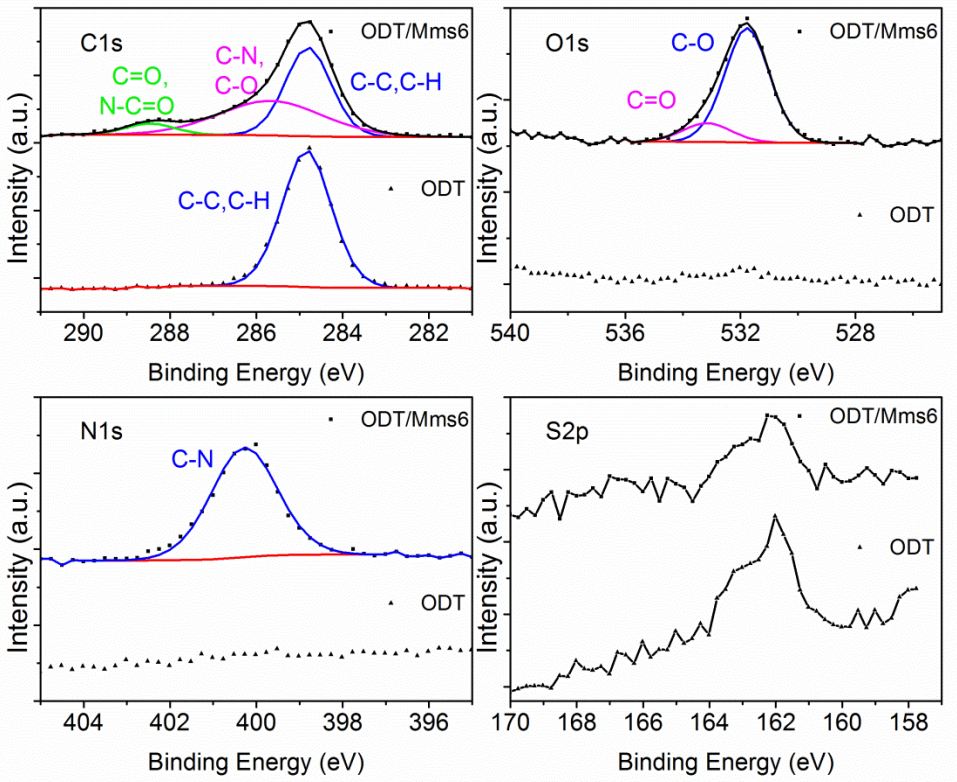

Figure 4.6 XPS results for ODT/Gold surfaces with (square) and without (triangle) Mms6 protein on them. The surface without Mms6 was still treated with Tris buffer for comparison. Binding energy was calibrated with Au $4f_{7/2}$ (84.0 eV) as a reference.

the ODT surfaces with and without Mms6. On the ODT surface after growing magnetite nanocrystals, the XPS spectra are similar to the pure ODT surface as most of magnetite nanoparticles were washed away during the washing process. On the contrary, on the Mms6-ODT surface, after growing magnetite the C-O, C-N, C=O, N-C=O components present in XPS spectra support the existence of Mms6 protein, and the Fe-O type moiety (530.0 eV) in the O1s spectrum and the extra Fe2p peaks indicate formation of magnetite nanocrystals on Mms6-ODT surface. The Fe2p spectrum with two constituent peaks (Fe $2p_{1/2}$ and Fe $2p_{3/2}$) and their satellites can be deconvoluted into components (Fe^{2+} $2p_{3/2}$, 710.8 eV; Fe^{3+} $2p_{3/2}$, 712.5 eV; Fe^{2+} $2p_{1/2}$, 723.9 eV; and Fe^{3+} $2p_{1/2}$, 725.6 eV) ascribed to $Fe^{3+}$and Fe^{2+} ions from magnetite.[42, 43] Therefore,

the XPS results confirm that Mms6 was present on the ODT surface and could promote magnetite formation, which is consistent with the AFM observations.

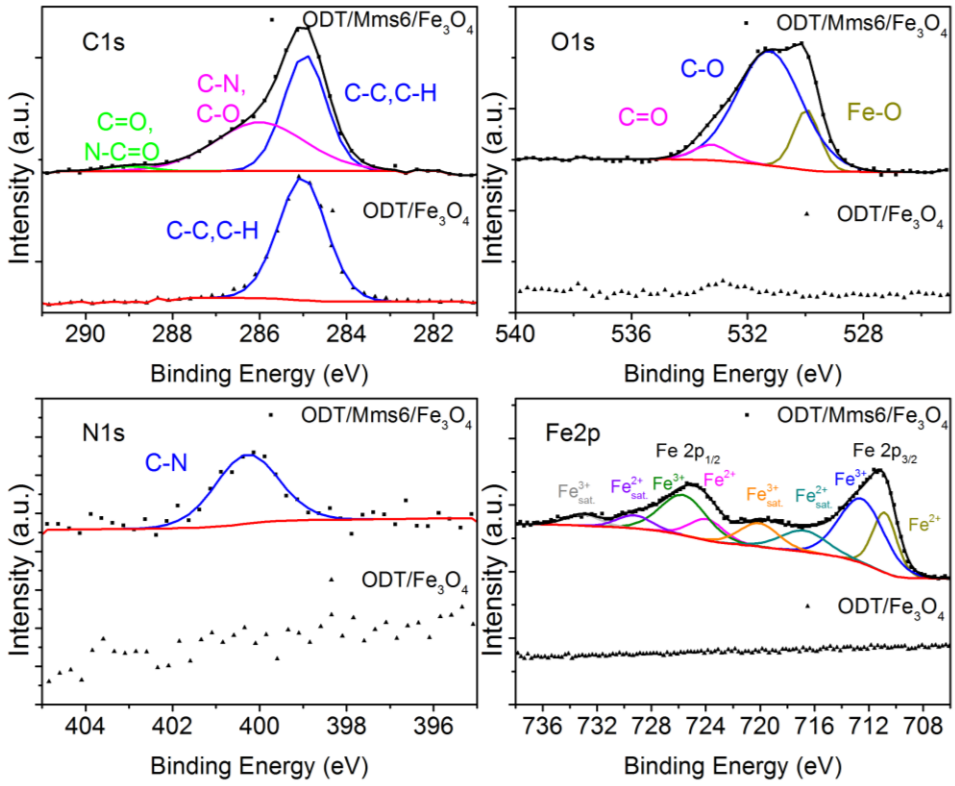

Figure 4.7 XPS results for the magnetite nanocrystals grown on ODT surfaces, with (square) and without (triangle) Mms6. The surface without Mms6 was still treated with Tris buffer for comparison. Binding energy was calibrated with Au $4f_{7/2}$ (84.0 eV) as a reference.

SEM was used to visualize the magnetite nanoparticles grown on ODT and gold surfaces with and without Mms6 (Figure 4.8 and 4.9). On ODT surfaces, nothing could be seen except crystal grains from polycrystalline gold underneath the ODT monolayer (Figure 4.8a). No clear information from surface topography and morphology could be observed in this secondary electron image, while the crystallographic contrast of gold grains due to the effect of electron channeling[44] was shown, which verified that the surface is very flat. Mms6 coating on ODT surfaces clearly increased the surface roughness uniformly (Figure 4.8b) resulting from formation of protein network. After magnetite nanocrystals were grown on the ODT surface and

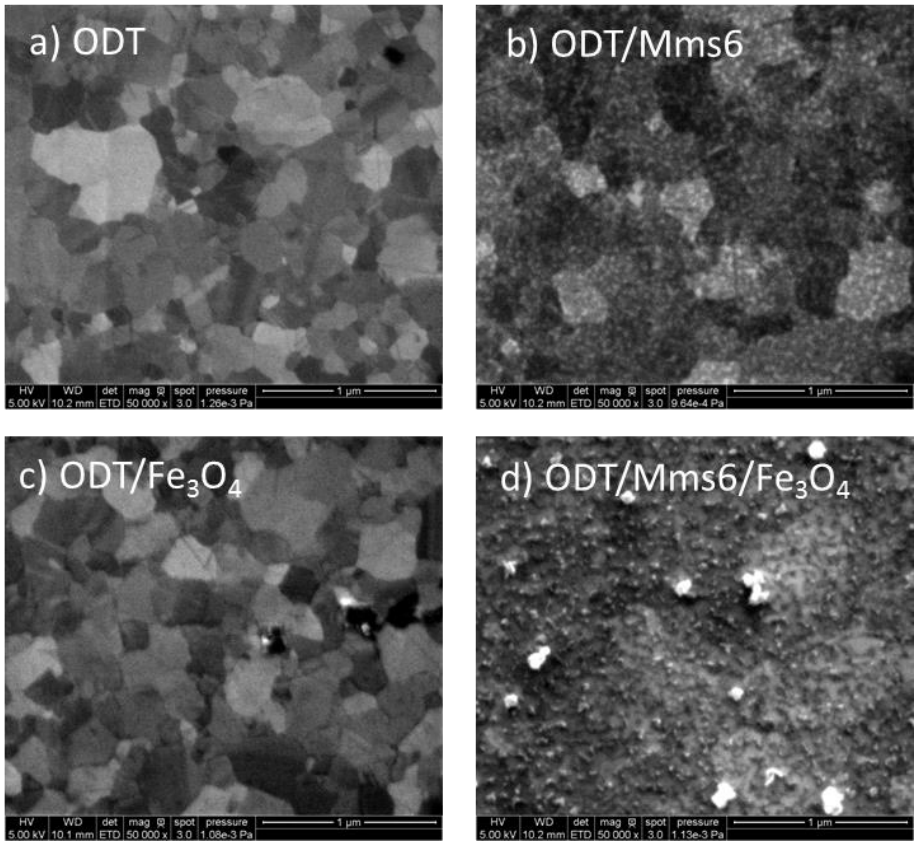

Figure 4.8 SEM secondary electron images of a) ODT surface, b) Mms6-coated ODT surface, c) magnetite grown on ODT surface and d) magnetite grown on Mms6-coated ODT surface.

Mms6-ODT surface, bright nanoparticles were found attached to the surface. Without ODT, the Mms6 coated gold surface looked flat (Figure 4.9a-b) compared to Mms6-ODT surface (Figure 4.8b), probably because the very small roughness of Mms6 on gold shown in AFM is beyond the detection limit of SEM. Nanoparticles on Mms6 coated gold surface formed very large aggregates (up to 2 μm) and were distributed on the surface without any order (Figure 4.9c-d). All the bright particles have strong Fe and O signals in energy-dispersive X-ray spectroscopy (EDS) spectrum (Figure S4.3), suggesting that they are magnetite nanoparticles. Compared with surfaces without ODT, only few of magnetite nanoparticles were left on ODT surface after washing (Figure 4.8c), while a large number of fine magnetite nanoparticles including some small aggregates uniformly covered the Mms6-ODT surface (Figure 4.8d and 4.9e-f), which is

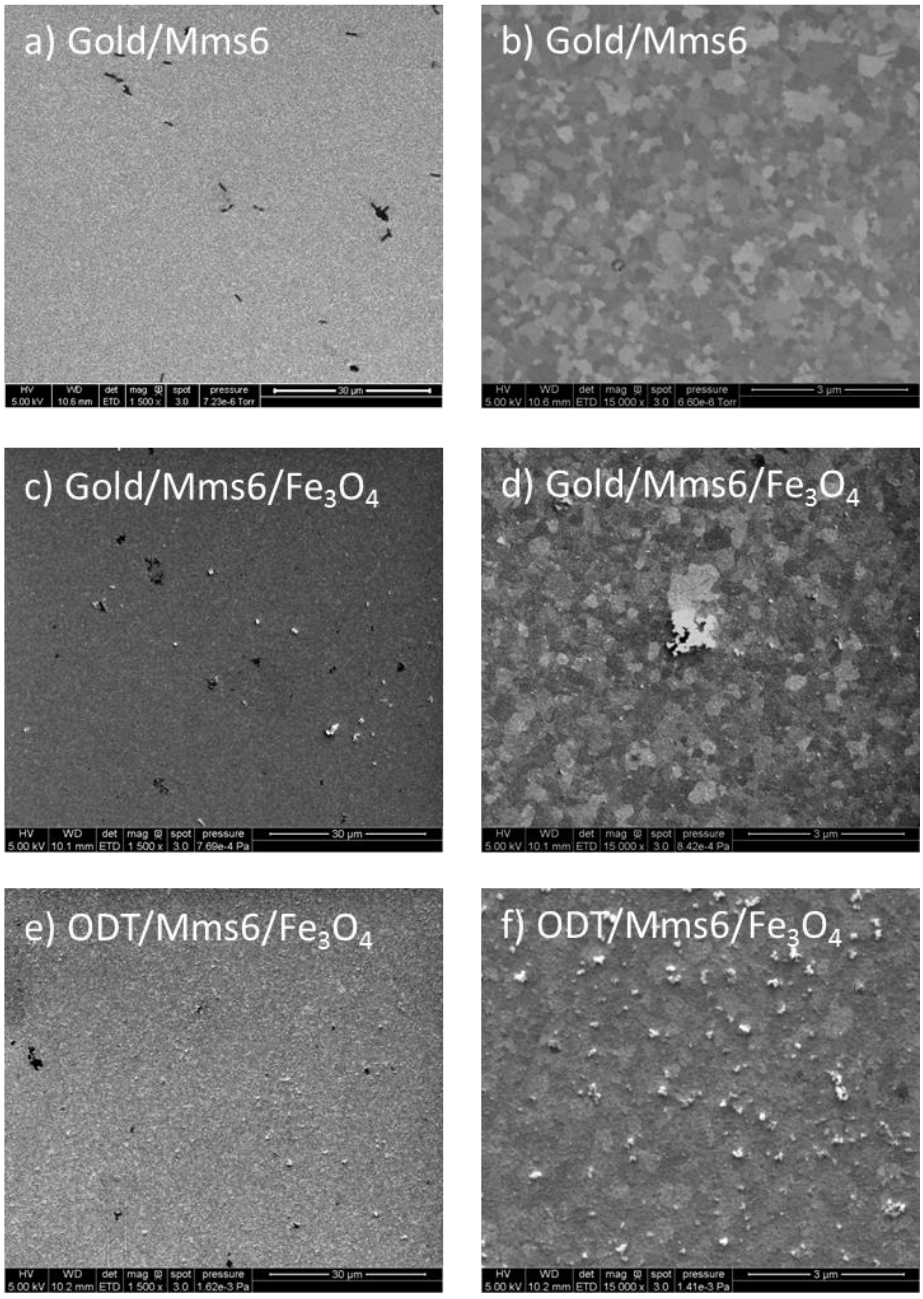

Figure 4.9 SEM secondary electron images with different magnifications of a-b) Mms6-coated gold surface, c-d) magnetite grown on Mms6-coated gold surface, e-f) magnetite grown on Mms6-coated ODT surface.

consistent with AFM results. Figure 4.9e shows the uniform distribution of magnetite nanoparticles on Mms6-ODT surface on a much larger scale than could be observed by AFM.

MFM was used to measure the magnetic response of the magnetite nanoparticles on the surfaces. If there is contrast in the MFM scan, it supports the presence of magnetic materials on

the surface. Areas with excess amount of magnetite nanoparticles were scanned. Therefore, if the MFM image had the same pattern as the AFM image, it may be due to the excess height of the surface and not due to the magnetic response. In Figure S4.4, only the magnetite nanoparticles grown on the ODT surface show a different contrast pattern on the MFM image than the AFM image, which could be an indication of a stronger magnetic response in that case due to more well-formed nanocrystals.

In summary, it was found that Mms6 can form a protein network on the hydrophobic ODT coated surface, and then promote the formation of magnetite nanoparticles of uniform sizes similar to those seen in nature. The ability of Mms6 to form a network on hydrophobic surfaces such as ODT may be due to its amphiphilic property and its demonstrated ability to incorporate into a hydrophobic lipid bilayers of liposomes.[25] The significant decrease in the contact angle of ODT surface after Mms6 coating (Figure 4.3) suggests that the proteins align on the hydrophobic surface with hydrophilic C-terminal domains on the top. Here we also show that the network-like structure of Mms6 functions *in vitro* in such a hydrophobic environment. Our previous study has indicated that in the bulk solution in the presence of iron ions, Mms6 micelles interact with iron ions and prefer to form 2D disk-like or 3D mass-fractal-like aggregates with large surface area, which may contribute to formation of large magnetite nanocrystals.[26] In this study, the ODT monolayer seems to allow Mms6 to self-assemble into a protein network that also provide a large surface area for iron binding, which, in turn, enables the formation of magnetic nanoparticles. The C-terminal domain of Mms6 is known to be necessary for promoting the magnetite formation, and mutants, such as m2Mms6, with changes to the C-terminal domain sequence, no longer promote magnetite formation effectively.[22, 25] Based on the results of this study, we propose that the hydrophobic N-terminal domain of Mms6 embeds in the hydrophobic ODT

surfaces, forming a protein network structure. It is worth noting that the Mms6 protein is amphiphilic and self-assembles to multimeric micelles in bulk solution,[25, 26] and these micelles have been shown to exist in solutions under constant equilibrium with the unimeric proteins by FPLC analysis of both wild-type and two mutants of Mms6.[28] The hydrophobic interaction between N-terminal domain of Mms6 and the ODT surface consumes free unimers in solution and changes the original equilibrium state to provide more unimers, which results in coating of Mms6 on ODT surface after incubation. The Mms6 protein is predicted as a transmembrane protein and the transmembrane helix contains only hydrophobic residues.[45] The ODT surface may create conditions for the protein that are more similar to its native lipid bilayer environment of magnetosome membrane, thus facilitating the formation of uniformly sized and more well-defined magnetite nanoparticles,[46] similar to those seen in nature.

4.5 Conclusions

We investigated Mms6 for its function of promoting magnetite nanocrystal formation on surfaces with different hydrophobicities. It was found that Mms6 on hydrophobic ODT monolayer on gold substrates could form a protein network structure that displayed better functionality in promoting the formation of uniformly sized magnetite nanoparticles on the surface. On the contrary, hydrophilic PEG surfaces exhibited protein resistance. Furthermore, Mms6 micelles adsorbed on bare gold surfaces without forming a protein network structure. Compared to magnetite grown on the Mms6 coated ODT surfaces, the magnetite nanocrystals formed on PEG and gold surfaces were smaller and less magnetic, and more easily washed away. Mms6 is believed to be a membrane protein *in vivo*, and we propose that the N-terminal domain of Mms6 interacts mainly through hydrophobic forces with the ODT surface in a way similar to Mms6 situated in the membrane *in vivo* and the C-terminal domain facilitates growth of

magnetite nanocrystals. Our results have also shown that Mms6 immobilized on surface by hydrophobic interaction can be used as a template for specific magnetite biomineralization on surfaces, which provides an effective and cheap bottom-up approach to fabricating magnetic devices with magnetite, cobalt doped magnetite[47] or cobalt ferrite[32] nanoparticles on surfaces at room temperature without using harsh chemicals. Moreover, the system in this study is very flexible and Mms6 can be exploited for surface magnetic nanomaterials synthesis, by which functionalized surfaces or patterned surfaces can used as substrates for synthesis. These surfaces, with site-specifically fabricated magnetic nanocrystals, can be further applied to the development of sensors or data storage devices. The work also provides a facile way to control the bioinspired synthesis by tailoring the hydrophobicity of the surfaces.

4.6 Acknowledgements

SKM is grateful for the inspiration provided by Prof. Doraiswami Ramkrishna through his outstanding body of work and through his graduate teaching at Purdue that directly impacted her. We thank Pierre Palo from Prof. Marit Nilsen-Hamilton's group at Ames Laboratory for preparing the Mms6 protein preparations. Research at Ames Laboratory was supported by the U.S. Department of Energy, Office of the Basic Energy Sciences, Division of Materials Sciences and Engineering. Ames Laboratory is operated for the U.S. Department of Energy by Iowa State University under Contract Number DE-AC02-07CH11358. The use of Magnetic Force Microscopy at the Argonne National Laboratory was supported by the U.S. Department of Energy under Contract Number DE-AC02-06CH11357.

4.7 Supporting Information (SI)

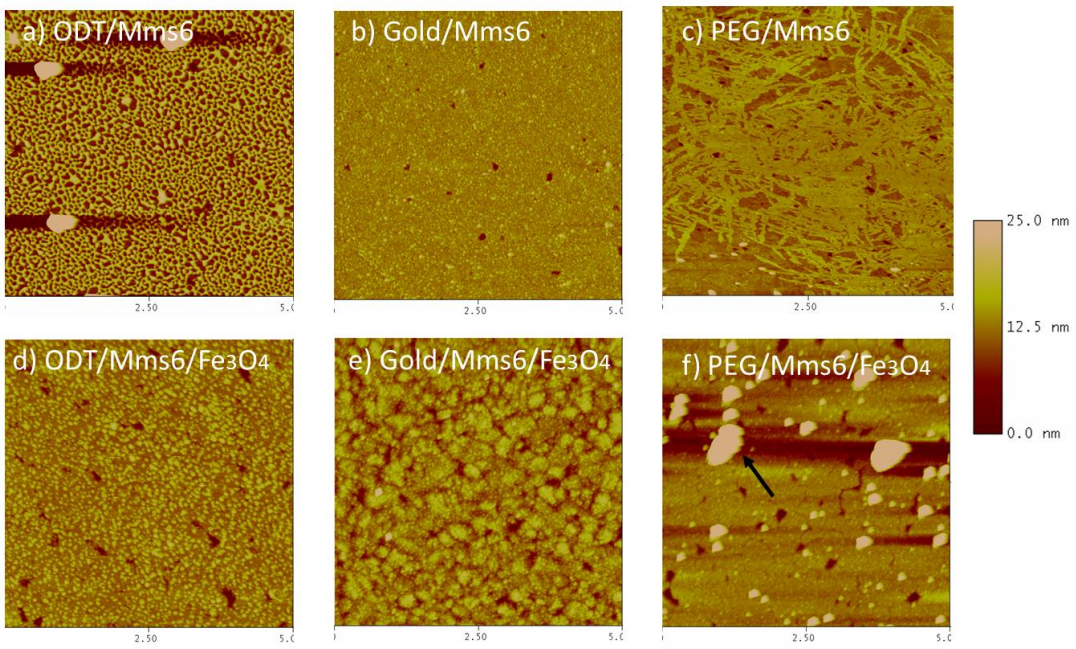

Figure S4.1 AFM scan of surfaces with Mms6 prior to magnetite nanoparticle synthesis: a) Mms6 coated ODT, b) Mms6 coated gold and c) Mms6 coated PEG surfaces; and after synthesis of magnetite nanoparticles: d) magnetite grown on Mms6-ODT surface, e) magnetite grown on Mms6-gold surface, and f) magnetite grown on Mms6-PEG surface. Scan area 5 μm × 5 μm. Mms6 shows different aggregation on the surfaces with different hydrophobicities.

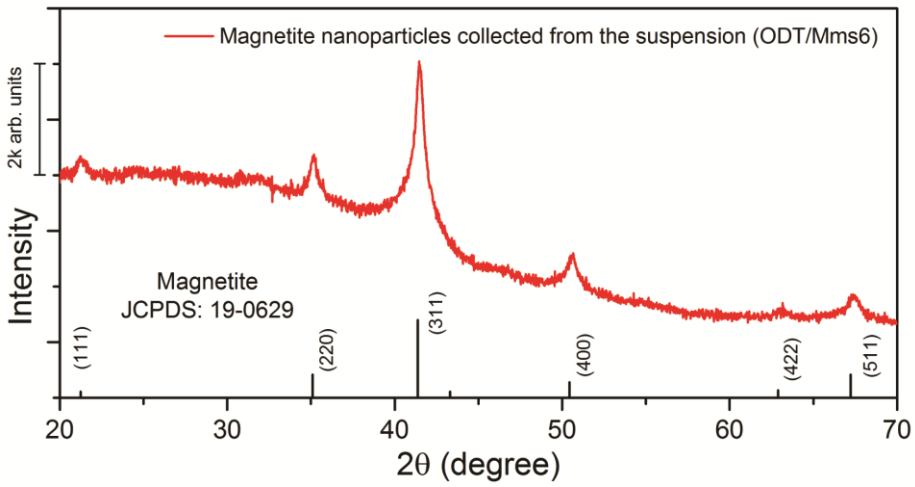

Figure S4.2 XRD pattern for the black precipitates collected from suspension in the Mms6-ODT surface sample.

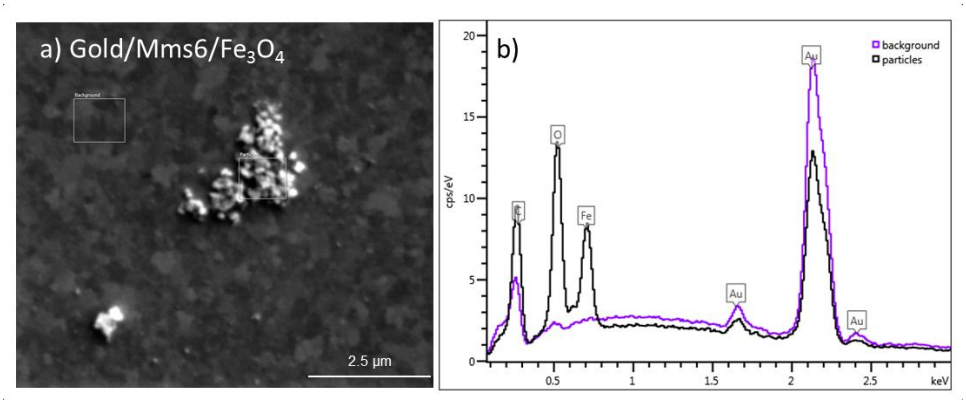

Figure S4.3 SEM image (a) and EDS analysis (b) of magnetite grown on Mms6 coated gold surface without ODT coating.

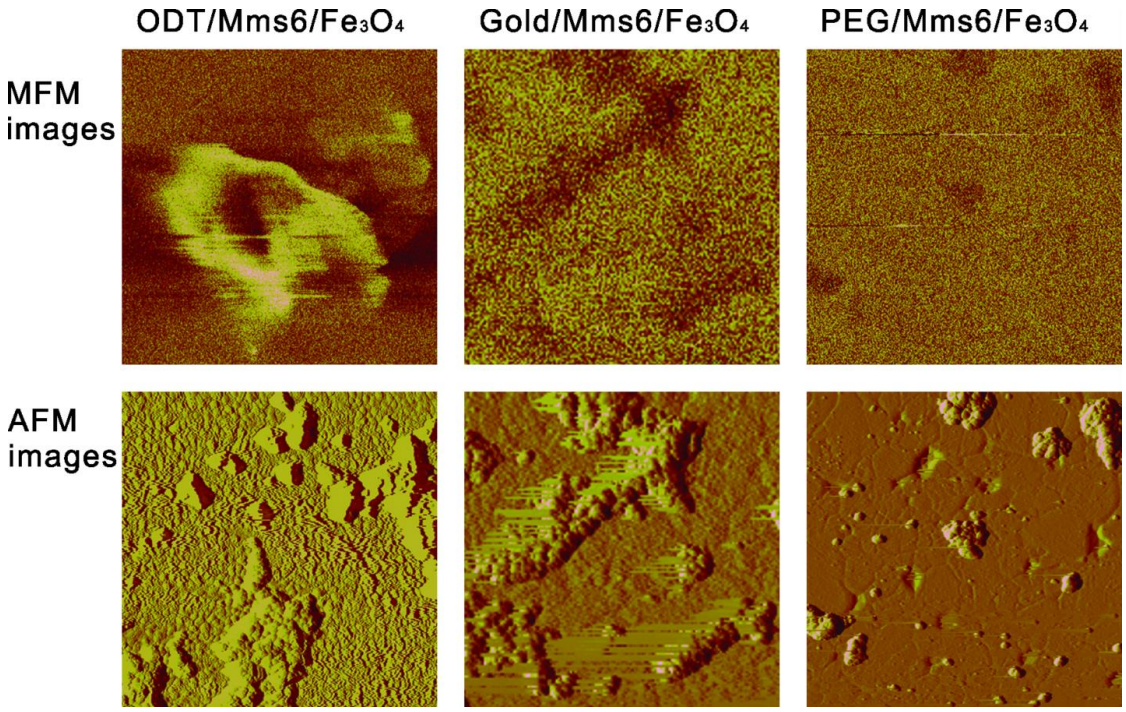

Figure S4.4 AFM and MFM scans in the same area of surfaces with magnetite nanoparticles grown on Mms6 coated surfaces: ODT, gold and PEG surfaces. Scan area 3 µm × 3 µm.

References

1. Lu, A.-H.; Salabas, E. L.; Schüth, F. Magnetic Nanoparticles: Synthesis, Protection, Functionalization, and Application. *Angew. Chem. Int. Ed.* 2007, 46, 1222-1244.
2. Jeong, U.; Teng, X.; Wang, Y.; Yang, H.; Xia, Y. Superparamagnetic Colloids: Controlled Synthesis and Niche Applications. *Adv. Mater.* 2007, 19, 33-60.
3. Gao, J.; Gu, H.; Xu, B. Multifunctional Magnetic Nanoparticles: Design, Synthesis, and Biomedical Applications. *Acc. Chem. Res.* 2009, 42, 1097-1107.

4. Hao, R.; Xing, R.; Xu, Z.; Hou, Y.; Gao, S.; Sun, S. Synthesis, Functionalization, and Biomedical Applications of Multifunctional Magnetic Nanoparticles. *Adv. Mater.* 2010, 22, 2729-2742.
5. Tartaj, P.; Morales, M. d. P.; Veintemillas-Verdaguer, S.; González-Carreño, T.; Serna, C. J. The preparation of magnetic nanoparticles for applications in biomedicine. *J. Phys. D: Appl. Phys.* 2003, 36, R182.
6. Park, J.; An, K.; Hwang, Y.; Park, J.-G.; Noh, H.-J.; Kim, J.-Y.; Park, J.-H.; Hwang, N.-M.; Hyeon, T. Ultra-large-scale syntheses of monodisperse nanocrystals. *Nat. Mater.* 2004, 3, 891-895.
7. Sun, S.; Zeng, H. Size-Controlled Synthesis of Magnetite Nanoparticles. *J. Am. Chem. Soc.* 2002, 124, 8204-8205.
8. Laurent, S.; Forge, D.; Port, M.; Roch, A.; Robic, C.; Vander Elst, L.; Muller, R. N. Magnetic Iron Oxide Nanoparticles: Synthesis, Stabilization, Vectorization, Physicochemical Characterizations, and Biological Applications. *Chem. Rev.* 2008, 108, 2064-2110.
9. Bazylinski, D. A.; Frankel, R. B. Magnetosome formation in prokaryotes. *Nat. Rev. Microbiol.* 2004, 2, 217-230.
10. Jimenez-Lopez, C.; Romanek, C. S.; Bazylinski, D. A. Magnetite as a prokaryotic biomarker: A review. *J. Geophys. Res.: Biogeosci.* 2010, 115, G00G03.
11. Siponen, M. I.; Legrand, P.; Widdrat, M.; Jones, S. R.; Zhang, W.-J.; Chang, M. C. Y.; Faivre, D.; Arnoux, P.; Pignol, D. Structural insight into magnetochrome-mediated magnetite biomineralization. *Nature* 2013, 502, 681-684.
12. Mann, S.; Sparks, N. H. C.; Frankel, R. B.; Bazylinski, D. A.; Jannasch, H. W. Biomineralization of ferrimagnetic greigite (Fe3S4) and iron pyrite (FeS2) in a magnetotactic bacterium. *Nature* 1990, 343, 258-261.
13. Lu, Y.; Dong, L.; Zhang, L.-C.; Su, Y.-D.; Yu, S.-H. Biogenic and biomimetic magnetic nanosized assemblies. *Nano Today* 2012, 7, 297-315.
14. Fdez-Gubieda, M. L.; Muela, A.; Alonso, J.; García-Prieto, A.; Olivi, L.; Fernández-Pacheco, R.; Barandiarán, J. M. Magnetite Biomineralization in Magnetospirillum gryphiswaldense: Time-Resolved Magnetic and Structural Studies. *ACS Nano* 2013, 7, 3297-3305.
15. Lefèvre, C. T.; Menguy, N.; Abreu, F.; Lins, U.; Pósfai, M.; Prozorov, T.; Pignol, D.; Frankel, R. B.; Bazylinski, D. A. A Cultured Greigite-Producing Magnetotactic Bacterium in a Novel Group of Sulfate-Reducing Bacteria. *Science* 2011, 334, 1720-1723.
16. Komeili, A. Molecular Mechanisms of Magnetosome Formation. *Annu. Rev. Biochem.* 2007, 76, 351-366.
17. Fratzl, P.; Weinkamer, R. Nature's hierarchical materials. *Prog. Mater. Sci.* 2007, 52, 1263-1334.
18. Cölfen, H.; Mann, S. Higher-Order Organization by Mesoscale Self-Assembly and Transformation of Hybrid Nanostructures. *Angew. Chem. Int. Ed.* 2003, 42, 2350-2365.
19. Prozorov, T.; Bazylinski, D. A.; Mallapragada, S. K.; Prozorov, R. Novel magnetic nanomaterials inspired by magnetotactic bacteria: Topical review. *Mater. Sci. Eng. R* 2013, 74, 133-172.
20. Kolinko, I.; Lohsze, A.; Borg, S.; Raschdorf, O.; Jogler, C.; Tu, Q.; Posfai, M.; Tompa, E.; Plitzko, J. M.; Brachmann, A.; Wanner, G.; Muller, R.; Zhang, Y.; Schuler, D.

Biosynthesis of magnetic nanostructures in a foreign organism by transfer of bacterial magnetosome gene clusters. *Nat. Nanotechnol.* 2014, 9, 193-197.

21. Arakaki, A.; Webb, J.; Matsunaga, T. A novel protein tightly bound to bacterial magnetic particles in Magnetospirillum magneticum strain AMB-1. *J. Biol. Chem.* 2003, 278, 8745-8750.
22. Prozorov, T.; Mallapragada, S. K.; Narasimhan, B.; Wang, L.; Palo, P.; Nilsen-Hamilton, M.; Williams, T. J.; Bazylinski, D. A.; Prozorov, R.; Canfield, P. C. Protein-Mediated Synthesis of Uniform Superparamagnetic Magnetite Nanocrystals. *Adv. Funct. Mater.* 2007, 17, 951-957.
23. Amemiya, Y.; Arakaki, A.; Staniland, S. S.; Tanaka, T.; Matsunaga, T. Controlled formation of magnetite crystal by partial oxidation of ferrous hydroxide in the presence of recombinant magnetotactic bacterial protein Mms6. *Biomaterials* 2007, 28, 5381-5389.
24. Arakaki, A.; Masuda, F.; Amemiya, Y.; Tanaka, T.; Matsunaga, T. Control of the morphology and size of magnetite particles with peptides mimicking the Mms6 protein from magnetotactic bacteria. *J. Colloid Interface Sci.* 2010, 343, 65-70.
25. Wang, L.; Prozorov, T.; Palo, P. E.; Liu, X.; Vaknin, D.; Prozorov, R.; Mallapragada, S.; Nilsen-Hamilton, M. Self-Assembly and Biphasic Iron-Binding Characteristics of Mms6, A Bacterial Protein That Promotes the Formation of Superparamagnetic Magnetite Nanoparticles of Uniform Size and Shape. *Biomacromolecules* 2012, 13, 98-105.
26. Zhang, H.; Liu, X.; Feng, S.; Wang, W.; Schmidt-Rohr, K.; Akinc, M.; Nilsen-Hamilton, M.; Vaknin, D.; Mallapragada, S. Morphological Transformations in the Magnetite Biomineralizing Protein Mms6 in Iron Solutions: A Small-Angle X-ray Scattering Study. *Langmuir* 2015, 31, 2818-2825.
27. Wang, W.; Bu, W.; Wang, L.; Palo, P. E.; Mallapragada, S.; Nilsen-Hamilton, M.; Vaknin, D. Interfacial Properties and Iron Binding to Bacterial Proteins That Promote the Growth of Magnetite Nanocrystals: X-ray Reflectivity and Surface Spectroscopy Studies. *Langmuir* 2012, 28, 4274-4282.
28. Feng, S.; Wang, L.; Palo, P.; Liu, X.; Mallapragada, S.; Nilsen-Hamilton, M. Integrated self-assembly of the mms6 magnetosome protein to form an iron-responsive structure. *Int. J. Mol. Sci.* 2013, 14, 14594-14606.
29. Arakaki, A.; Masuda, F.; Matsunaga, T. Iron oxide crystal formation on a substrate modified with the Mms6 protein from magnetotactic bacteria. *MRS Online Proc. Libr.* 2009.
30. Galloway, J. M.; Bramble, J. P.; Rawlings, A. E.; Burnell, G.; Evans, S. D.; Staniland, S. S. Biotemplated Magnetic Nanoparticle Arrays. *Small* 2012, 8, 204-208.
31. Galloway, J. M.; Bramble, J. P.; Rawlings, A. E.; Burnell, G.; Evans, S. D.; Staniland, S. S. Nanomagnetic arrays formed with the biomineralization protein Mms6. *J. Nano Res.* 2012, 17, 127-146.
32. Prozorov, T.; Palo, P.; Wang, L.; Nilsen-Hamilton, M.; Jones, D.; Orr, D.; Mallapragada, S. K.; Narasimhan, B.; Canfield, P. C.; Prozorov, R. Cobalt Ferrite Nanocrystals: Out-Performing Magnetotactic Bacteria. *ACS Nano* 2007, 1, 228-233.
33. Hegner, M.; Wagner, P.; Semenza, G. Ultralarge atomically flat template-stripped Au surfaces for scanning probe microscopy. *Surf. Sci.* 1993, 291, 39-46.

34. Bain, C. D.; Troughton, E. B.; Tao, Y. T.; Evall, J.; Whitesides, G. M.; Nuzzo, R. G. Formation of monolayer films by the spontaneous assembly of organic thiols from solution onto gold. *J. Am. Chem. Soc.* 1989, 111, 321-335.
35. Cerruti, M.; Fissolo, S.; Carraro, C.; Ricciardi, C.; Majumdar, A.; Maboudian, R. Poly(ethylene glycol) Monolayer Formation and Stability on Gold and Silicon Nitride Substrates. *Langmuir* 2008, 24, 10646-10653.
36. Harder, P.; Grunze, M.; Dahint, R.; Whitesides, G. M.; Laibinis, P. E. Molecular Conformation in Oligo(ethylene glycol)-Terminated Self-Assembled Monolayers on Gold and Silver Surfaces Determines Their Ability To Resist Protein Adsorption. *J. Phys. Chem. B* 1998, 102, 426-436.
37. Lokanathan, A. R.; Zhang, S.; Regina, V. R.; Cole, M. A.; Ogaki, R.; Dong, M.; Besenbacher, F.; Meyer, R. L.; Kingshott, P. Mixed poly (ethylene glycol) and oligo (ethylene glycol) layers on gold as nonfouling surfaces created by backfilling. *Biointerphases* 2011, 6, 180-188.
38. Unsworth, L. D.; Tun, Z.; Sheardown, H.; Brash, J. L. Chemisorption of thiolated poly(ethylene oxide) to gold: surface chain densities measured by ellipsometry and neutron reflectometry. *J. Colloid Interface Sci.* 2005, 281, 112-121.
39. Pfeiffer, C.; Rehbock, C.; Hühn, D.; Carrillo-Carrion, C.; de Aberasturi, D. J.; Merk, V.; Barcikowski, S.; Parak, W. J. Interaction of colloidal nanoparticles with their local environment: the (ionic) nanoenvironment around nanoparticles is different from bulk and determines the physico-chemical properties of the nanoparticles. *J. R. Soc. Interface* 2014, 11.
40. Illés, E.; Tombácz, E. The effect of humic acid adsorption on pH-dependent surface charging and aggregation of magnetite nanoparticles. *J. Colloid Interface Sci.* 2006, 295, 115-123.
41. Harris, J. M. *Poly(Ethylene Glycol) Chemistry: Biotechnical and Biomedical Applications*. Plenum Press: New York: 1992.
42. Bhargava, G.; Gouzman, I.; Chun, C. M.; Ramanarayanan, T. A.; Bernasek, S. L. Characterization of the "native" surface thin film on pure polycrystalline iron: A high resolution XPS and TEM study. *Appl. Surf. Sci.* 2007, 253, 4322-4329.
43. Nan, A.; Turcu, R.; Liebscher, J. Magnetite-polylactic acid core–shell nanoparticles by ring-opening polymerization under microwave irradiation. *J. Polym. Sci., Part A: Polym. Chem.* 2012, 50, 1485-1490.
44. LLOYD, G. Atomic number and crystallographic contrast images with the SEM: a review of backscattered electron techniques. *Mineral. Mag.* 1987, 51, 3-19.
45. Nudelman, H.; Zarivach, R. Structure prediction of magnetosome-associated proteins. *Front. Microbiol.* 2014, 5.
46. Rahn-Lee, L.; Komeili, A. The Magnetosome Model: Insights into the Mechanisms of Bacterial Biomineralization. *Front. Microbiol.* 2013, 4.
47. Galloway, J. M.; Arakaki, A.; Masuda, F.; Tanaka, T.; Matsunaga, T.; Staniland, S. S. Magnetic bacterial protein Mms6 controls morphology, crystallinity and magnetism of cobalt-doped magnetite nanoparticles in vitro. *J. Mater. Chem.* 2011, 21, 15244-15254.

CHAPTER 5. SELF-ASSEMBLY OF DNA FUNCTIONALIZED GOLD NANOPARTICLES AT THE LIQUID-VAPOR INTERFACE

Modified from a paper published in *Advanced Materials Interfaces*[¶]

Honghu Zhang, Wenjie Wang, Noah Hagen, Ivan Kuzmenko, Mufit Akinc, Alex Travesset, Surya Mallapragada, and David Vaknin[*]

5.1 Abstract

Surface sensitive synchrotron X-ray scattering and spectroscopy are used to monitor and characterize the spontaneous formation of two-dimensional (2D) Gibbs monolayers of thiolated single-stranded DNA-functionalized gold nanoparticles (ssDNA-AuNPs) at the vapor–solution interface by manipulating salt concentrations. Grazing-incidence small-angle X-ray scattering and X-ray reflectivity show that the non-complementary ssDNA-AuNPs dispersed in aqueous solution spontaneously accumulate at the vapor–liquid interface in the form of a single layer by increasing $MgCl_2$ or $CaCl_2$ concentrations. Furthermore, the mono-particle layer undergoes a transformation from short- to long-range (hexagonal) order above a threshold salt-concentration. Using various salts at similar ionic strength to those of $MgCl_2$ or $CaCl_2$ such as, NaCl or $LaCl_3$, we find that surface adsorbed NPs lack any order. X-ray fluorescence near total reflection of the same samples provides direct evidence of interfacial gold and more importantly a significant surface enrichment of the cations. Quantitative analysis reveals that divalent cations screen the charge of ssDNA, and that the hydrophobic hexyl-thiol group, commonly used to functionalize

---

[*] Corresponding Author: vaknin@ameslab.gov

the ssDNA, (for capping the AuNPs) is likely the driving force for the accumulation of the NPs at the interface.

5.2 Introduction

Although by now a plethora of various nanoparticles (NPs) can be produced in large quantities, manipulating and organizing them into hierarchical functional structures remains a challenge.[1–9] Naturally, the primary route to overcome this challenge has been to explore conditions that allow controlled self-assembly either by manipulating the medium in which the NPs are embedded in and/or by functionalizing them with "smart programmable molecules" (complementary single-stranded DNA, for instance).[1–9] Specifically organized two- and three-dimensional (2D and 3D) NPs have been highly desirable to theoretical engineers who conceive metamaterials with novel photonic, electronic and magnetic properties where the NPs play similar roles to those of atoms in functional materials such as, insulators, semiconductors, or metals.[8,10–18] Major advances have been made in the last decade in laying out engineering rules for crystallization of 3D[1,2,4,6,19–25] and 2D[5,26–30] superlattices; however the stability, scale of production, and specific organization are hurdles that need to be overcome to render these assemblies technological viability. These shortcomings can in part be affected by refocusing the exploration to fundamental understanding of molecular length scale mechanisms involved in self-assembly. The 2D self-assembly into long- or short-range order to a certain extent lessens the complexity inherent in 3D systems providing a suitable playground to unraveling the underlying interactions that can in turn be employed to the assembly process in 1D, 2D, and 3D structures. Indeed, it has been demonstrated that single-stranded DNA-functionalized AuNPs (ssDNA-AuNPs) can form so-called Gibbs layers by controlling salt concentrations and even spontaneously crystallize as 2D hexagonal

structures at the vapor/solution surfaces.[27,28] However, the mechanism by which these DNA-complexed AuNPs (or any other DNA-complexed NPs) migrate to the vapor/aqueous interface, or the forces that lead to crystallization have not been fully addressed yet. We have undertaken this synchrotron X-ray study to answer these questions and to determine the interactions that lead to the spontaneous accumulation and crystallization of ssDNA-AuNPs by manipulating salt concentrations. More details on the preparation of the materials, their characterization and the methods we use are provided in the Experimental Section below and in the Supporting Information online. Whereas Campolongo and coworkers use parallel small-angle X-ray scattering (parSAXS) from a drop-vapor interface[27,28] (1.5 μL droplet) which can be complicated by bulk scattering requiring spatial mapping of a solution droplet profile, we have adopted a more direct grazing-incidence SAXS (GISAXS) approach by scattering from a flat solution surface (60 × 60 mm^2) using a specialized liquid surfaces spectrometer. Furthermore, in addition to in-plane diffraction from the surface, our experimental setup expands on previous studies by enabling us to directly measure the reflectivity from the surface and more importantly to collect X-ray fluorescence near total reflection of specific emission lines from interfacial atoms[31] that allow valuable quantification of surface density of the NPs and density profile of the ions that induce the migration of the DNA-capped to the surface.

5.3 Results and Discussion

5.3.1 2D hexagonal superlattice induced by magnesium ions

Figure 5.1 shows GISAXS patterns as functions of Q_y and Q_z from non-complementary ssDNA-AuNPs in aqueous suspension with incident beam below the critical angle ($\alpha_c = 0.091$ deg.) for total reflection of evanescent wave with finite penetration depth

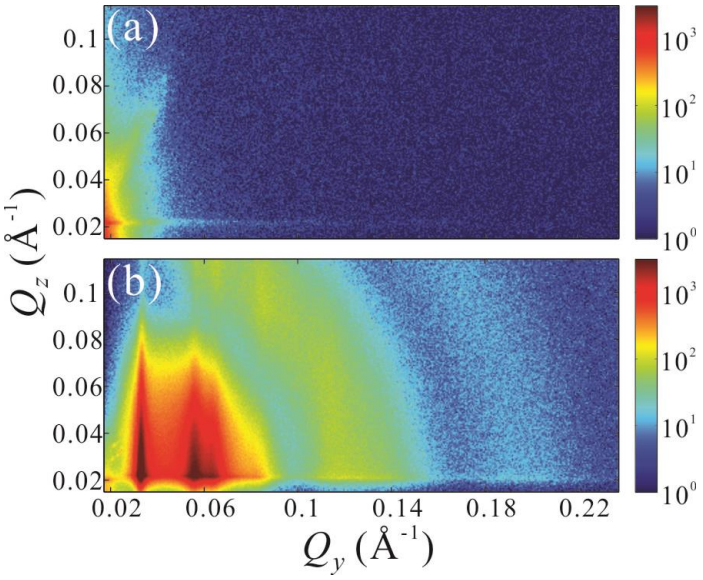

Figure 5.1 GISAXS patterns as functions of Q_y and Q_z for aqueous solutions of ssDNA-AuNPs (a) in the absence of salts and (b) in the presence of 50 mM $MgCl_2$. Intensities are displayed on logarithmic scales.

into the bulk solution, without salt (a) and with salt (b) in solution. In the presence of 50 mM $MgCl_2$ (Figure 5.1b), the pattern exhibits sharp rods due to the formation of a 2D crystalline Gibbs layer, and broad circular features associated with the form factor of the AuNPs, while no such features are observed in the pattern without any salts (Figure 5.1a). A linecut profile along Q_y direction at the critical angle from the pattern in Figure 5.1b are shown in Figure 5.2a along with a SAXS intensity profile of the bare AuNPs in bulk (obtained separately on a different instrument). Figure 5.2b shows the linecut at the low Q_y range (Q_y < 0.1 Å^{-1}). A fundamental diffraction peak (Q_1 = 0.0331 Å^{-1}) is followed by peaks with calculated relative positions to Q_1 at $Q_i/Q_1 \approx 1{:}\sqrt{3}{:}\ \sqrt{4}{:}\sqrt{7}$ (i = 1−4) indicating the formation of a 2D hexagonal crystalline structure (indexed (10), (11), (20) and (21) reflections) with an average inter-particle distance $a = 4\pi/(\sqrt{3}Q_1)$ = 220 Å. Based on the *FWHM* (full-width-at-half-maximum) of the first diffraction peak ($FWHM_{(10)} \approx 0.0028$ Å^{-1}) and the superior resolution function of the spectrometer, we estimate the average crystalline diameter to be on the order of 2200 Å implying long-range 2D crystalline structure that extends to about 10 × 10 unit cells. In Figure 5.2a, the broad features

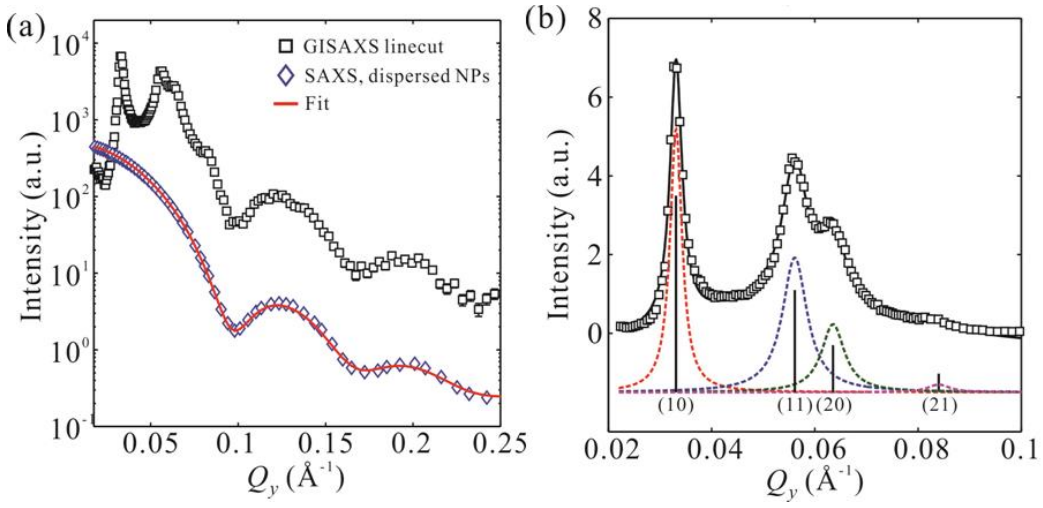

Figure 5.2 (a) A horizontal linecut profile (black squares) along Q_y direction at critical angle ($\alpha_f = \alpha_c = 0.091$ deg.) integrated over $\Delta Q_z = 6\times10^{-4}$ Å^{-1} in the GISAXS 2D pattern for a Gibbs monolayer of ssDNA-AuNPs mixed with 50 mM $MgCl_2$ (Figure 5.1b). Aslo shown is a SAXS pattern (blue diamonds) from bare AuNPs dispersed in aqueous solution prior to functionalization with ssDNA with a best fit (red solid line) using a form factor of spherical particles with polydispersity described by a Gaussian distribution. Similar form factor of spherical nanoparticles is observed in the linecut profile of the GISAXS pattern. The size distribution of AuNPs estimated by the best fit is $D = 8.9 \pm 0.8$ nm. (b) The GISAXS linecut profile at low Q_y range (0.02−0.1Å^{-1}), along with best fit (black solid line) to Lorentzian-shaped Bragg peaks and the corresponding peak components (dash lines). The peaks positions ratios with respect to the fundamental diffraction peak of ~1:√3: √4:√7 is consistent with a hexagonal packing of nanoparticles with corresponding diffraction indices (10), (11), (20), and (21). The plots in (a) are vertically shifted for clarity.

associated with the form factor that extends to larger Q_y (≈ 0.25 Å^{-1}) match those of the bare (uncapped) AuNPs strongly suggesting that the electron density of the ssDNA envelop (or corona) capping the AuNPs is not significantly different than that of the solution surrounding it. This indicates that the scattering from the surface is a superposition of crystalline and non-crystalline ssDNA functionalized AuNPs as demonstrated in Figure 5.2a. Indeed, in the absence of $MgCl_2$ in solution of the same ssDNA-AuNP concentration a corresponding linecut in Figure 5.3a does not show evidence of form-factor features as those shown in Figure 5.2a indicating that the non-complementary ssDNA-AuNPs are well dispersed in the aqueous solution and do not

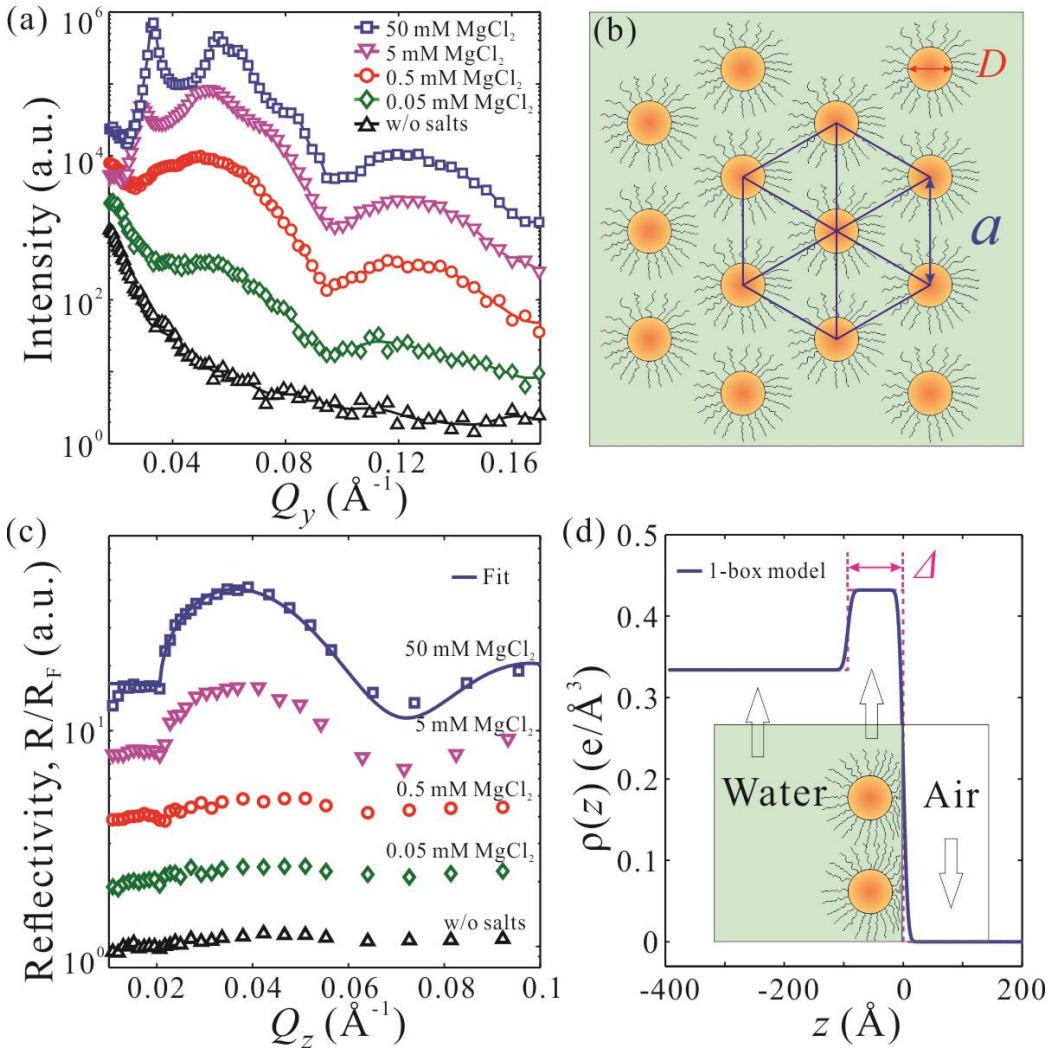

Figure 5.3 Increase of $MgCl_2$ concentrations (0.05−50 mM) promotes formation of a 2D long-range ordered hexagonal superlattice of non-base-pairing ssDNA-AuNPs (based on GISAXS) with a mono-particle thickness (based on XRR). (a) GISAXS linecut profiles along Q_y direction at various $MgCl_2$ concentrations as indicated and (b) a schematic depiction of the lateral packing of non-base-pairing ssDNA-AuNPs at 50 mM $MgCl_2$. (c) Normalized XRR from Gibbs monolayers of non-base-pairing ssDNA-AuNPs at various $MgCl_2$ concentrations as indicated and (d) the electron density profile across the interface obtained from the best fit to the XRR at 50 mM $MgCl_2$ shown in (c). The inset in (d) is an illustration of the surface-normal structure of the 2D superlattice. The plots in (a) and (c) are vertically shifted for clarity.

populate the surface without the addition of salt. Figure 5.3 shows the evolution of the formation of the crystalline Gibbs monolayer as a function of the $MgCl_2$ concentration as it is probed by the GISAXS (Figure 5.3a) and by X-ray reflectivity (XRR) (Figure 5.3c) from the same samples.

Both the GISAXS and the XRR show that gradual increase of salt concentration induces steady migration of capped-AuNPs to the surface. At concentrations of ~5 mM short-range order sets in and at threshold of ~50 mM, long-range order domains are formed, albeit with dispersed uncorrelated particles as discussed above.

Analysis of the X-ray reflectivity measurements in terms of a single layer yields[31,32] the best fit (solid line Figure 5.3c) with average layer thickness $\Delta \approx 93$ Å, electron density $\rho_e \approx 0.432$ $e \cdot Å^{-3}$, and surface roughness $\sigma \approx 6.0$ Å. The layer thickness is close to the diameter of the gold nanoparticles (89 ± 8 Å) confirming the formation of a mono-particle layer at the vapor/liquid interface. Based on the extracted ρ_e, we estimate the average crystalline coverage on the surface at ~25% at the highest salt concentration (see SI for details). Using $CaCl_2$ in solution, to induce the formation of ssDNA-AuNP Gibbs layer, yields practically the same behavior as that of $MgCl_2$ (see below and see SI).

Similar results using an equimolar mixture of two types of ssDNA-AuNPs with a complementary base-pairing region at the end of ssDNA by adjusting $MgCl_2$ concentrations are shown in Figure 5.4. GISAXS and X-ray reflectivity data clearly indicate salt-driven surface-enrichment of the capped-AuNPs with a threshold concentration ~0.5 mM $MgCl_2$ needed to induce short-range in-plane order. However, even for higher salt concentrations, GISAXS and X-ray reflectivity reveal in-plane and out-of-plane features different from those of the non-complementary ssDNA-AuNPs monolayer. First, only short-range hexagonal order is observed in the GISAXS linecut profile (Figure 5.4a). It is worth noting that the highest tested $MgCl_2$ concentration is 5 mM as the base-paired ssDNA-AuNPs form large visible precipitates at higher salt concentrations. At 5 mM $MgCl_2$ the average inter-particle distance a is ~210 Å (Q_1 = 0.0342 $Å^{-1}$) in a short-range hexagonal ordering (Figure 5.4b), just slightly smaller than a ~260 Å for

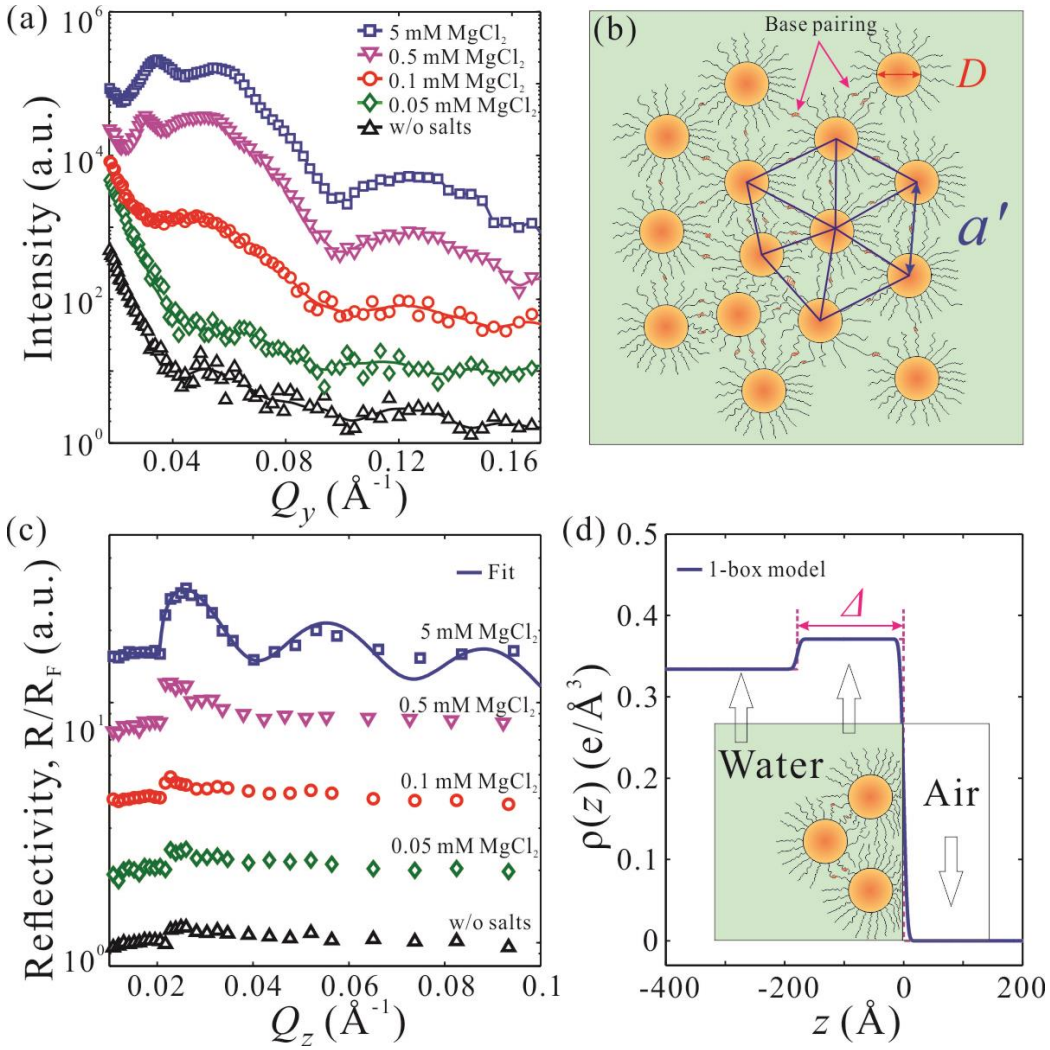

Figure 5.4 Increase of $MgCl_2$ concentrations (0.05−5 mM) promotes formation of a 2D short-range ordered superlattice of base-pairing ssDNA-AuNPs (based on GISAXS) with a nearly two-particle thickness (based on XRR). (a) GISAXS linecut profiles along Q_y direction at various $MgCl_2$ concentrations as indicated and (b) a schematic depiction of the lateral packing of base-pairing ssDNA-AuNPs at 5 mM $MgCl_2$. (c) Normalized XRR from Gibbs monolayers of base-pairing ssDNA-AuNPs at various $MgCl_2$ concentrations as indicated and (d) the electron density profile across the interface obtained from the best fit to the XRR at 5 mM $MgCl_2$ shown in (c). The inset in (d) is an illustration of the surface-normal structure of the 2D superlattice. The plots in (a) and (c) are vertically shifted for clarity.

non-base-paired at 5 mM salt. As discussed above, we estimate the average domain size in the short-range order regime to be 2 × 2 unit cells as the grain size is on the order of 500 Å ($FWHM_{(10)} \approx 0.0120$ Å^{-1}). The decrease of inter-particle distance indicates interdigitation as

partial base-pairing takes place among the particles. This is also verified in the bulk by SAXS measurements as shown in Figure S5.3 of the SI. This attraction has an effect on multilayering the film at the interface as is evidenced by the XRR shown in Figure 5.4c. The XRR shows well-defined fringes (at 5 mM $MgCl_2$) with a decrease in period compared to that shown in Figure 5.3c, corresponding to a thicker layer. The best fit parameters (solid line in Figure 5.4c) are $\Delta \approx$ 180 Å, $\rho_e \approx 0.37$ e·Å^{-3}, and $\sigma \approx 4.8$ Å. Contrary to the mono-particle layer of non-complementary ssDNA-AuNPs, the electron density profile shows that the nanoparticle film is thicker and likely consists of two particle-layers (the diameter of a bare AuNP $D = 89 \pm 8$ Å) as expected from the binding of complementary nanoparticles (Figure 5.4d). The reduction in electron density of this simple model, compared to the non-complementary system, is likely due to the fact that the second layer is incomplete.

5.3.2 Effect of cations with different valences

Although the assembly of complementary ssDNA-AuNPs into 3D crystalline structures requires the presence of NaCl,[1,2,4,8,9,19] for the 2D Gibbs monolayer of non-complementary ssDNA-AuNPs, it has been demonstrated that $MgCl_2$ as well as NaCl at various ionic strengths can also induce 2D crystallization.[28] The use of $MgCl_2$ is driven by its function in biological systems, but its role in the interfacial accumulation and crystallization of ssDNA-AuNPs still remains unknown. To better understand its role, we explore the effect of various mono and multivalent ions at same ionic strength as that of $MgCl_2$ concentration that induces the crystallization of the Gibbs layer. Figure 5.5 shows liquid surface GISAXS patterns of four salts (NaCl, $MgCl_2$, $CaCl_2$, $LaCl_3$) at the same level of ionic strength (~150 mM). Whereas NaCl or $LaCl_3$ do not show ordered structures at the interface (Figure 5.5b-c), with $CaCl_2$ we find that the GISAXS patterns, and evolution of the Gibbs monolayer as a function of $CaCl_2$ is practically the same as those obtained by adding $MgCl_2$ (see more details in Figure S5.2 in the

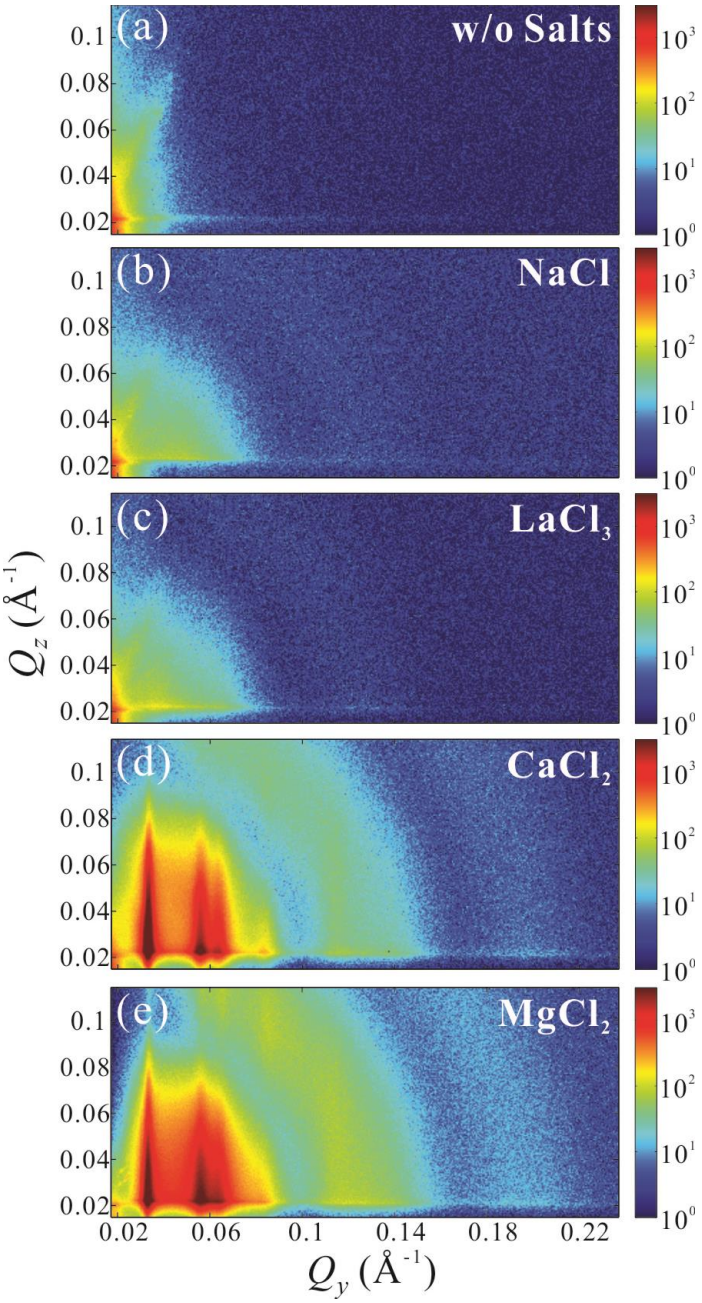

Figure 5.5 GISAXS patterns of non-base-pairing ssDNA-AuNPs in the absence of salts (a), and in the presence of (b) NaCl, (c) $LaCl_3$, (d) $CaCl_2$ and (e) $MgCl_2$ at the same ionic strength (IS ≈ 150 mM). The mixture of ssDNA-AuNPs and $LaCl_3$ are found to form precipitates. Intensities are displayed in logarithmic scales.

SI). We find that the ssDNA-AuNP superlattices induced by both divalent salts exhibit long-range hexagonal order with a practically identical lattice parameter ($a \approx 220$ Å) and grain size (2200−2400 Å) clearly demonstrating that these two divalent ions play a similar role in migrating and crystallizing the capped AuNPs to the liquid interface.

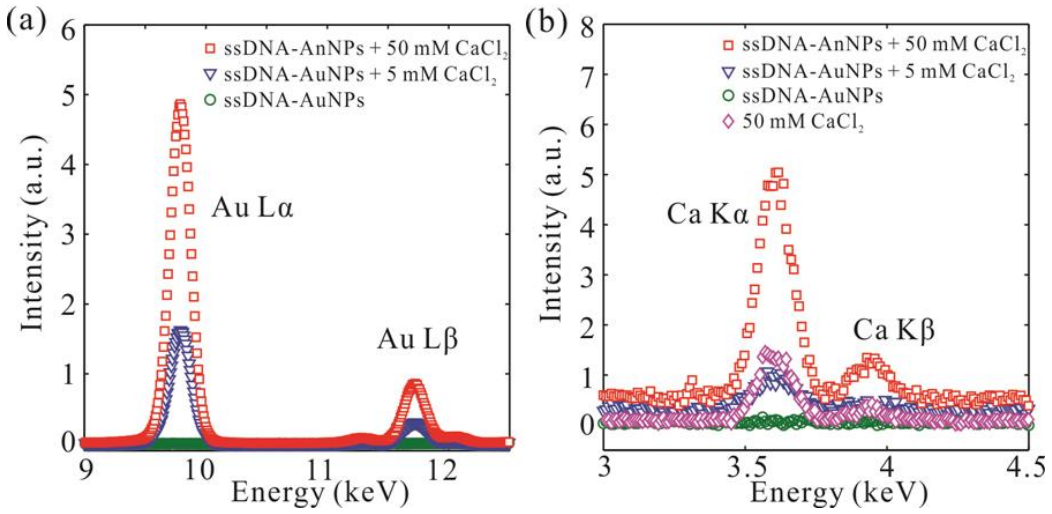

Figure 5.6 Fluorescence signals of (a) gold and (b) calcium (of same samples) integrated below the critical angle α_c from Gibbs monolayers of non-base-pairing ssDNA-AuNPs at the air-liquid interface for various $CaCl_2$ concentrations (5 mM and 50 mM) as indicated. A 50 mM $CaCl_2$ solution without any ssDNA-AuNPs and an ssDNA-AuNPs solution without $CaCl_2$ are used as references (for control and also for calculating surface density of ions at the interface). Each point of intensity is an integration over Q_z = 0.015−0.018 $Å^{-1}$.

The observation that the $CaCl_2$ induces self-assembly that is practically identical to that of $MgCl_2$ allows us to further explore the 2D Gibbs phenomena with the X-ray fluorescence technique near total reflection to directly and element-specifically quantify the interfacial ions. This is important, in view of the fact that it is impractical to apply this technique to Mg^{2+} since the emission-line signals from Mg (Kα = 1.25 keV, Kβ = 1.07 keV) are beyond the detection limit of the Vortex EDD as it is set up in our study. The X-ray fluorescence spectra below the critical angle α_c (at Q_z = 0.015−0.018 $Å^{-1}$) with non-base-paired ssDNA-AuNPs and in the absence and presence $CaCl_2$ are shown in Figure 5.6 in the energy range of L emission lines of Au (a) and K emission lines of Ca (b). At $\alpha_i < \alpha_c$, the evanescent X-ray wave (at Q_z = 0.015−0.018 $Å^{-1}$) penetrates into the solution only to a very shallow depth (less than 100 Å) along the surface-normal. Figure 5.6a shows the Lα and Lβ emission lines from gold for ssDNA-AuNPs dispersed in 0, 5 and 50 mM $CaCl_2$. Whereas the signal from Au is not detectable without $CaCl_2$, it shows strong enhancement when the salt is added, providing direct

evidence of the interfacial accumulation of ssDNA-AuNPs within the penetration depth of the X-ray beam. Meanwhile for the same samples, the corresponding calcium signals (Kα and Kβ emission lines) are also observed (Figure 5.6b) with intensities of same trend as that of Au with the increase $CaCl_2$ concentration. This indicates that the Ca^{2+} ions migrate with the ssDNA-AuNPs to the surface riding on the charged backbone of the ssDNA screening the charges of the PO_4^- groups on it. In Figure 5.6b, a 50 mM $CaCl_2$ solution without any ssDNA-AuNPs (magenta diamond symbols) is used as a reference to calibrate the spectral intensity of calcium. We generally find that the signal from bulk ions scales with the concentration, so for the 5 mM salt solution we expect a decrease by a factor of 10 compared to that with 50 mM. Notably, the calcium signal intensity from the interface of ssDNA-AuNPs solution mixed with 5 mM $CaCl_2$ is almost comparable to that of the pure 50 mM $CaCl_2$ solution (without AuNPs), suggesting an increase of the molarity at the interface to about 50 mM (i.e., an increase by factor of 10). Assuming that ions are homogeneously distributed in the thin illuminated layer, the surface concentration of ions can be quantified by integrating the intensity over its energy range and normalizing to a reference of known concentration.[31] The surface concentration of calcium is estimated at 27 mM and 164 mM at the interfaces with ssDNA-AuNPs in the presence of 5 mM and 50 mM $CaCl_2$, respectively.

Table 5.1 Parameters of 2D superlattice of non-base-pairing ssDNA-AuNPs induced by $MgCl_2$ and $CaCl_2$.

Parameters of the ssDNA-AuNP superlattice	5 mM $MgCl_2$	50 mM $MgCl_2$	50 mM $CaCl_2$
Lattice parameter of 2D superlattice, *a*	~26 nm	~22 nm	~22 nm
Grain size	~75 nm	~220 nm	~240 nm
Diameter of AuNPs, *D*	8.9 ± 0.8 nm	8.9 ± 0.8 nm	8.9 ± 0.8 nm
Number of DNA chains per ssDNA-AuNP, Σ	40−60[29,30]	40−60[29,30]	40−60[29,30]
Number of Ca^{2+} cations per ssDNA-AuNPs	NA	NA	380−1570
Number of Ca^{2+} cations per DNA base	NA	NA	0.15−0.62

The corresponding parameters of the 2D superlattices measured by GISAXS, X-ray reflectivity and X-ray fluorescence are presented in Table 5.1. Albeit with different parameter space (i.e., DNA sequence, particle size, salt species and concentrations), the trends that crystallinity increases and lattice constants decrease with salt concentration are similar to a recent study.[28] Notice that for the lower concentration (5 mM) the lattice constant is significantly larger than that observed with 50 mM, which is consistent with our explanation below, i.e., at this concentration the DNA is not yet fully neutral and Coulomb repulsion forces make the DNA arms extend and effectively increase the area per particle, as also evidenced in the dynamic light scattering results (See SI). In the 2D ssDNA-AuNP superlattice layer there are approximately 0.15−0.62 Ca^{2+} ions associated with each DNA base, suggesting that the divalent cations roughly balance the charge of the phosphate backbones of the DNA chains.

Although charge screening of DNA chains may lower the solubility of ssDNA-AuNPs, this by itself cannot drive the capped-NPs to the surface. To confirm that, we have conducted control experiments (X-ray reflectivity and fluorescence of Ca), with pure single-stranded DNA (same sequence without thiol modification as that used to functionalize the AuNPs) in solution and found that the addition of $CaCl_2$ to the solution (even close to 1 M $CaCl_2$) does not drive the DNA to the surface. So, the question is, what drives the ssDNA-AuNP-Ca complex to the surface and what is mechanism by which it crystallizes? It is worth noting that the thiol modification at the end of a DNA always contains a short hydrophobic carbon chain (in our case, $-(CH_2)_6-$) in all research related to ssDNA-AuNPs (Table S5.1), and the cumulative effect on each ssDNA-AuNP is equivalent to 40−60 carbon chains. We argue that, by adding salt to the solution and screening charges on the DNA, the net effect is a gradual predominance of hydrophobic effects. That is, the hydrophobicity of the carbon chains becomes dominant after charge screening the soluble DNA, leading to the formation of a Gibbs layer of ssDNA-AuNPs. Thus, the interfacial accumulation of ssDNA-AuNPs results from the hydrophilic

polyelectrolyte-like properties of DNA and the presence of hydrophobic carbon chains. We hypothesize that the interface becomes saturated as the hydrophobic hydrocarbon chains outbalance the affinity of DNA to water at the threshold concentration that induces 2D crystallization. Now, we estimate the critical salt concentration at which ssDNA-AuNPs become completely insoluble. In the ssDNA-AuNPs solution, water molecules are in contact with the Au core and fully solvate the hydrocarbon chains (See details in SI). The difference in chemical potential for transferring alkane from water to air is estimated from the surface tension of hydrocarbons $\gamma_s \approx 50$ mJ·m^{-2}. With a hydrocarbon van der Waals radius, r_{vdW} , of ~2 Å, it gives a surface area of *m*-hydrocarbons $A_m = 2\pi m r_{vdW} l_{CH2}$ when considering a carbon chain as a cylinder ($l_{CH2} \approx 1.27$ Å, $A_6 \approx 96$ Å^2 for $-(CH_2)_6-$), thus the free energy per chain for transferring from water to air,[33]

$$\Delta G_{hydro} \approx \gamma_s A_m = cmk_B T \tag{5.1}$$

where $c = 1.94$, k_B is the Boltzmann's constant, $T = 298$ K. The electrostatic free energy, which favors solubility of DNA, is estimated as

$$\Delta G_{elec} \approx n\left(k_B T \log\left(X_i\right) + \frac{|q_1 q_2|}{4\pi\varepsilon_0 \varepsilon_r d_{min}} \right) \tag{5.2}$$

where n is the number of bases in ssDNA, X_i is the molar fraction of the salt in water, q_1 and q_2 are charges of cations and the PO_4^- group in the DNA, ε_0 is vacuum permittivity, $\varepsilon_r = 78.5$ is relative permittivity of water at 298 K, and d_{min} is the minimum distance between the cation and the PO_4^- group (the sum of two ionic radii). This is a generalization of a similar argument used to compute the solubility of simple salts.[33] The critical salt concentration above which all nanoparticles will transfer to the interface occurs when $\Delta G_{hydro} + \Delta G_{elec} = 0$, yielding a threshold salt concentration for crystallization

$$\left[\text{salt}\right]_c = 55.5\text{e}^{-\frac{cm}{n} - \frac{|q_1 q_2|}{4\pi\varepsilon_0 \varepsilon_r d_{min} k_B T}} \tag{5.3}$$

where the constant 55.5 is a conversion to mole per litter. The calculated critical concentration for different salts are listed in Table 5.2, using the ionic radii from Ref. 34 (we use the radius of the OH^- group, 1.33 Å, to represent the O^- in the PO_4^- anion). These values give fairly reasonable estimates, which are comparable to the experimental values obtained at concentrations that induce crystallization. Overall, these calculations are less sensitive to the number of bases per chain, *n*, but more to ionic radii and valence. We note that the concentration of $LaCl_3$ we used (based on the ionic strength of $MgCl_2$) is much higher than the calculated critical concentration for which precipitates of NPs form and no surface crystallization is observed (see Figure 5.5). By contrast, adding NaCl at ionic strength (150 mM) is too low to induce the 2D crystallization (see Figure 5.5) as shown in Table 5.2.

Table 5.2 Measured and calculated critical solubility concentration (in M) for ssDNA-AuNPs with n = 50 bases in DNA chains using Equation 5.3.

Cations	Calculated	Measured
Na^+	2.1	~1.2−2.1[28]
Ca^{2+}	0.096	0.05
Mg^{2+}	0.042	0.05
La^{3+}	0.0054	NA

As for the crystallization of the ssDNA-AuNP-Ca complex we argue that it results from electrostatic correlations among interdigitated salt-neutral DNA strands in similar fashion to ionic crystals. For overall neutral (see Table 5.1) but charged nanoparticles, the energy is minimized when charges are as closely packed together as possible. Thus, nearest neighbor nanoparticles will experience an electrostatic attractive force (See more details in SI).

There are a few consequences to our study: 1. The common functionalization of AuNPs with thiolated-ssDNA introduces hydrophobic/hydrophilic character to the complexed DNA-AuNPs that by regulating salt concentration or pH can drive the complex to the surface. There is a gradual enrichment of capped-AuNPs with the increase of divalent salt such that at minute salt concentrations the particles

at the aqueous surface are not correlated. Increasing the salt concentrations enriches the surface further and the particles exhibit short-range order, and above a threshold concentration (~50 mM for divalent ions) 2D crystallization occurs. We note that the lattice constant gradually shrinks with the increase of salt concentration as the DNA becomes more and more neutral and repulsive electrostatic forces between DNA arms become weaker. 2. The reasonable agreement of calculated and measured critical salt concentration for crystallization at the surface strongly suggests for the non-complementary ssDNA-AuNP system the DNA plays electrostatic role with similar outcome if it is replaced by a simpler polyelectrolyte, consistent with conclusions of a recent study.[28] We note that in this study we used ssDNA of one length, but intuitively and inspection of Equation 5.3 clearly shows that the threshold crystallization concentration scales with the length of the DNA; namely, the longer the DNA is, the more salt is required for crystallization. In addition, we expect the lattice constant in the short- and long-range order phases to scale with the DNA length, as reported by other groups with similar material systems.[27–29] 3. Electrostatic correlations among interdigitated ssDNA induce an attractive interaction that drives the 2D crystallization. These electrostatic interactions, however, are too weak against DNA hybridizations driven by complementary strands when those are present. It is worth noting that all procedures for 3D crystallization ssDNA-AuNPs with complementary base-pairing require temperature cycling up to the melting temperature of base-paired DNA. We have not conducted such temperature cycling procedure.

5.4 Conclusion

Using surface-sensitive grazing incidence X-ray scattering and spectroscopic techniques, we have determined the role that salts play in inducing spontaneous formation of Gibbs monolayers from solutions of ssDNA-AuNPs at the vapor-liquid interface. GISAXS and XRR results demonstrate that for ssDNA-AuNPs, without complementary partners, gradual increase of the divalent ion (Mg^{2+} and

Ca^{2+}) concentrations steadily increases the migration of the particles to the surface and that beyond a threshold concentration, the mono-particle layer transforms from short- to long-range-in-plane order, consistent with a recent study that used similar ssDNA-AuNPs.[28] X-ray fluorescence provides quantitative cation enrichment at the surface that is correlated with charge screening of the DNA. Charge screening of DNA with cations, and the hydrophobicity of ssDNA-AuNPs due to the hydrocarbon chains accompanying the thiol group that modifies the DNA, account for the interfacial accumulations of nanoparticles. We also find that for the same ionic strength, monovalent (NaCl) and trivalent ($LaCl_3$) salts are much less effective than their divalent counterparts ($MgCl_2$ and $CaCl_2$) in migrating and inducing 2D crystallization. According to our measurements and model estimates, the formation of the Gibbs layer is not a function of the ionic strength but results from an interplay between hydrophobic forces and counterion polyelectrolyte electrostatics for which quantitative arguments are provided in this manuscript. Whereas crystallization with relatively long-range 2D order develops in the presence of divalent cations for ssDNA-AuNPs with non-base-paired partners, for complementary base-paired ssDNA-AuNPs solution, only 2D short-range ordering is observed with two interfacial layers. The main message of this study is that there is a hydrophobic "price" to adding the thiol group to ssDNA to functionalize AuNPs that may inadvertently affect the outcomes (favorable or not), nevertheless pointing to a new direction, where hydrophobicity and electrostatic (i.e., hydrocarbons and polyelectrolytes) can be used cooperatively to design and control organic and inorganic structures and their functions at interfaces.

5.5 Experimental Section

5.5.1 Sample preparation

Gold nanoparticles of 10 nm nominal diameter were purchased from Ted Pella and their actual distribution size measured by small-angle X-ray scattering (SAXS) is determined to be 8.9

± 0.8 nm (see details in Figure 5.2a). The 5'-thiolated single-stranded DNA was purchased from Integrated DNA Technologies as disulfides and the sequences are shown in Table S5.1. The single-stranded DNA functionalized gold nanoparticles (ssDNA-AuNPs) were synthesized according to published procedures[19,35–37] with slight modifications. Briefly, the disulfide was first cleaved in 50 mM dithiothreitol (Pierce Biotechnology, Thermo Scientific) solution for 30 min, followed by purification on a freshly flushed NAP-5 column (Sephadex G-25 DNA grade, GE Healthcare) with Millipore water (18.2 MΩ·cm). The cleaved thiolated ssDNA was quantified with a UV–visible spectrophotometer and then mixed with gold nanoparticles in an approximate ssDNA/AuNP molar ratio of 300. The mixture of AuNPs and thiolated ssDNA was allowed to incubate in a non-buffered solution at room temperature under orbital shaking for about half a day. The mixture of ssDNA and nanoparticles were buffered with a phosphate buffer (100 mM phosphate, pH 7.0) and the phosphate concentration was brought up to 10 mM. The mixture was annealed at room temperature for about 2 hours. In the salting process, the NaCl concentration of the mixture was initially increased to 0.025 M with another phosphate buffer (10 mM phosphate, 2 M NaCl, pH 7.0). The solution was sonicated for 10 seconds, followed by a 1-hour incubation period at room temperature. Then the buffer containing 2 M NaCl was added to the mixture stepwise so that the NaCl concentration was gradually increased to 0.1 M with 0.025 M increments for each step, and finally to 0.5 M with every 0.05 M increments. Each step also consists of 10-seconds sonication and additional 30-min incubation. The final mixture was aged at room temperature with orbital shaking for one day to allow for maximum DNA loading. The as-prepared ssDNA-AuNPs were washed with Millipore water at least three times with centrifugation (at 20000 g × 1 hour). The concentration of ssDNA-AuNPs was determined by

UV–vis analysis. The number of ssDNA chains loaded on each AuNP was reported to be 40–60 for the thiolated ssDNA and similar size AuNPs used in this work.[29,30]

5.5.2 Liquid surface X-ray scattering setup

A home-built square Teflon trough (60 mm × 60 mm) containing ssDNA-AuNPs solutions is placed in a sealed enclosure for X-ray scattering measurements. Typically, 9 mL of 4–5 nM ssDNA-AuNPs dispersed in Millipore water is added to the trough and the salt concentration is elevated to a certain level with high concentration salt solution. The chamber is sealed and air is displaced by flowing water-saturated helium to minimize radiation damage and reduce background scattering from air. Meanwhile, the ssDNA-AuNPs-salt-solution is allowed to equilibrate for ~30 min, and the trough is continuously purged with water-saturated helium to

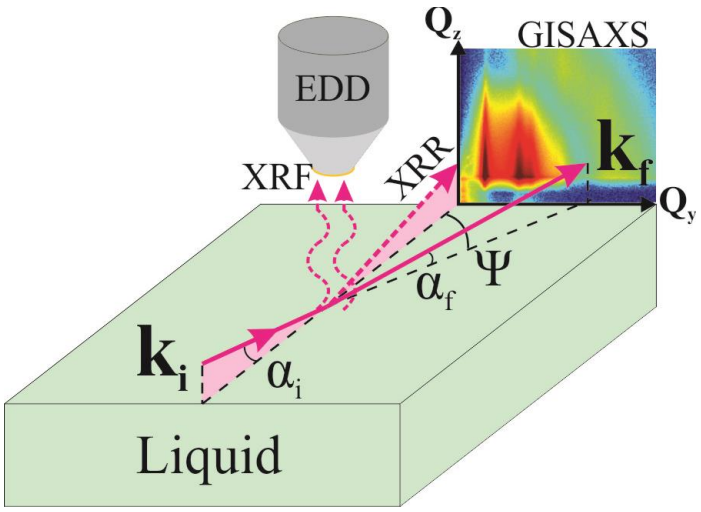

Figure 5.7 A schematic of the experimental setup of liquid surface X-ray scattering measurements for 2D self-assembly of nanoparticles at the air-liquid interface. A monochromatic X-ray beam with the wavevector k_i illuminates the liquid surface at an incident angle with respect to the surface, α_i. The beam is scattered by the electron density variations at the surface and displayed at a corresponding exit angle α_f and in-plane scattering angle ψ. The grazing incidence small-angle X-ray scattering (GISAXS) pattern is collected by an area detector. The X-ray reflectivity (XRR) ($\alpha_f = \alpha_i$, $\psi = 0°$) is recorded using a point detector and expressed as a function of Q_z, ($Q_z = 4\pi \sin \alpha_i / \lambda$). The X-ray fluorescence (XRF) excited from the surface is measured at different Q_z values with an energy dispersive detector (EDD) which collects the emitted signals along the surface-normal direction.

maintain a low oxygen level. Then, a highly monochromatic and collimated X-ray beam illuminate the liquid surface at an incident angle of α_i to obtain GISAXS, X-ray reflectivity and fluorescence (see Figure 5.7).

The 9ID-B liquid surface spectrometer (LSS) at the Advanced Photon Source (APS), Argonne National Laboratory was used for this study and was tuned to a monochromatic beam E = 13.474 keV (wavelength λ = 0.920 Å; and wave-vector k_0 = 6.8295 $Å^{-1}$). The illustration in Figure 5.7 shows the experimental setup that allows a combination of the grazing incidence small-angle X-ray scattering (GISAXS), X-ray reflectivity (XRR) and X-ray fluorescence (XRF) from the same samples. The lateral packing of nanoparticles self-assembly at the interface is determined from the GISAXS at α_i = 0.075 ° for which the scattered beam is collected by a 2D Pilatus100k detector (pixel size 172 μm). The sample-to-detector distance is calibrated with a silver behenate standard. The scattering is displayed as a (Q_y, Q_z) 2D map where $Q_y = 2k_0 \cos\alpha_f \sin(\Psi/2)$ and $Q_z = k_0(\sin\alpha_i + \sin\alpha_f)$ (Figure 5.7). The XRR intensity as a function of Q_z, ($Q_z = 4\pi \sin\alpha_i/\lambda$), measured with a point detector, provides the electron density profile normal to the surface by non-linear least square fit to a model system.[31,32] The combination of GISAXS and XRR presents the in-plane and surface-normal structural evolution of Gibbs monolayer of nanoparticles. Since salts play a critical role in Gibbs monolayer formation, XRF measurements are conducted at different Q_z using a Vortex energy dispersive detector (EDD) and used to determine quantitatively the density of specific ions that migrate from the salt bulk solution to the interface (more details can be found in elsewhere[38]). The fluorescence from pure salt solution in the absence of nanoparticles in solution serves as a reference to calibrate the detected intensity to obtain enriched ion densities at the surface.

5.6 Acknowledgements

The authors thank Xiaobing Zuo for technical support with SAXS measurements conducted at the 12ID-B beamline at the Advanced Photon Source. Research in the Ames Laboratory is supported by the U.S. Department of Energy, Office of Basic Energy Sciences, Division of Materials Sciences and Engineering through Iowa State University under Contract No. DE-AC02-07CH11358. Use of the Advanced Photon Source, an Office of Science User Facility operated for the U.S. Department of Energy Office of Science by Argonne National Laboratory, is supported by the U.S. Department of Energy under Contract No. DE-AC02-06CH11357.

5.7 Supporting Information

5.7.1 Properties of DNA functionalized gold nanoparticles

Table S5.1. The DNA sequences (5' to 3') used in this work. The thiol modification at 5'-end of DNA consists of a thiol group (−SH) and a carbon chain region (−$(CH_2)_6$−). The two types of DNA strands both have 50 bases in total and they share an identical non-base-pairing region of 35 bases including a polythymine spacer (−T_{12}−) bound to the carbon chain. They also contain a complementary region of 15 bases at 3'-end for hybridization with each other.

Type	Sequence (5' to 3')
Thiol modified DNA – A	HS−C_6H_{12}−TT TTT TTT TTT TCG TTG GCT GGA TAG CTG TGT TCT **TAA CCT AAC CTT CAT**
Thiol modified DNA – A'	HS−C_6H_{12}−TT TTT TTT TTT TCG TTG GCT GGA TAG CTG TGT TCT **ATG AAG GTT AGG TTA**

The maximum length of a stretched ssDNA molecule consisting of n bases is nd_b, where $d_b \approx 6.5$ Å, is the length per base. The diameter of ssDNA is $d_s = 10$ Å.

The maximum radius of ssDNA-AuNPs is defined as

$$R_{max} = R_{np} + l_{thiol} + nd_b, \quad \text{(S5.1)}$$

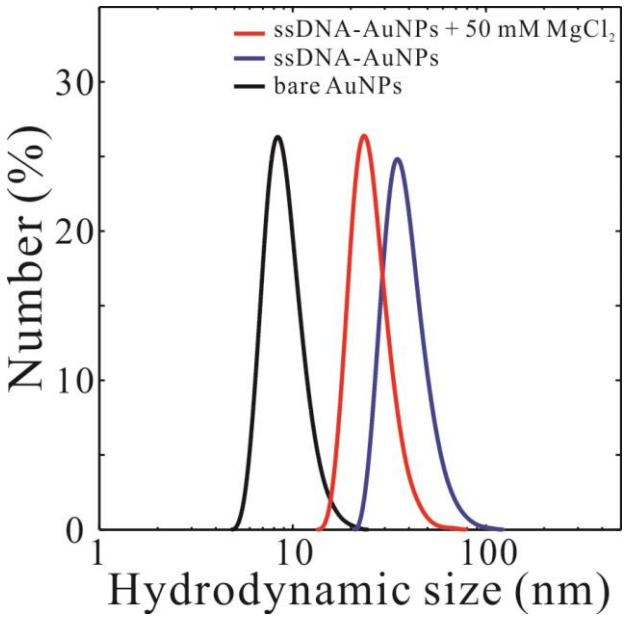

Figure S5.1 Dynamic light scattering (DLS) measurements of nanoparticles under different conditions as indicated.

Table S5.2 Hydrodynamic size of nanoparticles under different conditions measured by DLS.

Nanoparticles	Hydrodynamic (nm)
Bare AuNPs in water	9.2 ± 2.3
ssDNA-AuNPs in water	39.4 ± 11.1
ssDNA-AuNPs in 50 mM $MgCl_2$	25.8 ± 6.5

where R_{np} is radius of bare AuNPs, and l_{thiol} is length of a hexyl-thiol group attached to AuNPs. In this study, the maximum radius of ssDNA-AuNPs with R_{np} = 45 Å, $l_{thiol} \approx$ 10 Å, and n = 50 is estimated as $R_{max} \approx$ 380 Å, or equivalently, a diameter of 76 nm. The diameter of ssDNA-AuNPs dispersed in water measured by dynamic light scattering is 39.4 ± 11.1 nm and the size distribution extends up to 100 nm, which is consistent with the estimated maximum radius R_{max}. But in the presence of $MgCl_2$, the ssDNA-AuNP radius is considerably lower (~26 nm). In the 2D crystals at the liquid interface, the NP radius is more compressed (~ 22 nm).

There are about Σ_{DNA} = 50 DNA strands per NP, which gives a molecular area of DNA on the surface of AuNPs

$$A_c = \frac{4\pi R_{np}^2}{\Sigma_{DNA}} = 5.1 \text{ nm}^2, \quad \text{(S5.2)}$$

which, given the diameter of the DNA (d_s = 1 nm), implies that water is in contact with the Au core and fully solvating the hydrocarbon chains.

5.7.2 Estimating surface density of ssDNA-AuNP crystals

The following estimate of surface coverage of crystalline AuNPs is based on a space filling model using the electron density of one box model ($\rho_e \approx 0.432$ e·Å^{-3}, $\Delta \approx 93$ Å) extracted from the XRR and the 2D crystalline structure determined by GISAXS.

The electron density of pure gold is $\rho_{Au} = 79\rho N_A/M_{Au} = 4.66$ e·Å^{-3}, where $\rho = 19.3$ g·cm^{-3}, $N_A = 6.02\times10^{23}$ mol^{-1} and $M_{Au} = 196.97$ g·mol^{-1} are bulk gold density, Avogadro number and atomic weight of gold, respectively. Assuming that a 2D crystalline AuNP unit cell has a thickness of Δ in the box, the volume fraction of AuNPs is $\phi = V_{np} / (\Delta A_{2D}) \approx 9.5$ %, where the volume of an AuNP is $V_{np} = \pi D^3/6 \approx 3.7\times10^5$ Å^3, and the area of a 2D unit cell is $A_{2D} = \sqrt{3}a^2/2 \approx 4.2\times10^4$ Å^2. Using the space filling model, the electron density of 2D crystalline structure is $\rho_{2D} = \phi\rho_{Au} + (1 - \phi)\rho_w = 0.743$ e·Å^{-3}, where the electron density of pure water is $\rho_w = 0.334$ e·Å^{-3} (assuming the contribution of the DNA strands to the ED is the same as that of water, which is justified by our scattering results). Applying these numbers we find that the surface coverage of crystalline AuNPs is $(\rho_e - \rho_w) / (\rho_{2D} - \rho_w) \approx 25$ %.

5.7.3 2D hexagonal superlattice induced by $CaCl_2$

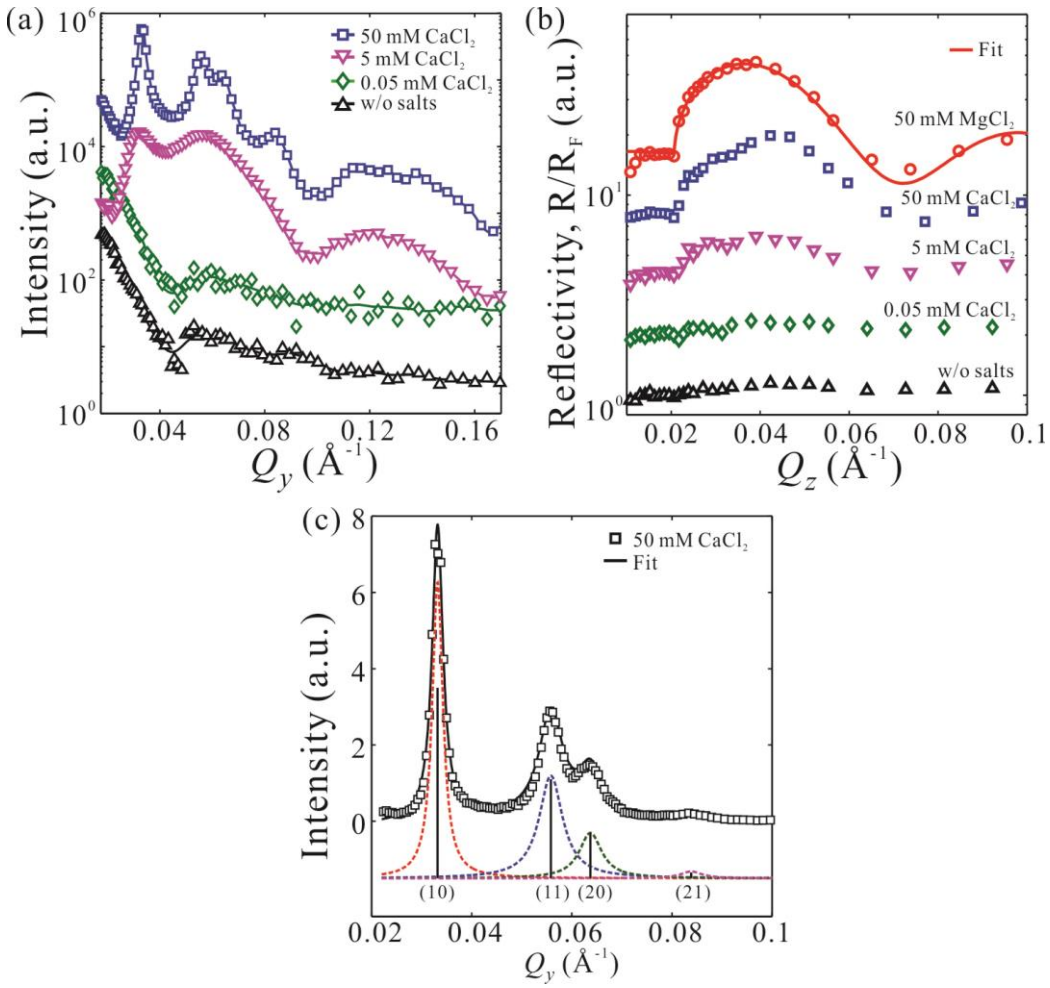

Figure S5.2 Formation of a long-range ordered 2D superlattice from base-pairing ssDNA-AuNPs in the presence of $CaCl_2$. (a) GISAXS linecut profiles along Q_y direction and (b) normalized X-ray reflectivity from Gibbs monolayers of ssDNA-AuNPs in the presence of $CaCl_2$ with different concentrations (0.05−50 mM). The curves are vertically shifted for clarity. The normalized X-ray reflectivity from Gibbs monolayers of ssDNA-AuNPs mixed with 50 mM $MgCl_2$ is plotted in (b) for comparison. (c) The GISAXS linecut profile of ssDNA-AuNPs mixed with 50 mM $CaCl_2$ (black square) at low Q_y range (0.02−0.1Å^{-1}) and a best fit (black solid line) with a Lorentzian-shaped Bragg peaks (dash lines). The peaks positions ratios with respect to the first-order peak of ~1:√3: √4:√7 reveal a hexagonal packing of nanoparticles with corresponding diffraction indices (10), (11), (20), and (21). This pattern is practically the same as that observed for the same nanoparticle system with $MgCl_2$ (See Figure 5.2).

5.7.4 SAXS of complementary ssDNA-AuNPs mixed with $MgCl_2$

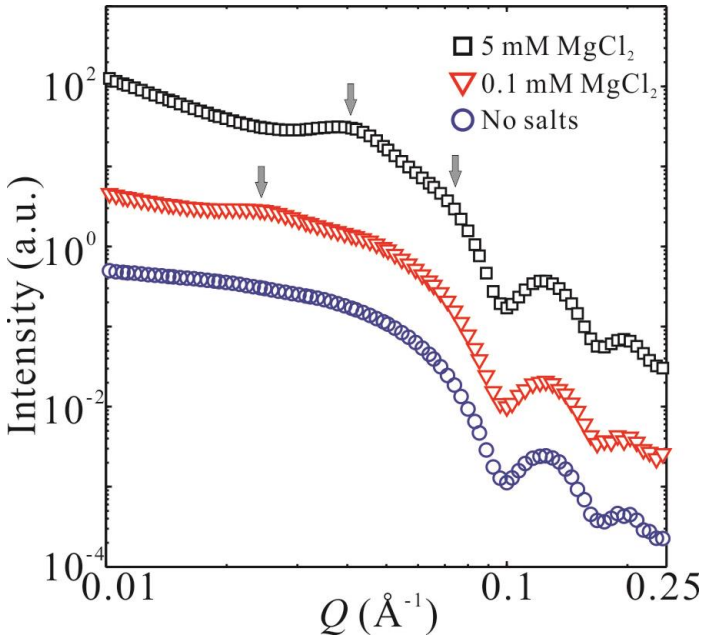

Figure S5.3 SAXS intensity profiles of base-paired ssDNA-AuNP suspension in the absence of salt (blue circles) and in the presence of 0.1 mM (red triangles) and 5 mM $MgCl_2$ (black squares). Without any salts, the intensity solely comes from form factor of AuNPs, while extra structural correlations between AuNPs (see gray arrows) show up when $MgCl_2$ is added. This reveals that base-pairing takes place in the system of complementary ssDNA-AuNPs mixed with $MgCl_2$. To obtain 3D crystalline structures, recycling the temperature to the melting temperature of DNA a few times is necessary,[4] but has not been done in this study. The curves are vertically shifted for clarity.

5.7.5 Attractive force driven crystallization

At the critical salt concentration $[salt]_c$ the interface is practically saturated, but usually this is not a sufficient condition for crystallization to occur.[33] We argue that crystallization occurs as a result of attractive forces between capped AuNPs by aligning positive and negative charges (as in ionic crystals) that by analogy yields cohesion energy

$$E = -\gamma q_1 q_2 / d \sim -\gamma q_1 q_2 \rho^{1/\mathbf{D}}, \qquad \text{(S5.3)}$$

where γ is the Madelung constant and d is the average inter-ions distance. The cohesive energy can also be expressed in terms of the ionic density ρ and dimension **D** of the system. Clearly, the

energy is minimized when the density is largest, which implies two nanoparticles will maximize their interdigitation (and thus attract each other). This attraction will continue until it is balanced by the unfavorable free energy of stretching the DNA. It is possible to account for DNA stretching and thus estimate the amount of overlap between two DNA-AuNPs, but this calculation is beyond the scope of this manuscript. We also note that experimentally we find that center-to-center distance is significantly smaller than the maximum radii R_{max}.

References

1. Nykypanchuk, D.; Maye, M. M.; van der Lelie, D.; Gang, O. DNA-guided crystallization of colloidal nanoparticles. *Nature* 2008, 451, 549-552.
2. Park, S. Y.; Lytton-Jean, A. K. R.; Lee, B.; Weigand, S.; Schatz, G. C.; Mirkin, C. A. DNA-programmable nanoparticle crystallization. *Nature* 2008, 451, 553-556.
3. Grzelczak, M.; Vermant, J.; Furst, E. M.; Liz-Marzán, L. M. Directed Self-Assembly of Nanoparticles. *ACS Nano* 2010, 4, 3591-3605.
4. Macfarlane, R. J.; Lee, B.; Jones, M. R.; Harris, N.; Schatz, G. C.; Mirkin, C. A. Nanoparticle Superlattice Engineering with DNA. *Science* 2011, 334, 204-208.
5. Bigioni, T. P.; Lin, X.-M.; Nguyen, T. T.; Corwin, E. I.; Witten, T. A.; Jaeger, H. M. Kinetically driven self assembly of highly ordered nanoparticle monolayers. *Nat. Mater.* 2006, 5, 265-270.
6. Bodnarchuk, M. I.; Kovalenko, M. V.; Heiss, W.; Talapin, D. V. Energetic and Entropic Contributions to Self-Assembly of Binary Nanocrystal Superlattices: Temperature as the Structure-Directing Factor. *J. Am. Chem. Soc.* 2010, 132, 11967-11977.
7. Shevchenko, E. V.; Talapin, D. V.; Kotov, N. A.; O'Brien, S.; Murray, C. B. Structural diversity in binary nanoparticle superlattices. *Nature* 2006, 439, 55-59.
8. Zhang, Y.; Lu, F.; Yager, K. G.; van der Lelie, D.; Gang, O. A general strategy for the DNA-mediated self-assembly of functional nanoparticles into heterogeneous systems. *Nat. Nanotechnol.* 2013, 8, 865-872.
9. Zhang, C.; Macfarlane, R. J.; Young, K. L.; Choi, C. H. J.; Hao, L.; Auyeung, E.; Liu, G.; Zhou, X.; Mirkin, C. A. A general approach to DNA-programmable atom equivalents. *Nat. Mater.* 2013, 12, 741-746.
10. Talapin, D. V.; Shevchenko, E. V.; Bodnarchuk, M. I.; Ye, X.; Chen, J.; Murray, C. B. Quasicrystalline order in self-assembled binary nanoparticle superlattices. *Nature* 2009, 461, 964-967.
11. Talapin, D. V.; Lee, J.-S.; Kovalenko, M. V.; Shevchenko, E. V. Prospects of Colloidal Nanocrystals for Electronic and Optoelectronic Applications. *Chem. Rev.* 2010, 110, 389-458.
12. Tan, S. J.; Campolongo, M. J.; Luo, D.; Cheng, W. Building plasmonic nanostructures with DNA. *Nat. Nanotechnol.* 2011, 6, 268-276.

13. Young, K. L.; Ross, M. B.; Blaber, M. G.; Rycenga, M.; Jones, M. R.; Zhang, C.; Senesi, A. J.; Lee, B.; Schatz, G. C.; Mirkin, C. A. Using DNA to Design Plasmonic Metamaterials with Tunable Optical Properties. *Adv. Mater.* 2014, 26, 653-659.
14. Tkachenko, A. V. Morphological Diversity of DNA-Colloidal Self-Assembly. *Phys. Rev. Lett.* 2002, 89, 148303.
15. Courty, A.; Mermet, A.; Albouy, P. A.; Duval, E.; Pileni, M. P. Vibrational coherence of self-organized silver nanocrystals in f.c.c. supra-crystals. *Nat. Mater.* 2005, 4, 395-398.
16. Sun, S.; Murray, C. B.; Weller, D.; Folks, L.; Moser, A. Monodisperse FePt Nanoparticles and Ferromagnetic FePt Nanocrystal Superlattices. *Science* 2000, 287, 1989-1992.
17. Cheon, J.; Park, J.-I.; Choi, J.-s.; Jun, Y.-w.; Kim, S.; Kim, M. G.; Kim, Y.-M.; Kim, Y. J. Magnetic superlattices and their nanoscale phase transition effects. *Proc. Natl. Acad. Sci. USA* 2006, 103, 3023-3027.
18. Xiong, H.; Sfeir, M. Y.; Gang, O. Assembly, Structure and Optical Response of Three-Dimensional Dynamically Tunable Multicomponent Superlattices. *Nano Lett.* 2010, 10, 4456-4462.
19. Maye, M. M.; Nykypanchuk, D.; Cuisinier, M.; van der Lelie, D.; Gang, O. Stepwise surface encoding for high-throughput assembly of nanoclusters. *Nat. Mater.* 2009, 8, 388-391.
20. Boles, M. A.; Talapin, D. V. Many-Body Effects in Nanocrystal Superlattices: Departure from Sphere Packing Explains Stability of Binary Phases. *J. Am. Chem. Soc.* 2015, 137, 4494-4502.
21. Knorowski, C.; Travesset, A. Materials design by DNA programmed self-assembly. *Curr. Opin. Solid State Mater. Sci.* 2011, 15, 262-270.
22. Knorowski, C.; Burleigh, S.; Travesset, A. Dynamics and Statics of DNA-Programmable Nanoparticle Self-Assembly and Crystallization. *Phys. Rev. Lett.* 2011, 106, 215501.
23. Li, T. I. N. G.; Sknepnek, R.; Macfarlane, R. J.; Mirkin, C. A.; Olvera de la Cruz, M. Modeling the Crystallization of Spherical Nucleic Acid Nanoparticle Conjugates with Molecular Dynamics Simulations. *Nano Lett.* 2012, 12, 2509-2514.
24. Travesset, A. Binary nanoparticle superlattices of soft-particle systems. *Proc. Natl. Acad. Sci. USA* 2015, 112, 9563-9567.
25. Horst, N.; Travesset, A. Prediction of binary nanoparticle superlattices from soft potentials. *J . Chem. Phys.* 2016, 144, 014502.
26. Cheng, W.; Hartman, M. R.; Smilgies, D.-M.; Long, R.; Campolongo, M. J.; Li, R.; Sekar, K.; Hui, C.-Y.; Luo, D. Probing in Real Time the Soft Crystallization of DNA-Capped Nanoparticles. *Angew. Chem. Int. Ed.* 2010, 49, 380-384.
27. Campolongo, M. J.; Tan, S. J.; Smilgies, D.-M.; Zhao, M.; Chen, Y.; Xhangolli, I.; Cheng, W.; Luo, D. Crystalline Gibbs Monolayers of DNA-Capped Nanoparticles at the Air–Liquid Interface. *ACS Nano* 2011, 5, 7978-7985.
28. Tan, S. J.; Kahn, J. S.; Derrien, T. L.; Campolongo, M. J.; Zhao, M.; Smilgies, D.-M.; Luo, D. Crystallization of DNA-Capped Gold Nanoparticles in High-Concentration, Divalent Salt Environments. *Angew. Chem. Int. Ed.* 2014, 53, 1316-1319.
29. Srivastava, S.; Nykypanchuk, D.; Fukuto, M.; Gang, O. Tunable Nanoparticle Arrays at Charged Interfaces. *ACS Nano* 2014, 8, 9857-9866.

30. Srivastava, S.; Nykypanchuk, D.; Fukuto, M.; Halverson, J. D.; Tkachenko, A. V.; Yager, K. G.; Gang, O. Two-Dimensional DNA-Programmable Assembly of Nanoparticles at Liquid Interfaces. *J. Am. Chem. Soc.* 2014, 136, 8323-8332.
31. Vaknin, D. X-Ray Diffraction and Spectroscopic Techniques for Liquid Surfaces and Interfaces. In *Characterization of Materials*, John Wiley & Sons, Inc.: 2002.
32. Parratt, L. G. Surface Studies of Solids by Total Reflection of X-Rays. *Phys. Rev.* 1954, 95, 359-369.
33. Israelachvili, J. N. *Intermolecular and Surface Forces*, Academic Press: 2011.
34. Marcus, Y. *Ions in Solution and their Solvation*, Wiley: 2015.
35. Hill, H. D.; Mirkin, C. A. The bio-barcode assay for the detection of protein and nucleic acid targets using DTT-induced ligand exchange. *Nat. Protoc.* 2006, 1, 324-336.
36. Hurst, S. J.; Lytton-Jean, A. K. R.; Mirkin, C. A. Maximizing DNA Loading on a Range of Gold Nanoparticle Sizes. *Anal. Chem.* 2006, 78, 8313-8318.
37. Maye, M. M.; Nykypanchuk, D.; van der Lelie, D.; Gang, O. A Simple Method for Kinetic Control of DNA-Induced Nanoparticle Assembly. *J. Am. Chem. Soc.* 2006, 128, 14020-14021.
38. Wang, W.; Park, R. Y.; Meyer, D. H.; Travesset, A.; Vaknin, D. Ionic Specificity in pH Regulated Charged Interfaces: Fe^{3+} versus La^{3+}. *Langmuir* 2011, 27, 11917-11924.

CHAPTER 6. MACROSCOPIC AND TUNABLE NANOPARTICLE SUPERLATTICES

Modified from a paper published in *Nanoscale*[⊥]

Honghu Zhang, Wenjie Wang, Surya Mallapragada, Alex Travesset, and David Vaknin[*]

6.1 Abstract

We describe a robust method to assemble nanoparticles into highly ordered superlattices by inducing aqueous phase separation of neutral capping polymers. Here we demonstrate the approach with thiolated polyethylene-glycol-functionalized gold nanoparticles (PEG-AuNPs) in the presence of salts (for example, K_2CO_3) in solutions that spontaneously migrate to the liquid–vapor interface to form a Gibbs monolayer. We show that by increasing salt concentration, PEG-AuNP monolayers transform from two-dimensional (2D) gas-like to liquid-like phase and eventually, beyond a threshold concentration, to a highly ordered hexagonal structure, as characterized by surface sensitive synchrotron X-ray reflectivity and grazing incidence X-ray diffraction. Furthermore, the method allows control of the inplane packing in the crystalline phase by varying the K_2CO_3 and PEG-AuNPs concentrations and the length of PEG. Using polymer-brush theory, we argue that the assembly and crystallization is driven by the need to reduce surface tension between PEG and the salt solution. Our approach of taking advantage of the phase separation of PEG in salt solutions is general (*i.e.*, can be used with any nanoparticles)

[⊥] Reprinted with permission of *Nanoscale* **2016**, DOI: 10.1039/C6NR07136H.

[*] Corresponding Author: vaknin@ameslab.gov

leads to high-quality macroscopic and tunable crystals. Finally, we discuss how the method can also be applied to the design of orderly 3D structures.

6.2 Introduction

Self-assembly of nanoparticles and molecular-scale building blocks into hierarchically designed ordered structures provides a promising route for the production of metamaterials and nanodevices through bottom-up approaches.[1–6] Particularly, chemically stable gold nanoparticles (AuNPs) that seem to possess desirable optical and electrical properties have been assembled into three-dimensional (3D) ordered structures by use of complementary single-stranded DNA or DNA origami with unique programmable features.[4–8] Concomitantly, two-dimensional (2D) self-assembly of AuNPs at solid– or vapor–liquid interfaces have also been developed,[9–11] providing valuable understanding of general mechanisms involved in self-assembly that can be readily applied in other dimensions. Employing a self- and guided-assembly approach, it has been shown that capped AuNPs, AgNPs, or magnetite with various surfactants (including thiolated-acyl chains, -PEG, and others) can be manipulated in a Langmuir trough to form ordered 2D domains, which can be transferred to solid support by the Langmuir–Blodgett technique for further applications.[12–21] Recently, it has been shown that unpaired thiolated ssDNA functionalized AuNPs (ssDNA-AuNPs) self-assemble and crystallize at gas–solution interfaces spontaneously simply by tuning various salts concentrations.[22–24] These studies established that the complexed ssDNA-AuNP is amphiphilic in character by virtue of the polyelectrolytic nature of DNA that competes with the hydrophobicity that is inadvertently introduced in the thiolating process of DNA.[24] Another approach to 2D assembly exploits electrostatic interactions between a positively charged template formed by a Langmuir monolayer and the negatively charged ssDNA-AuNPs or even unfunctionalized (bare) AuNPs.[25–27] These studies point to the possibility

that the functionalizing DNA can be replaced by macromolecules that display intrinsic amphiphilic character. Thus, inspired by our findings,[24] we have embarked on a robust approach to explore the interfacial and 3D self-assembly of gold nanoparticles by functionalizing them with polyelectrolytes and amphiphilic polymers. Here, we report on the properties and self-assembly of polyethylene-glycol (PEG)-functionalized AuNPs (PEG-AuNPs). PEG is a remarkable linear polymer that resides on the hydrophobic/hydrophilic edge where one or the other (hydrophobic or hydrophilic) can be readily tweaked by varying salts concentrations, pH, and temperature.[28,29] These properties of PEG mixed with dextran or salts have been widely used in the separation and extraction of macromolecules and organelles of cells by the so-called aqueous biphasic systems technique (ABS).[30–32] Owing to PEG's biocompatibility and the low cytotoxicity of Au, studies of PEG-AuNPs have been focused towards nanomedicine applications.[33–35] In this study, grazing incidence small-angle X-ray scattering (GISAXS) and X-ray reflectivity (XRR) are used to determine the in-plane structure and surface-normal density profile, respectively, of self-assembled PEG-AuNPs at the vapor–liquid interface by manipulating the concentration of a specific salt, K_2CO_3 that has been efficiently used in ABS.[30,31] The evolution of 2D PEG-AuNP superlattice formation is systematically studied with two kinds of PEG (molecular weight of 6000 and 800 Da) by manipulating K_2CO_3 and PEG-AuNP concentrations.

6.3 Experimental

6.3.1 Reagents and materials

Poly(ethylene glycol) methyl ether thiol (PEG-SH; Sigma-Aldrich) with average molecular weight of 800 and 6000 g mol^{-1} (the number of monomers N_r = 18 and 136, respectively; Kuhn length b = 7.24 Å; see the ESI) was dissolved in degassed Millipore water

with slight sonication. The freshly-prepared PEG-SH solution was added to aqueous suspension of citrate-stabilized gold nanoparticles (AuNPs, with nominal size of 10 nm; Ted Pella) in large excess (molar ratio of PEG-SH/AuNP ≈ 6000) under vigorous stirring. The mixture of PEG-SH and AuNPs was gently stirred at room temperature for one day to allow for maximum PEG loading after ligand exchange. The as-prepared PEG-AuNPs were concentrated *via* centrifugation (at 20 000g × 1 h). The supernatant was discarded and the precipitate was collected and redispersed in Millipore water. This washing process with centrifugation and redispersion was done at least twice prior to further measurements. The concentration of PEG-AuNPs was determined by UV-Visible absorption measurements. Aqueous solution of potassium carbonate (anhydrous, K_2CO_3; Fisher Scientific) was prepared and mixed with PEG-AuNPs suspensions at desired concentrations of K_2CO_3 (0.05–1000 mM) and PEG-AuNPs (0.05–10 nM) prior to X-ray measurements. We note that PEG-AuNPs form visible precipitates at 1 M K_2CO_3 after overnight incubation, while they are stable as suspension for months at low K_2CO_3 concentrations.

6.3.2 Experimental setup

Specular X-ray reflectivity (XRR) and grazing incidence small-angle X-ray scattering (GISAXS) measurements were conducted on the liquid surface spectrometer (LSS) at beamline 9ID-B, Advanced Photon Source (APS), Argonne National Laboratory. The aqueous solution of the PEG-AuNPs in absence and presence of K_2CO_3 was contained in a shallow trough (surface area 6 × 6 cm^2 and enclosed in gas tight canister) where the aqueous surface was illuminated with a highly collimated and monochromatic X-ray beam (photon energy E = 8.0 keV and wavelength λ = 1.5497 Å). For an XRR measurement, a point detector (Bicron) that moves within the scattering plane, was used to collect the X-ray reflection from the surface at the exit

angle (with respect to the surface) α_f in such way that $\alpha_f = \alpha_i$, α_i being the X-ray incident angle with respect to the surface. The reflectivity, *R*, is measured as a function of Q_z that equals $(4\pi/\lambda)$ sin α_i and is the *z*-component (along the surface normal) of the moment transfer $\boldsymbol{Q}$. The trough was allowed to move laterally to provide fresh portions of the surface in the course of the reflectivity measurement. For a GISAXS measurement, a digital, two-dimensional Pilatus 100K detector (487 × 195 pixels, 172 × 172 μm per pixel) was placed downstream from the sample and was calibrated with the standard calibrating material, *i.e.*, silver behenate powder. The GISAXS intensity was obtained as a function of the three orthogonal components denoted as (Q_x, Q_y, Q_z), where Q_z component is along the surface normal, while Q_x and Q_y components are parallel to the liquid surface. In this study, Q_y is defined as parallel to the detector surface while $Q_x \approx 0$. Thus, the magnitude of the in-plane scattering vector, Q_{xy}, defined as $\sqrt{Q_x^2 + Q_y^2}$, is practically equivalent to Q_y. In the small angle regime, $Q_y \approx (4\pi/\lambda)\theta$, 2θ being the in-plane scattering angle. The X-ray exposure time and incident beam attenuation are carefully chosen in such way that each GISAXS frame has a good signal to noise ratio and sample radiation damage is minimal. The trough was sealed in a canister that has Kapton windows for X-ray passage. It was purged with water-saturated helium in the course of the X-ray measurements to minimize the background scattering and radiation damage. More experimental details can be found elsewhere.[36] Solution small-angle X-ray scattering (SAXS) experiments for determining the size of the nanoparticles in suspension were performed at beamline 12ID-B at APS with similar setups employed for biomolecules before.[27,37]

6.4 Results and Discussion

GISAXS patterns as functions of Q_{xy} and Q_z for aqueous solutions of PEG_{6k}-AuNPs without salts and with 500 mM K_2CO_3 are shown in Figure 6.1a. In the absence of salts, sector-

shaped and broad circular features at low and high Q_{xy}ranges originate from the form factor of PEG_{6k}-AuNPs, which is dominated by the bare form factor of AuNPs (see ESI).[24,27] This indicates that PEG_{6k}-AuNPs spontaneously accumulate at the interface without any salts in solutions albeit dispersed at low coverage. As shown in Figure S6.1, the corresponding GISAXS pattern of unfunctionalized (bare) AuNPs without PEG does not show any features associated with the form factor. Although GISAXS patterns from aqueous solutions of pure PEG_{6k} without or with salts do not show any features different from water surface in the current Q_{xy} window

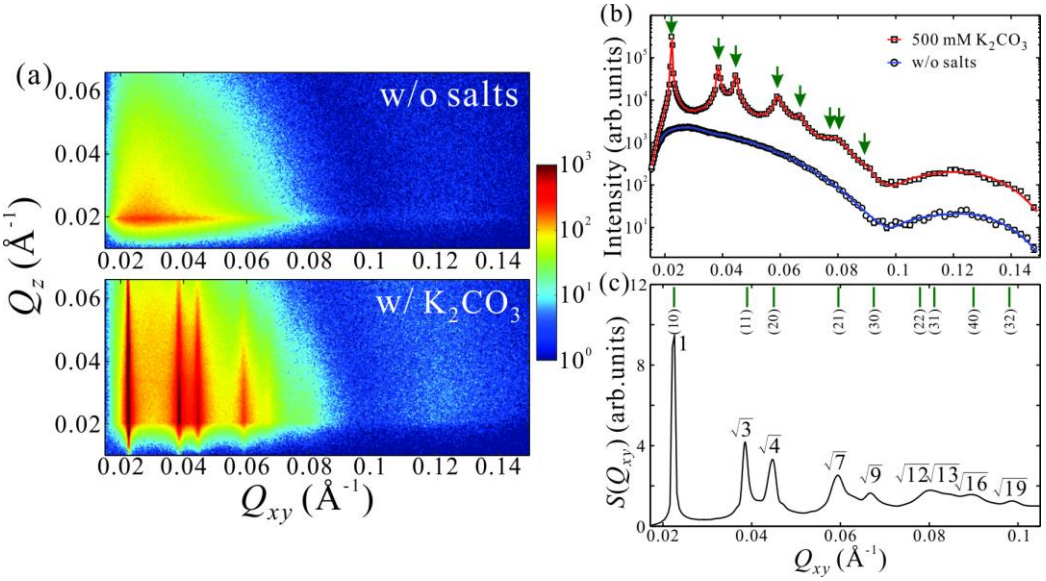

Figure 6.1 K_2CO_3 induced 2D superlattices of PEG_{6k}-AuNPs at the vapor–liquid interface. (a) GISAXS patterns as functions of Q_{xy} and Q_z for aqueous solutions of 5 nM PEG_{6k}-AuNPs in the absence of salts and in the presence of 500 mM K_2CO_3. Intensities are displayed on logarithmic scales. (b) Horizontal linecut profiles along Q_{xy} direction at Q_z = 0.020 Å^{-1} integrated over Q_z range 5 × 10^{-3} Å^{-1} in the GISAXS 2D patterns for Gibbs monolayers of PEG_{6k}-AuNPs in the absence of salts (circles) and in the presence of 500 mM K_2CO_3 (squares). Solid lines are guides to the eyes. The arrows point to the calculated positions of higher orders Bragg reflections based on the fundamental diffraction peak of a 2D hexagonal lattice. The plots are vertically shifted for clarity. (c) The extracted structure factor, $S(Q_{xy})$, profile at low Q_{xy} range (0.02–0.1 Å^{-1}) for the Gibbs monolayer of PEG_{6k}-AuNPs mixed with 500 mM K_2CO_3. The peak positions ratios with respect to the fundamental diffraction peak of 1:√3:√4:√7:√9… reveals a hexagonal packing of nanoparticles with corresponding diffraction indices (10), (11), (20), (21), (30) and higher-order Bragg reflections.

(Figure S6.1), PEG itself has been reported to form Gibbs monolayers at the air–water interface.[28,29,38–40] Clearly, PEG drives the functionalized PEG_{6k}-AuNPs to the gas–water interface. However, as the GISAXS pattern shows, the particles are not correlated. By contrast, in the presence of 500 mM K_2CO_3, up to 5 sharp Bragg rods become apparent, evidencing the formation of a long-range ordered crystalline layer of PEG_{6k}-AuNPs at the interface. Figure 6.1b shows horizontal linecut profiles along Q_{xy} direction (at Q_z = 0.020 $Å^{-1}$) from the GISAXS patterns in Figure 6.1a. The linecut profile from PEG_{6k}-AuNPs mixed with 500 mM K_2CO_3 represents a combination of both form factor (see SAXS data from bulk solution in Figure S6.2) and structure factor.[24,27] The extracted structure factor at the low Q_{xy} range (0.02–0.1 $Å^{-1}$) is plotted in Figure 6.1c. The diffraction peak-positions ratios with respect to the fundamental peak (Q_1 = 0.0225 $Å^{-1}$) satisfy $Q_i/Q_1 \approx 1{:}\sqrt{3}{:}\sqrt{4}{:}\sqrt{7}{:}\sqrt{9}\ldots(i = 1–9)$ revealing the formation of a long-range ordered 2D hexagonal superlattice of AuNPs with an inter-particle distance of $a_L = 4\pi/(\sqrt{3}Q_1)$ = 322 Å, where the corresponding diffraction peaks are indexed as (10), (11), (20), (21), (30) and higher-order Bragg reflections. This demonstrates that K_2CO_3 plays a crucial role in promoting interfacial self-assembly and crystallization of PEG_{6k}-AuNPs. Recently, single-stranded DNA functionalized AuNPs (ssDNA-AuNPs) have been found to form a Gibbs monolayer and crystallize as hexagonal superlattices at the vapor–liquid interface.[22–24] Here, the PEG_{6k}-AuNP/K_2CO_3 exhibits much higher crystalline quality exemplified by nine Bragg reflections. Below, we describe the evolution of PEG_{6k}-AuNP superlattices systematically by regulating K_2CO_3 or PEG-AuNP concentrations.

The GISAXS patterns in Figure 6.2a for aqueous solutions of 5 nM PEG_{6k}-AuNPs mixed in varying amounts of K_2CO_3 in the range of 0.05 mM–1 M indicate in-plane structural transformations from uncorrelated to short-range ordering, and eventually to long-range hexago-

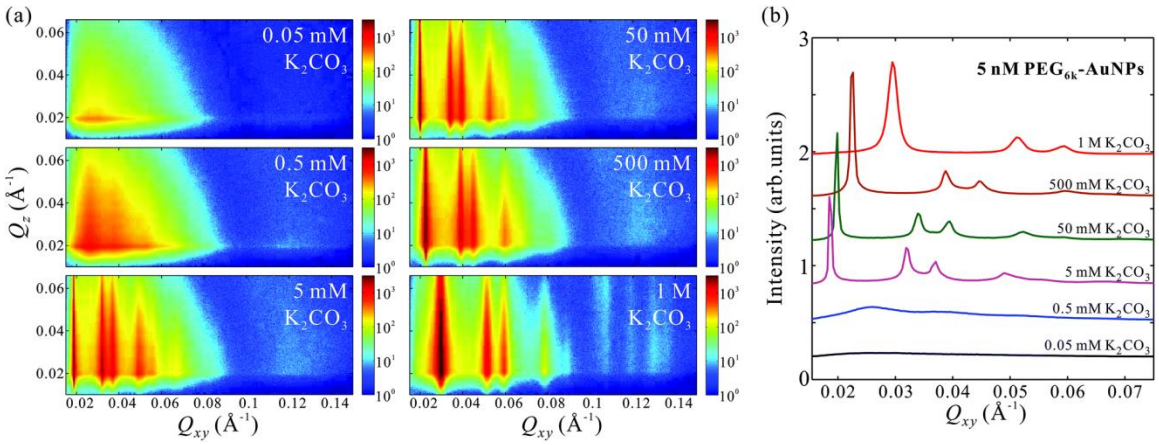

Figure 6.2 In-plane structure evolution of 2D superlattices from aqueous solutions of 5 nM PEG_{6k}-AuNPs at various K_2CO_3 concentrations. (a) GISAXS patterns as functions of Q_{xy} and Q_z for aqueous solutions of 5 nM PEG_{6k}-AuNPs in the presence of 0.05 mM to 1 M K_2CO_3. Intensities are displayed on logarithmic scales. (b) Horizontal linecut profiles along Q_{xy} direction at Q_z = 0.020 $Å^{-1}$ integrated over Q_z range 5×10^{-3} $Å^{-1}$ at low Q_{xy} range (0.02–0.07 $Å^{-1}$) for Gibbs monolayers of 5 nM PEG_{6k}-AuNPs at various K_2CO_3 concentrations as indicated. The plots are vertically shifted for clarity.

Table 6.1 Lattice parameters of 2D superlattice of PEG_{6k}-AuNPs at the vapor–liquid interface induced by K_2CO_3.

[PEG_{6k}-AuNPs] (nM)	[K_2CO_3] (mM)	Q_1 ($Å^{-1}$)	Lattice constant, a_L (Å)	FWHM ($Å^{-1}$)	Estimated crystalline size (Å)
5	5	0.0187	388 ± 4	~0.0003	2.1×10^4
5	50	0.0198	366 ± 5	~0.0004	1.5×10^4
5	500	0.0225	322 ± 3	~0.0006	1.0×10^4
5	1000	0.0296	245 ± 2	~0.0019	3.4×10^3
2.5	500	0.0215	338 ± 4	~0.0007	8.4×10^3
5	500	0.0225	322 ± 3	~0.0006	1.0×10^4
10	500	0.0235	309 ± 3	~0.0004	1.7×10^4

nal order at threshold concentration of about 5 mM K_2CO_3. Furthermore, the linecut prof-iles in Figure 6.2b show that the hexagonal inter-particle distance decreases with the increase of salt concentration, as evidenced by gradual peaks-positions shift to higher Q_{xy} values. This demonstrates that K_2CO_3 is capable of tuning the 2D hexagonal superlattice at the vapor–liquid

interface such that the lattice constant a_L takes values in the range a_L = 245–388 Å under the current tested conditions (see more details in Table 6.1). For concentrations 5–500 mM K_2CO_3, the diffraction peaks are extremely sharp with a peak full width at half maximum (FWHM) of the (10) reflection ($FWHM_{(10)} \approx$ 0.0003–0.0006 $Å^{-1}$) that is comparable to the instrumental resolution (≈0.0003 $Å^{-1}$), suggesting that the estimated crystalline size is on the micrometer scale, significantly larger than that found in 2D superlattices formed by ssDNA-AuNPs.[22,24] At the highest K_2CO_3 concentration (1 M) the $FWHM_{(10)} \approx 0.0019$ $Å^{-1}$ with a 2D crystalline size on the order of 3.4×10^3 Å, which is still superior than that found in ssDNA-AuNPs superlattices.[22,24] This trend suggests that higher K_2CO_3 concentrations, while promoting the formation of denser packing of AuNPs, induce defects in the superlattices and tend to decrease the crystalline size (Table 6.1).

In addition to its dependence on K_2CO_3 concentration, the self-assembly depends on the PEG_{6k}-AuNP concentration, as shown in Figure S6.3 at a fixed K_2CO_3 500 mM at various concentrations of PEG_{6k}-AuNPs (0.05–10 nM). The GISAXS patterns as well as the corresponding linecut profiles in Figure S6.3b show that short-range hexagonal order emerges at 0.25–0.5 nM PEG_{6k}-AuNPs, and at higher concentrations long-range order of micrometer size 2D crystallines sets in with a_L = 338 ± 4 Å and a_L = 309 ± 3 Å at 2.5 and 10 nM, respectively (see Table 6.1). Qualitatively, the effect of nanoparticle concentration on monolayer density and compressibility can be understood *via* generalized Gibbs adsorption. Increasing the nanoparticle concentration in the bulk leads to an increase of nanoparticle surface density and the corresponding increase of surface pressure, originating from the entropy and inter-particle interaction, similar to the soft crystallization of ssDNA-AuNPs.[8]

AuNPs functionalized with a shorter chain PEG (MW = 800 Da) show similar 2D superlattices under similar conditions to those used for PEG_{6k}-AuNPs discussed above. GISAXS patterns in Figure S6.4 show the evolution of the self-assembly and crystallization of a fixed concentration PEG_{800}-AuNPs and varying the amount of K_2CO_3 in solution, and Figure S6.5 shows the development at a fixed 500 mM K_2CO_3 for various PEG_{800}-AuNPs concentrations. Compared to PEG_{6k}-AuNPs, the diffractions peaks of PEG_{800}-AuNPs shift to larger Q_{xy} values, evidence for closer packing as expected for a shorter and smaller hydrodynamic radius of PEG_{800}-AuNPs (see Figure S6.7). We note that crystallization of PEG_{800}-AuNPs is observed only for high concentrations of K_2CO_3 and PEG-AuNPs, *i.e.*, a_L = 149 ± 1 Å at 1 M K_2CO_3 and 5 nM PEG_{800}-AuNPs, and a_L = 158 ± 3 Å at 500 mM K_2CO_3 and 10 nM PEG_{800}-AuNPs.

To determine the density profile of the crystalline film across the interface we employ X-ray reflectivity, which provides the electron density (ED) profile, ρ, as function of depth (along z-axis, *i.e.*, the surface normal) by refining a model that fits the reflectivity data through the Prarratt's recursive method.[36,41,42]

Figure 6.3 shows X-ray reflectivity normalized to that of ideally flat water, R/R_F, for PEG_{6k}-AuNPs and PEG_{800}-AuNPs at 5 nM in the presence of different amounts of K_2CO_3 in the aqueous subphase as indicated (these are the same samples on which the GISAXS described above have been performed). The dramatic increase of the first maximum in R/R_F with the concentration of K_2CO_3, as shown in both (a) and (c) signals a huge accumulation of capped-AuNPs at the interface. Quantitative analysis of the R/R_F, based on the effective-density model,[43] yields the corresponding ED profiles shown in (b) and (d) with an enhancement region over that of the solution on a ~100 Å length scale, very close to the diameter of AuNPs (D = 88

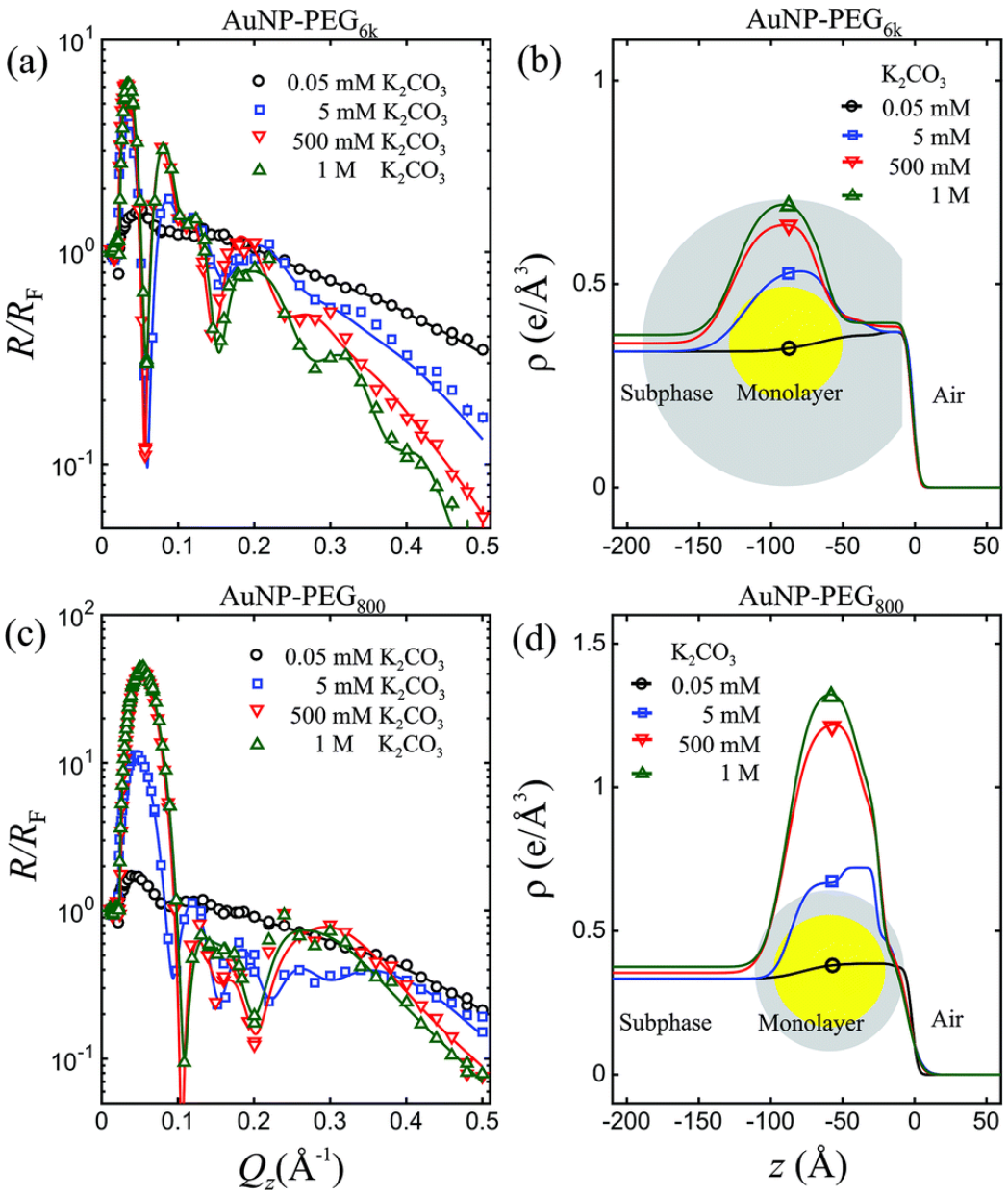

Figure 6.3 Surface-normal structure evolution of 2D superlattices from aqueous solutions of PEG-AuNPs mixed with different K_2CO_3 concentrations. Representative R/R_F data for (a) PEG_{6k}-AuNPs and (c) PEG_{800}-AuNPs with same nanoparticle concentration (5 nM) at various K_2CO_3 concentrations as indicated. (b) and (d) are one of the best-fit electron density (ED) profiles that regenerate the R/R_F in (a) and (c) (solid lines), respectively.

± 9 Å, see Figure S6.2). The ED of densely packed PEG as well as water-saturated-PEG is very close to that of the water subphase, therefore yielding only a small increase in the ED of the submerged polymer tails, whereas at the air/particle interface, a ~50 Å strata can be associated

with densely-packed PEG, as depicted in Figure 6.4. This practically indicates that the films that are formed at the surface consist of a mono-particle layer, and combination of the GISAXS and R/R_F results allows determination of surface coverage and conformation of the particles as discussed below. We note that the maximum R/R_F for PEG_{800}-AuNPs film are much higher than PEG_{6k}-AuNPs under otherwise identical conditions (*i.e.*, concentrations of AuNPs and K_2CO_3). This higher surface density compared to PEG_{6k}-AuNPs is consistent with the corresponding difference in lattice parameters of the two capped-AuNPs. Based on the measured lattice parameters obtained by GISAXS, the ED of a thin slab of 2D crystalline and using a simple space filling model (see details in ESI), we estimate the surface coverage of pure 2D hexagonal superlattice is nearly 100%. The observation of limited lattice constant tunability for the shorter PEG indicates that the relatively more rigid PEG_{800}-AuNPs remain in the liquid state (short range order) over a wider range of salt concentrations compared to the softer PEG_{6k}-AuNPs.

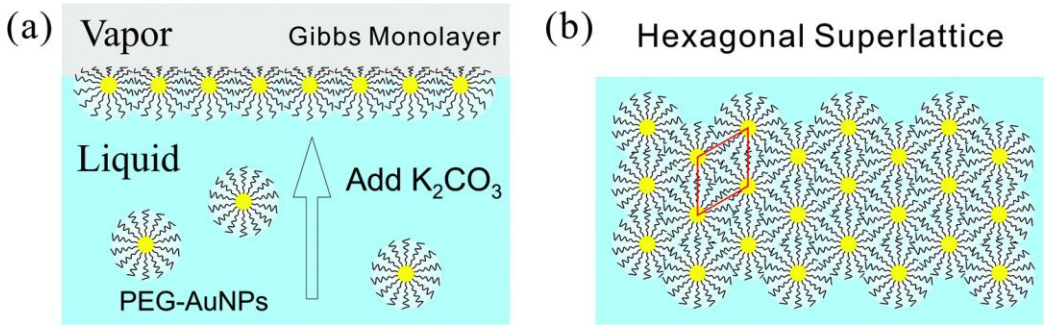

Figure 6.4 A schematic of 2D self-assembly and crystallization of PEG-AuNPs at liquid–vapor interface induced by K_2CO_3 (a) side view and (b) top view.

Our main results are summarized in phase-diagrams of PEG-AuNPs *versus* K_2CO_3 concentrations as shown in Figure 6.5 for both polymers. At low K_2CO_3 and PEG-AuNPs concentrations, the accumulated particles at the interface lack any order forming a gas-like phase. In the intermediate concentrations of K_2CO_3 and PEG-AuNPs, more PEG-AuNPs adsorb at the interface and promote formation of liquid-like state of short-range hexagonal order. At thr-

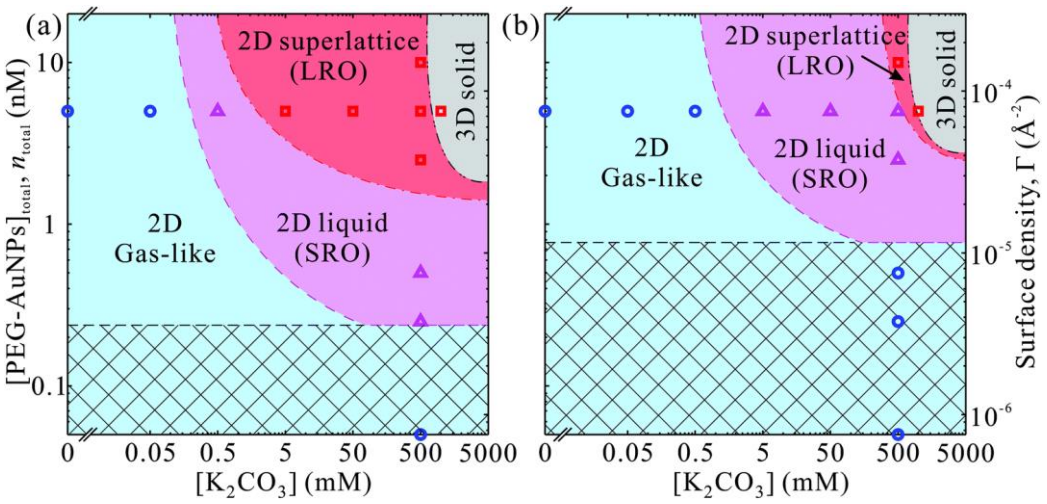

Figure 6.5 Phase diagram as functions of concentrations of K_2CO_3 and total PEG-AuNPs in the system of (a) PEG_{6k}-AuNPs, (b) PEG_{800}-AuNPs. The presumptive surface density of PEG-AuNPs (number of NPs/surface area) is provided on the right axes. The symbols (circles, triangles and squares) are presented as sample conditions measured by GISAXS and XRR. The Gibbs monolayer consists of 2D gas-like (uncorrelated), 2D liquid (short range ordering, SRO) and 2D superlattice (long range ordering, LRO) phases at various conditions. 2D superlattice phase becomes unstable and form visible precipitates (3D solid) above 1 M K_2CO_3 as confirmed by SAXS. The crosshatching area below the critical surface density Γ_c indicates that the interfaces could not be fully covered by PEG-AuNPs if all the PEG-AuNPs had migrated to the interfaces. The Γ_c is calculated as $1/(R_h + \Delta R_h)^2$, where R_h and ΔR_h are the mean and spread of hydrodynamic radii of PEG-AuNPs, respectively. Note: the phase boundaries are by no means exact and they are surmised based on the limited datasets.

eshold concentrations of K_2CO_3 and PEG-AuNPs, a long-range order phase of 2D hexagonal superlattices is established with total surface coverage (nearly 100%). At concentrations ≥1 M K_2CO_3 the PEG-AuNPs precipitate most likely in simple 3D structure (fcc, for instance). The phase diagram of PEG_{6k}-AuNPs shows that the lattice constant can be tuned by both K_2CO_3 and PEG-AuNP concentrations without loss of materials due to precipitation. By contrast, in the phase diagram of PEG_{800}-AuNPs, the phase boundaries between the three 2D phases shift to higher K_2CO_3 and PEG-AuNP concentrations, and thus the superlattice region without precipitation is suppressed. This indicates that the tunability in lattice constant PEG_{6k}-AuNPs is due to the compressibility of the corona from the longer chain PEG as shown schematically

in Figure 6.4. We argue that the tunability of the lattice constant of the PEG_{6k}-AuNP supercrystals is different from that in ssDNA-AuNP superlattices.[23,24] The ssDNA chains behave as polyelectrolytes such that the added salts screen charges of phosphate groups on the ssDNA backbones and cause the shrinkage of ssDNA chains as have been observed in X-ray scattering and dynamic lighting scattering (DLS) measurements accounting for lattice constant changes as a function of salt concentrations.[24] By contrast, while PEG-AuNPs show K_2CO_3 induced tunability of lattice parameters, the ED profiles extracted from the XRR do not show clear changes on overall monolayer thickness (including Au cores and PEG shells) along the surface-normal direction (Figure 6.3), and furthermore, the DLS measurements of PEG-AuNPs dispersed in the bulk solution with and without salts do not exhibit any differences of hydrodynamic size (Figure S6.7). This indicates that during formation of PEG-AuNP superlattices at the vapor–liquid interface the PEG shells bear in-plane isotropic forces leading to the hexagonal packing. Below, we provide brief general properties of the PEG used in this study based on literature[44] and theoretical characterization of the PEG-AuNPs in terms of brush-polymer on spherical surfaces, and rationalize the accumulation and crystallization at the solution interface (more details are provided in the ESI).

Based on the reported phase diagrams of PEG–salt solutions,[31,32] there are a single- and a two-phase regions, the latter, consisting of a high salt and a low salt plus PEG phases. Even in the region of the single component phase, our results show finite interfacial accumulation suggesting that there is a depletion of ions within the spherical brush, which induces an osmotic pressure gradient. Nevertheless, we find that the effect of salt (0 to 0.5 M) on the hydrodynamic radius of PEG-AuNPs is negligible (see ESI). This observation can be explained by a blob size ξ that is smaller than the thermal correlation length ξ_T, thus leading to chains that are ideal

and a solvent (water + salt) inside the brush that is at the θ-point.[45,46] Still, the overall surface tension of the entire brush with the poor solvent (high salt concentration) is very significant (of order 60–250 k_BT per PEG_{6k}-AuNPs), so the PEG-AuNPs readily migrate to the interface, where such surface tension can be drastically reduced. Under this picture, the effective (hydrodynamic) spherical radius of a given PEG-AuNP (R_h) with Au-core radius R is given by[45,46]

$$\left(\frac{R_h}{R}\right)^2 = 1 + 2\frac{Nb^2\sigma^{1/2}}{R}(2w_0)^{1/4}, \tag{6.1}$$

where N is the number of Kuhn monomers, b is the Kuhn length (b = 7.24 Å for PEG), σ is the grafting density (≈1.51 chains per nm^2), and w_0 is a dimensionless three body interaction, where we use the Flory result w_0 = 1/6, so that $(2w_0)^{1/4}$ = 0.76.[47,48] Using the parameters derived in the ESI yield $D_h = 2R_h$ = 35.5 nm consistent with the measured 39.9(13) nm for PEG_{6k}-AuNPs whereas for PEG_{800}-AuNPs, D_h = 15.3 nm, significantly shorter than the measured 22.3(7) nm. We note that Equation 6.1 is valid for an infinite chain and that PEG_{800} consists of only ≈9 independent (Kuhn-length) segments, suggesting a much more rigid polymer corona. Indeed the phase diagram for PEG_{800}-AuNPs shows a very narrow range of crystallinity as the corona around the particle is much less compressible than that of the longer polymer. It is interesting to note that the measured hydrodynamical radius R_h does not shrink with the increase of ionic strength, as is usually observed for polyelectrolytes-brushes or ssDNA-AuNPs,[24] but rather migrate to the interface to maintain minimal chain-contact with the poor solvent and form a densely packed hexagonal lattice – compressible for the long chain PEG and incompressible for the shorter chain. As detailed in the ESI and the use of dynamic lattice theory (DLT),[49] the lattice constant at the interface (a_L), can be determined by the balance between the surface tension and the compression of the brush, leading to a simplified form that shows the dependence of the

lattice constant on PEG-AuNP concentration n_s and the surface tension between PEG and the high salt solution γ_{AB},

$$\frac{a_L}{2} = R_h\left[1 - c_1\left(\frac{\gamma_{AB}b^2}{k_BT} - c_2 \log\frac{n_s}{c_3}\right)^{1/3}\right], \tag{6.2}$$

where the constants c_1, c_2, c_3 can be identified in Equation S6.24. Although, considerable approximations are made to derive Equation 6.2, the formula illustrates the dependence of the lattice constant on surface tension and PEG-AuNP concentration n_s, in particular, the requirement that $\gamma_{AB}b^2/(k_BT) > c_2 \log(n_s/c_3)$, which sets a threshold on the lowest PEG-AuNP concentration where crystallization occurs. To apply Equation 6.2 (or the more rigorous Equation S6.23) a dependence of γ_{AB} on ionic strength is needed, which is expected to vary as $\gamma_{AB}b^2/(k_BT) \approx (v/b^3)^2 = (1-2\chi)^2$, where v is the excluded volume and $\chi > 1/2$ is the Flory parameter for PEG in the poor solvent high salt solution. Although attempts to determine χ have not been very successful,[50,51] see ref. 30 and 31, χ is an increasing function of ionic strength. We have fitted Equation 6.2 to a simple logarithmic dependence, $\gamma_{AB}b^2/(k_BT) = \tau \log(I/I_0)$ (where τ and I_0 are constants and I is the K_2CO_3 concentration; see ESI), which captures qualitatively well the dependence of the lattice constant at moderate salt concentrations, is not too high, assuming solvent quality between $0.51 < \chi < 0.65$. This is consistent with the assumption that the blob size is less than the thermal correlation length. Perhaps the most important result of our analysis is that the dependence of the surface tension on ionic strength is considerably stronger than a simple logarithm at high ionic strengths, which may lead to the assembly of PEG-AuNPs *via* colloidal destabilization into 3D supercrystals.

6.5 Conclusions

Using synchrotron X-ray diffraction at small angles (GISAXS) and X-ray reflectivity (XRR) we demonstrate that functionalized complexed PEG-AuNPs in aqueous solutions can spontaneously accumulate at the vapor-solution interface by manipulating salt concentrations in the bulk (K_2CO_3, in this case). At very low salt concentrations, the XRR indicates the formation of a mono-particle layer and the GISAXS patterns show features of a form factor characteristic of individually uncorrelated spherical particles. As the salt concentration increases, short-range 2D hexagonal order develops and above a threshold concentration, the complexes exhibit highly ordered hexagonal crystallinity. Furthermore, the size of the hexagonal unit cell formed by the long chain PEG_{6k}-AuNPs can be varied appreciably by increasing salt concentration, such that the incipient lattice parameter a_L can be varied from 39 to 25 nm for 0.005 to 1 M K_2CO_3, respectively. Similar unit cell shrinkage can also be achieved by manipulating the PEG_{6k}-AuNP concentration at a moderate 0.5 M K_2CO_3. For the shorter chain PEG_{800}-AuNPs, the threshold salt concentration for crystallinity is significantly higher than that of the longer PEG_{6k} and the range of varying the unit cell size is much narrower, $a_L \sim 15 \pm 1$ nm. Our detailed analysis reveals a nearly perfect surface coverage (close to 100%) of densely packed macroscopic crystalline domains (average domain size larger than micro-meter). These results show that the surface density (*i.e.*, unit-cell size) scales with the chain-length but more importantly they also reflect on the conformation of the corona formed by tethered PEG brushes on curved surfaces. In a salt free solution, the long chain PEG_{6k} corona is consistent with an infinitely long brush in θ-solvent. However, we find that the hydrodynamic radius of the PEG-AuNPs is practically independent of salt concentration (up to 0.5 M). Heuristically, this can be explained in terms of an effective semipermeable membrane surrounding the corona that maintains a constant salt

concentration up to the θ-point. Effectively, the PEG-AuNPs reside in a low salt concentration (liquid A) that is separated at the boundaries of the corona from high concentration salt (liquid B) with an effective surface tension γ_{AB} between the two liquids. Even though the surface tension energy per polymer is low (less than k_BT), thus preventing the polymer from shrinking, the overall surface tension for the entire PEG-AuNP is very large (of order of 100 k_BT or more for the PEG_{6k}-AuNPs) and drives the self-assembly and, through optimization of the packing of PEG chains, to crystallization. The tunability of the 2D hexagonal superlattice structure can be achieved over a very wide range by manipulating salt or PEG-AuNPs concentrations and also by the choice of polymer length. Here, we also provide a method to engineer 3D crystals, since sufficiently high salt or PEG-AuNP concentrations induce the formation of 3D precipitates (see Figure 6.5), which will be further explored and optimized in the future.

6.6 Acknowledgements

We thank Ivan Kuzmenko at beamline 9ID-B, APS, Argonne National Laboratory for technical support with the liquid surface scattering measurements. We acknowledge Xiaobin Zuo at beamline 12ID-B, APS, Argonne National Laboratory for technical support in measuring bulk SAXS. H. Z. thanks Prof. Mufit Akinc (Ames Laboratory and Iowa State University) for useful discussions on the phase diagram. Research was supported by the U.S. Department of Energy (U.S. DOE), Office of Basic Energy Sciences, Division of Materials Sciences and Engineering. Ames Laboratory is operated for the U.S. DOE by Iowa State University under Contract No. DE-AC02-07CH11358. Use of the Advanced Photon Source, an Office of Science User Facility operated for the U.S. DOE Office of Science by Argonne National Laboratory, was supported by the U.S. DOE under Contract No. DE-AC02-06CH11357.

6.7 Electronic Supplementary Information (ESI)

6.7.1 Control experiments

Figure S6.1 (a-d) shows a few GISAXS patterns from various solutions as control experiments to demonstrate the importance of functionalizing the AuNPs with PEG and the effect of salt on the formation of superlattice structures. None of the patterns indicate surface enrichment. Figure S6.2 shows SAXS measurements of PEG-AuNPs and unfunctionalized (bare) AuNPs dispersed in solution (conducted at Sector 12ID-B at the Advanced Photon Source). The analysis of the measured form factors determines the size and size-distribution of the AuNPs. These results demonstrate that the form factor is dominated by Au cores regardless of functionalization as the corona formed by PEG around the AuNP has practically the same electron density as that of the water solution (the SAXS data in Figure S6.2 are obtained after subtraction of the SAXS of the solvent). This is crucial to the analysis of the X-ray reflectivity analysis given in the main manuscript that shows the ED of the film is dominated by the AuNPs and the submerged corona is practically indistinguishable from the solution.

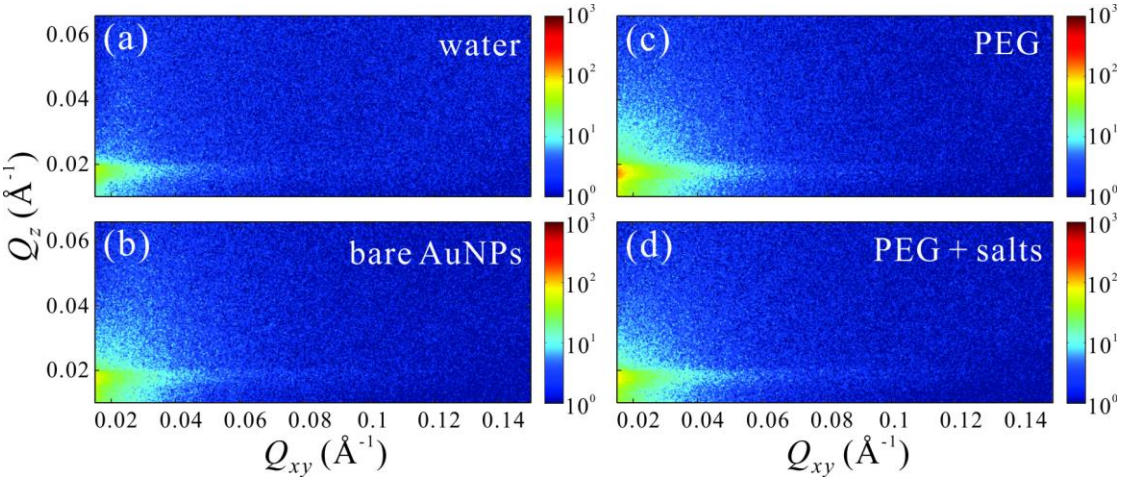

Figure S6.1 GISAXS patterns as functions of Q_{xy} and Q_z for (a) pure Millipore water, (b) aqueous solution of 10 nM bare AuNPs prior to PEG functionalization, (c) aqueous solution of 10 μM PEG_{6k}-SH with no salts and (d) PEG_{6k}-SH in 500 mM K_2CO_3. Intensities are displayed on logarithmic scales.

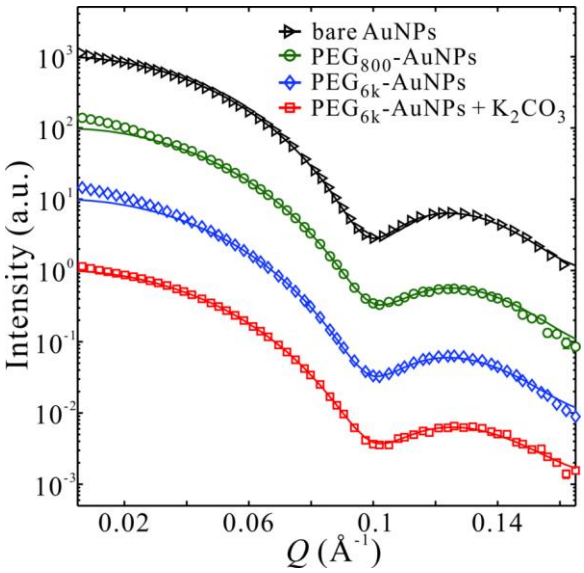

Figure S6.2 SAXS intensity profiles of aqueous suspension of unfunctionalized (bare) AuNPs (black triangles), PEG_{800}-AuNPs without salts (green circles), PEG_{6k}-AuNPs without salts (blue diamonds) and PEG_{6k}-AuNPs mixed with 500 mM K_2CO_3 (red squares). The solid lines are best fits using a form factor of spherical particles with polydispersity described by a Gaussian distribution. The size distributions of nanoparticles estimated by the best fits are D = 8.9 ± 0.8 nm (bare AuNPs), 8.7 ± 0.9 nm (PEG_{800}-AuNPs), 8.8 ± 0.9 nm (PEG_{6k}-AuNPs), and 8.7 ± 0.9 nm (PEG_{6k}-AuNPs with salts). These results show that the SAXS patterns are insensitive to the PEG shell around a AuNP (i.e., the corona) indicating that the electron density of the PEG corona in water solution is very close to that of pure water. The curves are vertically shifted for clarity.

6.7.2 Superlattice dependence on PEG_{6k}-AuNPs concentrations

In the main manuscript we show the tunability of the hexagonal superlattice by varyingsalt concentration. Figure S6.3 shows the GISAXS patterns from various concentrations of PEG_{6k}-AuNPs at a fixed 0.5 M of K_2CO_3. Our theoretical model shows a dependence of the lattice constant that is logarithmic in the AuNPs concentration.

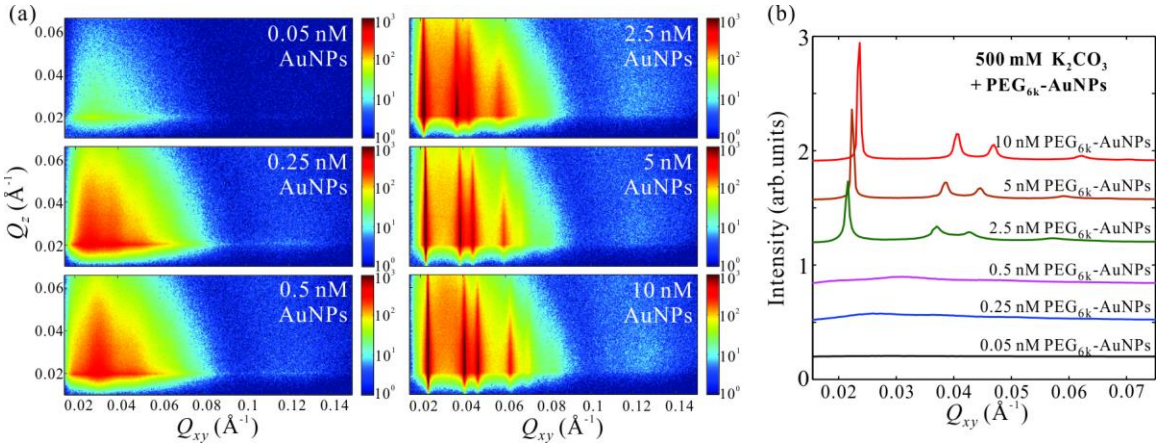

Figure S6.3 (a) GISAXS patterns as functions of Q_{xy} and Q_z for aqueous solutions of PEG_{6k}-AuNPs at different nanoparticle concentrations (0.05 – 10 nM) in the presence of 0.5 M K_2CO_3. Intensities are displayed on logarithmic scales. (b) Horizontal linecut profiles along Q_{xy} direction at Q_z = 0.020 Å^{-1} integrated over Q_z range 5 × 10^{-3} Å^{-1} at low Q_{xy} range (0.02–0.07 Å^{-1}) from GISAXS patterns in (a). The plots are vertically shifted for clarity.

6.7.3 Short chain PEG800-AuNPs crystallization

In this Section, we present the evolution of the Gibbs monolayer from the gas- to liquid- to superlattice-crystallization of PEG_{800}-AuNPs both as a function of salt concentration, Figure S6.4 and as a function of PEG-AuNP concentration, Figure S6.5. The analysis shows that the cr-

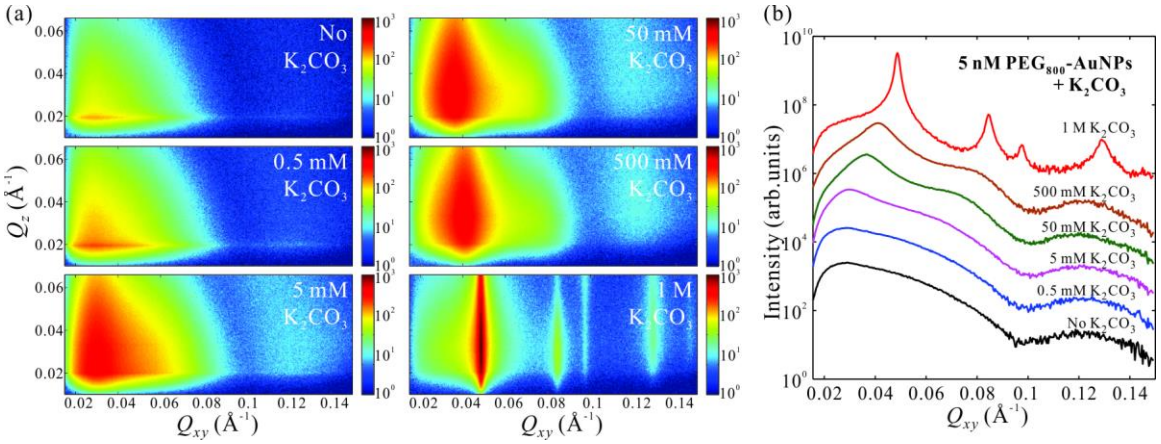

Figure S6.4 (a) GISAXS patterns as functions of Q_{xy} and Q_z for aqueous solutions of 5 nM PEG_{800}-AuNPs in the absence of salts and in the presence of different concentrations of K_2CO_3 (0.5 mM– 1 M). Intensities are displayed on logarithmic scales. (b) Horizontal linecut profiles along Q_{xy} direction at Q_z = 0.020 Å^{-1} integrated over Q_z range 5 × 10^{-3} Å^{-1} at low Q_{xy} range (0.02–0.07 Å^{-1}) from GISAXS patterns in (a). The plots are vertically shifted for clarity.

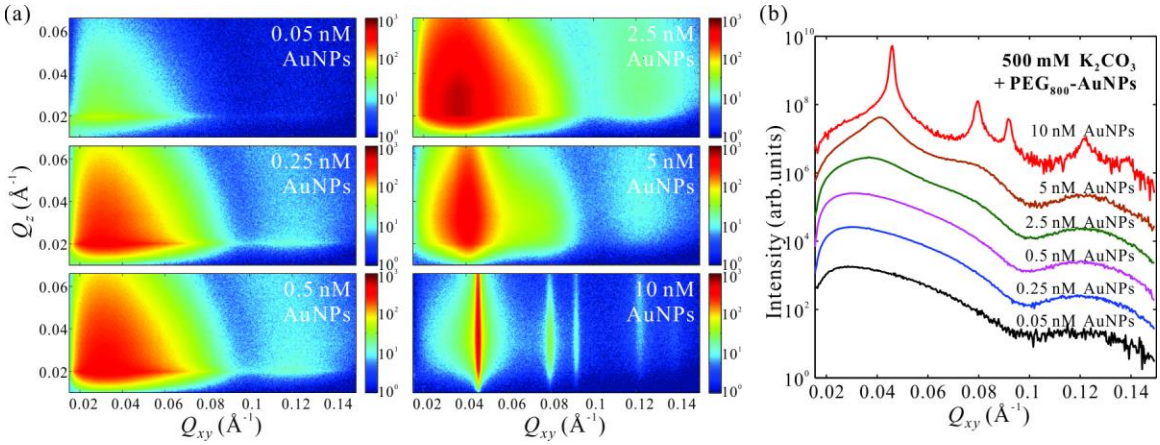

Figure S6.5 (a) GISAXS patterns as functions of Q_{xy} and Q_z for aqueous solutions of PEG_{800}-AuNPs with different nanoparticle concentrations (0.05 – 10 nM) in the presence of 0.5 M K_2CO_3. Intensities are displayed on logarithmic scales. (b) Horizontal linecut profiles along Q_{xy} direction at Q_z = 0.020 Å^{-1} integrated over Q_z range 5 × 10^{-3} Å^{-1} at low Q_{xy} range (0.02–0.07 Å^{-1}) from GISAXS patterns in (a). The plots are vertically shifted for clarity.

ystallization takes place only at much higher K_2CO_3 concentrations than for PEG6k-AuNPs and as expected the lattice constant scales with the length of PEG, thus the length of PEG can be used as a knob to tune the lattice constant as well.

6.7.4 Estimated surface coverage of crystalline PEG-AuNP superlattices

Here, we estimate the maximum in the electron density (ED) of monolayers of 2D crystalline PEG-AuNPs based on a space filling model using the known EDs of water and pure Au, and the 2D crystalline structures determined by GISAXS. We then compare our calculated maximum ED to the one obtained from the X-ray reflectivity (ρ_{max}) to estimate the macroscopic surface coverage of the 2D crystalline PEG-AuNPs.

We assume that in the mono-particle layer of the 2D crystalline, all AuNPs are perfectly packed in the same plane, leading to a maximum ED at the plane occupied by the centers of AuNPs as illustrated in Figure S6.6a. The corresponding sectional view at the maximum ED position is shown in Figure S6.6b. In this maximum ED plane, the area fraction of AuNPs in the unit cell of a 2D hexagonal crystalline is $\phi = A_{np}/A_{2D}$, where the area occupied by an AuNP is A_{np}

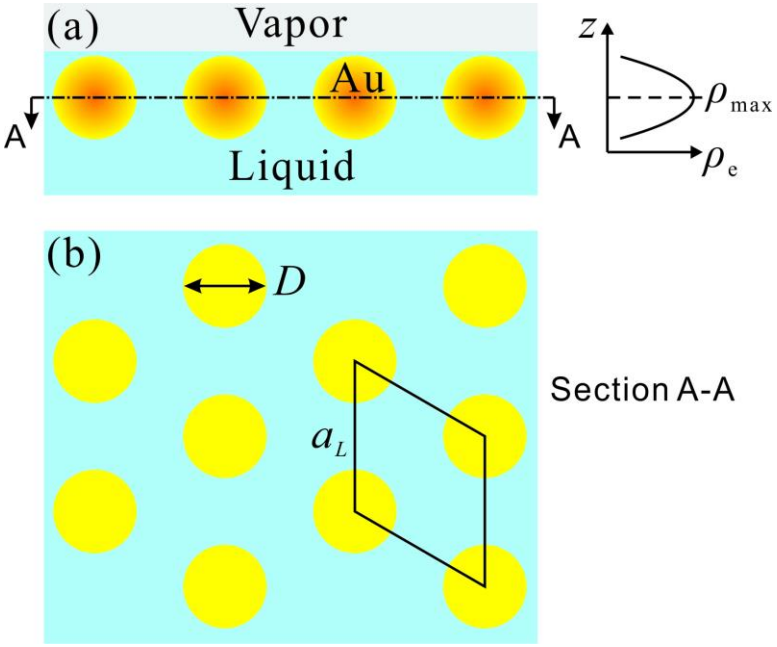

Figure S6.6 A schematic of a nanoparticle monolayer at the vapor-liquid interface with corresponding ED profile along surface-normal direction, associated with the sectional view at the maximum ED position.

Table S6.1 Maximum electron density of 2D PEG-AuNP superlattices at the vapor−liquid interface

PEG MW	n_s (nM)	[K_2CO_3] (M)	a_L (Å)	ρ_{K2CO3} (e/Å^3)	ρ_{2Dmax} (e/Å^3)	ρ_{max} (e/Å^3)	ψ
6000	5	0.005	388 ± 4	0.3342	0.532—0.540	~0.531	≥ 96%
6000	5	0.05	366 ± 5	0.3360	0.557—0.569	~0.557	≥ 95%
6000	5	0.5	322 ± 3	0.3545	0.641—0.652	~0.645	≥ 98%
6000	5	1	245 ± 2	0.3749	0.868—0.885	~0.695	≥ 63%
6000	2.5	0.5	338 ± 4	0.3545	0.613—0.626	~0.589	≥ 87%
6000	10	0.5	309 ± 3	0.3545	0.665—0.677	~0.617	≥ 81%
800	5	1	149 ± 1	0.3749	1.712—1.749	~1.322	≥ 69%
800	10	0.5	159 ± 3	0.3545	1.551—1.581	~1.783	~100%

$= \pi D^2/4$, and the area of a 2D unit cell with a lattice constant a_L is $A_{2D} = \sqrt{3}a_L^2/2$. The ED of pure gold is $\rho_{Au} = 79\rho N_A/M_{Au} = 4.66$ e/Å^3, where $\rho = 19.3$ g/cm^3, $N_A = 6.02 \times 10^{23}$ mol^{-1} and $M_{Au} = 196.97$ g/mol are bulk gold density, Avogadro number and atomic weight of gold, respectively.

The ED of subphase area surrounding the AuNPs (ρ_{sub}) is considered as ED of pure K_2CO_3 solution with the same concentration to the bulk (contribution of the PEG shell to the ED is the same as that of surrounding media, which is justified by our SAXS results; see Figure S6.2). Assuming that K_2CO_3 solids dissolved in pure water increase the ED of aqueous solution without changing the solution volume, the ED of K_2CO_3 solution at the concentration of c (in Molar) is estimated to be $\rho_{K2CO3} = \rho_w + 68cN_A/10^{27} = 0.334 + 0.0410c$ e/Å^3. Using the space filling model, the maximum ED of 2D crystalline structure is $\rho_{2Dmax} = \rho_{Au}\phi + \rho_{sub}(1-\phi)$. The calculated maximum ED results are summarized in Table S6.1 below. Overall, the estimates are close to the results measured by XRR. Applying the calculated ρ_{2Dmax} and the measured maximum ED ρ_{max} extracted from XRR, the surface coverage of 2D crystalline is $\psi = (\rho_{max}-\rho_{sub})/(\rho_{2Dmax}-\rho_{sub})$ (See Table S6.1). The surface coverage is nearly 100%. We note that in this simple model the surface coverage of 2D crystalline is underestimated owing to the assumption of perfect lateral packing of AuNPs in the same plane and the negligence of surface roughness.

6.7.5 Hydrodynamic size of AuNPs and PEG-AuNPs in salts

Using dynamic light scattering we estimate the hydrodynamic size of bare and PEG-capped particles. Unlike polyelectrolyte-capped AuNPs (including ssDNA-AuNPs), as shown in Figure S6.7, the hydrodynamic size distribution of PEG-AuNPs remains practically the same in the presence of salts. This also shows that the polymer in PEG_{800}-AuNPs is too short to behave like the theoretically infinitely long polymer brush.

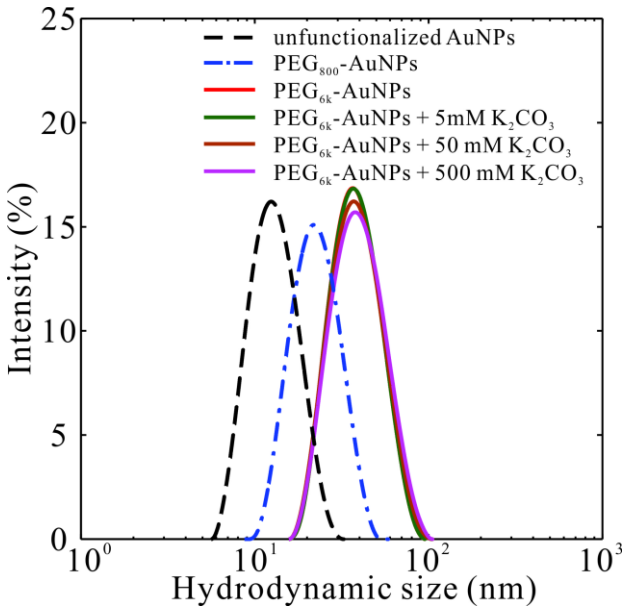

Figure S6.7 Dynamic light scattering (DLS) measurements of unfunctionalized AuNPs, PEG_{800}-AuNPs and PEG_{6k}-AuNPs dispersed in the bulk solution under different conditions as indicated. The AuNPs with PEG shells clearly show larger hydrodynamic size than that of the bare Au cores (unfunctionalized AuNPs). In addition, DLS results of PEG_{6k}-AuNPs with or without K_2CO_3 indicate that the presence of K_2CO_3 in the solution (up to 0.5 M) have little effect on the hydrodynamic size of nanoparticles in the bulk.

6.7.6 Grafting density of PEG on AuNPs

Thermogravimetric analysis (TGA) is used to estimate the grafting density of PEG on AuNPs. The concentrated PEG-AuNPs is dried at 60°C for 4 hours prior to TGA measurements. The TGA is carried out under a nitrogen atmosphere from 25 to 800°C at a ramp rate of 10°C/min. The weight loss between 300°C and 450°C corresponds to the thermal degradation of the PEG. For instance, the weight loss of PEG_{6k}-AuNPs as function of temperature is shown in Figure S6.8. The weight percentage at 300°C and 450°C are 94.66% and 61.96%, respectively. Therefore, 32.70% of weight is related to the PEG_{6k} loaded on AuNPs, and 61.96% of weight is from pure AuNPs. The weight of each AuNP is $m_{np} = \rho\pi D^3/6$, where ρ = 19.3 g/cm^3 is bulk gold density, D = 8.8 ± 0.9 nm is the diameter of the AuNP. The molecular weight of PEG_{6k} is m_{PEG} =

6000. Thus, the number of PEG_{6k} per AuNP is n = (32.70 m_{np})/(61.96 m_{PEG}) = 367. The grafting density is $\sigma = n/(\pi D^2)$ = 1.51 chains/nm^2.

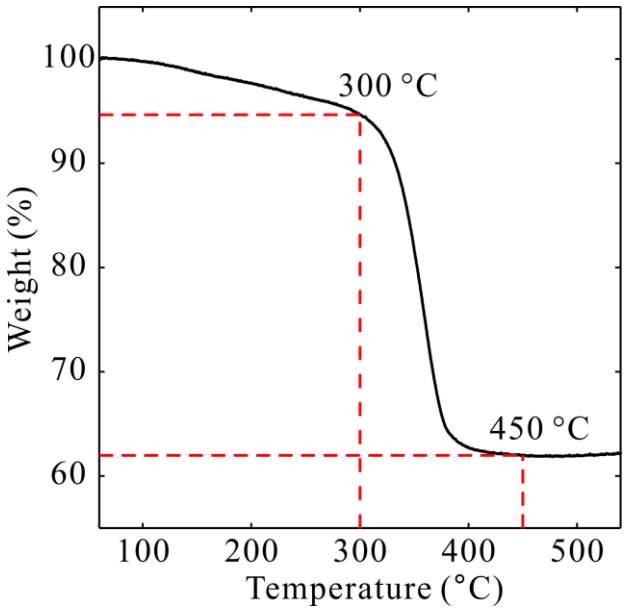

Figure S6.8 Weight loss of PEG_{6k}-AuNPs as function of temperature. The weight loss between 300°C and 450°C corresponds to the thermal degradation of the PEG.

6.7.7 Theoretical Model

6.7.7.1 Physical parameters of PEG

There is a considerable range of values for the Kuhn length, Flory characteristic ratio C_n and Kuhn monomer mass M_0 in the literature. The values used here are calculated from Mark and Flory[44], who report the values for PEG (also called PEO) in salt at the θ-point, the exact conditions analyzed in this paper, as

$$\left\langle r^2 \right\rangle / ml^2 = C_\infty = 4.1(0.4), \tag{S6.1}$$

where $\left\langle r^2 \right\rangle$ is the mean square unperturbed end-to-end distance for a real chain, $l^2=(2l_{co}^2+l_{cc}^2)/3.0$ and l_{co}=1.43 Å, l_{cc}=1.53 Å are the O−C and C−C bond lengths, and $m=3N_r$ is

the number of bonds and N_r is the number of C−C−O groups in the polymer. The maximum extension of a PEO chain is therefore

$$R_{\max} = (2l_{co} + l_{cc})\cos(\theta/2)N_r = 3.64N_r \text{ (Å)}, \quad \text{(S6.2)}$$

where θ=68° is the bond angle, which is the same for all three atoms in the monomer. The Kuhn length is[47]

$$b = \frac{C_\infty l^2 m}{R_{\max}} = 7.24 \text{ (Å)} \quad \text{(S6.3)}$$

and the equivalent number of monomers of a Gaussian chain is

$$N = \frac{R_{\max}^2}{C_\infty l^2 m} = 0.503N_r . \quad \text{(S6.4)}$$

Using that the molecular weight of a PEO monomer is $M_1 = 2M_C + M_O + 4M_H$=44.052, it is

$$M_0 = M_1 / 0.503 = 87.6 . \quad \text{(S6.5)}$$

Thus for the two PEO used in this paper, the number of independent Kuhn monomers is

$$N_{6k} = 6000/87.6 = 68.5 \, (N_r = 136), \quad \text{(S6.6)}$$

$$N_{800} = 800/87.6 = 9.13 \, (N_r = 18). \quad \text{(S6.7)}$$

For the PEG_{800}, the approximation $C_n \approx C_\infty$ is certainly questionable, and explains the larger hydrodynamic radius than the theoretical estimate.

6.7.7.2 PEG-AuNPs in solution

As described in refs,[30,31] the three component system water-salt-PEG typically separates into two phases, an all PEG solvated by liquid A and liquid B. Liquid A consists of water and a relatively low salt concentration (a few percent weight or less), and liquid B with a higher salt concentration of ten percent or more. Early efforts to predict the phase diagram of this three component system showed a limited success[50,51] as it was noted that there is a specific salt-PEG

interaction, presumably through the ether oxygens and the salt cations. Therefore, we consider a model where the salt is implicit, based on the following assumptions:

- Liquid A is a θ-solvent for PEG.
- Liquid B is a poor solvent for PEG.
- When equilibrium is established, an interface between liquid A and liquid B is formed with surface tension γ_{AB}.

The first assumption is justified as liquid A is the phase boundary for PEG. The second assumption follows from the fact that no PEG is found in liquid.[30,31]

We consider a PEG-AuNP as consisting of n flexible chains with N monomers covalently grafted at the surface of the nanoparticle core, whose radius is R. The grafting density is thus $\sigma = n/(4\pi R^2)$. We first treat PEG-AuNPs in solution and then its crystallization at the interface.

Following ref. 46, we consider PEG as Gaussian chains with three-body interactions at the θ-point (first assumption). The monomer density at a distance r from the center is given (for $r > R$)

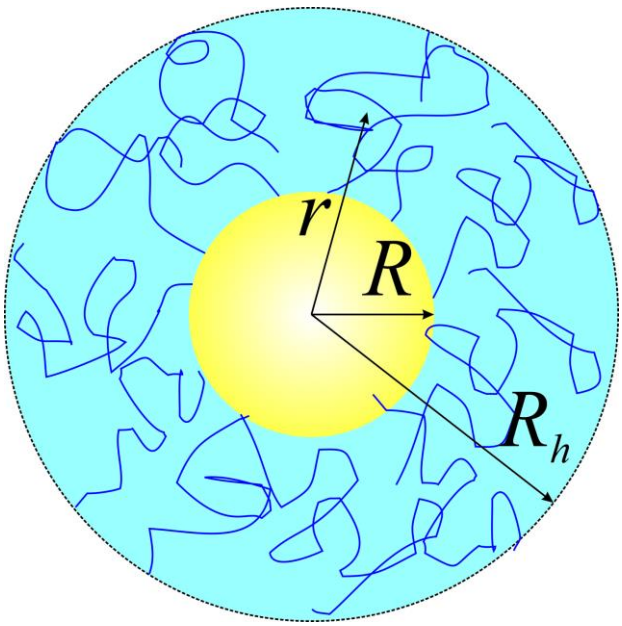

Figure S6.9 Depiction of PEG-AuNP brush, and the parameters used

$$\phi(r) = \frac{R}{r}\left(\sigma b^2\right)^{1/2}\left(2w_0\right)^{-1/4}, \tag{S6.8}$$

where b is the Kuhn length, σ is the grafting density and w_0 is the dimensionless three-body interaction. The spherical radii R_h is obtained by imposing that the integral of the above density is equal to the total number of monomers, Nnb^3, leading

$$\left(\frac{R_h}{R}\right)^2 = 1 + 2\frac{Nb^2\sigma^{1/2}}{R}\left(2w_0\right)^{1/4}. \tag{S6.9}$$

For future reference, we will also need the free energy for the spherical brush at the θ point. It is given as

$$\frac{f_r}{k_B T} = 4\pi\left(\frac{R}{b}\right)^3\left(\sigma b^2\right)^{3/2}\left(2w_0\right)^{1/4}\log\left[1 + 2\frac{Nb^2\sigma^{1/2}}{R}\left(2w_0\right)^{1/4}\right]. \tag{S6.10}$$

To this free energy, there is an additional term that arises from the surface tension between polymer/liquid A and liquid B. We will assume that liquid B is a slightly poor solvent for PEG. This latter condition is defined by $\xi(r = R_h) < \xi_T$, where $\xi(r) = r/R\sqrt{\sigma}$ and $\xi_T = b/(2\chi - 1)$ is the thermal correlation length,[47] and $\chi > 1/2$ parameterizes the quality of solvent B to PEG. In the opposite limit $\xi(r = R_h) > \xi_T$, which is not discussed here, PEG would collapse into globules, and the size of the PEG-AuNPs is not described by Equation S6.8. The surface tension free energy is given by

$$f_s = \gamma_{AB} 4\pi R_h^2. \tag{S6.11}$$

Based on general arguments, we expect $\gamma_{AB} \approx k_B T(2\chi - 1)^2/b^2$.

Finally, because the PEG-AuNPs are in solution, there is the ideal term

$$F_t = N_s k_B T\left[\log\left(n_s v_0\right) - 1\right], \tag{S6.12}$$

where N_s is the number of PEG-AuNPs in solution and $n_s = N_s/V$ its number density. The chemical potential of the bulk PEG-AuNPs is given by

$$\mu_B = \frac{\partial F}{\partial N_s} = f_r + f_s + k_B T \log\left(n_s v_0\right). \tag{S6.13}$$

6.7.7.3 PEG-AuNPs at the interface

At the interface, the free energy of the PEG-AuNPs is modified in three ways: the brushes are compressed, the surface area of contact with solvent B is much reduced, and finally, there is a reduction of translational entropy.

The stretching energy of two compressed brushes has been authoritative reviewed in ref 48. Unfortunately, no simple expression is available for the experimental conditions, and a full calculation is beyond the scope of this paper. Therefore, we opt for a more heuristic derivation, based on the modified Derjaguin approximation for the excess free energy

$$F_e(z) = 2\pi R^2 (R+z) \int_z^{H_0} \frac{f(H) - f(H_0)}{(R+H)^2} \mathrm{d}H \equiv 2\pi R^2 (R+z) \int_z^{H_0} \frac{\Delta f(H)}{(R+H)^2} \mathrm{d}H \,. \tag{S6.14}$$

Here, $2(R + z)$ is the center-to-center distance of the two brushes and $H_0 = R_h - R$ is the uncompressed brush height. The quantity $f(H)$ is the free energy per unit area of a uniformly compressed spherical brush at a radius $H < H_0$. It is given as

$$\Delta f(y) = \frac{R}{b} \left(\sigma b^2\right)^{3/2} (2w_0)^{1/4} \frac{1}{b^2} G(y) \,, \tag{S6.15}$$

where $y = (R + z)/R_h$. Note that the function $G(x)$ satisfies that $G'(1) = 0$, $G''(1) \approx 32.6 > 0$, and the latter condition is the statement that the uncompressed brush is a minimum of the free energy. Detailed derivations for these results will be published elsewhere. The actual potential between two PEG-AuNPs is then given as

$$F_e(z) = 2\pi \left(\frac{R}{b}\right)^3 \left(\sigma b^2\right)^{3/2} (2w_0)^{1/4} yH(y) \,, \tag{S6.16}$$

where $H(y)=\int_y^1 \frac{dw}{w^2} G(w)$, and $G(y)$ has been defined in the previous equation. Note that $H(1) = H'(1) = H''(1) = 0$. For small compressions, $1 - y << 1$, the above expression reduces to

$$F_e(z) = 2\pi\left(\frac{R}{b}\right)^3 (\sigma b^2)^{3/2} (2w_0)^{1/4} \frac{G''(1)}{6}(1-y)^3 \ . \quad \text{(S6.17)}$$

It should be noted, however, that the exact formula shows that the approximation Equation S6.17 has a small range of applicability as the resulting potential quickly picks up significant non-harmonic contributions for $y \leq 0.85$.

We assume that the surface in contact with solvent B is the area of the plane occupied by the PEG-AuNPs at the interface. The free energy of a single nanoparticle is given as

$$F_s(z) = \gamma_{AB} 2\sqrt{3}(R+z)^2 \ . \quad \text{(S6.18)}$$

Finally, the entropic term is given, within dynamic lattice theory (DLT),[49]

$$F_d(z) = k_B T\left[g(R_h) + \log v_0\right] , \quad \text{(S6.19)}$$

where $g(z)=\frac{1}{2N_i}\log\left[\det\left(\frac{D_{ij}}{2\pi k_B T}\right)\right]$, where N_i is the number of particles at the interface and D_{ij} is the dynamical matrix. Although it is possible to calculate the above determinant exactly for a hexagonal two dimensional lattice, the formula is excessively complex. We therefore make the free volume approximation

$$F_d(z) = k_B T \log[\, v_0 /(4\pi y^2 R_h^3 / 3)] \ . \quad \text{(S6.20)}$$

The chemical potential of the PEG-Au at the interface is given by

$$\mu_I = F_s(z) + qF_e(z) + F_r + k_B T \log[\, v_0 /(4\pi y^2 R_h^3 / 3)] . \quad \text{(S6.21)}$$

6.7.7.4 Equilibrium condition

The condition of equilibrium between bulk and interface leads to the equation

$$\mu_I = \mu_B \ , \tag{S6.22}$$

or, in explicit form,

$$\begin{aligned}\left(4\pi - 2\sqrt{3}\right)\frac{\gamma_{AB}}{k_B T} R_h^2 + \log\left(\frac{4\pi n_s R_h^3}{3}\right) = \\ -2\sqrt{3}\,\frac{\gamma_{AB}}{k_B T} R_h^2\left(1-y^2\right) + 2\pi\left(\frac{R}{b}\right)^3 \left(\sigma b^2\right)^{3/2}\left(2w_0\right)^{1/4} yH(y) - \log\left(y^2\right)\end{aligned} \ , \tag{S6.23}$$

which determines y, and from it, the lattice constant a_L from $y = (2R_h - a_L)/(2R_h)$, as a function of the physical parameters. The above equations illustrate a physical mechanism where the dramatic reduction in surface tension that occurs when particles reach the interface entirely drives the crystallization process.

For the purposes of illustrating the physical mechanism, one can assume that the reduction of surface tension is opposed by the stretching or compression energy, and that the small compression limit Equation S6.17 can be applied. With these approximations, it follows:

$$\left(1-\frac{a_L}{2R_h}\right)^3 = \left(4-\frac{2\sqrt{3}}{\pi}\right)\frac{6N}{\sigma R^2 qG''(1)}\left(\frac{\gamma_{AB} b^2}{k_B T} + \frac{b/R\log(n_s v_l)}{(8\pi - 4\sqrt{3})N(\sigma b^2)^{1/2}(2w_0)^{1/4}}\right), \tag{S6.24}$$

which $v_l = 4\pi R_h^3/3$.

6.7.7.5 Quality of the solvent

From the reported values of $(2R_h - a_L)/(2R_h)$ (Table S6.1), and the assumption that the solvent quality parameter is described by the two parameter formula

$$\gamma_{AB} b^2/(k_B T) = \tau \log(I/I_0) \ , \tag{S6.25}$$

a fit is performed, with I_0 = 0.0046 M and τ = 0.0021. Here I is the K_2CO_3 concentration, i.e., [K_2CO_3]. Although the quality of the fit is adequate up to about 0.5 M, it illustrates that the data is consistent with a moderately poor solvent, not far from ideal. The point at the higher salt concentration illustrates that the surface tension grows more rapidly than the logarithmic fit Equation S6.25 at high ionic strengths consistent with the onset of precipitates into 3D solids.

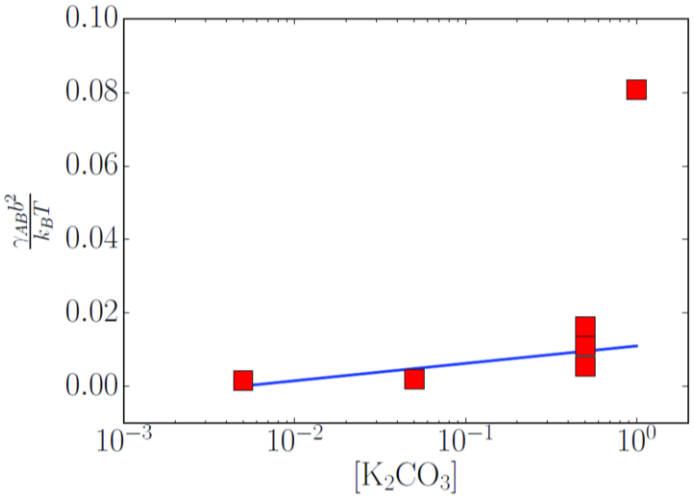

Figure S6.10 Fit of the solvent quality as described below. The results are for PEG_{6k}-AuNPs. Clearly, the last point, corresponding to 1 M K_2CO_3 concentration, is not consistent with a simple logarithmic dependence.

References

1. Shevchenko, E. V.; Talapin, D. V.; Kotov, N. A.; O'Brien, S.; Murray, C. B. Structural diversity in binary nanoparticle superlattices. *Nature* 2006, 439, 55-59.
2. Zhang, Y.; Lu, F.; Yager, K. G.; van der Lelie, D.; Gang, O. A general strategy for the DNA-mediated self-assembly of functional nanoparticles into heterogeneous systems. *Nat. Nanotechnol.* 2013, 8, 865-872.
3. Young, K. L.; Ross, M. B.; Blaber, M. G.; Rycenga, M.; Jones, M. R.; Zhang, C.; Senesi, A. J.; Lee, B.; Schatz, G. C.; Mirkin, C. A. Using DNA to Design Plasmonic Metamaterials with Tunable Optical Properties. *Adv. Mater.* 2014, 26, 653-659.
4. Nykypanchuk, D.; Maye, M. M.; van der Lelie, D.; Gang, O. DNA-guided crystallization of colloidal nanoparticles. *Nature* 2008, 451, 549-552.
5. Park, S. Y.; Lytton-Jean, A. K. R.; Lee, B.; Weigand, S.; Schatz, G. C.; Mirkin, C. A. DNA-programmable nanoparticle crystallization. *Nature* 2008, 451, 553-556.
6. Macfarlane, R. J.; Lee, B.; Jones, M. R.; Harris, N.; Schatz, G. C.; Mirkin, C. A. Nanoparticle Superlattice Engineering with DNA. *Science* 2011, 334, 204-208.

7. Liu, W.; Tagawa, M.; Xin, H. L.; Wang, T.; Emamy, H.; Li, H.; Yager, K. G.; Starr, F. W.; Tkachenko, A. V.; Gang, O. Diamond family of nanoparticle superlattices. *Science* 2016, 351, 582-586.
8. Cheng, W.; Hartman, M. R.; Smilgies, D.-M.; Long, R.; Campolongo, M. J.; Li, R.; Sekar, K.; Hui, C.-Y.; Luo, D. Probing in Real Time the Soft Crystallization of DNA-Capped Nanoparticles. *Angew. Chem. Int. Ed.* 2010, 49, 380-384.
9. Narayanan, S.; Wang, J.; Lin, X.-M. Dynamical Self-Assembly of Nanocrystal Superlattices during Colloidal Droplet Evaporation by \textit{in situ} Small Angle X-Ray Scattering. *Phys. Rev. Lett.* 2004, 93, 135503.
10. Bigioni, T. P.; Lin, X.-M.; Nguyen, T. T.; Corwin, E. I.; Witten, T. A.; Jaeger, H. M. Kinetically driven self assembly of highly ordered nanoparticle monolayers. *Nat. Mater.* 2006, 5, 265-270.
11. Schultz, D. G.; Lin, X.-M.; Li, D.; Gebhardt, J.; Meron, M.; Viccaro, J.; Lin, B. Structure, Wrinkling, and Reversibility of Langmuir Monolayers of Gold Nanoparticles. *J. Phys. Chem. B* 2006, 110, 24522-24529.
12. Tao, A.; Sinsermsuksakul, P.; Yang, P. Tunable plasmonic lattices of silver nanocrystals. *Nat. Nanotechnol.* 2007, 2, 435-440.
13. Aleksandrovic, V.; Greshnykh, D.; Randjelovic, I.; Frömsdorf, A.; Kornowski, A.; Roth, S. V.; Klinke, C.; Weller, H. Preparation and Electrical Properties of Cobalt−Platinum Nanoparticle Monolayers Deposited by the Langmuir−Blodgett Technique. *ACS Nano* 2008, 2, 1123-1130.
14. Siffalovic, P.; Chitu, L.; Majkova, E.; Vegso, K.; Jergel, M.; Luby, S.; Capek, I.; Satka, A.; Maier, G. A.; Keckes, J.; Timmann, A.; Roth, S. V. Kinetics of Nanoparticle Reassembly Mediated by UV-Photolysis of Surfactant. *Langmuir* 2010, 26, 5451-5455.
15. Heitsch, A. T.; Patel, R. N.; Goodfellow, B. W.; Smilgies, D.-M.; Korgel, B. A. GISAXS Characterization of Order in Hexagonal Monolayers of FePt Nanocrystals. *J. Phys. Chem. C* 2010, 114, 14427-14432.
16. Stefaniu, C.; Chanana, M.; Wang, D.; Novikov, D. V.; Brezesinski, G.; Möhwald, H. Biocompatible Magnetite Nanoparticles Trapped at the Air/Water Interface. *ChemPhysChem* 2010, 11, 3585-3588.
17. Stefaniu, C.; Chanana, M.; Wang, D.; Novikov, D. V.; Brezesinski, G.; Möhwald, H. Langmuir and Gibbs Magnetite NP Layers at the Air/Water Interface. *Langmuir* 2011, 27, 1192-1199.
18. Stefaniu, C.; Chanana, M.; Wang, D.; Brezesinski, G.; Möhwald, H. Stimuli-Responsive Magnetite Nanoparticle Monolayers. *J. Phys. Chem. C* 2011, 115, 5478-5484.
19. Stefaniu, C.; Chanana, M.; Ahrens, H.; Wang, D.; Brezesinski, G.; Mohwald, H. Conformational induced behaviour of copolymer-capped magnetite nanoparticles at the air/water interface. *Soft Matter* 2011, 7, 4267-4275.
20. Mahmoud, M. A.; O'Neil, D.; El-Sayed, M. A. Hollow and Solid Metallic Nanoparticles in Sensing and in Nanocatalysis. *Chem. Mater.* 2014, 26, 44-58.
21. Mahmoud, M. A. Effective Optoelectrical Switching by Using Pseudo-Single Crystal of Monolayer Array of 2D Polymer–Plasmonic Nanoparticles System. *J. Phys. Chem. C* 2015, 119, 29095-29104.
22. Campolongo, M. J.; Tan, S. J.; Smilgies, D.-M.; Zhao, M.; Chen, Y.; Xhangolli, I.; Cheng, W.; Luo, D. Crystalline Gibbs Monolayers of DNA-Capped Nanoparticles at the Air–Liquid Interface. *ACS Nano* 2011, 5, 7978-7985.

23. Tan, S. J.; Kahn, J. S.; Derrien, T. L.; Campolongo, M. J.; Zhao, M.; Smilgies, D.-M.; Luo, D. Crystallization of DNA-Capped Gold Nanoparticles in High-Concentration, Divalent Salt Environments. *Angew. Chem. Int. Ed.* 2014, 53, 1316-1319.
24. Zhang, H.; Wang, W.; Hagen, N.; Kuzmenko, I.; Akinc, M.; Travesset, A.; Mallapragada, S.; Vaknin, D. Self-Assembly of DNA Functionalized Gold Nanoparticles at the Liquid-Vapor Interface. *Adv. Mater. Interfaces* 2016, 3, 1600180.
25. Srivastava, S.; Nykypanchuk, D.; Fukuto, M.; Gang, O. Tunable Nanoparticle Arrays at Charged Interfaces. *ACS Nano* 2014, 8, 9857-9866.
26. Srivastava, S.; Nykypanchuk, D.; Fukuto, M.; Halverson, J. D.; Tkachenko, A. V.; Yager, K. G.; Gang, O. Two-Dimensional DNA-Programmable Assembly of Nanoparticles at Liquid Interfaces. *J. Am. Chem. Soc.* 2014, 136, 8323-8332.
27. Wang, W.; Zhang, H.; Kuzmenko, I.; Mallapragada, S.; Vaknin, D. Assembling Bare Au Nanoparticles at Positively Charged Templates. *Sci. Rep.* 2016, 6, 26462.
28. Israelachvili, J. The different faces of poly(ethylene glycol). *Proc. Natl. Acad. Sci. USA* 1997, 94, 8378-8379.
29. Zhou, J.; Ke, F.; Tong, Y.-y.; Li, Z.-c.; Liang, D. Solution behavior of copolymers with poly(ethylene oxide) as the "hydrophobic" block. *Soft Matter* 2011, 7, 9956-9961.
30. Willauer, H. D.; Huddleston, J. G.; Rogers, R. D. Solute Partitioning in Aqueous Biphasic Systems Composed of Polyethylene Glycol and Salt: The Partitioning of Small Neutral Organic Species. *Ind. Eng. Chem. Res.* 2002, 41, 1892-1904.
31. Huddleston, J. G.; Willauer, H. D.; Rogers, R. D. Phase Diagram Data for Several PEG + Salt Aqueous Biphasic Systems at 25 °C. *J. Chem. Eng. Data* 2003, 48, 1230-1236.
32. Walter, H. *Partitioning In Aqueous Two – Phase System: Theory, Methods, Uses, And Applications To Biotechnology*. Elsevier Science: 2012.
33. Choi, C. H. J.; Zuckerman, J. E.; Webster, P.; Davis, M. E. Targeting kidney mesangium by nanoparticles of defined size. *Proc. Natl. Acad. Sci. USA* 2011, 108, 6656-6661.
34. Zhang, X.-D.; Wu, D.; Shen, X.; Chen, J.; Sun, Y.-M.; Liu, P.-X.; Liang, X.-J. Size-dependent radiosensitization of PEG-coated gold nanoparticles for cancer radiation therapy. *Biomaterials* 2012, 33, 6408-6419.
35. Rahme, K.; Chen, L.; Hobbs, R. G.; Morris, M. A.; O'Driscoll, C.; Holmes, J. D. PEGylated gold nanoparticles: polymer quantification as a function of PEG lengths and nanoparticle dimensions. *RSC Adv.* 2013, 3, 6085-6094.
36. Vaknin, D. X-Ray Diffraction and Spectroscopic Techniques for Liquid Surfaces and Interfaces. In *Characterization of Materials*, John Wiley & Sons, Inc.: 2002.
37. Zhang, H.; Liu, X.; Feng, S.; Wang, W.; Schmidt-Rohr, K.; Akinc, M.; Nilsen-Hamilton, M.; Vaknin, D.; Mallapragada, S. Morphological Transformations in the Magnetite Biomineralizing Protein Mms6 in Iron Solutions: A Small-Angle X-ray Scattering Study. *Langmuir* 2015, 31, 2818-2825.
38. Winterhalter, M.; Bürner, H.; Marzinka, S.; Benz, R.; Kasianowicz, J. J. Interaction of poly(ethylene-glycols) with air-water interfaces and lipid monolayers: investigations on surface pressure and surface potential. *Biophys. J.* 1995, 69, 1372-1381.
39. Prasitnok, K.; Wilson, M. R. A coarse-grained model for polyethylene glycol in bulk water and at a water/air interface. *Phys. Chem. Chem. Phys.* 2013, 15, 17093-17104.
40. Fuchs, C.; Hussain, H.; Amado, E.; Busse, K.; Kressler, J. Self-Organization of Poly(ethylene oxide) on the Surface of Aqueous Salt Solutions. *Macromol. Rapid Commun.* 2015, 36, 211-218.

41. Als-Nielsen, J.; McMorrow, D. *Elements of modern X-ray physics*. John Wiley & Sons: 2011.
42. Pershan, P. S.; Schlossman, M. *Liquid Surfaces and Interfaces: Synchrotron X-ray Methods*. Cambridge University Press: 2012.
43. Tolan, M. *X-Ray Scattering from Soft-Matter Thin Films: Materials Science and Basic Research*. Springer Berlin Heidelberg: 1998.
44. Mark, J. E.; Flory, P. J. The Configuration of the Polyoxyethylene Chain. *J. Am. Chem. Soc.* 1965, 87, 1415-1423.
45. Daoud, M.; Cotton, J. P. Star shaped polymers : a model for the conformation and its concentration dependence. *J. Phys. France* 1982, 43, 531-538.
46. Wijmans, C. M.; Zhulina, E. B. Polymer brushes at curved surfaces. *Macromolecules* 1993, 26, 7214-7224.
47. Rubinstein, M.; Colby, R. H. *Polymer Physics*. Oxford University Press: 2003.
48. Binder, K.; Milchev, A. Polymer brushes on flat and curved surfaces: How computer simulations can help to test theories and to interpret experiments. *J. Polym. Sci., Part B: Polym. Phys.* 2012, 50, 1515-1555.
49. Travesset, A. Phase diagram of power law and Lennard-Jones systems: Crystal phases. *J . Chem. Phys.* 2014, 141, 164501.
50. Hino, T.; Prausnitz, J. M. Lattice thermodynamics for aqueous salt–polymer two-phase systems. *J. Appl. Polym. Sci.* 1998, 68, 2007-2017.
51. Kenkare, P. U.; Hall, C. K. Modeling of phase separation in PEG–salt aqueous two-phase systems. *AIChE J.* 1996, 42, 3508-3522.

CHAPTER 7. THREE-DIMENSIONAL ASSEMBLIES OF POLYMER-GRAFTED NANOPARTICLES

Modified from a paper to be submitted

Honghu Zhang, Wenjie Wang, Mufit Akinc, Surya Mallapragada, Alex Travesset, and David Vaknin*

7.1 Abstract

Taking advantage of aqueous biphasic systems of polyethylene glycol (PEG)/salts, it has been demonstrated recently that PEG-grafted gold nanoparticles (PEG-AuNPs) self-assemble and crystallize into highly ordered and tunable hexagonal structures at the liquid-vapor interfaces by adjusting salt concentration (i.e., K_2CO_3) of an aqueous PEG-AuNP suspension. Experimental phase diagrams and a theoretical model indicate that high salt concentrations can lead to three-dimensional (3D) ordered nanoparticle precipitates. Analysis of small-angle X-ray scattering (SAXS) profiles shows that the assemblies exhibit 3D crystallinity albeit of short-range order compatible with the FCC symmetry. We argue that the assembly into FCC crystals at high salt concentrations is most likely driven by the nucleation in the bulk *via* colloidal destabilization. We have functionalized AuNPs of various diameters in the range of 10 to 50 nm and found a strong correlation between nearest-neighbors distances and the diameter of the AuNPs. Brush-polymer theoretical modeling of the SAXS results reveals that the nearest-neighbor distance was governed by the size of inorganic core, the intrinsic characteristics of the polymer (Kuhn length

* Corresponding Author: vaknin@ameslab.gov

and the number of independent Kuhn monomers) and the polymer grafting density that was found to systematically decrease with the size of inorganic core.

7.2 Introduction

State-of-the-art developments of nanoparticle synthesis and post-synthetic modification enable self-organizing individual nanoparticles into macroscopic superlattices with a diversity of structures, similar to atoms in crystals.[1] Such nanoparticle assemblies possess intriguingly collective photonic, electronic, magnetic and catalytic properties that are different from those of individual ones, and exhibit great potential in technological applications.[2-5] Albeit numerous strategies for self-assembly of nanoparticles in two and three dimensions (2D and 3D), the self-assembly process is governed by nanoparticle size and shape, and interparticle interactions which are influenced by the assembly environment.[6] For instance, gold nanoparticles functionalized with DNA self-assemble into 2D and 3D superlattices by exploiting charge-charge interaction and unique hybridization feature, respectively.[7-17] Meanwhile, hydrocarbon- and polymer-capped nanoparticles form 2D and 3D assemblies on solid supports via careful evaporation of organic solvents.[18-26] Recently, by simply manipulating salt levels of the aqueous solutions, DNA- and polymer-grafted nanoparticles were reported to spontaneously form crystalline Gibbs monolayers at the liquid-vapor interfaces.[27-30] In particular, 2D nanoparticles superlattices with highly ordered hexagonal structures were developed by introducing a salt (i.e., K_2CO_3) to aqueous suspension of polyethylene-glycol-grafted gold nanoparticles (PEG-AuNPs),[30] inspired by aqueous biphasic systems (ABS) composed of PEG and salts.[31, 32] Our theoretical model states that the interfacial assembly and crystallization is driven by the need to reduce surface tension between grafted PEG and the salt solution, leading to tunable lattice constants of 2D crystals, which could be well modeled by the balance between the surface tension and the

compression of the polymer brush.[30] More importantly, a sufficiently high level of salt was predicted to induce formation of 3D ordered assemblies via colloidal destabilization. Following our previous studies and corresponding theoretical consideration, this work aims to extend 2D crystallization of PEG-AuNPs into 3D assemblies under aqueous condition by elevating the K_2CO_3 concentration. The structure of 3D assemblies of PEG-AuNPs with various core sizes (10-50 nm) were investigated by small-angle X-ray scattering (SAXS) with theoretical analysis.

7.3 Results and Discussion

AuNPs were grafted with thiolated PEG (molecular weight 6000 Da) via a ligand exchange method[30, 33] and PEG-AuNPs were characterized by dynamic light scattering (DLS) and ultraviolet-visible spectroscopy (UV-Vis) measurements, which showed that significant increase of hydrodynamic size and distinct red-shift (2-3 nm) of surface plasmon resonance (SPR) peaks, respectively, with respect to unfunctionalized AuNPs (Figure S7.2, S7.4). It was found earlier that aqueous PEG-AuNP suspension is stable in water as well as K_2CO_3 solutions at low concentration ($\leq$ 0.5M). However, visible macroscopic precipitates are formed after a few hours at high concentration of K_2CO_3 ($\geq$ 1M), which showed strong intensity drop along with SPR peak broadening in the time-dependent evolution of UV-Vis spectra for PEG-AuNPs at 1M and 3M K_2CO_3 (Figure S7.5). SAXS was applied to probe structures of PEG-AuNPs in the suspensions (without salts and 0.5 M K_2CO_3) and precipitates (1M and 3M K_2CO_3).

Figure 7.1a shows the evolution of SAXS profiles for aqueous solutions of PEG-AuNPs (nominal core size of 10 nm) with increasing K_2CO_3 concentrations. Without any salts, PEG-AuNPs are well dispersed in the solution, and the overall SAXS intensity solely originates from form factor $P(Q)$ of the nanoparticles, particularly, Au cores as the electron density (ED) of PEG (compared to ED of Au) is similar to that of the solution surrounding it (Figure S7.1). Such a pr-

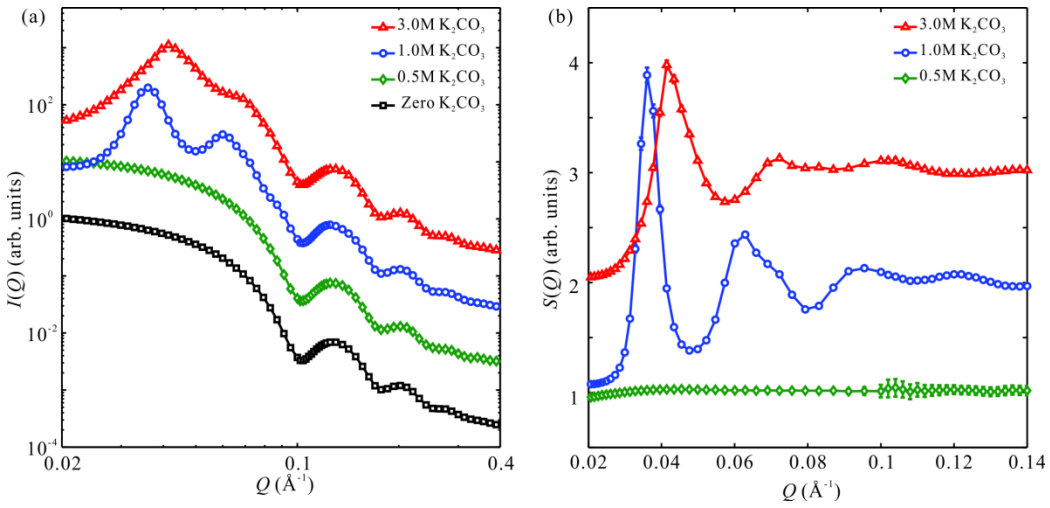

Figure 7.1 (a) SAXS intensity profiles as functions of Q for PEG-AuNPs with the nominal core size of 10 nm in absence and presence of K_2CO_3. (b) The extracted structure factor $S(Q)$ for PEG-AuNPs mixed with K_2CO_3. Solid lines are guides to the eyes. All the plots are vertically shifted for display purpose.

ofile allows for analysis of the actual particle size and its distribution, which is D = 8.7 ± 0.8 nm from a best fit with an assumption that particles are solid spheres with polydispersity described by a Gaussian distribution (Figure S7.1, Table S7.1). At the low level of K_2CO_3 (0.5 M), SAXS intensity from the bulk solution is still dominated by the form factor, even though a well-defined nanoparticle monolayer with superior two-dimensional (2D) crystallization was observed at the vapor-liquid interface.[30] The extracted structure factor $S(Q)$ is nearly identical to unity, as shown in Figure 7.1b, by considering the SAXS profile of PEG-AuNPs from the zero-salt solution as the real form factor of PEG-AuNPs. This indicates that PEG-AuNPs in the bulk (underneath the 2D superlattice) are randomly distributed without any coherent interference. When the K_2CO_3 concentration is increased above 1M, PEG-AuNPs form visible black precipitates. Scattering peaks at low Q ($Q \leq 0.1$ Å^{-1}) from SAXS profiles (Figure 7.1a) as well as the extract $S(Q)$ (Figure 7.1b) exhibit extra structural correlation inside the 3D assemblies. The primary peak position Q_0 shifts to high Q, suggesting a closer packing, when the K_2CO_3 concentration is

increased from 1M to 3M. The *d* spacings from primary peaks (estimated as $2\pi/Q_0$) are about 17.4 and 15.1 nm for 1 and 3M K_2CO_3, respectively.

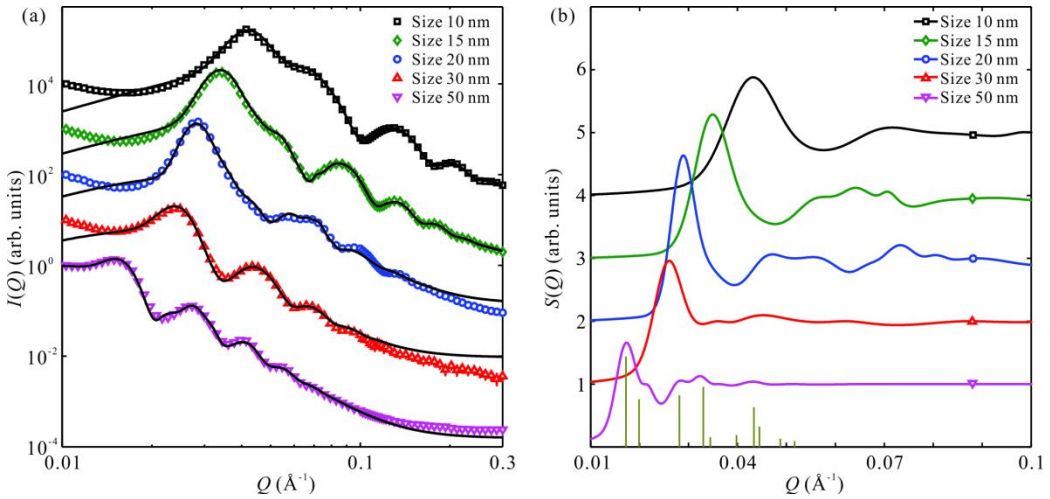

Figure 7.2 (a) SAXS intensity profiles as functions of *Q* for 3D assemblies of PEG-AuNPs with a variety of nominal core sizes (10-50 nm) in presence of 3.0 M K_2CO_3. The black solid lines are best fits from a full profile analysis using FCC structures. (b) The extracted structure factor *S*(*Q*) from the best fits. A group of vertical lines is inserted as a representative of peak positions and relative intensities from the fitted FCC structure. All the plots are vertically shifted for display purpose

Various 3D assemblies are obtained using the same method for AuNPs with different core sizes (nominal core size of 10-50 nm) but with identical PEG functionalization. Prior to the assembly process, SAXS was used to determine the actual size (*D*) information of AuNPs before and after PEG coating (Figure S7.1, Table S7.1). The hydrodynamic sizes D_h of different PEG-AuNPs dispersed in aqueous solutions were measured by DLS and modeled using polymer-brush theory developed earlier (Figure S7.3).[30] Figure 7.2a shows SAXS profiles of 3D assemblies in the presence of 3M K_2CO_3. The SAXS profiles of 3D assemblies exhibit a combination of form factor and structure factor as discussed above. The primary peak positions shift to low *Q* when the core sizes are increased, leading to an increase of *d* spacings. To quantitatively study these 3D assemblies, a full profile analysis is adopted for the SAXS profiles and it takes into account scattering peaks as well as form factor, size polydispersity and potential diffuse scattering (See

the SI).[34, 35] Even though one could interpret SAXS profiles from nanoparticle suspensions as form factors of nanoparticles in the assemblies, and extract structure factors for further analyses from the overall SAXS profiles for 3D assemblies, it is worth noting that the form factor from randomly distributed nanoparticle suspensions are not necessarily identical to that in the assemblies if the nanoparticles have size polydispersity. As the FCC structure is most common one for assemblies of nearly spherical hard particles, we performed full profile analysis using the FCC structure. As shown in Figure 7.2a, the calculated profiles are in good agreement with the experimental ones (See details of fits in SI). The structure factors extracted from best fits showing fairly large breadth for scattering peaks except the primary ones (i.e. (111) peaks) reveal short-range ordering of FCC (Figure 7.2b). The (111) peaks allow for a further study of nearest neighbor distance $d_n = \sqrt{6}\pi/Q_{(111)}$ of PEG-AuNPs in assemblies as discussed below.

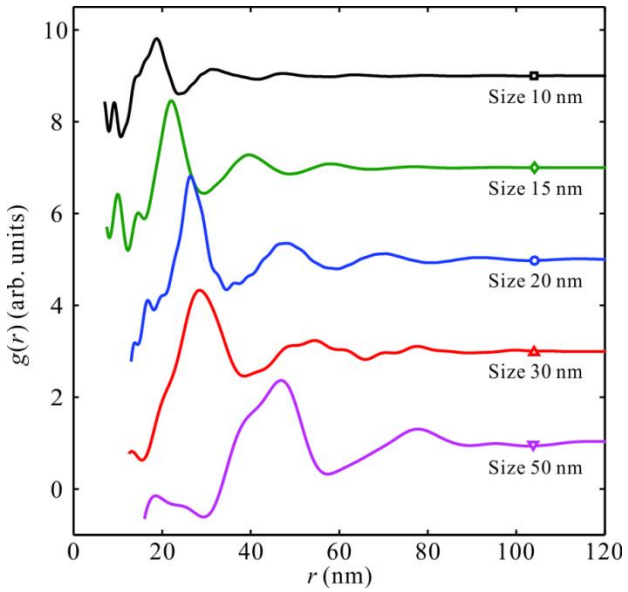

Figure 7.3 The radial distribution function $g(r)$ calculated from experimental structure $S(Q)$ with an assumption that form factor $P(Q)$ of nanoparticles in assemblies is the same as that of nanoparticles homogeneously distributed in solution. Due to loss of knowledge of the particle number density in assemblies (n_p), the amplitude of each plot is an estimated but not absolute value. However, the peak position is by no means affected by the amplitude. All the plots are vertically shifted for display purpose.

Another approach to analyze organization of particles in assemblies is to calculate the radial distribution function or pair distribution function $g(r)$ from the experimental structure factor $S(Q)$. As $S(Q)-1$ is the Fourier transform of $g(r)-1$, the nearest neighbor distance can be determined by SAXS measurements even without any assumption of symmetry for the particle arrangement in the assemblies.[35] As the form factor and the particle size extracted by the full profile fitting of assemblies are similar to those modeled directly from SAXS of nanoparticle suspensions (Table S7.3), we assume that the form factor $P(Q)$ of nanoparticles is always the same regardless of whether the nanoparticles are distributed homogeneously in solution or organized into assemblies. The experimental $P(Q)$ is removed from the overall SAXS intensity to obtain the experimental $S(Q)$ (Figure S7.7). Figure 7.3 shows the radial distribution function $g(r)$ calculated from the experimental $S(Q)$ extracted from SAXS profiles in Figure 7.2a. The peak positions of the highest intensity peaks correspond to the nearest neighbor distance d_n. Clearly d_n

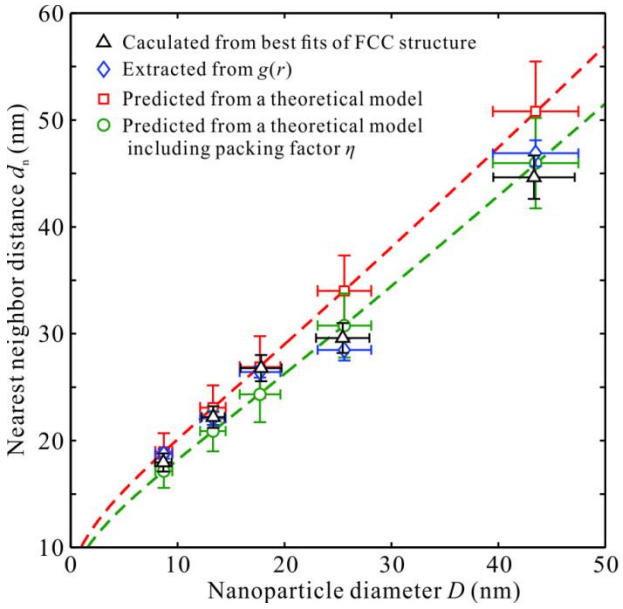

Figure 7.4 The nearest neighbor distance d_n calculated from FCC structures in the full profile fitting (black triangle) and extracted from $g(r)$ (blue diamond) for 3D assemblies of PEG-AuNPs with various core sizes. Prediction is calculated from the theoretical model Equation 7.1 (red squares) as well as the modified model including packing factor η_{HS} (green circles).

increases as the particle size changes from 10 to 50 nm. The nearest neighbor distance d_n calculated from a full profile fitting as well as extracted from $g(r)$ is summarized in Figure 7.4, which shows good agreement, suggesting the FCC structure is likely favorable in this system.

To understand the organization of PEG-AuNPs into 3D ordering, we extended our previous theoretical model of polymer-capped nanoparticles from the liquid surface to the bulk solution, which states that the solvent inside the polymer shell of PEG-AuNPs is in the θ-point while the high-salt solution outside the PEG-AuNPs is a poor solvent for PEG.[30] We argue that the 3D assemblies nucleate and grow after the surface tension of high-salt solution is minimized by full and dense coverage of the PEG-AuNPs at the interface. The nearest neighbor distance d_n of PEG-AuNPs in the assemblies is modeled by

$$\frac{d_n}{2R} = \left(1 + 3\frac{Nb^3\sigma v^2}{R}\right)^{1/3} \quad , \qquad (7.1)$$

where R is the radius of the Au core, N is the number of Kuhn monomers of PEG, b is the Kuhn length (b = 7.24 Å for PEG), σ is the grafting density of PEG on AuNPs, and v^2 = 0.341 is the PEG cross-sectional area in Kuhn length units (See details in SI). When the packing factor for the closed packed structure of hard spheres $\eta_{HS} = \pi/(3\sqrt{2})$ is taken into account, the low limit of nearest neighbor distance is given by $d_n^* = d_n\eta_{HS}^{1/3}$. Figure 7.4 shows the predicted d_n and d_n^* based on the measured grafting density of PEG-AuNPs for different core sizes (Figure S7.3). The prediction from our model is consistent with the results from SAXS measurements and analyses.

7.4 Conclusions

In summary, PEG-AuNPs are well dispersed in aqueous solutions with hydrodynamic sizes predicted fairly well using polymer-brush theory. At the intermediate levels of salt

(K_2CO_3), PEG-AuNPs in the bulk underneath the formed 2D crystalline Gibb monolayer were still uncorrelated. By elevating the salt concentration of the PEG-AuNPs to high enough levels, PEG-AuNPs self-assembled into macroscopic precipitates. We explored the 3D nanoparticle assemblies with various core sizes. The assemblies exhibited short-range ordering with probable FCC structure as probed by small-angle X-ray scattering, followed by a full-profile fitting and radial distribution function analyses. We presented a theoretical model to predict the nearest neighbor distance in the 3D assemblies, which is in good agreement with the experimental results extracted from data analysis.

7.5 Acknowledgements

We acknowledge Xiaobin Zuo at beamline 12ID-B, Advanced Photon Source (APS), Argonne National Laboratory for technical support in SAXS measurements. H.Z. thanks Byeongdu Lee at 12ID-B, APS, Argonne National Laboratory for technical help in structural analysis. Research was supported by the U.S. Department of Energy (DOE), Office of Basic Energy Sciences, Division of Materials Sciences and Engineering. Ames Laboratory is operated for the U.S. DOE by Iowa State University under Contract No. DE-AC02-07CH11358. Use of the Advanced Photon Source, an Office of Science User Facility operated for the U.S. DOE Office of Science by Argonne National Laboratory, was supported by the U.S. DOE under Contract No. DE-AC02-06CH11357.

7.6 Supporting Information (SI)

7.6.1 Reagents and materials

Poly(ethylene glycol) methyl ether thiol (PEG-SH) with average molecular weight of 6000 Da was purchased from Sigma-Aldrich, and bare gold nanoparticles (AuNPs) with citrate

stabilization with nominal diameter of 10-50 nm were purchased from Ted Pella. The PEG functionalized AuNPs (PEG-AuNPs) were synthesized using a simple ligand exchange procedure as reported earlier.[30] Briefly, PEG-SH, dissolved in degassed Millipore water with slight sonication, was added to AuNPs in large excess under vigorous stirring, followed by incubation for 1-2 days under gentle stirring to allow for maximum PEG loading. The as-prepared PEG-AuNPs were washed with Millipore water by at least three cycles of centrifugation and redispersion. The concentration of PEG-AuNPs was determined by UV-Visible absorption measurements with extinction coefficients reported by the company. Anhydrous potassium carbonate (K_2CO_3) was purchased from Fisher Scientific. High concentration K_2CO_3 solution (up to 5M) with surface cleaning to remove potential surfactant was mixed with PEG-AuNPs at desired final K_2CO_3 concentrations. PEG-AuNPs formed visible precipitates at $\geq$ 1M K_2CO_3 after overnight incubation and all the precipitates were aged for another 2 days prior to SAXS measurements.

7.6.2 Experimental setup

Small-angle X-ray scattering (SAXS) in transmission mode was carried out at the beamline 12ID-B (photon energy E =14.0 keV and wavelength λ = 0.8856 Å) at the Advanced Photon Source (APS), Argonne National Laboratory. SAXS data were collected by a 2D detector Pilatus2m and the scattering vector magnitude Q, ($Q = 4\pi\sin(\theta)/\lambda$, 2θ being the scattering angle), was calibrated with a silver behenate standard. For nanoparticle suspensions without precipitates, sample solutions were loaded into a vertical flow cell normal to the incident X-ray beam, and maintained at a constant flow rate during the X-ray exposure period.[14] The precipitates were carefully loaded into quartz capillary tubes with glass Pasteur pipettes, and multiple spots on

precipitates were chosen and examined. The 2D SAXS images were converted to 1D data by radial average for further data analysis.

7.6.3 Form factor of AuNPs

The form factor of AuNPs with and without PEG coating was measured by SAXS. Figure S7.1 shows SAXS profiles of unfunctionalized (bare) AuNPs and PEG-AuNPs (with nominal sizes 10-50 nm) dispersed in water after background subtraction. Such SAXS data allow for determination of the actual size information.[14] Here we assume that the size polydispersity obeys a Gaussian distribution function. The profile fitting of the measured form factor (solid lines in Figure S7.1) provides the actual particle size in Table S7.1. The actual size is slightly smaller than the nominal size, and the polydispersity (spread) is about 10 % of the mean size. For the particles with same nominal size, the actual size of bare AuNPs is identical to that of PEG-AuNPs. This indicates that the form factor is dominated by Au cores. In fact, as PEG has similar electron density to that of water, the PEG shell surrounding AuNPs is practically indistinguishable from the solution.

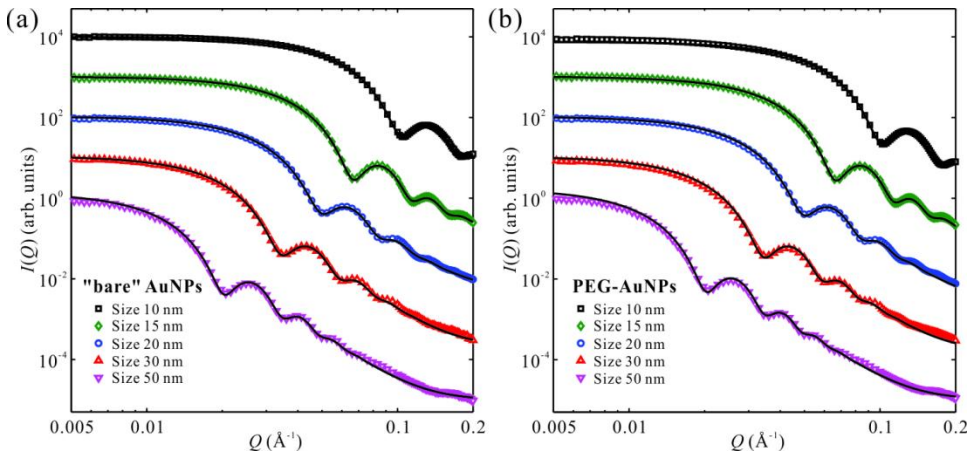

Figure S7.1 SAXS profiles of (a) bare (unfunctionalized) AuNPs and (b) PEG-AuNPs with various nominal core sizes. Solid lines are best fits using form factor of spherical solid particles with polydispersity modeled by a Gaussian distribution. All the plots are vertically shifted for display purpose.

Table S7.1 Nanoparticle size distribution determined by profile-fitting of SAXS data collected from the suspension

Nominal size (nm)	Size of bare AuNPs (nm)	Size of PEG-AuNPs (nm)
10	8.5 ± 0.8	8.7 ± 0.8
15	13.3 ±1.2	13.3 ± 1.2
20	17.6 ± 2.0	17.7 ± 1.9
30	25.5 ± 2.7	25.6 ± 2.5
50	43.4 ± 4.1	43.5 ± 4.0

7.6.4 Hydrodynamic size of AuNPs

The hydrodynamic size D_h of unfunctionalized (bare) AuNPs stabilized with citrate and PEG-AuNPs in aqueous solutions were measured by dynamic light scattering (DLS). Figure S7.2 and Table S7.2 show hydrodynamic size distribution of citrate-stabilized AuNPs and PEG-AuNPs (with nominal core sizes 10-50 nm). The size distribution shifts to the large size due to PEG coating.

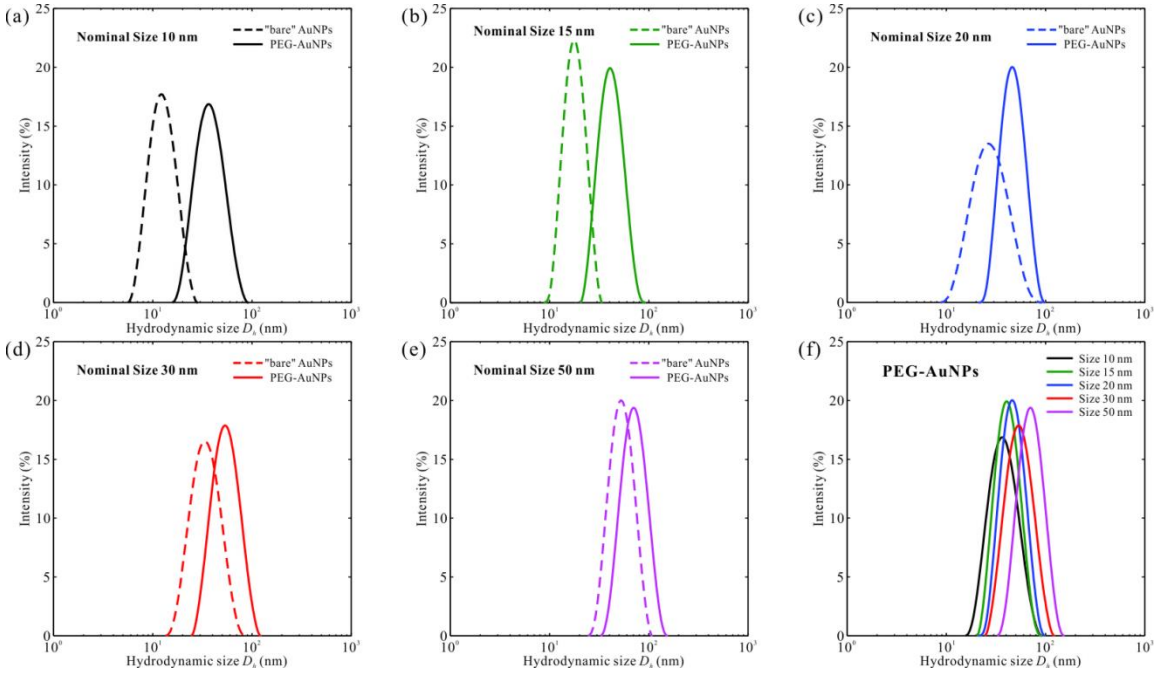

Figure S7.2 Hydrodynamic sizes D_h measured by dynamic light scattering for unfunctionalized (bare) citrate-stabilized AuNPs and PEG-AuNPs with different nominal core sizes: (a) 10 nm, (b) 15 nm, (c) 20 nm, (d) 30 nm, (e) 50 nm. (f) Comparison of D_h for PEG-AuNPs with various nominal sizes.

Table S7.2 Hydrodynamic size distribution by dynamic light scattering before and after PEG coating. PEG coating leads to a shift of size distribution.

Nominal size (nm)	Citrate-stabilized AuNPs (nm)	PEG-AuNPs (nm)	Shift of distribution center (nm)
10	13.0 ± 3.9	39.1 ± 12.6	26.1
15	18.4 ± 4.4	42.5 ± 11.5	24.1
20	29.2 ± 11.9	49.7 ± 13.1	20.5
30	35.7 ± 11.5	56.1 ± 16.9	20.4
50	54.7 ± 14.5	73.9 ± 20.3	19.2

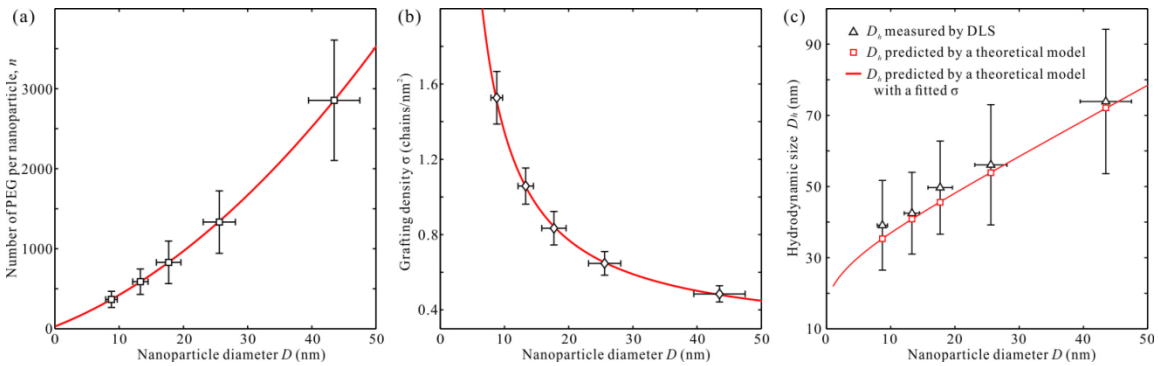

Figure S7.3 (a) The number of PEG per AuNP n for various nanoparticle sizes measured by thermogravimetric analysis (TGA). The red solid line is a best fit with a polynomial function. (b) The corresponding grafting density σ. The solid line is adopted from the best fit in (a). (c) The hydrodynamic size D_h measured by dynamic light scattering (DLS) and predicted by the theoretical model of Equation S7.1. The solid line is calculated using the fitted σ in (b). The error bars for D and D_h are the spread of size distribution.

According to our previous model[30], the hydrodynamic size D_h of a given PEG-AuNP with Au core size D is given by

$$\left(\frac{D_h}{D}\right) = 1 + 4\frac{Nb^2\sigma^{1/2}}{D}(2w_0)^{1/4}, \tag{S7.1}$$

where b = 7.24 Å is the Kuhn length of PEG, N = 68.5 is the number of Kuhn monomers for PEG with the molecular weight of 6000, σ is the grafting density, and w_0 is a dimensionless three body interaction, where we use the Flory result w_0 = 1/6. This model reveals that the hydrodynamic size depends on the grafting density. In this study, the grafting density of PEG on

AuNPs is estimated by a thermogravimetric analysis (TGA) as reported.[30, 33] Figure S7.3a-b shows the number of PEG (MW = 6000) molecules per AuNP, n, and the grafting density $\sigma = n/(\pi D^2)$ for different particle sizes. The red line in Figure S7.3a is a best fit with a polynomial function $n = a_2D^2 + a_1D + a_0$, where $a_2 = 0.762$ nm^{-2}, $a_1 = 31.8$ nm^{-1} and $a_0 = 28$. The corresponding fit of σ is provided in Figure S7.3b. Clearly, in current size range the grafting density decreases with increased particle size. In fact, surface curvature plays an important role in the grafting density of thiolated molecules attached on gold. This behavior has been observed in measured grafting density of PEG-SH with larger large molecular weight (MW = 10000) on similar gold nanoparticles[33] as well as structural information determined in atomic scale for short thiolated molecules grafted on smaller gold nanoparticles.[36] With the measured grafting density and the best fit, the dynamic size of PEG-AuNPs and its trend versus Au core size are predicted by the theoretical model, showing in Figure S7.3c. The prediction is in good agreement with the measured results.

7.6.5 UV-Vis spectra of AuNPs

The UV-Vis absorption of unfunctionalized (bare) AuNPs stabilized with citrate and PEG-AuNPs in aqueous solution was measured by a UV-Visible spectrophotometer. Figure S7.4 shows spectra of AuNPs (with nominal core sizes 10-50 nm) in water before and after PEG coating. The slight red shift (2-3 nm) of surface plasmon resonance (SPR) peaks corresponds to the ligand change on nanoparticle surfaces.

The absorption of PEG-AuNPs is changed when PEG-AuNPs are exposed to K_2CO_3 solutions. PEG-AuNPs are stable in water and low concentration K_2CO_3 solutions ($\leq$ 0.5M), while visible macroscopic precipitates are formed after hours at high concentration of K_2CO_3 ($\geq$ 1M). Figure S7.5a shows UV-Vis spectra for PEG-AuNPs with nominal core size of 10 nm in

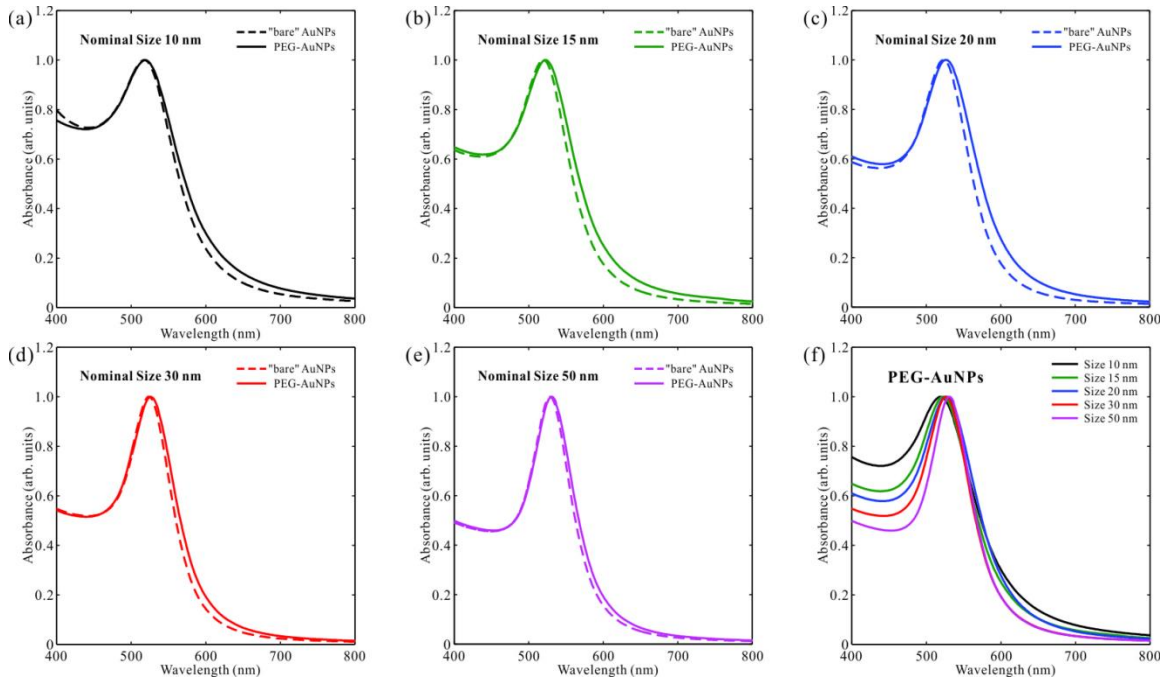

Figure S7.4 UV-Vis spectra for unfunctionalized (bare) AuNPs and PEG-AuNPs with different nominal core sizes: (a) 10 nm, (b) 15 nm, (c) 20 nm, (d) 30 nm, (e) 50 nm. (f) Comparison of absorption for PEG-AuNPs with various nominal sizes.

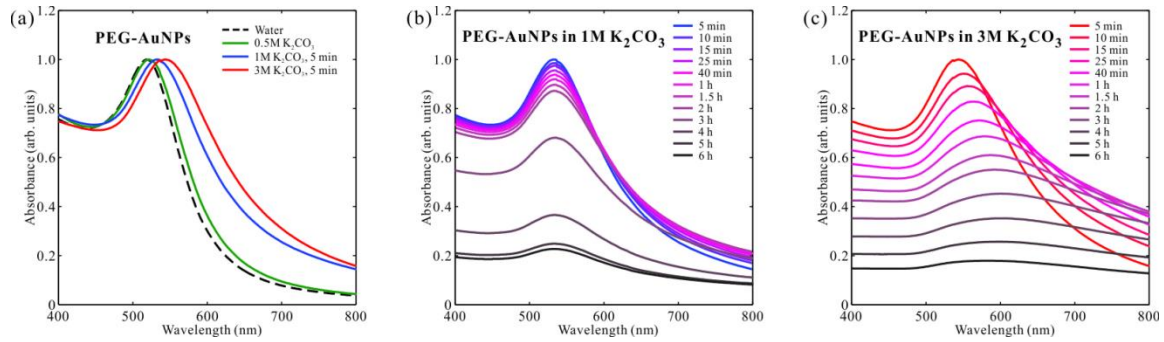

Figure S7.5 UV-Vis spectra for PEG-AuNPs with Au core size of 10 nm in the presence of K_2CO_3. (a) Absorption of PEG-AuNPs measured in water and 0.5-3M K_2CO_3. The time dependence of adsorption takes place for PEG-AuNPs in the presence of (b) 1M K_2CO_3 and (c) 3M K_2CO_3. Only the spectra for PEG-AuNPs in 1M and 3M K_2CO_3 measured at 5 min after sample preparation were plotted in (a) for comparison.

the absence and presence of K_2CO_3. SPR peaks shift to longer wavelengths with the increase of K_2CO_3 concentrations, as adding K_2CO_3 increased the refractive index of the media where PEG-AuNPs were dispersed. No clear adsorption change was observed within months for PEG-AuNPs in water and in 0.5M K_2CO_3. However, the spectral intensity decreased dramatically

along with the SPR peak broadening for PEG-AuNPs at higher concentration of K_2CO_3 as shown in Figure S7.5b-c, which reveals nanoparticle aggregation takes place at high level of salts. Upon close looking into the time-dependence of spectra on the same timescale, SPR peaks did not shift within hours at 1M K_2CO_3, while there was a strong red-shift of SPR peaks measured at 3M K_2CO_3, indicating that 1M and 3M K_2CO_3 exhibited different effects on the aggregation of PEG-AuNPs. In particular, at 3M K_2CO_3, PEG-AuNPs were in close proximity to each other, thus SPR peaks shifted to longer wavelength due to the plasmon coupling between nanoparticles.

7.6.6 Full profile analysis of SAXS

Full profile analysis of SAXS data from particle assemblies (including all peaks as well as form factor and potential diffuse scattering) provides higher accuracy and more information than solely analyzing a collection of decomposed peaks.[35] According to the literature,[34, 35] for a system of single-type components, when particle size polydispersity, diffuse scattering and local positional fluctuations are considered, the overall scattering intensity from ordered particle assemblies is given by

$$I(Q) = N_{\mathrm{p}} P(Q)\{1 + [Z(Q) - 1]\beta(Q)G(Q)\}, \tag{S7.2}$$

where N_{p} is the number of particles, $P(Q) = \left\langle \left| F(\mathbf{Q}) \right|^2 \right\rangle$ is the form factor with $F(\mathbf{Q})$ being the form factor amplitude, $\beta(Q) = \left\langle \left| F(\mathbf{Q}) \right| \right\rangle^2 \Big/ P(Q)$ is the diffuse scattering, $G(Q) = \exp(-\sigma_{\mathrm{D}}^2 Q_{hkl}^2 d_n^2)$ is the isotropic Debye-Waller factor (d_n is the nearest neighbor distance, σ_{D} describes local positional fluctuation), and $Z(Q)$ is the lattice factor. $Z(Q)$ is expressed as

$$Z(Q) = \sum_{hkl} Z_0(Q_{hkl}) \Pi(Q; Q_{hkl}, \sigma_s), \tag{S7.3}$$

where $\Pi(Q;Q_{hkl},\sigma_s)$ is the peak shape function. In this study, we use a Gaussian function with the position of peak center Q_{hkl}, spread of the peak σ_s, and the integrated area 1. $Z_0(Q_{hkl})$ is the sum of the squares of the phase factors of the (*hkl*) reflection, normalized by the number of particles in a unit cell, the solid angle of the reciprocal space at Q_{hkl} and the dimensional measure (i.e. length, area or volume) of the unit cell.[34] For a three-dimensionally randomly oriented FCC structure, $Z_0(Q_{hkl})$ is written as

$$Z_0(Q_{hkl}) = \frac{8\pi^2}{a^3 Q_{hkl}^2} m_{hkl}, \tag{S7.4}$$

where a is the lattice constant, and m_{hkl} is the multiplicity of the (*hkl*) reflection.

Figure S7.6a-e show results of full profile fitting as well as extracted form factor $P(Q)$ and structure factor $S(Q) = I(Q)/[N_p P(Q)]$ from best fits. The extracted $P(Q)$ for various Au sizes

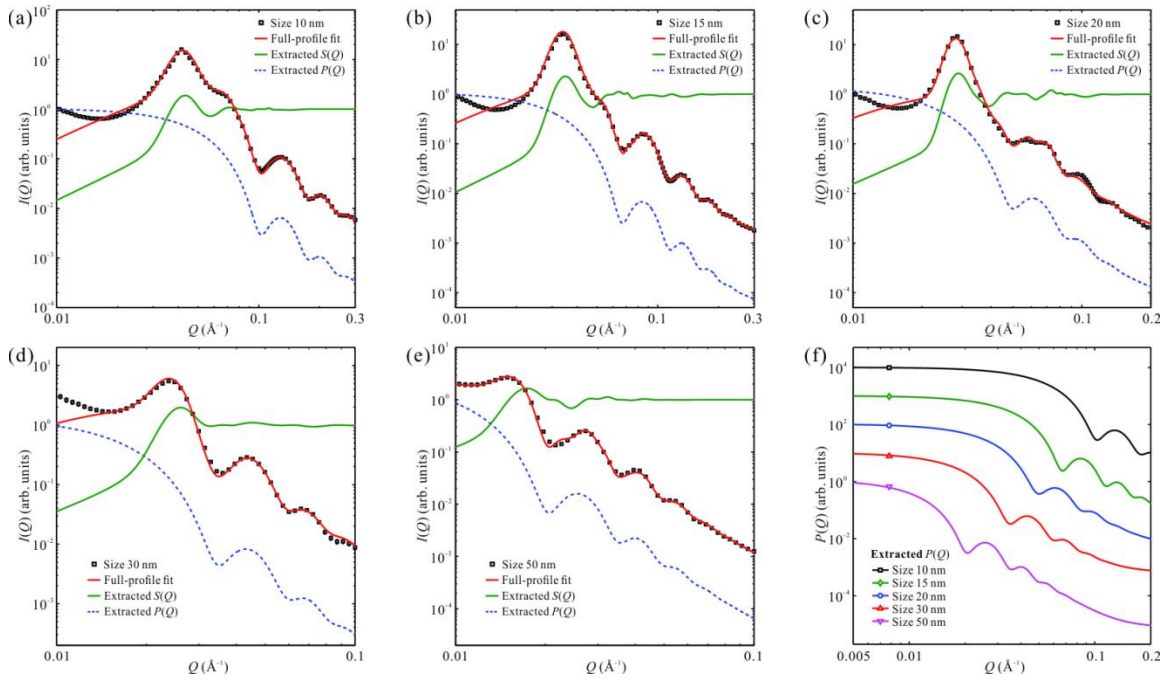

Figure S7.6 Full profile analysis with extracted form factor $P(Q)$ and structure factor $S(Q) = I(Q)/[N_p P(Q)]$ for SAXS data of PEG-AuNP assemblies with different nominal core sizes: (a) 10 nm, (b) 15 nm, (c) 20 nm, (d) 30 nm, (e) 50 nm. (f) Comparison of the extracted $P(Q)$ from full profile fits. All the plots are vertically shifted for display purpose.

Table S7.3 Comparison between core sizes of PEG-AuNPs determined from profile-fitting of SAXS data collected from the suspension and the assemblies

Nominal size (nm)	Size of PEG-AuNPs in suspension (nm)	Size of PEG-AuNPs in assemblies (nm)
10	8.7 ± 0.8	8.7 ± 0.8
15	13.3 ±1.2	13.3 ± 1.1
20	17.7 ± 1.9	17.8 ± 1.9
30	25.6 ± 2.5	25.4 ± 2.5
50	43.5 ± 4.0	43.3 ± 3.8

is shown in Figure S7.6f and the corresponding refined size information is provided in Table S7.3. Overall, the particle size extracted from the full profile fitting of the assemblies is consistent with the sizes modeled directly from SAXS of nanoparticle suspension.

7.6.7 Calculation of Radial Distribution Function

The inverse Fourier transform of the structure factor $S(Q)$ results in the radial distribution function or pair distribution function $g(r)$, which is expressed as[35, 37]

$$g(r) = 1 + \frac{1}{2\pi^2 n_p} \int_0^\infty [S(Q) - 1] Q^2 \frac{\sin(Qr)}{Qr} \, dQ, \tag{S7.5}$$

where n_p is the particle number density in assemblies.

The experimental structure factor $S(Q)$ was obtained by taking SAXS profiles from nanoparticle suspension as the experimental form factor $P(Q)$ and removing the experimental $P(Q)$ from the SAXS measurements of nanoparticle assemblies (Figure S7.7). Here, $P(Q)$ is assumed to be the same for nanoparticles either distributed randomly in suspension or assembled into particle clusters, as $P(Q)$ and the corresponding particle size distribution extracted from full profile analysis of the assemblies are in good agreement with the experimental $P(Q)$ and the modeled size information (Table S7.3).

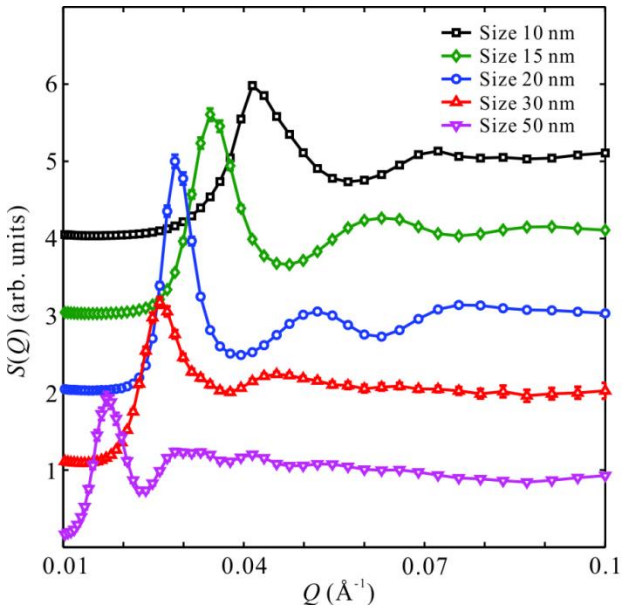

Figure S7.7 The experimental structure factor $S(Q)$ for assemblies of PEG-AuNPs with different core sizes. Solid lines are guides to the eyes. All the plots are vertically shifted for display purpose.

In the present study, n_p is practically unknown. To a good approximation, $n_p = \sqrt{2}/(D+2h)$ for a close-packed particle assembly with perfect contact of each particle with a core-shell structure (core diameter D and shell thickness h). Simply, we take core size of AuNPs as D, and estimate the brush height of PEG shell capped on AuNPs to be 5 nm based on previous results of full profile-fitting. We note that according to Equation S7.5, n_p only determines the amplitude of $g(r)$, and by no means affects any oscillation positions that provide valuable information of the nearest neighbor distance.

7.6.8 Theoretical model

The density of a melt of PEG can be calculated as

$$\rho = \frac{M_1 N_r / N}{N_A b^3 v^2}, \tag{S7.6}$$

where N_r/N is the number of PEG monomers per unit Kuhn unit, N_A is Avogadro number, M_1 is the molecular weight of PEG monomer, b is the Kuhn length, and v^2 is the PEG cross-sectional

area in Kuhn length units, where $\nu < 1$. Agreement between Equation S7.6 and the known density of PEG ρ =1.123 g/cm^3 implies using the same parameters as in our previous study, ν^2 = 0.341 or ν = 0.584.

In ref.[30] we introduced a model, where the polymer within the PEG-AuNP is at the the θ point and is under surface tension, which results from the osmotic pressure induced by the different ion concentrations inside and outside the polymer shell. Further evidence is provided in Figure S7.3 (ref.[30]), where the measured hydrodynamic for a wide range of sizes and grafting densities is in excellent agreement with those assumptions. It should be noted that the salt-rich environment that defines the outside of a PEG-AuNP in bulk remains a poor solvent for PEG. As shown in ref.[30], decreasing the solvent quality further by increasing salt concentration leads to a collapse transition and the PEG-AuNP becomes insoluble. It is precisely at this point that the 3D supercrystal is observed. Thus, such crystal results from a process of colloidal destabilization.

The nearest neighbor distance between PEG-AuNP can be obtained from assuming that the solid has negligible amounts of solvent, both ions and water. As discussed in the context of NP capped with hydrocarbon ligands,[38] it is convenient to consider the monomer packing fraction, defined as

$$\eta_m = \frac{\text{Volume of mater}}{\text{Volume total}} = \frac{4\pi R^3 + A_P L n}{V_{WS} d_n}, \tag{S7.7}$$

where A_P is the cross section of a PEG polymer, L its maximum length, n is the number of chains per NP and $V_{ws} \equiv V_{0,WS}\, d_n^3$ is the volume of the Wigner-Seitz cell. Following standard conventions, we define the softness $\lambda = L/R$ and dimensionless coverage as $\xi = A_P\, \sigma \equiv A_P/A_0 < 1$. With this notation, Equation S7.7 becomes

$$\eta_m = \frac{\pi}{6V_0}\left(\frac{2R\tau}{d_n}\right)^3 = \eta_{HS}\left(\frac{2R\tau}{d_n}\right)^3, \tag{S7.8}$$

where η_{HS} is the hard sphere packing fraction for the corresponding lattice, ex. $\eta_{HS} = \pi/(3\sqrt{2}) \approx 0.7405$ for a closed packed FCC or HCP structure. Note that we have

$$\tau = \left(1 + 3\sigma \frac{A_P L}{R}\right)^{1/3} = \left(1 + 3\xi\lambda\right)^{1/3} = \left(1 + 3\frac{Nb^3\sigma\nu^2}{R}\right)^{1/3}, \tag{S7.9}$$

where to obtain the last expression, ν^2 has been employed. There are two obvious choices for the nearest neighbor distance d_n, namely

$$\frac{d_n}{2R} = \begin{cases} \frac{d_{OPM}}{2R} = \tau \quad (\eta_m = \eta_{HS}) \\ \frac{d_{MIN}}{2R} = \eta_{HS}^{1/3}\tau \quad (\eta_m = 1) \end{cases}. \tag{S7.10}$$

The first result is known as the optimal packing model (OPM)[39] and is satisfied for high grafting densities $\xi \approx 1$ and short ligands $\lambda \leq 2$. The second is the minimum possible separation, where the polymer is distributed as a melt with maximal constant density. As discussed in ref.[38], separations $d_n < d_{OPM}$ involve polymer textures that require consideration of topological defects.

References

1. Murray, C. B.; Kagan, C. R.; Bawendi, M. G. Synthesis and Characterization of Monodisperse Nanocrystals and Close-Packed Nanocrystal Assemblies. *Annu. Rev. Mater. Sci.* 2000, 30, 545-610.
2. Nie, Z.; Petukhova, A.; Kumacheva, E. Properties and emerging applications of self-assembled structures made from inorganic nanoparticles. *Nat. Nanotechnol.* 2010, 5, 15-25.
3. Talapin, D. V.; Lee, J.-S.; Kovalenko, M. V.; Shevchenko, E. V. Prospects of Colloidal Nanocrystals for Electronic and Optoelectronic Applications. *Chem. Rev.* 2010, 110, 389-458.
4. Sun, S.; Murray, C. B.; Weller, D.; Folks, L.; Moser, A. Monodisperse FePt Nanoparticles and Ferromagnetic FePt Nanocrystal Superlattices. *Science* 2000, 287, 1989-1992.
5. Young, K. L.; Ross, M. B.; Blaber, M. G.; Rycenga, M.; Jones, M. R.; Zhang, C.; Senesi, A. J.; Lee, B.; Schatz, G. C.; Mirkin, C. A. Using DNA to Design Plasmonic Metamaterials with Tunable Optical Properties. *Adv. Mater.* 2014, 26, 653-659.
6. Boles, M. A.; Engel, M.; Talapin, D. V. Self-Assembly of Colloidal Nanocrystals: From Intricate Structures to Functional Materials. *Chem. Rev.* 2016, 116, 11220-11289.

7. Nykypanchuk, D.; Maye, M. M.; van der Lelie, D.; Gang, O. DNA-guided crystallization of colloidal nanoparticles. *Nature* 2008, 451, 549-552.
8. Park, S. Y.; Lytton-Jean, A. K. R.; Lee, B.; Weigand, S.; Schatz, G. C.; Mirkin, C. A. DNA-programmable nanoparticle crystallization. *Nature* 2008, 451, 553-556.
9. Macfarlane, R. J.; Lee, B.; Jones, M. R.; Harris, N.; Schatz, G. C.; Mirkin, C. A. Nanoparticle Superlattice Engineering with DNA. *Science* 2011, 334, 204-208.
10. Zhang, Y.; Lu, F.; Yager, K. G.; van der Lelie, D.; Gang, O. A general strategy for the DNA-mediated self-assembly of functional nanoparticles into heterogeneous systems. *Nat. Nanotechnol.* 2013, 8, 865-872.
11. Liu, W.; Tagawa, M.; Xin, H. L.; Wang, T.; Emamy, H.; Li, H.; Yager, K. G.; Starr, F. W.; Tkachenko, A. V.; Gang, O. Diamond family of nanoparticle superlattices. *Science* 2016, 351, 582-586.
12. Srivastava, S.; Nykypanchuk, D.; Fukuto, M.; Halverson, J. D.; Tkachenko, A. V.; Yager, K. G.; Gang, O. Two-Dimensional DNA-Programmable Assembly of Nanoparticles at Liquid Interfaces. *J. Am. Chem. Soc.* 2014, 136, 8323-8332.
13. Srivastava, S.; Nykypanchuk, D.; Fukuto, M.; Gang, O. Tunable Nanoparticle Arrays at Charged Interfaces. *ACS Nano* 2014, 8, 9857-9866.
14. Wang, W.; Zhang, H.; Kuzmenko, I.; Mallapragada, S.; Vaknin, D. Assembling Bare Au Nanoparticles at Positively Charged Templates. *Sci. Rep.* 2016, 6, 26462.
15. Knorowski, C.; Travesset, A. Materials design by DNA programmed self-assembly. *Curr. Opin. Solid State Mater. Sci.* 2011, 15, 262-270.
16. Knorowski, C.; Burleigh, S.; Travesset, A. Dynamics and Statics of DNA-Programmable Nanoparticle Self-Assembly and Crystallization. *Phys. Rev. Lett.* 2011, 106, 215501.
17. Li, T. I. N. G.; Sknepnek, R.; Macfarlane, R. J.; Mirkin, C. A.; Olvera de la Cruz, M. Modeling the Crystallization of Spherical Nucleic Acid Nanoparticle Conjugates with Molecular Dynamics Simulations. *Nano Lett.* 2012, 12, 2509-2514.
18. Shevchenko, E. V.; Talapin, D. V.; Kotov, N. A.; O'Brien, S.; Murray, C. B. Structural diversity in binary nanoparticle superlattices. *Nature* 2006, 439, 55-59.
19. Talapin, D. V.; Shevchenko, E. V.; Bodnarchuk, M. I.; Ye, X.; Chen, J.; Murray, C. B. Quasicrystalline order in self-assembled binary nanoparticle superlattices. *Nature* 2009, 461, 964-967.
20. Bodnarchuk, M. I.; Kovalenko, M. V.; Heiss, W.; Talapin, D. V. Energetic and Entropic Contributions to Self-Assembly of Binary Nanocrystal Superlattices: Temperature as the Structure-Directing Factor. *J. Am. Chem. Soc.* 2010, 132, 11967-11977.
21. Boles, M. A.; Talapin, D. V. Many-Body Effects in Nanocrystal Superlattices: Departure from Sphere Packing Explains Stability of Binary Phases. *J. Am. Chem. Soc.* 2015, 137, 4494-4502.
22. Ye, X.; Zhu, C.; Ercius, P.; Raja, S. N.; He, B.; Jones, M. R.; Hauwiller, M. R.; Liu, Y.; Xu, T.; Alivisatos, A. P. Structural diversity in binary superlattices self-assembled from polymer-grafted nanocrystals. *Nat. Commun.* 2015, 6.
23. Narayanan, S.; Wang, J.; Lin, X.-M. Dynamical Self-Assembly of Nanocrystal Superlattices during Colloidal Droplet Evaporation by \textit{in situ} Small Angle X-Ray Scattering. *Phys. Rev. Lett.* 2004, 93, 135503.
24. Bigioni, T. P.; Lin, X.-M.; Nguyen, T. T.; Corwin, E. I.; Witten, T. A.; Jaeger, H. M. Kinetically driven self assembly of highly ordered nanoparticle monolayers. *Nat. Mater.* 2006, 5, 265-270.

25. Travesset, A. Binary nanoparticle superlattices of soft-particle systems. *Proc. Natl. Acad. Sci. USA* 2015, 112, 9563-9567.
26. Horst, N.; Travesset, A. Prediction of binary nanoparticle superlattices from soft potentials. *J . Chem. Phys.* 2016, 144, 014502.
27. Campolongo, M. J.; Tan, S. J.; Smilgies, D.-M.; Zhao, M.; Chen, Y.; Xhangolli, I.; Cheng, W.; Luo, D. Crystalline Gibbs Monolayers of DNA-Capped Nanoparticles at the Air–Liquid Interface. *ACS Nano* 2011, 5, 7978-7985.
28. Tan, S. J.; Kahn, J. S.; Derrien, T. L.; Campolongo, M. J.; Zhao, M.; Smilgies, D.-M.; Luo, D. Crystallization of DNA-Capped Gold Nanoparticles in High-Concentration, Divalent Salt Environments. *Angew. Chem. Int. Ed.* 2014, 53, 1316-1319.
29. Zhang, H.; Wang, W.; Hagen, N.; Kuzmenko, I.; Akinc, M.; Travesset, A.; Mallapragada, S.; Vaknin, D. Self-Assembly of DNA Functionalized Gold Nanoparticles at the Liquid-Vapor Interface. *Adv. Mater. Interfaces* 2016, 3, 1600180.
30. Zhang, H.; Wang, W.; Mallapragada, S.; Travesset, A.; Vaknin, D. Macroscopic and tunable nanoparticle superlattices. *Nanoscale* 2016.
31. Willauer, H. D.; Huddleston, J. G.; Rogers, R. D. Solute Partitioning in Aqueous Biphasic Systems Composed of Polyethylene Glycol and Salt: The Partitioning of Small Neutral Organic Species. *Ind. Eng. Chem. Res.* 2002, 41, 1892-1904.
32. Huddleston, J. G.; Willauer, H. D.; Rogers, R. D. Phase Diagram Data for Several PEG + Salt Aqueous Biphasic Systems at 25 °C. *J. Chem. Eng. Data* 2003, 48, 1230-1236.
33. Rahme, K.; Chen, L.; Hobbs, R. G.; Morris, M. A.; O'Driscoll, C.; Holmes, J. D. PEGylated gold nanoparticles: polymer quantification as a function of PEG lengths and nanoparticle dimensions. *RSC Adv.* 2013, 3, 6085-6094.
34. Senesi, A. J.; Lee, B. Small-angle scattering of particle assemblies. *J. Appl. Crystallogr.* 2015, 48, 1172-1182.
35. Li, T.; Senesi, A. J.; Lee, B. Small Angle X-ray Scattering for Nanoparticle Research. *Chem. Rev.* 2016, 116, 11128-11180.
36. Jadzinsky, P. D.; Calero, G.; Ackerson, C. J.; Bushnell, D. A.; Kornberg, R. D. Structure of a Thiol Monolayer-Protected Gold Nanoparticle at 1.1 Å Resolution. *Science* 2007, 318, 430-433.
37. Als-Nielsen, J.; McMorrow, D. *Elements of modern X-ray physics*. John Wiley & Sons: 2011.
38. Travesset, A. Topological structure prediction in binary nanoparticle superlattices. *Soft Matter* 2016.
39. Landman, U.; Luedtke, W. D. Small is different: energetic, structural, thermal, and mechanical properties of passivated nanocluster assemblies. *Farad. Discuss.* 2004, 125, 1-22.

CHAPTER 8. CONCLUSIONS AND FUTURE WORK

8.1 Conclusions

Overall, the dissertation work has focused on the synthesis and self-assembly of functional inorganic nanomaterials templated by specialized macromolecules including proteins, DNA and polymers. The underlying theme has been the development of synthesis and self-assembly methods involving nanoparticles and macromolecules, and the development and use of X-ray scattering methods to probe the mechanisms of formation and to characterize self-assembled structures formed.

Previous research indicated that Mms6, a biomineralization protein from magnetotactic bacteria plays a role in the formation of uniform magnetite nanocrystals *in vitro*. Here we have investigated the mechanism of Mms6 biomineralization using small-angle X-ray scattering (SAXS), and further synthesized complex magnetic nanomaterials in the bulk and on surfaces to expand the biomineralization process to beyond natural materials. SAXS studies in physiological solutions have revealed that Mms6 forms compact globular three-dimensional (3D) micelles of approximately 10 nm in diameter, that resemble core−corona structures of amphiphilic polymers. The spherical core is formed by the hydrophobic N-terminal domains of Mms6, while the corona shell with Gaussian-chain-like structure consists of hydrophilic C-terminal domains, which are the charged regions responsible for initial iron binding. Introducing iron ions to the protein solutions, the general micellar morphology of Mms6 is preserved, but associations among micelles are induced to form 2D disk-like or 3D mass-fractal-like aggregates with large surface area, which is implied to contribute to formation of large magnetite nanocrystals. By immobilizing Mms6 on a hydrophobic octadecanethiol (ODT) monolayer through hydrophobic

interactions between N-terminal domains and ODT, Mms6 has been found to form a network-like structure, which also provides a large surface area for iron binding. Indeed, such a protein network has displayed better functionality in facilitating formation of uniformly sized magnetite nanoparticles on surfaces than Mms6 adsorbed on hydrophilic substrates. The Mms6 immobilized on hydrophobic substrates mimics Mms6 situated in the membrane *in vivo*, providing a general template for magnetite biomineralization on surfaces. In addition, we have also investigated aqueous-phase synthesis of magnetite nanoparticles with tunable sizes and magnetic properties under mild conditions. Gadolinium (Gd) doping has been exploited to influence the nanocrystal growth process via a simple co-precipitation method leading to large crystal sizes that are controllable with the doping level. Gd doping with simultaneous crystal growth has demonstrated to be an effective route to modulating magnetic properties of magnetite nanocrystals. Therefore, inspired by the biomineralization process of Mms6, hybrid magnetic nanomaterials seen in nature, as well as beyond, can be synthesized on surfaces and in the bulk using bottom-up approaches.

Earlier work on self-assembly of DNA-functionalized plasmonic gold nanocrystals into 2D and 3D ordered structures revealed a promising route to fabricate next-generation materials such as metamaterials. Here, we employed X-ray scattering and spectroscopy techniques to study the 2D self-assembly of DNA-capped gold nanoparticles (DNA-AuNPs) at the air–water interface, and, more importantly, the self-assembly mechanism that has further become an inspiration for development of robust approaches to construct 2D and 3D superlattices by functionalizing nanocrystals with polymers. DNA-AuNPs have been observed to self-assemble and form 2D hexagonal superlattices at air–water interfaces by simply adjusting concentrations of divalent salts. Quantitative analysis has shown that the DNA-AuNPs are overall amphiphilic

in character owing to the polyelectrolytic nature of DNA and the hydrophobic hexyl-thiol groups commonly used to functionalize DNA for capping AuNPs. Tuning the amphiphilic character by charge screening of DNA with divalent cations has driven the interfacial accumulation and crystallization of DNA-AuNPs. Inspired by such findings, polyethylene glycol (PEG) has been used to functionalize AuNPs to form 2D superlattices as the hydrophobicity of PEG is readily controlled with salt concentrations and temperature. We have observed that K_2CO_3 is effective to induce macroscopic and tunable 2D nanoparticle superlattices with much higher crystallinity than those of DNA-AuNPs. The 2D superlattices exhibit high tunability of lattice parameters by adjusting the K_2CO_3 and PEG-AuNP concentrations and the length of PEG. Furthermore, at high concentrations of K_2CO_3 ($\geq$ 1M), 3D assemblies have been found to form in the bulk. The 3D assemblies have shown the crystallinity of short-range ordering, compatible with the FCC symmetry. Using polymer-brush theory, we have demonstrated that the self-assembly of PEG-AuNPs into 2D and 3D structures is driven by the need to reduce surface tension between the PEG shell and the surrounded salt solution. Thus, by functionalization with specialized macromolecules, inorganic nanocrystals are able to self-assemble tunably into superlattices by controlling the assembly environment.

Using bioinspired methods, complex magnetic nanomaterials have been synthesized and 2D and 3D superlattices of plasmonic nanocrystals have been fabricated. Specialized macromolecules including proteins, DNA and polymers act as effective templates for synthesis and self-assembly of nanomaterials. Such bottom-up approaches provide promising routes to fabricate hybrid organic–inorganic nanomaterials with rationally designed hierarchical structures for potential applications.

8.2 Future Work

8.2.1 Interfacial self-assembly of gold nanoparticles functionalized with polyelectrolytes

Our study on interfacial self-assembly of DNA-AuNPs (a Gibbs monolayer) induced by divalent salts ($MgCl_2$ and $CaCl_2$) suggested that the negatively charged DNA chains could be viewed as natural polyelectrolytes. Addition of salts could be used to control the solubility of polyelectrolytes through charge screening, and at a threshold salt concentration, the hydrophobic effect mainly arising from the hexyl-thiol groups overcomes the DNA's affinity to water, leading to interfacial accumulation of DNA-AuNPs. This study points to a new direction, where hydrophilic/hydrophobic effects of macromolecules can be exploited to design and construct organic-inorganic ordered structures at interfaces. Exploiting this concept, synthetic polyelectrolytes such as poly(acrylic acid) (PAA) grafted to gold nanoparticles via alkane thiol can be used to assemble nanoparticles at interfaces. Preliminary results have shown that the interfacial self-assembly and crystallization of PAA-AuNPs could be triggered by both salt concentrations and pH values. The critical salt concentration or pH appears to depend on the relative lengths of the hydrophilic PAA and hydrophobic alkane. Theoretical considerations can focus on the electrostatic free energy of PAA in the presence of salts as well as the effect of pH on the PAA hydrolysis.

The surface charge (zeta potential) of nanoparticles could be modified through functionalization with polyelectrolytes. 2D self-assembly of nanoparticles can be obtained by exploiting the electrostatic interactions between polyelectrolyte-functionalized nanoparticles and oppositely charged templates at the air−water interfaces. One choice of the charged templates is a Langmuir monolayer formed by lipids with head-groups of desired charge. Recently, it has been reported that negatively charged DNA-AuNPs or citrate-stabilized AuNPs were adsorbed to

positively charged templates such as a Langmuir monolayer of 1,2-dihexadecanoyl-3-trimethylammonium-propane (DPTAP) to form 2D tunable superlattices.[1, 2] 2D superlattices with the DPTAP monolayer and PAA-AuNPs can be explored. The relationship between lattice parameter and the length of PAA and core size of nanoparticles can be investigated.

8.2.2 Effect of salts on self-assembly of gold nanoparticles capped with polyethylene glycol

Our studies have demonstrated that the 2D and 3D self-assembly of PEG-AuNPs in aqueous solution is triggered by a salt, i.e., K_2CO_3, which is one of the specific salts that induce aqueous phase separation of PEG to form aqueous biphasic systems (ABS). It has been found that various salts including K_2CO_3, K_3PO_4, $(NH_4)_2SO_4$, Li_2SO_4, $MnSO_4$, $ZnSO_4$, and NaOH are effective to form APS of PEG, while some others such as NaCl, KCl and $MgCl_2$ are not.[3, 4] Meanwhile, in spite of experimental observations, attempts to elucidate underlying mechanism and related theory on ABS of PEG+salts are still lacking.[5, 6] Following our previous study, we can focus our efforts on the effect of various salts on formation of 2D superlattices by PEG-AuNPs. Surprisingly, our initial results have shown that a list of salts including NaCl and KCl exhibited ability to inducing 2D self-assembly and crystallization of PEG-AuNPs at the air−water interfaces and various salts showed subtle differences. The interfacial self-assembly of PEG-AuNPs induced by salts appears to be a more general phenomenon than the ABS of PEG+salts. More importantly, various options of salts allow for further exploration of the distribution of PEG and salts at the air−water interface. For instance, we have observed that Cs_2SO_4 slats affect 2D self-assembly of PEG-AuNPs and the fluorescence energy of Cs_2SO_4 is detectible. X-ray fluorescence near total reflection at different penetrating depths can be used to determine the vertical distribution of Cs^+ and SO_4^{2-} at the interfaces. This will provide insight on theoretical explanations of 2D self-assembly of PEG-AuNPs.

Our theoretical argument has pointed out that the interfacial self-assembly is driven by the need to reduce surface tension between the PEG shell and the surrounded salt solution. The PEG-AuNPs migrated to the air−water interfaces leading to lowering the surface tension of aqueous solutions. To confirm the theoretical consideration, we can reduce the surface tension of PEG-AuNP aqueous solution by loading a monolayer of simple lipids dihexadecyl phosphate (DHDP). The interfacial self-assembly of PEG-AuNPs can be studied with K_3PO_4 that shares the same phosphate group with the lipids. Our preliminary results have shown that DHDP monolayer prevented formation of interfacial self-assembly of PEG-AuNPs in the presence of K_3PO_4, which is in agreement with our theory. Future work can focus on systematic studies of the effect of K_3PO_4 on 2D self-assembly of PEG-AuNPs in the presence of DHDP. The surface tension of all the solutions in the absence and presence of DPDH and K_3PO_4 can be measured as well.

We have found that 3D assemblies of PEG-AuNPs formed following 2D self-assembly showed only short-range ordering using the salt K_2CO_3. Ways to achieve high crystallinity of the 3D assemblies of PEG-AuNPs can be explored in the future. The various options of salts and their subtle differences on the effect on 2D self-assembly may have influence on the long-range crystallization of 3D assemblies. Meanwhile, the effect of length of PEG can also be investigated.

8.2.3 Extending liquid-phase self-assembly of nanoparticle to functional nanodevices

All the methods we have developed for fabricating 2D and 3D assemblies are governed by the organic macromolecules and independent of inorganic nanoparticles. Thus our methods are general and readily applicable to other nanoparticles with different functionalities. For instance, magnetic nanoparticles such as magnetite and cobalt ferrite can be functionalized with PEG using a silane group.[7] Such PEG capped magnetic nanoparticles can be used to construct

tunable superlattices induced by the salts such as K_2CO_3. In the future, we can extend current method to a general one for self-assembly of plasmonic, magnetic, catalytic and luminescent nanoparticles.

Currently our studies have focused on the self-assembly of gold nanoparticles at the air−water interfaces or in the bulk. In order to fabricate real nanomaterials with various types of functionalities for potential applications, one needs to transfer the 2D and 3D assemblies to solid substrates. One approach to transfer 2D assemblies is the Langmuir–Blodgett technique. We can use this technique and others to fabricate tunable superlattices on solid substrates followed by functional characterizations. Functional nanodevices such as metamaterials can then be explored.

References

1. Srivastava, S.; Nykypanchuk, D.; Fukuto, M.; Halverson, J. D.; Tkachenko, A. V.; Yager, K. G.; Gang, O. Two-Dimensional DNA-Programmable Assembly of Nanoparticles at Liquid Interfaces. *J. Am. Chem. Soc.* 2014, 136, 8323-8332.
2. Srivastava, S.; Nykypanchuk, D.; Fukuto, M.; Gang, O. Tunable Nanoparticle Arrays at Charged Interfaces. *ACS Nano* 2014, 8, 9857-9866.
3. Willauer, H. D.; Huddleston, J. G.; Rogers, R. D. Solute Partitioning in Aqueous Biphasic Systems Composed of Polyethylene Glycol and Salt: The Partitioning of Small Neutral Organic Species. *Ind. Eng. Chem. Res.* 2002, 41, 1892-1904.
4. Huddleston, J. G.; Willauer, H. D.; Rogers, R. D. Phase Diagram Data for Several PEG + Salt Aqueous Biphasic Systems at 25 °C. *J. Chem. Eng. Data* 2003, 48, 1230-1236.
5. Hino, T.; Prausnitz, J. M. Lattice thermodynamics for aqueous salt–polymer two-phase systems. *J. Appl. Polym. Sci.* 1998, 68, 2007-2017.
6. Kenkare, P. U.; Hall, C. K. Modeling of phase separation in PEG–salt aqueous two-phase systems. *AIChE J.* 1996, 42, 3508-3522.
7. Larsen, E. K. U.; Nielsen, T.; Wittenborn, T.; Birkedal, H.; Vorup-Jensen, T.; Jakobsen, M. H.; Østergaard, L.; Horsman, M. R.; Besenbacher, F.; Howard, K. A.; Kjems, J. Size-Dependent Accumulation of PEGylated Silane-Coated Magnetic Iron Oxide Nanoparticles in Murine Tumors. *ACS Nano* 2009, 3, 1947-1951.